



HAL
open science

Energy management optimization of a wind-storage based hybrid power plant connected to an island power grid

Rubén Lopez Rodriguez

► **To cite this version:**

Rubén Lopez Rodriguez. Energy management optimization of a wind-storage based hybrid power plant connected to an island power grid. Electric power. Université Grenoble Alpes [2020-..], 2021. English. NNT : 2021GRALT020 . tel-03338743

HAL Id: tel-03338743

<https://theses.hal.science/tel-03338743>

Submitted on 9 Sep 2021

HAL is a multi-disciplinary open access archive for the deposit and dissemination of scientific research documents, whether they are published or not. The documents may come from teaching and research institutions in France or abroad, or from public or private research centers.

L'archive ouverte pluridisciplinaire **HAL**, est destinée au dépôt et à la diffusion de documents scientifiques de niveau recherche, publiés ou non, émanant des établissements d'enseignement et de recherche français ou étrangers, des laboratoires publics ou privés.

THÈSE

Pour obtenir le grade de

DOCTEUR DE L'UNIVERSITÉ GRENOBLE ALPES

Spécialité : GENIE ELECTRIQUE

Arrêté ministériel : 25 mai 2016

Présentée par

Rubén LOPEZ RODRIGUEZ

Thèse dirigée par **Ionel VECHIU**, Professeur, ESTIA
et codirigée par **Seddik BACHA**, Professeur des Universités,
Université Grenoble Alpes

préparée au sein du **Laboratoire ESTIA-Recherche / G2ELAB**
dans **l'École Doctorale EEATS**

Optimisation de la gestion de l'énergie d'une centrale hybride ferme éolienne-stockage connectée à un réseau électrique insulaire

Energy management optimization of a wind- storage based hybrid power plant connected to an island power grid

Thèse soutenue publiquement le **30 mars 2021**, devant le jury
composé de :

M. Ionel VECHIU

PROFESSEUR, ESTIA, Directeur de thèse

M. Seddik BACHA

PROFESSEUR DES UNIVERSITES, Université Grenoble Alpes,
Co-directeur de thèse

M. Jean Paul GAUBERT

PROFESSEUR, Université de Poitiers, Président

M. Cristian NICHITA

PROFESSEUR EMERITE, Université Le Havre Normandie, Rapporteur

M. Abdelkrim BENCHAI

DIRECTEUR DE RECHERCHE, Supergrid Institute, Rapporteur

Mme. Adriana AGUILERA GONZALEZ

PROFESSEUR ASSOCIE, ESTIA, Examinatrice

M. Edris POURESMAIL

PROFESSEUR ASSOCIE, Aalto University, Invité



(This page is intentionally left blank)

*I do not know anything, but I do know that everything
is interesting if you go into it deeply enough.*

Richard P. Feynman

(This page is intentionally left blank)

Acknowledgments

Firstly, I would like to express my admiration and gratitude to Prof. Ionel Vechiu (ESTIA) and Prof. Seddik Bacha (Université Grenoble Alpes), the supervisor and co-supervisor of my thesis, for their guidance and patience.

I would also like to show my gratitude to Prof. Jean Paul Gaubert (Université de Poitiers) for presiding the jury, to Prof. Cristian Nichita, (Université Le Havre), and Abdelkrim Benchaib, R&D manager at Supergrid Institute, for having reviewed this dissertation, as well as to Assoc. Prof. Edris Pouresmaeil (Aalto University) for his remarks that helped me improving the manuscript. This dissertation could not have been written without the continuous support of Assoc. Prof. Adriana Aguilera Gonzalez (ESTIA), who was also part of the jury.

I am grateful to the PhD students with whom I shared so many good times during my stay at the French Basque Country: Quentin, Samuel, Daniela, Sylvain, Barbara, Angel, Gilberto, Delphine, Itzel, Asmaâ, Michel, Michael, Adama, Ahmed, Zina, Valentine and Maxime, as well as to David, Octavian, Laura, Denis, Ignacio, Benjamin, Jean, Sylvie, Jean-Luc, Charlotte and all the colleagues of ESTIA. A special thank you is extended to Nadine Couture and Patxi Elissalde, research director and director general at ESTIA.

I must finish these acknowledgments by thanking my parents and sister, who were always by my side even though the distance, along with my loving wife Priscille for her kind support and comprehension during this difficult journey. This dissertation is dedicated to you.

(This page is intentionally left blank)

Titre : Optimisation de la gestion de l'énergie d'une centrale hybride ferme éolienne-stockage connectée à un réseau électrique insulaire

Résumé

Les îles sont des endroits propices au développement de l'énergie éolienne, mais les réseaux insulaires sont plus fragiles que les réseaux interconnectés et l'augmentation du taux de pénétration éolienne peut avoir des impacts sur la qualité de l'énergie et la stabilité du réseau. Dans un contexte d'augmentation de la part de l'énergie éolienne dans les DOM-TOM, les parcs éoliens sont de plus en plus confrontés aux exigences d'engagement sur la production malgré le caractère stochastique des ressources renouvelables.

Cette thèse porte sur la modélisation, la simulation et la gestion optimisée de l'énergie produite par une centrale hybride éolien/stockage électrochimique connectée sur le réseau insulaire de Guadeloupe. La centrale doit être capable d'injecter l'énergie dans le réseau en considérant plusieurs conditions de fonctionnement, y-compris le respect d'un engagement pris un jour à l'avance. Comme le non-respect du profil engageant entraîne des pénalités, la maximisation des revenus de la centrale exige une stratégie optimisée pour la gestion du système de stockage.

Pour y parvenir, la solution mise au point pendant cette thèse est basée sur une stratégie de commande prédictive à base de modèle (Model Predictive Control) et un algorithme d'optimisation quadratique. Cette stratégie permet de maximiser les revenus et en même temps de préserver la durée de vie du système de stockage. La méthodologie intègre les prévisions de production et peut être adaptée à plusieurs types d'énergies renouvelables et technologies de stockage.

Les performances de la centrale hybride éolien/stockage Lithium-ion pilotée par cette stratégie de commande innovante ont été analysées et validées dans le contexte du réseau insulaire de Guadeloupe grâce à l'environnement de co-simulation Matlab/PowerFactory.

Mots clés : réseau insulaire, réseau faible, éolienne, stockage, centrale hybride, gestion d'énergie, EMS, contrôle optimal, contrôle prédictif par modèle, programmation quadratique, garantie d'injection, profil engageant, énergies renouvelables.

Soutiens : Les travaux de recherche menés avec cette thèse doctorale ont été co-financés par la Région Nouvelle-Aquitaine, BPI France et la Fondation d'entreprises ESTIA dans le cadre du projet FUI Insul'Grid.

(This page is intentionally left blank)

Title : Energy management optimization of a wind-storage based hybrid power plant connected to an island power grid

Abstract

Often wind resources are abundant islands, making them good places for the development of wind power. However, island grids are more fragile than interconnected grids and increasing wind turbines penetration rates can affect grid stability and power quality. In a context of an increasing share of wind energy in the French overseas departments and territories, wind farms are increasingly faced with firm power requirements despite the stochastic nature of renewable resources.

This thesis focuses on the modeling, simulation and energy management optimization of the power output of a hybrid wind farm-battery storage power plant connected to the electrical system of Guadeloupe island. The plant must inject power into the grid considering several operating conditions, including the fulfillment of a commitment profile made one day in advance. As the disrespect of the commitment entails penalties, the plant revenues maximization requires a management strategy to optimally control the storage system.

To achieve this, a model predictive control and quadratic optimization-based strategy is proposed. This strategy maximizes revenues and at the same time preserves the lifespan of the storage system. The strategy integrates production forecasts in the optimization problem and can be adapted to several types of renewable energy and storage technologies.

The performance of the wind farm-Lithium-ion storage hybrid power plant driven by this innovative control strategy has been analyzed and validated considering the island grid context through a PowerFactory/ Matlab co-simulation environment.

Keywords: island grid, weak grid, wind turbine, energy storage, hybrid power plant, energy management, EMS, optimal control, model predictive control, quadratic programming, firm power injection, commitment profile, renewable energies.

Support: The research work carried out with this doctoral thesis was co-funded by the Nouvelle-Aquitaine Region, BPI France and the ESTIA Business Foundation as part of the FUI project Insul'Grid.

(This page is intentionally left blank)

Título: Modelado y simulación de la operación de una central híbrida para la integración de energías renovables en sistemas insulares

Resumen

Las islas son sitios usualmente adecuados para el desarrollo de la energía eólica. Las redes eléctricas de islas y sitios remotos, sin embargo, son más frágiles que las redes interconectadas y el aumento de la tasa de penetración de la generación eólica puede afectar la calidad de la energía y la estabilidad de la red. En un contexto de creciente participación de las turbinas eólicas en los departamentos y territorios franceses de ultramar, los parques eólicos se enfrentan cada vez más a requisitos de compromiso de producción.

Esta tesis se centra en el modelado, simulación y gestión optimizada de la energía producida por una planta híbrida parque eólico-baterías conectada a la red de la isla de Guadalupe. La planta debe inyectar energía a la red considerando varias condiciones de operación, incluyendo el cumplimiento de un compromiso de potencia adquirido con un día de anticipación. Dado que el incumplimiento del compromiso conlleva al pago de multas, la maximización de los ingresos de la central requiere de un sistema de gestión de la energía que controle eficazmente el sistema de almacenamiento.

Para lograrlo, la estrategia de gestión desarrollada asocia control predictivo de modelos (MPC) y optimización cuadrática, e integra en el problema de optimización las previsiones de producción eólica. La metodología maximiza los ingresos de la central y al mismo tiempo preserva la vida útil del sistema de almacenamiento.

El desempeño de la central híbrida gestionada por la estrategia de control propuesta ha sido analizado y validado considerando el contexto de la red insular en co-simulación dentro de los entornos PowerFactory y Matlab.

Palabras clave: red insular, red débil, turbina eólica, almacenamiento de energía, central híbrida, gestión de la energía, EMS, control óptimo, control predictivo por modelos, programación cuadrática, suministro firme de electricidad, perfil de compromiso, energías renovables.

Financiamiento: Los trabajos de investigación realizados en esta tesis doctoral fueron cofinanciados por la Región de Nueva Aquitania, BPI France y la Fundación Empresarial ESTIA como parte del proyecto FUI Insul'Grid.

(This page is intentionally left blank)

Acronyms

AC	Alternative current	MWp	Megawatts peak
EMS	Energy management system	NLP	Non-linear programming
ESS	Energy storage system	P	Active power
BESS	Battery energy storage system	PHS	Pumped hydro storage
CAES	Compressed air energy storage	PI	Proportional-integral
DC	Direct current	PCC	Point of Common Coupling
DFIG	Doubly fed induction generator	PV	Photovoltaic
DG	Distributed generation	QP	Quadratic programming
DoD	Depth-of-discharge	RE	Renewable energy
DSO	Distribution system operator	RES	Renewable energy source
FES	Flywheel energy storage	RSC	Rotor side converter
HPP	Hybrid power plant	SO	System operator
LSC	Line-side controller	SoC	State-of-charge
LP	Linear programming	TSO	Transmission system operator
MILP	Mixed-integer linear programming	VSC	Voltage source converter
MPC	Model predictive control	WECS	Wind energy conversion system
MPPT	Maximum power point tracking		

Symbols

A	System matrix	Q_{max}	Maximum battery cell capacity (Ah)
A	Exponential zone amplitude(V)	Q_u	Matrix weighting and adjusting the control effort of the inputs
A_{ineq}	Matrix containing information of the trajectory constraints	R	Battery cell internal resistance (Ω)
B	Input matrix	SoC	State-of-charge (%)
B	Exponential zone time constant inverse (Ah) ⁻¹	SoC_{ref}	State-of-charge set-point (%)
b_{ineq}	Matrix containing information of the trajectory constraints	SoC^{min}	State-of-charge lower threshold (%)

\mathbf{C}	Output matrix	SoC^{max}	State-of-charge upper threshold (%)
\mathbf{C}_c	Matrix of constrained variables	\mathbf{Q}_y	Matrix giving a weight to the different control objectives
\mathbf{C}_r	Matrix of regulated state variables	t, k	Current time of the optimization process
\mathbf{D}	Feedthrough matrix	$tolerance$	Distance between P_{SCHED} and the tolerated injection region limits (% of P_{MAX})
DoD	Depth-of-discharge	\mathbf{u}	Control action vector
E_0	Open-circuit voltage constant (V)	$\tilde{\mathbf{u}}(k)$	Control actions sequence at time k
\mathbf{f}	Matrix containing information of the outputs prediction	\mathbf{u}^T	Transposed of the control action vector
\mathbf{H}	Hessian matrix	v_{BESS}	BESS voltage
i^*	Filtered current (A)	$\mathbf{x}(t), \mathbf{x}(k)$	Continuous and discrete-time state vector
it	Battery cell extracted capacity (Ah)	$\dot{\mathbf{x}}(t), \dot{\mathbf{x}}(k)$	State vector Derivative
K	Polarization resistance (Ω) or polarization constant (V/Ah)	$\tilde{\mathbf{x}}(k)$	State trajectory vector
n	Number of state variables	$\mathbf{x}(k+1)$	One-step-ahead prediction of the state vector
n_c	Number of constrained variables	$\mathbf{x}(k+i)$	Prediction of the state vector for any $i \in \{1, \dots, N_p\}$
n_r	Number of regulated outputs	$\mathbf{y}_r(k)$	Vector of regulated outputs
n_u	Number of inputs	$\tilde{\mathbf{y}}_r(k)$	Sequence of the predictions for the regulated outputs
N_c	Control window length	$\tilde{\mathbf{y}}_{ref}(k)$	Vector of future desired outputs
N_p	Control and optimization window length	$\mathbf{y}_r(k)$	Vector of regulated outputs
P_{BESS}	BESS Power (MW)	α	Current filter mitigating factor
$P_{BESSref}$	BESS power set-point	Δt	BESS model step time

P_{INJ}	Power transferred to the grid	Γ	Objective function
$P_{lower\ limit}$	Tolerated injection region lower threshold (MW)	λ_i	Sub-cost weight
$P_{upper\ limit}$	Tolerated injection region upper threshold (MW)	Π_i	Selection matrix giving the i -th vector of $\tilde{\mathbf{u}}, i \in \{1, \dots, N_p\}$
P_{MAX}	WECS' installed capacity	Φ	Constant matrix involved in the prediction that depends on \mathbf{A}
P_{SCHED}	Committed power injection	Ψ	Constant prediction matrix that depends on \mathbf{A} and \mathbf{B}
P_{WECS}	Wind-generated power	τ	BESS model current filter time constant
Q	Reactive power (Mvar)		

(This page is intentionally left blank)

General introduction

Towards a smarter grid

Although the electricity is as old as nature itself, it took centuries of progress and ultimately science for the mankind to start understanding it. It was barely in the late 1900s that the electrical power systems started developing to gradually transform into the large networks equipped with sophisticated devices and centralized operation we know nowadays. Under the current energy paradigm, electrical systems are three-phase, 50 or 60 Hz AC networks that can be separated into [1]:

- Generation sites, large units located at strategic locations usually from several kilometers to a few hundreds of kilometers away from consumption sites.
- Transmission lines, high-voltage aerial cables connecting the generation sites to distribution grids through step-up and step-down substations.
- Distribution grids, radial networks allowing the unidirectional flow of electricity towards passive end-users.

In a context of growing carbon footprint awareness, sustainable development has become a means for social welfare improvement. The requirements for clean and reliable power supply have led to the establishment of incentives favoring the use of renewable energies. The connection of this kind of energy sources at the transmission and distribution levels, the arrival of smart meters and consumers that produce and consume energy, the advent of electric vehicles and the possibility to store the generated energy in DC batteries or other storage technologies, are all signs of a new power system paradigm: the Smart Grid [1]. The Smart grid term appeared for the first time in 2003 in an article of *Public Utility Fortnightly Magazine* [2], [3]. According to the European commission's Smart Specialisation Platform (S3P) [4] a smart grid is an electricity network that employs amongst others a communication infrastructure, intelligent electronic devices, sensors, cyber security devices and an advanced metering infrastructure. Therefore, it can integrate the actions of all users connected to it in order to ensure an economic, efficient, sustainable and secure electricity supply.

In a few words it consists of adding control, sensors, and information technologies to the existing power grids so rendering them “smarter”.

Renewable energy sources and weak island grids

Up to now, the growth seen by renewable sources has been mainly associated with continental-scale interconnected grids. The penetration of renewable sources in those systems is however very low if compared with the capacity installed. This implies that in large electrical networks the variability in the output of renewable facilities is absorbed by the system [1]. In contrast, as the penetration of renewable energy resources in islands and remote areas grow, ensuring power quality and reliability based on sources whose outputs are more variable becomes a challenging task. Moreover, overseas territories power systems are weak grids in which the frequency stability is highly vulnerable to load variations.

Remote islands grids are also characterized by:

- Having geographical locations that favor the access to solar radiation and wind, making them good candidates for wind turbines and PV panels deployments.
- Impractical interconnecting to neighboring grids due to remoteness or other constraints related to climate conditions or subsea conditions.
- Dependence on imported and usually expensive fossil fuels, which means carbon dioxide emissions and higher kWh prices for consumers.

Hybrid plants combining wind turbines and battery storage

While the power output of flexible generation facilities such as hydroelectric dams or natural gas power plants can be rapidly increased or decreased, wind-generated power depends on wind currents that cannot be controlled or stored. Hence, even if a wind turbine can be shut off or slowed down, nothing can be done if the power demand is high during low wind speed conditions.

When paired with wind turbines, battery energy storage systems (BES) add the capacity to absorb power production fluctuations and to adjust the power output. Within a grid-connected wind farm-battery storage hybrid power plant (HPP) the dispatch of generation and storage resources to meet day-ahead power production plans requires an energy management system (EMS). In the current case, the EMS must control the battery system charges and discharges according to the instant variations in the wind energy conversion system (WECS) output while respecting the generation schedule. Commonly, EMSs are focused not in one but several objectives at the same time (making the maximum possible profit, obtaining the minimum possible losses, etc).

The efficient arbitrage of the power exchanges within the hybrid plant so the plant output (the power injected into the island grid) respect both the contractual supply commitment and the applicable grid codes is a power dispatch problem. The sizing of the plant (WECS and

BESS) is not part of the reach of this PhD. The spotlight is rather put on both on the plant's EMS and the modeling of the HPP and the utility grid.

Objectives of this PhD

Within the frame described above, the general objective of this PhD. is:

- **To develop an energy management strategy ensuring the wind farm-Li-Ion BESS Hybrid Power Plant the provision of a grid service that consists in complying a day-ahead power injection commitment as the WECS output evolves.**
- **The main case of application which is considered is the Guadeloupean electricity network.**

In addition to this main objective, the secondary goals of the present work are:

- To review the management techniques applied in island grids.
- To take into account the grid code requirements for wind energy conversion systems in island networks.
- To review energy management approaches for the optimal control of the BESS.
- To implement models describing the functioning of the wind farm-BESS HPP and for the Guadeloupean utility grid.
- To develop advanced control strategies for the control of the BESS.
- To test and validate the developed energy management strategy in a simulator considering the HPP and island network models.

Therefore, in the scope of this thesis, first, the management strategies applied in island grids are analyzed, followed by the review of the grid code specifications for wind turbine systems in isolated grids. From this analysis are reviewed the possible energy management and optimization algorithms. Then, the modeling takes place alongside the development of the advanced control strategy. Then after, the resulting strategy is tested through simulation without the interaction with the utility grid and finally, considering all the models developed .

Overview of this PhD

This doctoral dissertation is organized into seven chapters.

The first chapter describes the grid management aspects of island grids as well as the grid code requirements for the supply of power using wind turbines in such isolated context. After discussing the benefits of associating energy storage and wind power, the chapter ends with the definition of the operational requirements for the hybrid power plant.

Then, the second chapter deals with wind-storage hybrid power plants. A review of architectures and the different strategies employed for the energy management of hybrid renewable-storage power plants is presented.

The third chapter establishes the models for the main grid and the hybrid power plant systems. The software tools employed for the modeling implementation and validation are DIgSILENT PowerFactory and Matlab.

Next, the fourth chapter presents the design of the model predictive control (MPC) strategy for the energy management of the hybrid power plant. For this purpose, several steps are defined comprising the problem definition, the optimization method selection and the cost function definition, which converge in a global mathematical description of the strategy.

The fifth chapter presents the validation of the proposed control and optimization strategy through Matlab/Simulink simulations. A rule-based algorithm is employed for comparison.

In the sixth chapter the proposed control and optimization strategy is applied to the management of the grid-connected power plant in PowerFactory.

Finally, chapter 7 presents the concluding points and contributions offering future lines about the developed topics. A diagram to present the chapters and their organization is presented in Fig. 0.1.

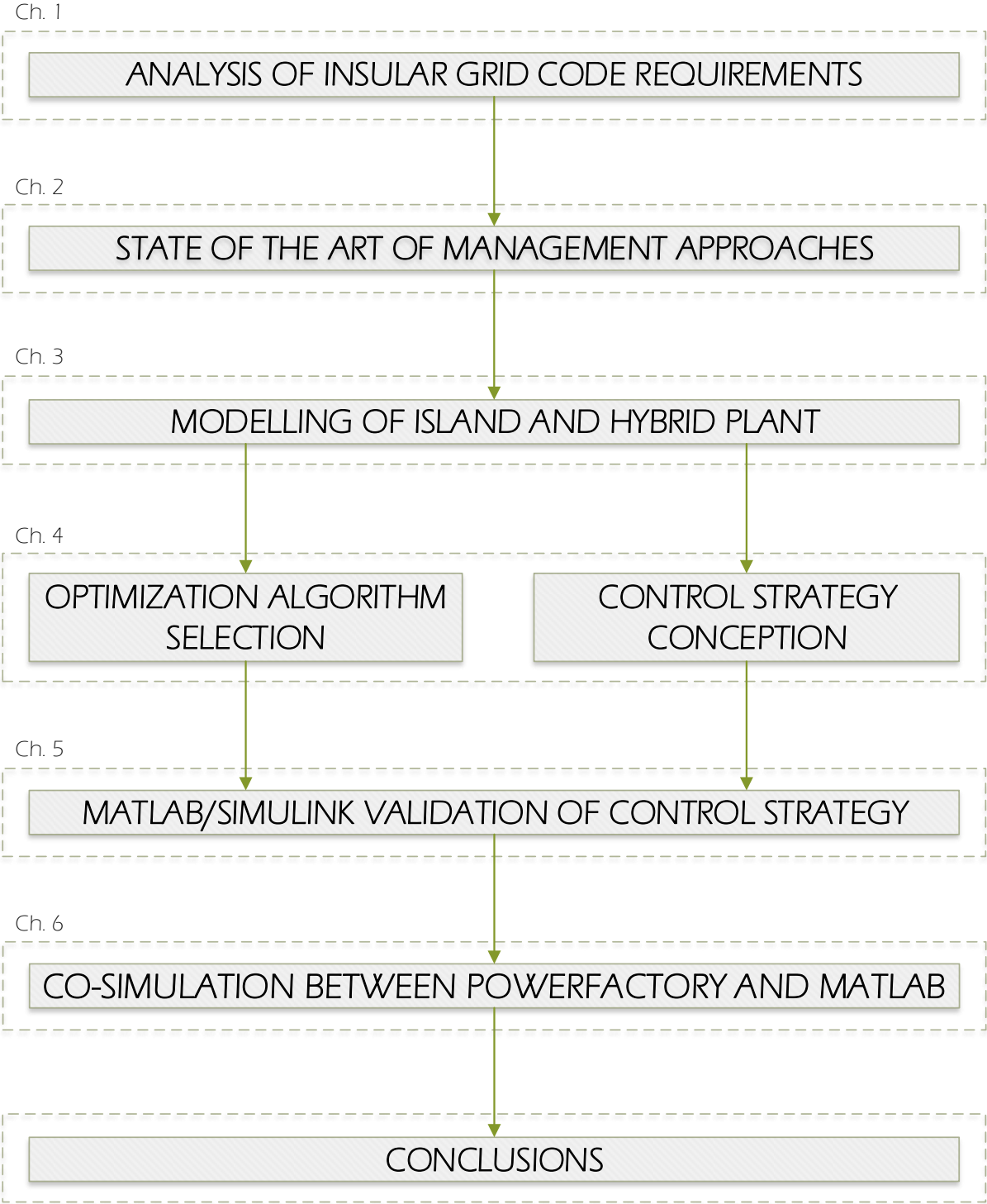


Fig. 0.1. Chapters organization diagram.

(This page is intentionally left blank)

CHAPTER

1

Grid code requirements for island grid-connected wind-storage hybrid power plants

Summary

1.1 Introduction	8
1.2 Island grids features and management	8
1.2.1 Island grids management: possibilities and challenges	10
1.2.1.1 Active power-frequency control	10
1.2.1.2 Reactive power-voltage control	12
1.3 Grid codes requirements.....	13
1.3.1 Grid code for RE in weak grids	14
1.3.1.1 Regulations for continuous operation	14
1.3.1.2 Specific requirements under network disturbances	19
1.4 Wind power and energy storage.....	22
1.4.1 Wind power and commitment profiles	22
1.4.1.1 Wind power in the electricity markets	23
1.4.1.2 Commitment profile and injection band	25
1.4.2 ESS applications for grid-connected WECS	26
1.4.2.1 ESS applications for WECS integration	26
1.4.2.2 ESS applications for grid support	27
1.4.2.3 Demand-side applications of ESS.....	28
1.5 Definition of the operating conditions for the wind-storage hybrid power plant.....	28
1.6 Chapter conclusions	30

Chapter overview

This Chapter describes the grid management aspects of island grids as well as the grid code requirements for the supply of power using wind turbines in such isolated context. After discussing the benefits of associating energy storage and wind power, the Chapter ends with the definition of the operation requirements for the hybrid power plant.

1.1 Introduction

This thesis was prepared in the context of the Insul'Grid project. Headed by VALOREM, this project promotes the deployment of RES technologies on non-interconnected island networks and aims at the energy independence of those remote territories. Even with abundance of renewable energy resources such as wind and sun, weak grids pose challenges for the integration of RE-based facilities. The project's main objective is the development of an 8 MW wind turbine system, 4 MW / 2,32 MWh Li-Ion battery storage hybrid power plant (HPP) to supply power to the Guadeloupean electrical system.

The problems of storage system type selection and sizing, as well as the generation technology choice and design, and plant architecture definition are not part of the scope of the thesis. Other project partners carried out those studies, and therefore, the results they found are here considered as input data. The efforts are focused on the formulation of an energy management strategy to effectively manage the HPP power flows to provide guaranteed (firm) power to the utility grid. The development of the simulation models allowing the test of the proposed EMS is also part of this work.

This first Chapter starts with a description of the differences between mainland and island grids. Then, the grid code requirements for supplying power from wind turbines into insular grids is presented. After describing the possibilities offered by associating a storage system to wind power, the Chapter ends with the specification of the HPP contractual operation conditions.

1.2 Island grids features and management

The main feature characterizing island power grids is their very limited size. Two types of island grids can be identified:

- Non-interconnected island power systems (like Guadeloupe or Nouvelle Calédonie).

- Partially interconnected islands (like Corse, relied through the AC link Sardinia-Corse).

By contrast, island grids non-linked to a mainland power system are characterized by:

- Low short-circuit power: the transmission-level voltages are usually lower in small island systems if compared to large interconnected mainland systems. Moreover, isolated island systems comprise a lower number of generation units whose installed capacity is also lower. All this leads to small short-circuit power values.
- High sensitivity to production variations: the frequency variations in mainland systems are minor since the instantaneous mismatches between generation and loads are small compared to the amount of synchronous generation dispatched. In small islands, the frequency deviations are more important and can lead to frequency collapse.
- Limited installed capacity: due to technical and economic reasons the maximum power of the generation units is limited, leading to higher installation costs per kilowatt.

The latter two island systems characteristics lead to primary reserve requirements that are important (in percent of the total installed capacity). This is contrary to the mainland grid case where the instant primary reserve values are very small with respect to the total amount of power produced. The maximum available power supply minus the expected peak demand is known as the reserve margin.

In order to ensure that the primary reserve required is available, some generators in the power system are operated below their rated power, lowering the efficiency of the transformation from primary energy to useful energy. The considerable margins of reserves involve significant costs and have an important impact on the cost price of the energy produced in the island grid. Thus, reserve margins need to be reduced as much as possible while maintaining the reliability of the electricity system. As outages compromising the existing capacity may occur, load-shedding procedures are a common means for restoring the balance between generation and consumption.

In addition to the above points, island grids do not present the following advantages of mainland systems [5]:

- The possibility of relying on larger and cheaper power stations.

- The load smoothing due to the distribution of the consumption centers throughout a continental-size power grid, which eases the daily power consumption forecasting and generation scheduling.

1.2.1 Island grids management: possibilities and challenges

An electrical system can be characterized by its frequency and voltage levels. The stability of these variables around contractual values ensuring the system stability. It is important for the network's operator to satisfy the system load in the best possible way, that is ensuring the economical and reliable operation of the grid while ensuring that the different grid elements are within permissible limits.

Variations in active power affect mainly the grid frequency whereas reactive power is principally dependent on voltage magnitude. Hence, active power-frequency and reactive power-voltage are controlled separately [6]. The main characteristics of these controls are briefly presented in the following sections.

1.2.1.1 Active power-frequency control

The frequency in a conventional power system represents the speed of synchronous generators (all alternators run at the same electrical speed). Frequency stability is ensured by the balance between production and consumption. The balance between production and consumption provides frequency stability. Thus, load or production variations have the effect of modifying the system frequency. When the production is greater than the consumption, the frequency increases and vice versa. The grid frequency is maintained at its set-point (50 Hz in Europe) by acting on the generation units. This is made possible by power reserves distributed over different generation units and according to a three-levels hierarchical control, called primary, secondary and tertiary frequency control [7].

Primary control

After a disturbance, the governors of the units participating in the primary frequency control increase or decrease their turbine power to drive the frequency close to the set-point value. Primary control aims to re-establish a balance between generation and demand within a few seconds. According to the frequency deviation the generator power is changed.

Shortly following a disturbance, the governors of the units participating in primary control will increase/decrease their turbine power and drive the frequency close to its nominal value. The change in the generator power is proportional to the frequency deviation and is shared among participating units according to the gain $1/\partial$, of their primary controllers.

$$(P - P_0) = \frac{1}{\partial} (f - f_N) \quad \text{Eq. 1.1}$$

where ∂ represents the slope of the droop (%), P is the modified power output of the generator (MW), P_0 is the scheduled active power of the generator (MW) that is supplied at nominal frequency, f_N (Hz), and f is the grid frequency (Hz), Fig. 1.1.

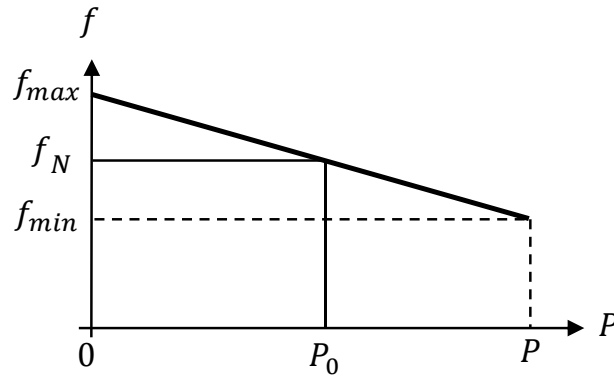


Fig. 1.1. Frequency droop characteristic curve.

Two concepts that intervene in this control strategy are the primary reserve and the power frequency characteristic. The first corresponds to the system's ability to restore production-consumption balance when consumption is in excess. For that, the system must have enough power reserve, $P - P_0$. The power frequency characteristic, K (MW/Hz), of the generator corresponds to the variation of power compared to the variation of frequency.

$$K = \frac{1}{\partial} \frac{P_N}{f_N} \quad \text{Eq. 1.2}$$

This expression is valid for productions below the nominal power. In an island grid a critical incident could lead to the saturation of the production units, making the power frequency characteristic difficult to determine [5].

Secondary control

The primary control permits re-establishing the balance between production and consumption. Nonetheless, it leads to a gap Δf among the grid frequency and the set-point value. In an island network the secondary regulation has a single objective which is to bring out the system frequency at its set-point. In an interconnected system, secondary regulation has the additional objective of restoring the power exchanges between adjacent control areas to their contractual values. The secondary frequency control intervenes about 10 seconds after the primary control has stabilized the system frequency, when generation units not participating of the secondary control rebuild their primary reserve by returning to their initial operating point.

Tertiary control

Following an incident in the island system, it is possible that the secondary reserve is exhausted before completely resolving the frequency deviation. Tertiary control modifies the dispatch set-points of the generation units participating so that the secondary reserve can be restored, and the frequency restored to its nominal value. It also compensates for the imbalances among production and consumption as this difference slowly evolves. In island systems tertiary control is basically composed by combustion turbine generators.

Critical case: load shedding

In critical situations caused by the sudden loss of a substantial part of the production, primary control may not be enough to limit the frequency drop. In this case, some loads are shed in order to stabilize the system as quickly as possible. In island environments where such situations occur more frequently, certain critical loads are preserved and not considered for shedding. Also, the interconnections affected by the load shedding are varied periodically (e.g. every month) not to affect the same consumers each time there is a grid event [5], [7].

1.2.1.2 Reactive power-voltage control

This section presents the main characteristics of voltage regulation in island networks.

Same as for active power, the overall balance of the reactive power produced and consumed in the electrical system must be maintained. The aims of reactive power control in the network are [5]:

- Maintain the system voltage profile within the contractual ranges.
- Reduce overall network losses.
- Maximization transmission capacities of active power in the lines;
- Maintain high stability margins.

While the loads in an electrical system present active power and reactive power components, the reactive power absorbed in the system is delivered by generation units and reactive compensators. The active and reactive power exchanges between sources and loads lead to voltage variations. Given the small size of an island network, the difference between sending and receiving end voltage of a transmission line can be expressed as

$$\Delta V = \frac{R \cdot P + X \cdot Q}{V} \quad \text{Eq. 1.3}$$

where ΔV is voltage variation (V), V is the receiving end voltage (V), R and X are the line resistance and reactance (Ω), P (MW) and Q (Mvar) are the amounts of active and reactive power being transmitted.

In order to reduce the transits of reactive power between transmission and distribution networks (Q in Eq. 1.3), the reactive compensators should be installed near the loads, in consumption nodes. Moreover, high-voltage level lines in the transmission network being more inductive than resistive, the reactive power transits induce important voltage drops in those lines. In the case of transmission lines in an island grid, the reactances are typically five times bigger than the resistances [5].

Voltage control in continental grids is hierarchical and operates at three different levels temporary and spatially independent. Primary control keeps the voltage at the terminal of the generators at their set-point values. Secondary voltage regulation's first objective is the automatic voltage control at the power system's main transmission buses. Tertiary regulation is a nationwide voltage-reactive power optimization function providing voltage set-points to ensure the safe and economic system operation. Unlike mainland systems like France's transmission network comprising about 35 voltage control zones, insular grids usually contain only one control zone [8]. Thus, the tertiary regulation of island systems becomes secondary regulation. Two types of adjustments can be identified in non-interconnected grids:

Primary control

Primary control of generators stator voltages is realized by devices known as automatic voltage regulators (AVR). Rapid voltage variations at the generator's terminals are compensated by the primary control which brings the voltage back to a value close to the set-point [8].

Secondary control

Secondary voltage regulation is a manual adjustment through which the network's operator coordinates the control actions required to maintain the voltage profile within permissible limits. For economic (losses reduction) and safety (stability of the generating sets and dynamic withstand of the voltage) reasons weak grid network operators seeks to maintain the voltage profile as high as possible [5].

1.3 Grid codes requirements

Grid codes are technical specifications defining the requirements for grid-connected facilities (power plants or loads) to ensure the safe, secure and economic operation of the electricity system. Severe penalties may be incurred if the facilities do not meet the requirements. It is the corresponding transmission system operators (TSO) or distribution system operators (DSO) who determines the requirements for a given project. Nonetheless, grid

codes are more or less standardized among countries with developed electrical networks, aiming at the simplification of the planning and implementation of new projects [9].

1.3.1 Grid code for RE in weak grids

Wind turbines power levels steady growth has led to an important penetration of wind energy into the existing power systems [10]. Consequently, WECS are increasingly coping with system stability support requirements, that historically were handled by conventional power stations.

In the context of island grids, the issue of variability in the output of RES-based sources like wind turbine or PV panels is more pronounced as penetration increases [11], [12]. Power quality issues associated with RES include voltage transients, harmonics and frequency deviation. For that, maintaining reliability, stability and efficiency of insular grids with highly variable energy resources is a particularly complex task [11], [13]. To provide stability and power quality, several technical requirements known as grid codes have been gradually developed by TSOs or DSOs regarding the interconnection of WECSs with the electric power systems.

Several relevant publications are available that deal with grid code requirements for wind turbine (WT) technology. Reviews of the grid code requirements for integration of WECSs in mainland systems have been provided [9, 13-20]. However, academic literature discussing island grid code requirements is scarcer. Grid code requirements for large-scale integration of renewables in an insular context are discussed in [21], [11], references on which the description presented below is mainly based .

Grid codes define the physical connection point requirements to be followed by the energy production equipment for being connected to the grid. Moreover, it should provide rules for a regulatory framework for renewable energy plants to support grid stability [21], [11].

1.3.1.1 Regulations for continuous operation

Voltage and frequency

The voltage fluctuation sensed at the PCC is linked to the connection point's short circuit impedance and the real/reactive power output of the renewable energy plant. For this, maintaining the voltage stable within a desired range of values may be challenging for the continuous operation of the renewable plant. Consequently, the weaker the isolated system, the more difficult becomes the injection of additional renewable generation. In addition to that, the requirements set by the corresponding system operator vary depending on each insular power grid's characteristics (in terms of size or strength).

Frequency nominal range is dictated by the power connections' strength, extension and size of the power reserve, and overall inertia of the installed power generation infrastructure. Fig. 1.2 presents, as an example, the operation area of voltage and frequency defined for the French insular grid code.

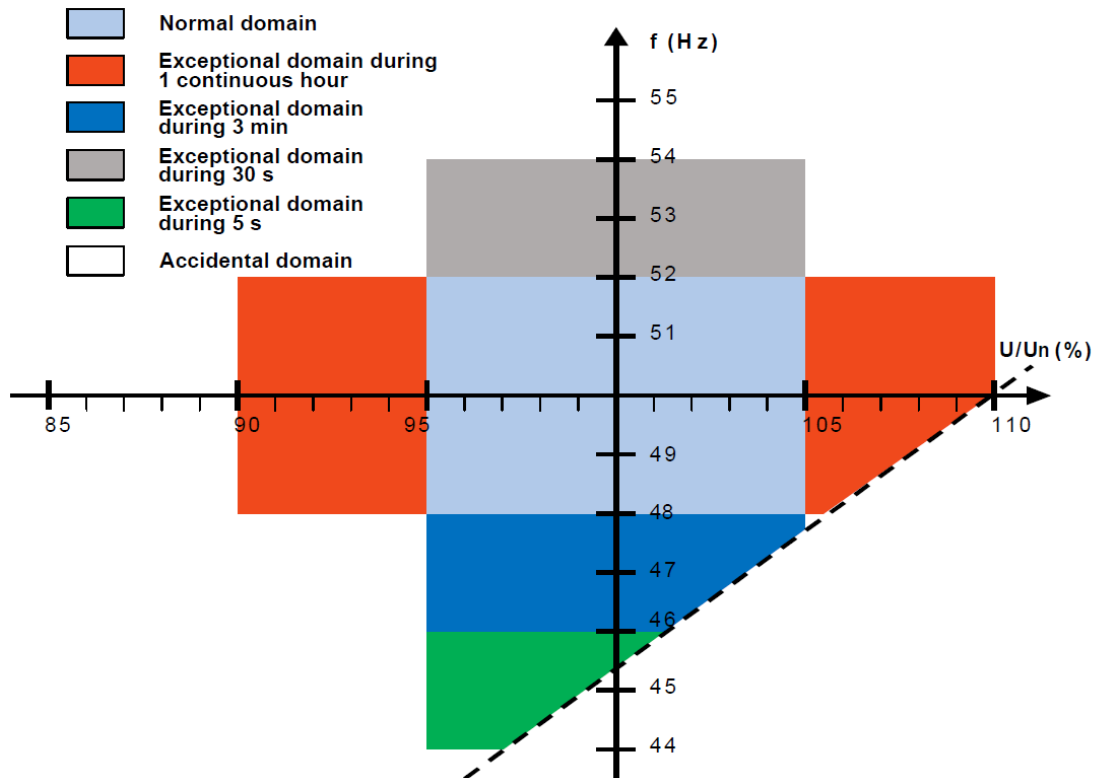


Fig. 1.2. Operating area of voltage and frequency, French insular grid code [22].

Active power control

Active power control refers to control rules to manage the power the generation units deliver to the grid. Solar power plants and wind turbine systems must comply with this requirement by incorporating local and remote active power control capabilities. Wind turbine systems must be able to adjust their power output to a given level (active power curtailment), either by disconnecting wind turbines or by pitch control action [15].

- Upper limitation: parameter intended for restricting the renewable plant's maximum power output. Allows the SO to prevent instabilities in the active power balance caused by the stochastic nature of wind and solar resources.
- Range control: unlike conventional generation units, renewable sources are non-dispatchable. To introduce output power dispatch flexibility and extend the primary control function to RES-based facilities, renewable generation units need to be equipped to curtail their power production. With their active power production modulated to a

range given by a minimum and a maximum of their rated capacity, output power dispatch flexibility can be introduced, and the primary control function can be extended to RES-based facilities.

- *Ramping control*: the ramping speed of active power production must be limited in upwards direction (increased production due to increased wind speed or due to modification of the upper limitation) [16]. Faster wind power output variations are filtered through the imposition of a ramp rate.
- *Delta control*: delta control is a way of securing spinning reserve based on renewable generation. The output power is artificially lowered below the available power at the time when the generation takes place. The difference is kept as a reserve and can be released for frequency regulation (primary and secondary control) and to support the grid voltage through the injection of reactive power into the grid.

Power-frequency response

Energy unbalances deviate the power grid frequency from its nominal value. As the unbalance grows, a larger deviation of frequency is expected to occur, threatening normal power operation. To maintain the deviations within safe levels, frequency monitoring and corrective actions are handled by conventional generators (primary control), and if necessary, the system operator activates the spinning reserve (secondary control). In the case of European grid islands, frequency regulation from wind farms is not required by local grid codes [11]. However, the capability to restore generation/demand balance is required by some European countries [11], [23-26]. Usually, mainland TSOs impose the wind power plants a droop characteristic for primary reserves activation while no compliance of these regulations is directly required for solar power plants.

As an example, in Fig. 1.3 is presented the droop characteristic for activation of primary reserves corresponding to the requirements set out by the Irish regulations for wind power plants. Points *A* to *E* are determined by the TSO before the beginning of operation of the generation unit. The activation of the power reserves is to be overseen by automatic local controllers. At nominal system frequency, the power extracted from the WECS is below its available active power. This derated operation allowing the WECS to supply positive and negative power reserves (i.e. to ramp power both upwards and downwards in response to deviations in the system frequency [18]). Thus, once the frequency falls below the point *B*, the frequency response system must ramp the WECS power output upwards in accordance with the trajectory *B – A*. If the frequency rises to a level above the point *D*, the WECS output shall

ramp down following the trajectory $C - D - E$. For frequencies at or above E , no active power output is expected from the WECS [15].

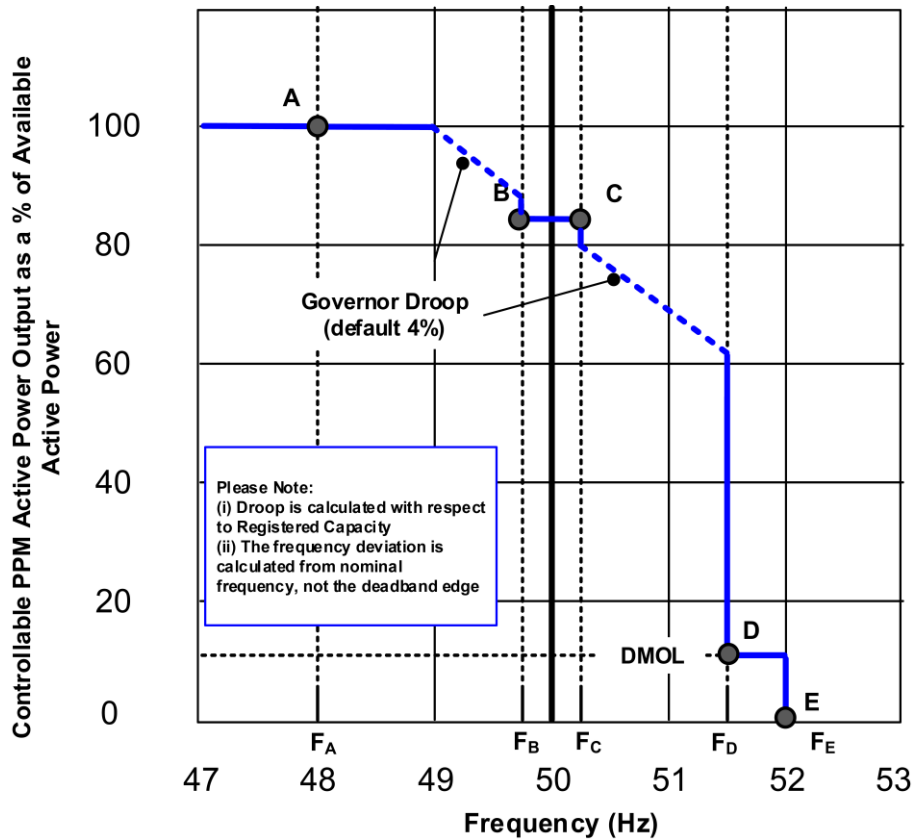


Fig. 1.3. Power-frequency response according to requirements set by Irish regulation for wind power plants [25]

Reactive power control

Reactive power control helps compensate transmission equipment like cables and transformers, as well as maintaining voltage stability. Reactive power control is then an important technical requirement for ensuring the reliable and efficient operation of transmission and distribution grids [10]. While at the distribution level voltage regulation is still controlled by the distribution substations, wind turbines are no longer operated to maintain the power factor at 1, as in early implementations, and the task of ensuring bulk system voltage regulation at the transmission-level is not exclusive to synchronous generators. In fact, most European grid codes in the mainland context have extended reactive power capability along with active power generation to wind turbines and solar PV. Similarly, the strong technical constraints associated with the increasing propagation of RES-based plants in insular systems, will force the incorporation of this ancillary service for security reasons [21].

WECs deployed in remote areas are often connected at weak points in the insular grid. For this, grid vulnerability to voltage drop due to the energy transit at the point of common

coupling is high. Alongside this is the fact that the variability of RES introduces complexity to the task of maintaining the voltage the acceptable limits.

Since each isolated power network has its own specificities, reactive power needs must be dealt with to meet local interconnection issues. This requirement is intervening in three different ways: by power factor control, by means of a Q set-point or by managing reactive power flows as a function of the grid voltage. For now, the insular approach relies on a power factor band specification that must be respected by the wind power facility under normal operating conditions. Common power factors range go from 0,95 lagging to 0,95 leading at full active power with voltage within 90 % and 110 % of nominal. Other power factor ranges may go from 0,86 inductive to 1.

Given the alternative ways to express reactive power support are not imposed by island grid operators, the P-Q and V-Q specifications for two European countries are shown in Fig. 1.4 as examples. the reactive power requirement Q_g as a function of the active power P_g according to the German grid code Fig. 1.4.a show, whereas Fig. 1.4.b displays Q_g as a function of the grid voltage V_g specified in the Spanish grid code. When the wind farm provides nominal active power, it should be able to deliver 0,41 pu or to absorb 0,33 pu reactive power. The power factor should then be adjusted somewhere between 0,93 leading and 0,95 lagging. At 20 % of the rated active power, the power factor ranges between 0,44 leading and 0,52 lagging. Between 0 and 20 % of the rated power the reactive power requirement is variable [10].

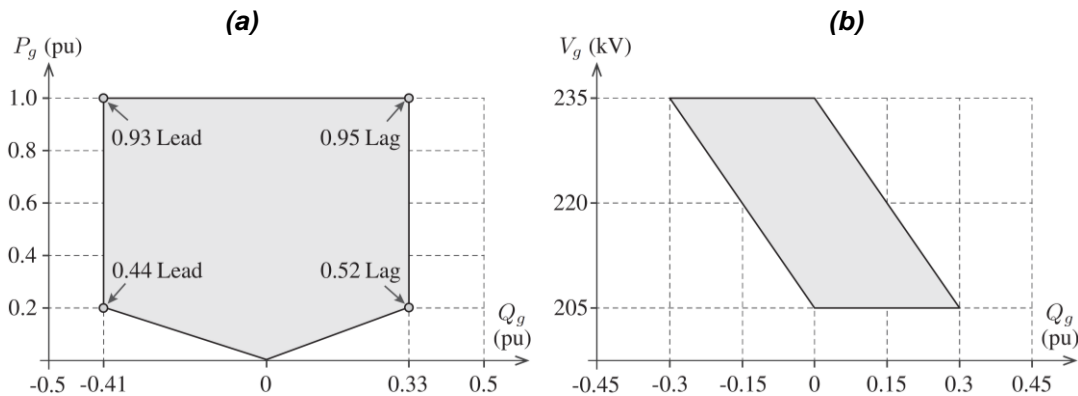


Fig. 1.4. Reactive power requirements for grid-connected wind power facilities: (a) P-Q profile in Germany, and (b) V-Q profile in Spain. Modified from [10].

Modern WECS configurations like the doubly-fed induction generator (DFIG) or the permanent magnet synchronous generator (PMSG) types can deliver or absorb reactive power while at the same time active power is generated, configurations that will be explained in Chapter 2. These capabilities also apply to PV power stations which can be relied to the grid through the same topologies of power converters.

According to the reactive power compensation method according to the grid voltage (Fig. 1.4.b), the wind turbines have to meet the reactive power capability contained in by the polygon specified by the TSO.

Emulating inertia of conventional power plants

When there is a failure in one of the generation groups, or new loads are connected, grid frequency drops at a rate determined by the inertia sum of all generators. One of the characteristics of small island grids is lower grid inertia in comparison to mainland continental-size power networks [11]. “Virtual” wind inertia is a relatively new concept that can increase wind turbine’s power-frequency capability to act on the grid frequency. Using additional control loops a variable-speed wind turbine can provide emulated inertia. The concept is based on the utilization of the kinetic energy stored in the rotating masses of the wind turbines [27]. An alternative method for generating emulated inertia consists in increasing the wind turbine torque allowing a reduction in the system’s load-generation imbalance[11]. In [28], it is demonstrated that virtual wind inertia can exceed the inertial power response of a DFIG or PMSG generator with the same inertia [21], [28].

1.3.1.2 Specific requirements under network disturbances

Whereas conventional power plants, such as synchronous generation groups-based plants, have strong capabilities to withstand symmetrical and asymmetrical faults without being disconnected, when the deployment of wind turbines started, grid faults handling was not critical. This means wind turbine were disconnected during grid faults. In an island grid scenario in which the energy mix comprises considerable RE generation if a large wind power facility is unexpectedly shutdown, the impact on frequency stability can be important. For grid security reasons, RE plants in an island grid context should tolerate grid faults for a short time, at least for the fault clearance.

Fault ride-through (FRT) capability

Grid disturbances like voltage sags/swells may lead to the disconnection of large-scale wind generation units. FRT requirements are imposed to overcome instability scenarios in the utility grid stimulated by the sudden disconnection of generation units. Starting with the German utility operator E.ON in early 2003, the TSO and DSO of various countries imposed similar FRT profiles with diverse voltage dip magnitudes and grid fault durations [10], [29], [30]. The FRT requirement is a general category covering zero-voltage ride-through (ZVRT), low-voltage ride-through (LVRT), and high-voltage ride-through (HVRT). ZVRT and LVRT

stipulations are related to grid voltage sags, while the HVRT corresponds to grid voltage swells. In the ZVRT profile, the grid voltage becomes zero during a grid fault, whereas in the LVRT profile, the voltage becomes 15-25 % of its rated value [10].

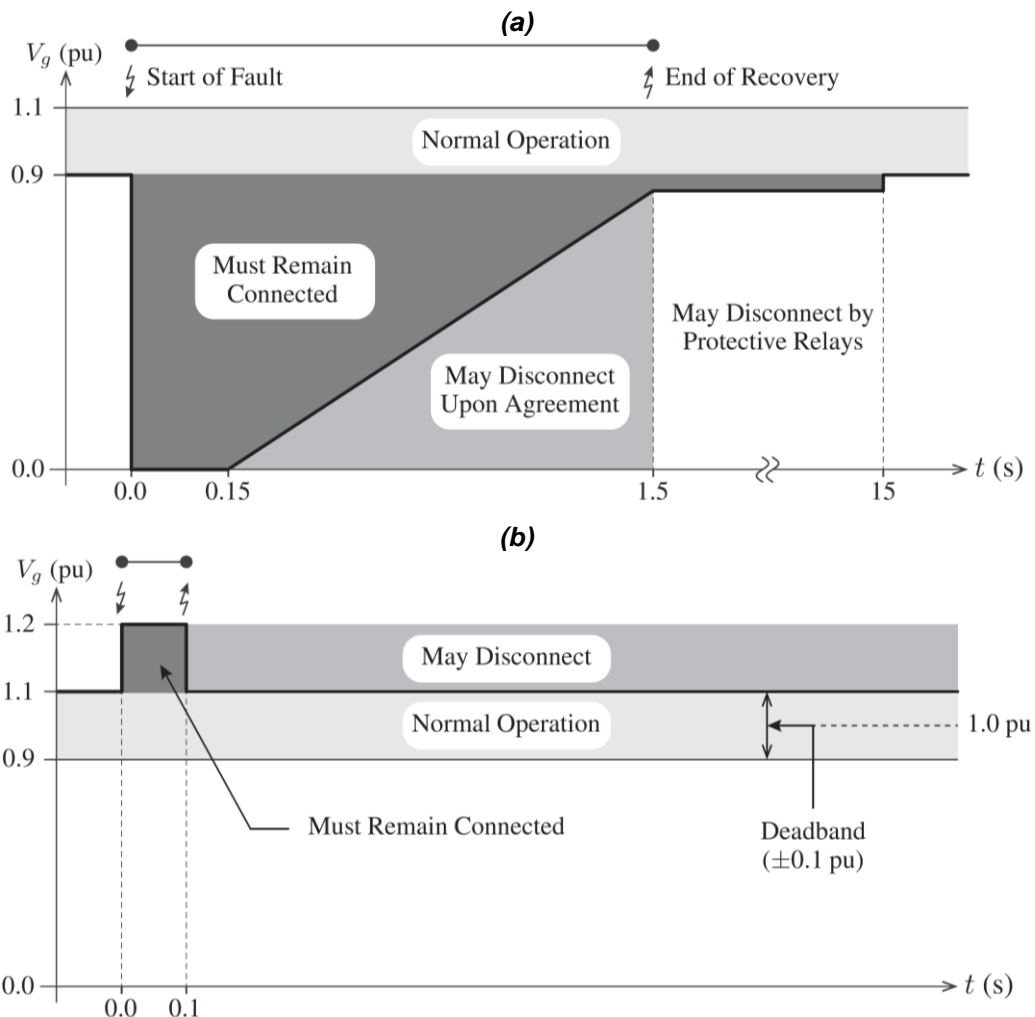


Fig. 1.5. FRT requirement of E.ON regulation: (a) ZVRT profile, and (b) HVRT profile [10], [29].

Fig. 1.5.a and Fig. 1.5.b present the ZVRT and HVRT curves of the E.ON regulation. According to this, during a fault at PCC, the wind turbine should “ride-through” instead of trip. In Fig. 1.5.a, in the event of a grid voltage sag the FRT should start working within one cycle (20 ms), withstanding the voltage drop for a time duration of 150 ms when the grid voltage drops below 0,9 pu and should deliver 1,0 pu reactive power. If the grid voltage falls below the ZVRT limit, the wind turbine disconnection is allowed. In the event of a voltage swell where the grid voltage swells to 1,2 pu, the wind turbine must ride-through for 0,1 seconds (Fig. 1.5.b.). The wind turbine should absorb 1,0 pu reactive power to ensure grid voltage recovery [10].

LVRT compliance has been imposed in large European island territories, such as the Crete Island (Greece) or the Canary archipelago (Spain) . In Fig. 1.6 are compared the profiles

for Crete, Canary islands and French islands [21], [26], [31-33]. When compared to the FRT of E.ON regulation mainland system presented in Fig. 1.5.a, the requirements from Fig. 1.6 look alike.

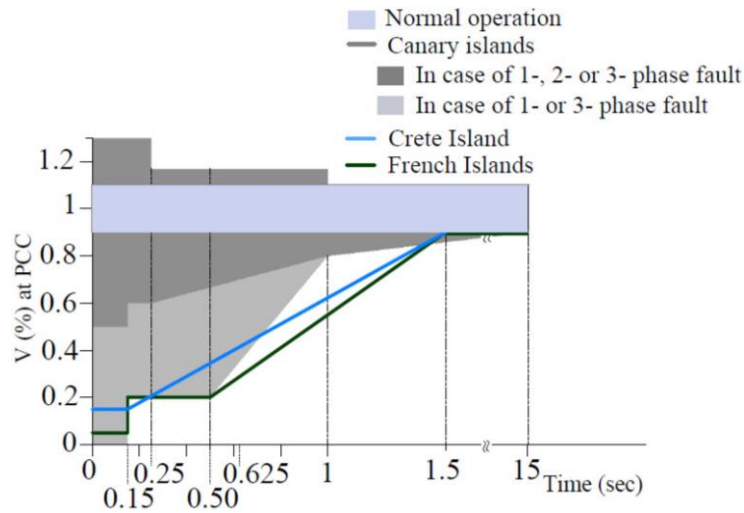


Fig. 1.6. FRT profile examples in European island grids [21].

Reactive power response

In order to reduce the contribution of conventional generators to the restoration of the grid voltage after default, this role needs to be also assumed by non-dispatchable power sources. The reactive energy support mechanism employed in the recovery of an under-voltage event, must be followed by the progressive reintroduction of active power at the RE unit output. The latter allows securing the consumption- generation balance, necessary to keep the frequency within the acceptance range. This capability is more critical in the case of island grids given their size and typical weak connection, implying any disturbed operating condition is sensed everywhere in the network. On top of that, island grids usually present low short circuit power which further promotes instability, implying for instance a significant variation in the voltage when a faulty condition appears [11].

Fig. 1.7 compares the reactive power requirements during voltage disturbances. The grid code of Canary Islands is compared with the specification for two European mainland systems. As can be appreciated, in the case of the insular grid code the consumption of reactive power takes place when the voltage disturbance recovery is still present. Moreover, for voltage drops beyond 50 % of the rated voltage, the reactive current is not bigger than 90 % of the global current, and reactive power consumption is not allowed while the voltage disturbance has not been cleared. According to the German grid code, when required the wind turbine must provide pure reactive current while providing at the same time active power. This meaning that, in order

to provided reactive power capability, the power converter must be sized according to the maximum possible active and reactive current.

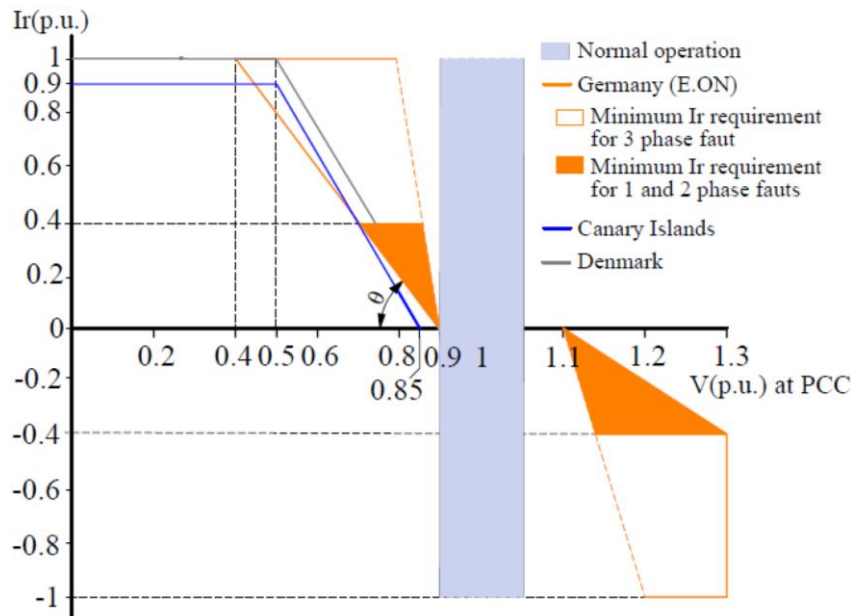


Fig. 1.7. Comparison of reactive power specifications during grid voltage disturbance [11].

1.4 Wind power and energy storage systems

Pollution reduction, global warming slowdown and risk reduction of nuclear disasters are among the reasons behind the current concern for improving the way in which energy is generated and used [34]. Renewable energy technologies such as biomass, hydroelectric, wind power and photovoltaic (PV) solar power, produce energy from natural resources that will not run out while releasing low quantities of greenhouse gas emissions. For these reasons over the last decades, decision-makers have been facilitating the development of renewable energy.

Next, wind power and energy storage systems are dealt with.

1.4.1 Wind power and commitment profiles

For thousands of years wind power has been used for sailing, grinding grain, or for pumping water. Starting from the 1980s, wind turbines have developed from 50 kW class machines to 10 MW turbines being unveiled nowadays [35]. While initially, the construction of wind turbines was a costly venture, thanks to recent improvements, wind power has begun to set peak prices in wholesale energy markets and cut into the revenues and profits of the fossil industry [36].

According to the report issued by WindEurope on February 2020, Europe has 205 GW of wind energy capacity: 183 GW onshore and 22 GW offshore, and wind accounted for 15 % of the electricity the European Union consumed in 2019. The same year, Spain (2,3 GW),

Sweden (1,6 GW) and France (1,3 GW) led the installation of onshore wind farms. Germany was fourth with 1,1 GW [37]. The European Commission claims Europe will need among 230 GW and 450 GW of offshore wind by 2050, making it a cornerstone in the energy mix together with onshore wind. 450 GW would meet 30 % of Europe's demand for electricity in 2050, which would have grown 50 % compared to 2015 [38].

1.4.1.1 Wind power in the electricity markets

The electrical systems evolved from their historical paradigm based on vertical integration, with regional or state enterprises owning and controlling the whole energy chain (generation, transmission, distribution and retail), towards a free competitive market. Within such a liberalized framework, competition is promoted mainly in generation and retail. In contrast, the grid-related activities (transmission and distribution) remain natural monopolies as it is not possible creating several competitive transmission and distribution system infrastructures [39].

Wholesale market transactions (such as power exchanges between neighboring systems or countries) happen via transmission grids. Their operation is ensured by transmission system operators, in charge of ensuring the security of the electrical grid and guaranteeing non-discriminatory access. Meanwhile, distribution grids allow the management of the energy delivered to end-users. Distribution system operators also manage the connection of RESs with power rating below a certain threshold (about 10 MW in France) [39].

The power transactions related to the generation of renewable energies take place within a liberalized framework. In such a framework, future wind power generation is offered through contracts and auctions mechanisms, therefore based on forecasts [40].

Short-term markets trading floors

Two different trading floors are typically available in electricity markets. Trading on long-term horizons takes place in medium/long-term markets (also known as futures markets). The participants in these markets can trade by mean of forward contracts, signed between two parties to buy or sell a certain amount of energy at a future time. Base load and peak load contracts are two examples of standard products in forward contracts [40].

On their part, short-term markets (also known as electricity pools), allow trading of electricity daily or hourly horizons. Day-ahead, intraday and balancing markets among the trading floors included in short-term markets [40]:

- ***Day-ahead market***: in the day-ahead market, energy transactions are agreed 1 day prior to delivery. Bid/offer and buy/sell proposals with the maximum/minimum price and the

quantity of energy the participants (buyers and sellers) are willing to consume/provide, are submitted to a market operator. The buy offers are ranked in price-decreasing order to form a cumulative buying curve. Similarly, the cumulative selling curve is formed by ordering the sell offers in price-increasing order. The intersection of the curves gives the market-clearing price and volume. Offers on the left of the clearing volume are accepted (and generally remunerated at the clearing price) whereas those at the left are rejected.

- *Intraday market*: the intraday adjustment market is the market for the energy transactions performed the day of delivery. It takes place between noon, when the day-ahead market closes, and before the delivery (the next day). At this market, the participants (conventional and stochastic producers and buyers) can change their positions close to real-time, when futures and day-ahead markets have closed and based on more accurate forecasts. The intraday market allows the continuous placement of offers/bids which are automatically matched.
- *Balancing market*: the balancing market permits balancing supply and demand close to real-time. Regulating power for upward and downward regulation is usually provided by conventional generators whereas stochastic producers participate in this market to fix deviations from contracted production. Typically taking place in a separated session for every trading period, balancing markets allow to trade, besides electrical energy, ancillary services.

Conventional generation plants can contract part of their capacity in medium/long-term agreements that allow fixed revenues, and the remaining capacity in electricity pools. In contrast, given their stochastic nature, it is hard for renewable generation facilities such as wind farms or solar plants to guarantee a certain level of production long time before operation [40].

In the present dissertation, market participation is represented by the application of a remuneration system determining the energy producer profit that includes the amount of power supplied and the occurrence of commitment failure penalties, according to a commitment profile agreed the day-ahead. The available information on the basis of which the dispatch decisions are made, are references related to both the commitment profile and the supply ancillary services, as well as measurements of the current system state. Participation in the intraday adjustment market or balancing market mechanism are left for future works.

1.4.1.2 Commitment profile and injection band

The two main advantages of using wind power in small and non-interconnected islands are lower electricity production costs and CO₂ emissions reduction, as the import of expensive fuels is replaced by the utilization of local energy supplies. However, the variability and uncertain scheduling and dispatch of wind power combined with the smaller inertia of those grids translates into the need for extra spinning reserve, mostly fossil fuels based.

The use of production forecasts is one of the ways to cut the need for spinning reserve. Energy storage enters the equation to cope with the errors in the forecast, which is never perfect. In this manner, the association wind power, energy storage and day-ahead wind forecasts make it possible the respect of day-ahead commitment profiles [41].

Deviations between contracted generation and actual deliveries may induce financial penalties. For this, in the decision-making problem of dispatching a RES-based generation site according to a contractual generation schedule, the energy producer should make optimal use of all the information available [40].

Forecast data (or the appropriate forecast software) being usually unavailable, most academic literature dealing with energy management of wind-storage systems follow a stochastic approach. Firm commitment profiles (injection commitment profiles in the present case) are generated by treating available production data and by adding some synthetic random error [41]. The first assumption consists in considering the production data as forecast data. The second assumption is considering the resulting profile to be the offer bade the day-ahead (day D-1) to the power generation and accepted by the market operator.

Following the project stipulations, the commitment profile must be composed by 30 minutes steps corresponding to the 48 volumes of power the production facility engaged in supplying during the day D. In Fig. 1.8.a is presented, as an example, a commitment profile obtained by averaging some production data and then, adding a random error.

According to this profile, average productions under 3 MW are then expected during the early morning, until gradually increase since 07:30. From before 09:30 and until the end of the day, the variations in the mean of the output power range mostly between 4 and 6 MW, as the foreseen wind speeds are stronger.

Fig. 1.8.b. shows the injection band established based on the commitment profile. If tolerance of 20 % is chosen, and the WECS installed capacity (P_{MAX}) is of 8 MW, the band is given by

$$P_{up\ lim} = P_{SCHED} + 0,2 \cdot 8 \times 10^6 = P_{SCHED} + 1,6 \times 10^6$$

$$P_{low\ lim} = P_{SCHED} - 0,2 \cdot 8 \times 10^6 = P_{SCHED} - 1,6 \times 10^6$$

Eq. 1.4

Where the profile P_{SCHED} is one of the inputs to the problem of dispatching the power flows of the grid-connected HPP.

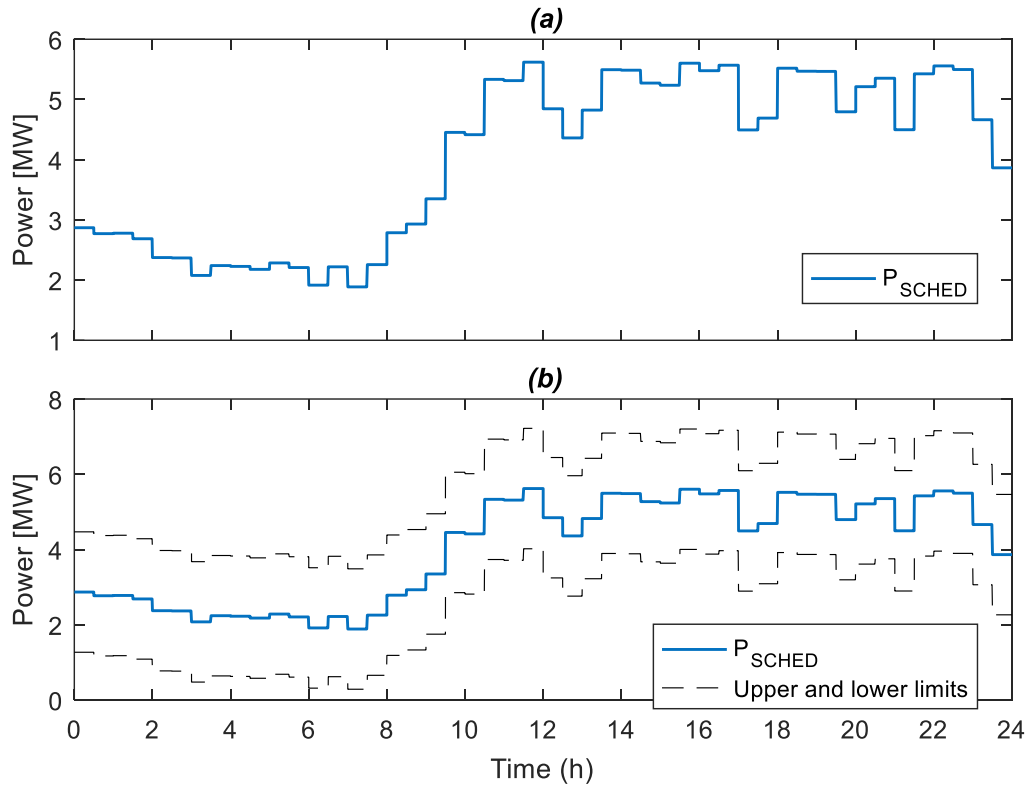


Fig. 1.8. (a) commitment profile determined from the day-ahead production forecast, (b) injection band for the same period.

1.4.2 ESS applications for grid-connected WECS

The applications of adding an ESS to a WECS are not reduced to the peak shaving and smoothing of the wind turbine generated power, and represent advantages for different stakeholders: hybrid plant operator, grid operator and energy consumer [42].

1.4.2.1 ESS applications for WECS integration

The issues of output intermittency and variability, and ramp rate requirements are the main challenges of wind power systems. ESSs are power sources that can be charged and discharged. The Associating with an ESS may represent for the wind farm improvements in terms of dispatchability and grid-friendliness.

- Generation-demand time correlation: wind power non-dispatchability implies the availability of the wind-generated power cannot be guaranteed during peak demand

periods. In the same way, high wind power can take during off-peak demand periods. The possibility to store the surplus and compensate for the lack of power represents then a substantial benefit.

- *Output smoothing*: the variable nature of wind power can introduce fluctuations in both the frequency and the voltage at the connection point. The smoothing made available by the ESS reduces the need for power quality and ancillary services in the system [42], [43].
- *Transmission utilization efficiency*: often wind resources are abundant in rural/remote areas that are away from the transmission lines. Additional ESSs can reduce the transmission lines congestion, defer or avoid the expansion of distribution and transmission systems [42], [44].

1.4.2.2 ESS applications for grid support

The ESS can provide ancillary services and contribute to meeting the grid codes imposed by the network operator.

- *Energy arbitrage/load leveling*: with varying electricity prices a possibility ESSs can be used to store low-cost peak-off energy to be discharged when the price is higher, which can help reducing market risk exposure to volatile peak prices.
- *Frequency regulation*: using a droop controller ESSs could be managed to provide active power in response to frequency deviations (primary frequency control) [42], [45]. With a control procedure centralized by the network operator ESSs can also provide secondary frequency control.
- *Inertia emulation*: increased grid inertia reduces frequency variability to sudden generation and/or load variations. Addition of a supplementary loop to the active power control of the ESS can permit the increment of the system's apparent inertia [42].
- *Oscillation damping*: in interconnected systems, sudden changes in the power being transmitted through a tie line might introduce frequency oscillations ranging between 0,5 and 1 Hz [42], [46]. Applications of EMS to reduce frequency oscillations in wind-EMS systems have been reported in the literature [42], [47, 48].
- *Voltage control support*: wind power variability can degrade the stability of the grid voltage [42], [49]. Using the appropriate power conversion interface, ESSs can be controlled to provide reactive power to maintain the local voltage level. This aspect is discussed in section 2.4.

- *LVRT support*: some grid codes require wind turbines to supply up to maximum reactive current during to grid voltage sags. To compensate for switching losses associated with the provision of reactive power, the converter should withdraw active power from the utility grid. During severe faults no power can be withdrawn, and the DC voltage falls. ESS can support the DC voltage during the faulty conditions [42].
- *Reserve*: due to wind power's forecast error additional reserves are required. According to their response time and discharge duration some ESS technologies can be suitable for providing primary, secondary or tertiary frequency reserve. In section 2.3 are described several of these storage technologies that can be associated with wind turbines or farms.
- *Emergency power supply/black start*: after a blackout, ESS may be used to support the energize an islanded portion of a grid. This function is called black-start [42].
- *Transmission utilization efficiency*: ESS can be utilized by grid operators to use the transmission system more efficiently, reduce transmission costs and defer the expansion of transmission systems [42].

1.4.2.3 Demand-side applications of ESS

In the consumer side, ESS can not only be used to support the integration of REs, but also to enable demand-side-management¹ related applications [42], [50].

Moreover, electrical vehicles (EV) vehicle-to-grid (V2G) feature, making possible the transfer of energy to the grid when the car is not being used, imply the possibility for the batteries inside those cars of supporting the grid and reducing the consumer's energy bill. Thus, the energy stored could help regulate the grid frequency or reduce the amount of energy purchased at peak times.

1.5 Definition of the operating conditions for the wind-storage hybrid power plant

According to the stipulations of the Insul'Grid project, next is explained the basis of the desired operating conditions for the HPP:

- *Forecasts*: the plant operation is based on 24 hours of wind speed/power forecasts for the period 0:00 – 23:59. A scheduling algorithm represents the commitment injection in the form of a half-hourly stepped profile. The injection within a time step is assumed to be constant.

¹ Modification of consumer energy consumption habits through methods usually involving education and financial incentives.

- Power injection band bounds: the injection limits are determined from the 24 hours half-hourly stepped production profile, which is taken here as daily day-ahead electricity commitment generation schedule (P_{SCHED}) as depicted in Fig. 1.9. According to the project's stipulations, the BESS must be controlled so that the 30 minutes duration scheduled injection steps can be met even though the wind farm output variability. During the first year of operation of the HPP, the BESS should allow the respect of a tolerance region of 25 % of the installed power P_{MAX} , above and below the scheduled injection. The band will be narrowed down to 20 % the second year and to 15 % from the third year. The tests carried out in this thesis consider the tolerance for the first year, namely 25 %.

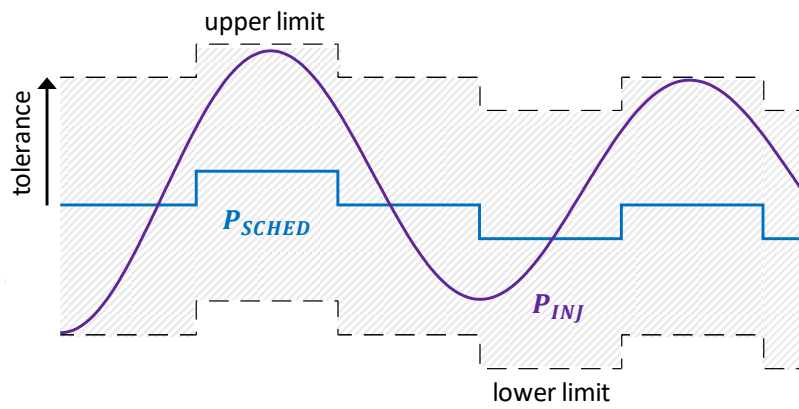


Fig. 1.9. Power injection limits.

- Penalties: power injections of with excursions of 60 consecutive seconds outside the limits are penalized with non-payment of the power supplied to the grid for the next 10 minutes.
- Power variation speed limits: during upward or downward step changes of the generation schedule, the injected power must respect the next variation speed bounds. According to this, the time for the injected power to go from 0 to P^{max} must be within 30 seconds and 5 minutes. Also, to go from P^{max} to 0 the time taken must be within 1 and 10 minutes, or:

$$\begin{aligned} \frac{dP_{INJ_{uw}}^{min}}{dt} &\leq \frac{dP_{INJ}}{dt} \leq \frac{dP_{INJ_{uw}}^{max}}{dt} \\ \frac{dP_{INJ_{dw}}^{min}}{dt} &\leq \frac{-dP_{INJ}}{dt} \leq \frac{dP_{INJ_{dw}}^{max}}{dt} \end{aligned} \quad \text{Eq. 1.5}$$

where:

$$\begin{aligned} \frac{dP_{INJ_{uw}}^{min}}{dt} &= \frac{P_{MAX}}{300} \text{ [MW/s]}; & \frac{dP_{INJ_{uw}}^{max}}{dt} &= \frac{P_{MAX}}{30} \text{ [MW/s]} \\ \frac{dP_{INJ_{dw}}^{min}}{dt} &= \frac{-P_{MAX}}{600} \text{ [MW/s]}; & \frac{dP_{INJ_{dw}}^{max}}{dt} &= \frac{-P_{MAX}}{60} \text{ [MW/s]} \end{aligned} \quad \text{Eq. 1.6}$$

- *State-of-charge*: the storage system must be operated with a maximum deep-of-discharge of 60 % so that replacements of the BESS are not required during the project duration (15 years).

1.6 Chapter conclusions

Island electric grids are weak systems whose management differs from that of mainland, continental-size grids. The management of the key variables in the system is done by means of two hierarchical control schemes: active power-frequency control and reactive power-voltage control. Each of these control schemes is composed of three different levels of control loops operating temporary and spatially independent called primary, secondary and tertiary control. Given the size of island grids, the reactive power-voltage control can be understood as composed only of primary and secondary control.

Next, the technical specifications regulating the operation of grid-connected facilities both under normal and faulty conditions are denominated grid codes. In this case the attention is focused on the requirements wind turbines operating in island grids. If all the specificities of the operation of a wind farm are not covered by a grid code dedicated to operation in island grids (this is true for France and other countries), in practice DSOs and TSOs establish the regulations the generation facilities must follow. Moreover, the operation conditions for the HPP presented in this Chapter are part of the contractual agreement signed between the DSO and the plant operator. Some of the aspects found in the grid codes review are part of these contractual conditions (e.g. ramp rate limitations and upper power output limitation).

The hybrid power plant control must be done by means of an EMS having access to the production forecasts and the ESS state-of-charge. Such an EMS must send orders to the ESS in such a way that the plant's operation conditions are met.

The aim of the energy management scheme required is to provide a grid service that consists of complying a day-ahead power injection commitment. The use of forecasts data (in this case the forecasts translate into a commitment profile) and energy storage respond to the economic burden that would imply depending only on power reserves to comply with the commitment.

CHAPTER

2

State of the art of energy management approaches for wind power and energy storage hybrid plants

Summary

2.1 Introduction	32
2.2 Hybrid power plants and MicroGrids definition	32
2.2.1 Components of a hybrid power plant	34
2.2.2 Wind energy-based HPPs	35
2.2.2.1 Wind and PV power	36
2.2.2.2 Wind power and diesel generator	36
2.2.2.3 Wind power and hydro storage	37
2.3 Energy storage technologies for wind power integration.....	38
2.3.1 Long-term storage technologies	39
2.3.1.1 Pumped hydro storage (PHS).....	39
2.3.1.2 Battery energy storage (BES)	39
2.3.1.3 Hydrogen energy storage (HES).....	40
2.3.1.4 Compressed air energy storage (CAES)	41
2.3.2 Short-term storage technologies	41
2.3.2.1 Flywheel energy storage (FES).....	41
2.3.2.2 Super capacitor (SC) storage.....	42
2.3.2.3 Superconducting magnetic storage (SMES)	43
2.4 Architectures of grid-connected wind-storage hybrid plants in islands.....	45
2.4.1 HPP with wind power and distributed storage	45

2.4.2 HPP with wind power and aggregated storage	46
2.5 Energy management approaches for HPPs	47
2.5.1 Hybrid systems and dynamic optimization	49
2.5.2 Control and optimization of wind-storage hybrid systems.....	51
2.5.2.1 Approaches not optimizing a cost function.....	52
2.5.2.2 Approaches optimizing a cost function.....	55
2.6 Chapter conclusions	61

Chapter overview

This Chapter deals with wind/storage hybrid power plants. A review of architectures and the different strategies employed for the energy management of hybrid renewable/storage power plants is presented. The Chapter finishes with some concluding thoughts.

2.1 Introduction

The present Chapter starts by defining HPPs, energy production systems born as a consequence of the changing trends the energy industry has been experiencing during the last decades.

A wide range of renewable energy sources is available for generating electricity through HPPs. However, the focus in this dissertation is on wind power-based systems supplying electricity and ancillary services into island grids including several combinations of wind turbines and other RES: wind/PV, wind/diesel, wind/hydro and wind/diesel/hydro, followed by the description of the short and long-term storage technologies suitable for the HPP dealt with in the present thesis.

Next, distributed and centralized storage architectures within wind power-based HPPs architectures are briefly explained.

The last section of the Chapter is dedicated to Energy Management Systems (EMS) for HPPs. The investigated EMSs is developed based on control and optimization strategies to optimally manage the production facilities power flows. A literature review of management strategies applied to hybrid systems combining RES and different energy storage systems is presented at the end of the Chapter.

2.2 Hybrid power plants and MicroGrids definition

2. State of the art of energy management approaches for wind power and energy storage hybrid plants

Hybrid energy systems are defined as the integration of several types of energy generation equipment such as electricity generators, electrical energy storage systems, and renewable energy sources.

A hybrid power plant (HPP) is an electricity generation facility associating localized renewable energy resources (such as wind generator, PV panel, etc.) and conventional generators (such as a diesel engine), with energy storage devices (such as batteries or fuel cells) [51], [52]. Generally, HPPs operate connected to the Low Voltage (LV) or Medium Voltage (MV) distribution network in a unique point called Point of Common Coupling (PCC).

The generation and storage units within an HPP are interfaced between them but also with the distribution network through an EMS, as shown in Fig. 2.1.

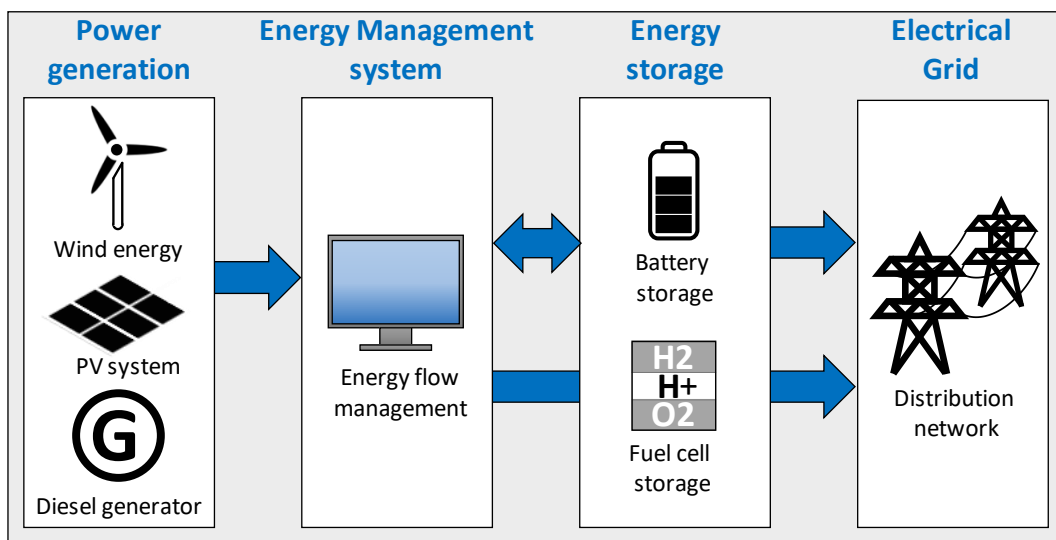


Fig. 2.1. Components of an HPP.

The hybrid system depicted in Fig. 2.2 is a microgrid (MG). In opposition to HPPs, whose aim is injecting power into loads connected to the main grid, MGs are conceived for supplying power to local loads. In this case, the power exchanged with the grid is bidirectional so that the loads supply can be ensured even in situations of low power production and depleted energy storage means.

A MG is generally defined as a weak electric grid based on localized grouping of electricity Distributed Generation, loads and storage systems operating connected to the LV or MV distribution network.

From the grid point of view, a MG can be regarded as a controlled entity that can be operated as a single aggregated load or even as a small power source or ancillary service supporting the network. From the customer's point of view, a MG provides enhanced power quality and reliable energy supply. The most important characteristic of a MG is its ability to

operate in grid-connected or islanding mode. According to the definitions given, HPPs and MGs are closely related terms.

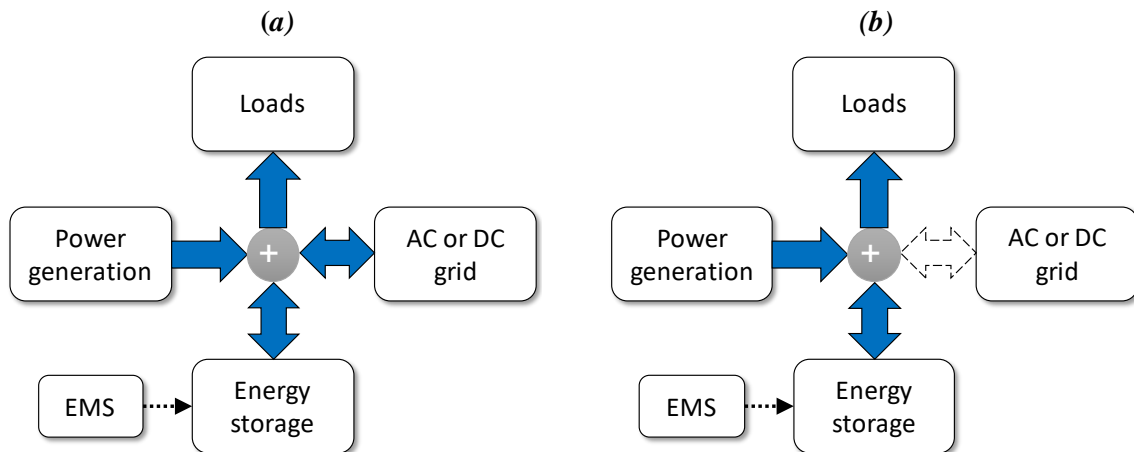


Fig. 2.2. Generic structure of a microgrid: (a) grid-connected operation, and (b) islanding mode.

2.2.1 Components of a hybrid power plant

Generation sites pairing at least one type of RES with an energy storage system (ESS) and an adapted EMS are defined here as HPPs. The mix of different types of renewable sources, energy storage technologies together with the use of conventional generators is also covered by this definition of HPP.

Not only hybrid power plants can accommodate several types of production and storage resources, but their integration into conventional power grids can bring reliability and efficiency to supply the demand. Moreover, the cost of renewable energy production components is expected to decrease [51]. The sources intermittencies and stochastic nature make the control of HPPs a complex task, though.

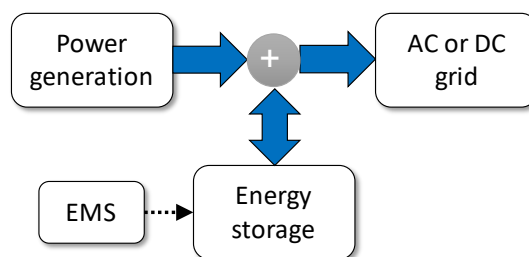


Fig. 2.3. Generic structure of an HPP.

The generic structure of an HPP is presented in Fig. 2.3. As shown, the system's aim is injecting power into the main grid, exploiting the local resources

In such a generation facility, an ESS is a necessary backup as the power generation is not constant. Also, an EMS must control the ESS charges and discharges according to the instant production and other considerations such as the level of ancillary services required by the grid (primary reserve, frequency and voltage regulation, etc.).

Commonly, the energy dispatch decisions determined by the EMS (active and reactive power extraction from sources and absorption or the injection of power from the storage units) are executed using power electronic converters (not shown in the figure).

The EMS's aim is that of guarantying that the power supply is always available within a time interval covered by a commitment. Different strategies can be adopted to accomplish that. For instance, a PV panels-based plant which supplies power during the day can be controlled to store as much as possible the energy excess during the day or to reach a target charge level needed for the next day.

As for the nonrenewable sources, diesel generators are commonly used as backup resources in HPPs. Storage technologies such as batteries are considered bidirectional backup resources, characterized by their capacity to absorb and inject power. On the other side, unidirectional backup sources, like diesel generators, can only inject. The principle of the first is storing energy during surplus production periods and supplying when renewable energy production is not enough. In contrast, unidirectional backup supply power for long periods, depending on the fuel tank level, but their use implies CO₂ emissions [53].

In the case of HPP connected to island electricity grids, an additional drawback of unidirectional backup sources is their reliance on imported fuels which are usually expensive, increasing the cost of the electricity (\$/kWh) sold to the grid by the producer. In those territories, resources like wind and solar energy are abundant, making wind power and PV panels good candidates for producing electricity and supplying ancillary services with the aid of an ESS. Depending upon the island's geographic conditions, some other types of sources can be exploited (e.g. geothermal, tidal or biomass generation, hydroelectric storage, etc.).

2.2.2 Wind energy-based HPPs

Fossil fuels like gas, diesel or coal, used in the production of electricity, are often hardly available on islands and overseas territories. When needed, their supply depends on transportation chains that increase electricity production costs and environmental impact. In contrast, resources like wind and solar irradiance are abundant in those territories and are free. Moreover, depending on the island's specific topography conditions (presence of volcanos, waterfalls, caves, etc.), additional forms of primary energy resources can be at disposal for electricity production.

If conventional generation means can guarantee the power supply when the demand is highest, wind-generated power is not correlated to the consumption needs. Hybridization (i.e.

combination with other types of RES and with conventional power stations) and energy storage are the main ways to cope with this issue of wind power.

Following are described sources combinations involving wind power that can be found in grid-connected HPPs in islands.

2.2.2.1 Wind and PV power

The common practice in HPPs based on wind power and PV panels as the sources is the use of a centralized ESS which is shared by all the generation units. Typically, in this case, the storage technology used is battery storage (see Fig. 2.4). Also, the integration of the two types of sources allows systems with higher capacity factor² than in the separated situation and a lower cost, since the infrastructure of power conversion, storage and distribution is shared [54].

The Tilos project, in the island with the same name in Greece, tests the capacity of a small wind/PV/battery storage generation facility plant to provide the local grid with firm power while contributing to the frequency regulation [55-57].

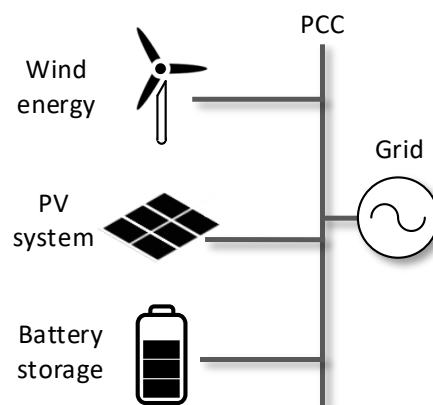


Fig. 2.4. Wind/PV/battery HPP.

2.2.2.2 Wind power and diesel generator

Wind/diesel hybrid plants are commonly found at small size in the power supply of isolated communities' local grids. Grid-connected or not, the infrastructure in this type of HPP is shared by the wind turbines and diesel units which are commonly combined with battery banks. The diesel generators are used as backup units meaning they are used when the wind turbines and batteries cannot ensure a smooth power output (see Fig. 2.5). In many cases the EMS in wind/diesel/battery HPPs and microgrids counts among the optimization objectives with the minimization of CO₂ emissions, meaning reducing the consumption of diesel fuel. The

² Ratio of energy generated (by a generation facility or generating unit) over a period of time, to the hypothetical maximum possible.

2. State of the art of energy management approaches for wind power and energy storage hybrid plants

component of wind turbines usually having a larger part in the installed capacity of the plant [54].

An example of Wind/diesel combination is the Ross Island research station project which also integrates flywheel storage [58].

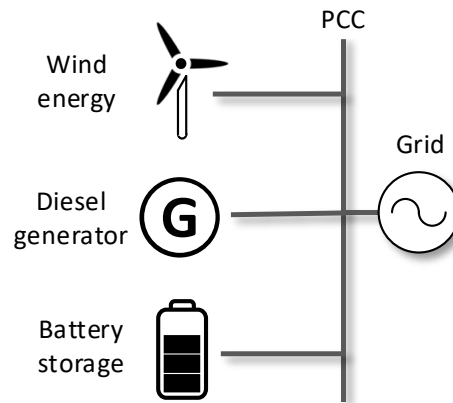


Fig. 2.5. Wind/diesel/battery HPP.

2.2.2.3 Wind power and hydro storage

Wind/hydro-based power plants use wind power to pump water at a higher-level reservoir. Commonly, this is done during the night, when the energy demand is low. The

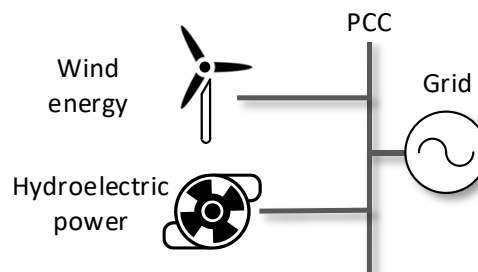


Fig. 2.6. Wind/hydro HPP.

machines connected to the hydraulic turbines are used as motors for pumping water, and as generators when water is released to turn the turbines. In this type of HPP, hydro storage is used for smoothing the power generated by the wind turbines. This kind of system present rather higher efficiency as they involve only mechanical-electrical energy conversion [54].

El Hierro, an 100% renewable hybrid system based on wind and hydro was installed in the Canary Islands, Spain [59-61]. Sometimes this kind of hybrid power system is complemented by a diesel generator which is only used in cases of deficit of power, allowing increased reliability. The EMS in this type of facility, controls the internal power flows by acting on the wind generators, hydraulic plant motor/generator units, and the diesel generator(s) through power converters. The Kodiak Island project is an example in Alaska, the United States,

which uses wind/diesel/hydro and flywheel storage to provide smooth power will contributing to grid frequency regulation [62],[63].

2.3 Energy storage technologies for wind power integration

The variable nature and uncertainty of wind energy pose substantial challenges for the operation and planning of the power systems. This is even more challenging in weak or isolated grids. For those reasons, grid codes related to wind power plants generally require for output power adjustment and ancillary services supply. Recent developments in energy storage technologies add up to the reasons for the interest in associating wind power with energy storage systems.

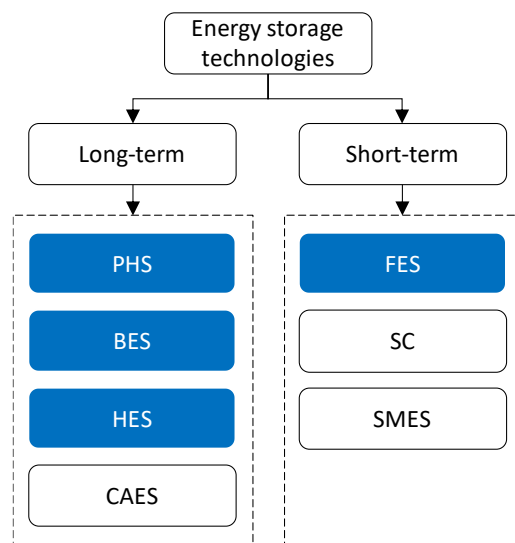


Fig. 2.7. Short and long-term energy storage technologies for wind farms and wind power-based hybrid systems.

Discharge duration (or energy capacity, in MWh) and power rating (MW) are design parameters varied to select the ESS suitable for a given application. Based on their discharge duration, energy storage systems used in combination with wind power can be classified into long term (minutes or hours) and short-term (a few seconds or minutes) systems [64].

In Fig. 2.7 are depicted the storage technologies that are co-located with wind turbines or farms, that can be mechanical, electrochemical and electrical. Pumped hydro storage (PHS), flywheel energy storage (FES) and compressed air energy storage (CAES) are examples of mechanical storage. For electrochemical storage, battery energy storage (BES) and hydrogen energy storage (HES) are considered. Finally, super capacitor (SC) and super conductive magnetic storage (SMES) are examples of electrical storage [65]. The technologies for which applications in wind-storage systems in non-interconnected islands were identified are highlighted in Fig. 2.7.

Next, those storage technologies are described.

2.3.1 Long-term storage technologies

Long-term storage systems absorb and supply power during minutes or hours and are mainly applied in energy management, frequency regulation and grid congestion management [64].

2.3.1.1 Pumped hydro storage (PHS)

PHS is the most common type of long-term ESS. Typically, PHS involves a lower and an upper water reservoir. The charging procedure takes place during peak-off periods and consists of pumping water from the lower to the upper reservoir. In the discharging process, water is released from the upper reservoir to generate through hydro turbines during peak periods. When PHS is a high-power (for instance, the Bath County Pumped Storage Station capacity is of 3,030 MW) and high-energy resource (can supply power during several hours continuously) it is suitable to integrate wind power variations handling and hourly dispatch, frequency control, and non-spinning reserve supply [66], [42]. If high-power and high-energy PHS is useful for reducing the fluctuations of wind power, the main problems for building these stations are the lack of appropriate places and the environmental impact.

Nonetheless, the El Hierro 100% Renewable Project (11,5 MW total wind farm power, 6 MW pumps and 11,32 MW in hydro turbines) is an example of a small-scale hydro wind power plant supplying power since 2014 to El Hierro Island in the Spanish Canaries. Managed by Gorona del Viento El Hierro S. A., the initiative aims at supplying the island's electricity requirements with renewable energy. The power plant comprises five wind turbines, a system of pumps for moving seawater from a lower to a higher deposit with energy supplied by the wind farm and 4 Pelton wheels.

Located in Gaildorf Germany, the Naturstromspeicher pilot project is a second example of a small wind hydro project (17,3 MW wind farm, 16 MW / 70 MWh pump hydro system using reversible machines). The particularity of this promising initiative rendering wind supply dispatchable and providing ancillary services to the continental grid is it utilizes the towers and bases of wind turbines as water reservoirs. Participation in the 15-minute reserve market is part of the services proposed by the owners of the project, currently in the pilot phase.

2.3.1.2 Battery energy storage (BES)

A battery storage system consists of a set of series and parallel-connected low-voltage cells arranged to achieve a desired electrical characteristic [42]. The several BES technologies used for providing short-term fluctuation reduction, power quality applications, and some

ancillary services, differentiate from each other in terms of energy density, lifetime, cost and efficiency [66].

Among those technologies are lithium-ion (Li-ion), lead-acid (LA), nickel-cadmium (NiCd), nickel-metal hydride (NiMH) and sodium-sulfur (NaS) [66], [42]. Others like vanadium redox (VRB) and zinc-bromine (ZnBr) correspond to the flow battery type distinguished by using a liquid electrolyte and for having higher energy density making them more suitable for the arbitrage of wind energy while offering the benefits of the other batteries with regard to response time [66].

Husahagi wind farm is a demonstrator project using wind-battery storage hybrid system. It is connected to the Danish Faroe Island isolated electrical system. A wind installed capacity of 11.7 MW is combined with a 2.3 MW /700 kWh Li-ion battery ESS. Ramp rate control of the wind power plant reduces the network's operator need for demanding other producers to change output rapidly. Variations at a maximum rate of 1 MW / minute are tolerated. During downward wind variations, the BESS is used to keep the power output level constant. In the case of upward variations, ramp rate control is ensured by both the BESS and the wind turbines via active power control, to reduce their power output. The storage system also provides capacity firming while respecting the MW/min rate and eliminating rapid voltage and power swings on the grid. Moreover, frequency regulation is ensured through charging and discharging the storage system when needed [67], [68].

2.3.1.3 Hydrogen energy storage (HES)

Hydrogen storage systems comprise an electrolyzer, a hydrogen tank, and a fuel cell. To generate power, hydrogen and oxygen resultant from the electrolysis of water flow into the fuel cell where they react delivering water, and heat is discharged producing electricity [64]. The advantage of the hydrogen fuel cell is its low environmental impact, and the main drawbacks are the low density per volume and price.

NTU (Nanyang Technological University), ENGIE and Schneider Electric collaborate with several other stakeholders in the SPORE (Sustainable Powering of Off-Grid Regions) project in Semakau Island, located approximately 8 km south of Singapore. The project is part of the REIDS initiative (Renewable Energy Integration Demonstrator – Singapore) which aims at the development of the world's largest microgrid demonstrator in the tropics.

SPORE microgrid uses hydrogen to complement the 200 kW / 200 kWh Li-Ion BESS. With a storage capacity of 2 MWh for 80 kg of hydrogen, the HES system is advantageous to mitigate the impact of seasonal changes. Meanwhile, the battery system is more suitable for

shorter-term storage, particularly to support the daily consumption of 5 to 10 households [69]. The microgrid also involves a 100 kW wind turbine (Singapore's first long-span wind turbine), two PV systems for a total capacity of 77 kW, and the hydrogen production required for a vehicle hydrogen refueling station [69], [70].

2.3.1.4 Compressed air energy storage (CAES)

CAES consists of using the potential energy of compressed air to generate electricity. At a first time, the air is pumped into either an underground structure (e.g. a cavern or a mine) or an above-ground system of pipes [42]. The air is heated, expanded and directed to a high-pressure turbine, and then it is mixed with fuel to drive a gas low-pressure turbine [66]. This storage technology provides high-storage and high-energy as PHS. For this, it also can be integrated with wind turbines offering to the grid arbitrage and ancillary services support at quick response times [66]. However, CAES is only suitable for large scale storage. CAES plants use to be at the scale of hundreds of MW or GW, i.e. larger than island-scale wind power facilities, like for instance the Huntorf CAES plant in Germany which provides a peak output of 290 MW for two hours.

Nonetheless, the Canadian company Hydrostor is developing underwater compressed air electrical storage (UW-CAES) systems for grid-scale energy storage applications. The company claims the storage solution costs half as the Li-ion batteries and that device's lifetime would be of around 30 years. As for Mars 2019, Hydrostor had multiple CAES projects under construction or in operation in Canada and Australia as the 0.7 MW Toronto island project which is in service since late 2015, or the 1.75 MW / 7 MW Goderich project system, currently under construction [71-73].

2.3.2 Short-term storage technologies

Short-term systems have high power density (MW/m^3) and typically can absorb or supply electrical energy during few seconds or minutes and are commonly used in power quality improvement, particularly for maintaining voltage stability during transients [64]. Next are presented some short-term storage technologies used in wind power hybrid systems.

2.3.2.1 Flywheel energy storage (FES)

FES consists in storing energy in the form of rotational energy in a massively accelerated rotor. During the charging process, a motor is used to accelerate the rotor to a high speed and the energy is stored by keeping the rotor rotating at a constant speed. In the discharge process, the flywheel releases energy to drive the machine which is working in this case as a generator. Flywheels can ramp up very quick but they offer short discharge times allowing them to

suppress wind power fluctuations, under-voltage ride through to interruptions and perform fast response regulation of the grid frequency, but only over short periods (a few seconds or minutes) [66], [42]. For instance, the Kodiak Island project located in Alaska (9 MW wind farm, 33 MW hydro, 30.9 MW diesel microgrid, 2 MW / 33 MWs flywheel and 3 MW / 2 MWh lead-acid battery) pairs two 1 MW flywheel systems and a battery system to smooth the wind power fluctuations while taking advantage of the different discharge times the two storage technologies offer.

2.3.2.2 Super capacitor (SC) storage

SCs contain an electrolyte solution placed between the two solid electrodes instead of the solid dielectric between two conductors found in conventional capacitors and present much larger capacitance (thousands of farads [74]) and energy density, as well as fast charging and discharging due to their low inner resistance, unlimited cycle stability, and very high-power density. Among the advantages of supercapacitors are the durability, reliability, no maintenance, low environmental impacts and operation in diverse environments over a large temperature range. Their discharge time is in the range of seconds to hours and are applied to the power leveling of wind farms just like for smoothing fast fluctuations in combination with batteries [42].

A 300 kW / 150 kWh energy storage facility combining super capacitor and Li-ion batteries was connected to the Irish distribution network in 2015. The network is essentially an island grid with only limited connection to the UK [75]. Additionally, over 23% of Ireland's total electricity demand was supplied through wind-generated power that year [76]. The battery system is used for peak shifting and operative reserve, taking advantage of its higher storage capacity, whereas the super capacitor's ability to provide more immediate power allows it to perform fast functions such as frequency response.

Nonetheless, some research works have been carried out studying the use of ESS based only in SCs for the integration of wind energy in grid-connected facilities. For instance, the authors in [77] exploit a super capacitor storage system to minimize the short-term fluctuations of a grid-connected permanent magnet synchronous generator (PMSG)-based wind turbine generator. During a grid fault, the proposed controller forces the wind turbine generated power to be stored in the super capacitor, allowing the generation system to continue to operate during grid faults (capability known as fault-ride-through - FTR). In normal operation conditions, the controller exploits the ESS to minimize the power fluctuations caused by the varying wind speed.

2.3.2.3 Superconducting magnetic storage (SMES)

Direct current flowing a superconducting cryogenically cooled coil at low temperatures create a magnetic field in which energy is stored [64]. The stored energy can be released to the system when required. The main advantage of SMES is its quick charge and discharge making

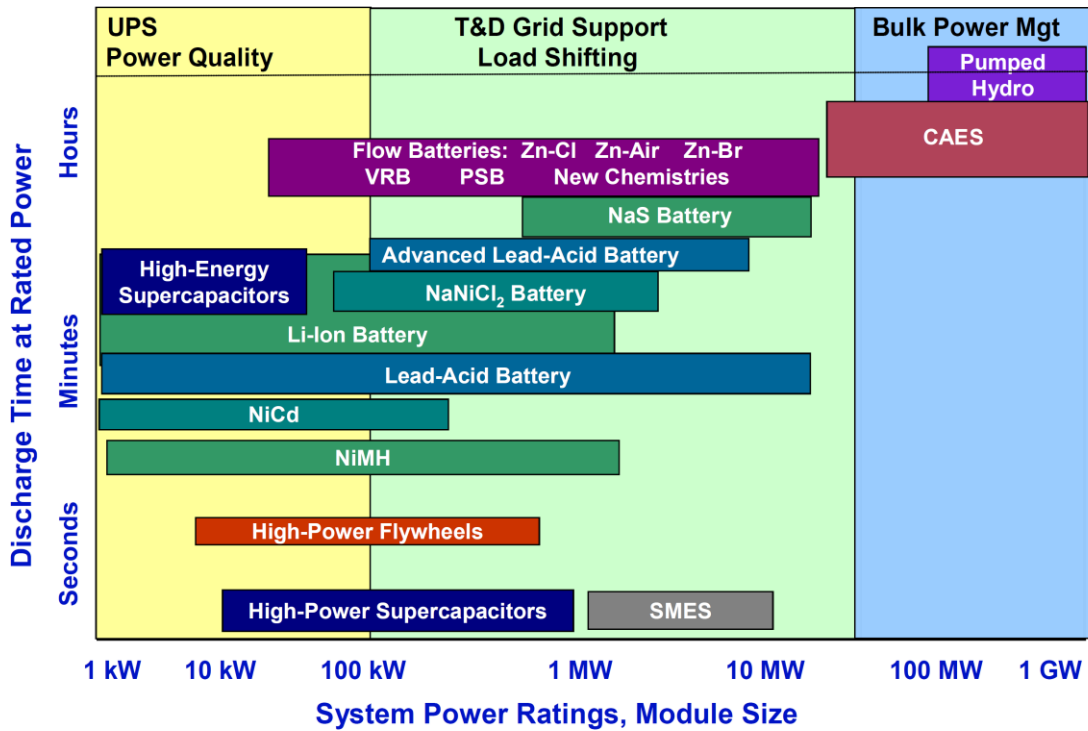


Fig. 2.8. Positioning of energy storage technologies [78]

power to be available almost instantaneously [79]. An overview of the applications of SMES in power systems, including those related to wind power integration, is introduced in [80] and

Table 2.1 Typical parameters of storage technologies for wind power systems

Technology	Power rating (MW)	Typical discharge time	Response time
PHS	100-5000	1-24 h+	min
CAES	5-300	1-24 h+	min
FES	0-0.25	s-h	<s
LA	0-20	s-h	<s
NiCd	0-40	s-h	<s
Li-ion	0-0.1	min-h	<s
NaS	0.05-8	s-h	<s
VRB	0.03-3	s-10 h	s
ZnBr	0.05-2	s-10 h	s
FC	0-50	s-24 h+	s-min
SC	0-0.3	ms-1 h	<s
SMES	0.1-10	ms-8 s	<s

a performance comparison is presented in [81], of several case studies reported in the literature of SMES for stabilizing grids integrated with wind power.

Table 2.2 Application examples of hybrid wind power/storage systems for islands

Project name	Sources		Storage system		Functionalities	Location	Ref.
	Type	Power	Type	Capacity			
AGIOS EFSTRATIOS-GREEN ISLAND	WT PV H2G	800 kW 200 kW 100 kW	N/S BESS	1 MW / 2,5 MWh	N/S	Agios Efratios, Greece	[82], [83]
Auwahi Wind Farm	WT	21 MW	Li-Ion BESS	11 MW / 4,4 MWh	Frequency regulation Voltage regulation	Kula, Hawaii, United States	[84]
El Hierro 100% renewable	WT Hydro	6 MW 11,3 MW	PHS	6 MW	N/S	Canary Islands, Spain	[59-61]
Husahagi wind farm	WT	11,7 MW	Li-Ion BESS	2,3 MW / 0,7 MWh	Ramp rates smoothing Frequency regulation Capacity firming	Faroe Island, Denmark	[67],[68]
Insul'Grid	WT	8 MW	Li-Ion BESS	4 MW / 2 MWh	Frequency regulation Voltage regulation Ramp rates smoothing Active power reserves Capacity firming	Sainte-Rose, Guadeloupe, France	[59-61]
Kodiak Island	WT Hydro Diesel	9 MW 33 MW 30,1 MW	Flywheel	2 MW / 33 MWs	Frequency regulation Wind power smoothing	Alaska, United States	[62],[63]
Nijijima Island Microgrid	WT PV Diesel	N/S (~1 MW in total)	Li Ion BESS	1 MW / 0,5 MWh	Frequency Regulation Ramp rates smoothing Capacity Firming	Nijijima, Izu Island, Japan	[63],[85],[86]
Porto Santo	WT PV Diesel	1.5 MW 2.25 MW 16 MW	N/S BESS	4 MW / 3 MWh	Frequency regulation Voltage regulation	Porto Santo, Portugal	[63]
Sustainable Powering of Off-Grid Regions (SPORE)	WT PV	100 kW 77 kW	Li Ion BESS Hydrogen	200 kW / 200 kWh 2 MWh	N/S	Semakau Island, Singapore	[69],[70]
Ross Island research station	WT Diesel	900 kW 1100 kW	Flywheel	500 kW	N/S	Ross Island, Antarctica	[58]
Tilos	WT PV	800kW 160kWp	NaNiCl2 BESS	2.8 MWh	Frequency Regulation Ramp rates smoothing Capacity firming	Tilos Island, Greece	[55-57]

Diesel: Diesel generator

N/S: No specified

WT: Wind turbines

H2G: Hydrogen driven genset

PHS: Pumped hydro storage

Hydro: Hydroelectric power plant

PV: photovoltaic panels

The portfolio of storage technologies associated with wind power was introduced in this section. Fig. 2.8 summarizes the capabilities of various storage technologies providing services to the electric grid. The positioning of the technologies is done with respect to their power ratings and energy relationship of those technologies. It is clarified that the comparison presented in the figure is a generalization, meaning that some of the storage options considered can present broader discharge time and power ranges [78].

In addition, in Table 2.1 are shown the discharge and response times for the storage technologies described above, according to typical power rating values [42]. In the table, common power capacities for PHS and CAES technologies are quite big in comparison with the needs of wind power-based facilities for islands.

Wind power-PHS storage for islands projects such as El Hierro or Naturstromspeicher remain for now exceptional uses of technologies historically employed in interconnected power grids.

Several pilot and demonstrator projects have been put into operation to test the capacity of wind power-based hybrid facilities to contribute to supply the need for electricity in non-interconnected island grids. Table 2.2 presents a non-exhaustive summary of demonstrators and initiatives of implementation of hybrid systems in non-interconnected island territories using ESSs with wind turbines and other renewable and non-renewable sources.

In the following, attention is given to the HPP architecture. The analysis considers wind turbines, for the power production, and a generic storage energy system.

2.4 Architectures of grid-connected wind-storage hybrid plants in islands

Even though wind is an abundant resource in island territories, it is variable and has a stochastic nature. Consequently, in order to achieve their smooth operation, WTGs are combined with an ESS. Interfacing power converters rely generators, storage units and island grid. Moreover, the controller operation is dispatched from an energy management system (EMS) [87]. The energy storage units in a wind power-based hybrid facility can be configured in an aggregated way serving the whole wind farm, or it can be distributed in which case there is a storage unit associated locally to each WT.

2.4.1 HPP with wind power and distributed storage

Distributed architecture is shown in Fig. 2.9. It consists of small storage units along with each wind turbine generator placed with the aim of providing smooth output power [87]. In this case, a back-to-back voltage source converter (VSC) interconnects the sources with the low or

medium voltage level of the AC grid. In this structure, the wind turbines are controlled by AC-DC converters to deliver the maximum amount of energy. Also, the ESS is connected to the dc-link through a DC/DC converter in charge of maintaining the DC bus voltage and controlling the power extracted or absorbed by the storage unit. Distributed storage is more suitable in small wind generation facilities comprising a few wind turbines as installing a single ESS for each WTG is economically viable and allows smoothing the outputs of the generators [88]. Finally, the converter in the grid-side must be controlled to allow the continuous supply of good quality energy. All this is achieved with an adapted control scheme [89].

Numerous control strategies have been developed. A detailed operation of a configuration with wind power and distributed storage connected through a power converter DC-link, is presented in [90]. In that work, the battery system is used to smooth the wind turbine output fluctuations and to reduce the import of power from the grid. The robust nonlinear controller developed for this application works in grid-connected and standalone modes.

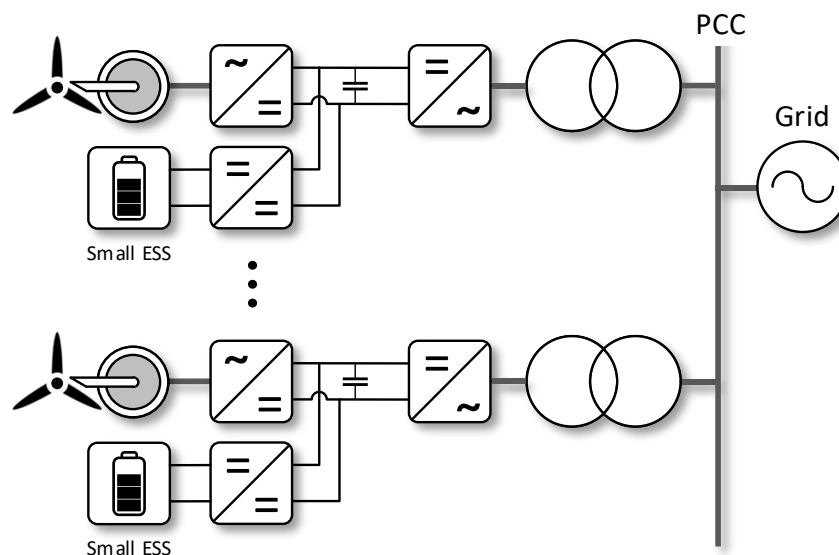


Fig. 2.9. Distributed storage configuration.

2.4.2 HPP with wind power and aggregated storage

Aggregated storage consists of an extensive system that permits storing significant amounts of energy for power management and grid improvement services purposes.

A number of studies have investigated the smoothing effects of the spatial distribution of wind turbines on the output fluctuation [91-93]. Due to this phenomenon, the fluctuation of total wind farm power is smaller than that of every wind generator. Therefore, as the capacity and size of the WECS increases (for instance up to a few hundreds of MW or more), using aggregated storage becomes cheaper as it implies substantially less MWh of energy capacity than in the case of distributed storage, and also fewer power converters and smaller losses in

the power conversion. A comparative analysis of the ESS capacity required for a large wind power plant in the case of using aggregated or distributed storage is presented in [88].

In the present configuration, the centralized ESS is connected to the point of common coupling in AC through a DC/AC VSC (see Fig. 2.10). Moreover, the WTGs can be integrated to inject power at the PCC at grid frequency by using either back-to-back or partial-scale converter with a doubly-fed induction generator (DFIG) configuration.

An example of an aggregated storage configuration operation is detailed in [94], where a power management strategy based on fuzzy logic is employed to calculate the active and reactive power references for the components of a system comprising a 1.5 MW DFIG generator, and a 100 kWh battery - 2.5 kWh super capacitor ESS. The strategy combines the SC fast response and the large battery capacity for the hybrid operation according to the grid requirements and storage restrictions.

After discussing production, storage and architectures of wind-storage hybrid power plants, the two remaining Chapter sections are dedicated to energy management strategies. As EMSs are about control and optimization, a literature review is presented covering several

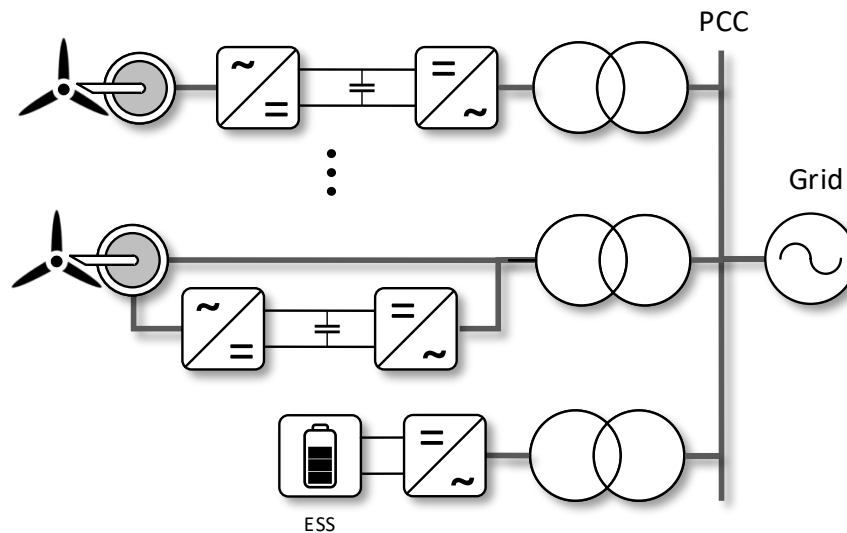


Fig. 2.10. Aggregated storage configuration

strategies for the dispatch of the power flows within hybrid generation facilities pairing wind turbines and energy storage.

2.5 Energy management approaches for HPPs

In order to find the most suitable management approach for a hybrid system, several aspects must be considered. Among these elements are the generation facility design, the operation requirements, and the choice of a control or optimization strategy.

Different energy management approaches have been proposed to tackle the energy flows management of generation sites combining renewable power and storage. The next list, far from being exhaustive, shows that before the present thesis several works that deal with this subject have been published by G2ELAB and ESTIA-Recherche (host laboratories): in [95] the authors use a linear programming (LP) based method to limit the output power variations of a wind-hydro power system. A study case is formulated to test the method through simulation. The results show that the optimization of the storage management allows the system to meet the power grid demand. Reference [96] presents a deterministic non-optimal management approach for a distribution grid connected PV-batteries storage-loads system where the power can flow towards the grid or towards the. An objective function is minimized considering production forecasts, storage system ageing and electricity prices. The aim is supplying the load with the minimum cost while limiting the power exchanged amplitude fluctuation. The algorithm can be used to analyze the sizing and energy management of renewable power-storage systems. An innovative control strategy for a four-leg inverter under unbalanced load conditions is studied in [97]. The inverter is proposed for transformerless hybrid power systems to supply single-phase and three-phase AC loads with constant frequency and balanced voltage. The strategy performance in transient and steady-state operation conditions is tested through simulation and experimental tests. The authors in [98] propose a predictive control-based energy management strategy for a PV-batteries storage-load system. Simulation results with a stand-alone operation case study show the objectives of home energy comfort and economic size of the system are met. The work [99] studies the use of a three-level neutral point clamped (3LNPC) converter for controlling the power flow and interconnecting to a microgrid a hybrid energy storage system. The knowledge of the power division due to the architecture of the 3LNPC converter allowed the authors to analyze the converter operation limits. Consequently, the control structure developed integrates the storage system management limits which made possible the optimization of the storage use. In [100] a simple power management strategy for a hybrid PV-wind turbine- battery storage system implemented experimentally is applied using the LabVIEW software. The authors in [101] apply a centralized predictive controller on a group of microgrids interconnected with a main grid. The objective is maximizing the benefits for both the microgrids elements and the grid itself. The algorithm requires forecast data for energy process and production and consumption power. Simulation results highlight the algorithm's capacity to maximize the benefits for all the elements considered in the network. The importance of cooperation between MG to sell their excess of power and provide a higher benefit if compared to standalone operation mode is proved. In [102], a gas microturbine-solid

oxide fuel cell hybrid power plant allows electrically valorizing the biogas produced by transformation of organic waste in a rural area. In order to obtain the best efficiency while ensuring a safe operation, the HPP is controlled using a 3LNPC inverter. Digital robust R-S-T controllers are designed to control the fuel cell power in the DC-side of the inverter as well as the voltage and frequency in the AC-side, in an islanded microgrid. The performance of the 3LNPC inverter and the controllers is then evaluated in simulation and experimentally. In [103], a second-order sliding mode controller is developed for the power flow control of the ESS in a hybrid renewable power source-VRB and Li-Ion battery storage. A four-leg 3LNPC power converter topology is proposed for interfacing the hybrid plant within a micro-grid. Simulations and experimental results show the strategy can manage the storage system to control the injection of renewable energy into a microgrid while improving the power quality and grid stability. In reference [104], the authors present a universal method to generate accurate state-space models for controlled power converters used to interface intermittent energy sources with the grid and while also improving power quality and grid stability. The proposed method accuracy is demonstrated through simulation on a four-leg three-level Flying Capacitor (3LFC) topology associated with a LCL filter. Finally, in [105] a comprehensive literature review of the main hierarchical control algorithms for building microgrids is discussed, emphasizing their main strengths and weaknesses.

2.5.1 Hybrid systems and dynamic optimization

The optimal operation of renewable energy systems is attained through optimization techniques. Optimization concerns the systematic selection from among a set of feasible solutions of values that minimize or maximize a function. Some typical examples of optimization problems found in renewable energy systems and more specifically in HPPs and MicroGrids, are:

- Optimal sizing and siting of renewable energy-based production units.
- Optimal dispatch of MicroGrids including renewable sources.
- Optimal operation of single and multi-source renewable energy-based plants.
- Optimal sizing of energy storage systems for renewable energy-based power plants.

For solving such optimization problems, multiple algorithms have been developed and there exist several criteria to classify optimization problem types. For instance, when the optimal solution obtained is valid for a specific instant, the problem can be understood as a one-decision-making problem and is said static. Conversely, in dynamic optimization, multiple

decisions are made over time, and the optimization performance relies on all the decisions made [106].

For this and given that representing dynamic phenomena often requires more variables than for static systems, higher computational efforts associated with the resolution of dynamic optimization problems.

Based on whether or not the evolution of all the variables is known for the whole investigated time interval in a given problem, dynamic optimization problems can be divided into global (also known as predictive) and reactive optimization [106], [107]:

- *Global optimization*: in global optimization, the “future” is known with certainty and hence the optimal solution is calculated through a single execution of the optimization algorithm. Such “a priori” knowledge of the future is commonly associated in power flow management problems with forecasts. Typical examples of problems that can be solved through global optimization are the sizing of the storage system for a hybrid plant while assuming the energy production for the next 10 years is known, or the determination of a day-ahead generation schedule from wind forecast data. In [108], a global approach for the energy management and sizing of a MicroGrid with PV panels and flywheel storage is presented. The authors test through simulation several power flow dispatching strategies for predicting the optimal references for power flows based on nonlinear programming (NLP). Also, as the second optimization step related to the MicroGrid components sizing requires for wide horizon simulations, a fast power dispatching approach based on mixed-integer linear programming (MILP) techniques is proposed. In reference [109], linear programming (LP) is used for the optimal sizing of the renewable power sources in a hybrid wind/tidal/PV/batteries system. Seeking a configuration to match with high reliability the off-grid Ouessant French Island load demand, several scenarios are studied varying conditions such as the location, solar radiation, and temperature. In line with the results, the optimal scenario is that combining several renewable resources. The authors in [110], present an approach based on DIviding RECTangles (DIRECT algorithm) to calculate the optimal number of wind turbines, PV panels and batteries in a hybrid wind-PV system. Six months of data corresponding to wind speed, ambient temperature, and solar irradiation estimates are used in the optimization process. In [111], the authors investigate the sizing of hybrid wind-PV-storage system for a 4 people household. The hybrid system size was optimized considering economic aspects, using 25 years of 1-hour irradiance, wind speed and temperature data. Reference [112] applies particle swarm optimization (PSO)

to the constrained multi-objective problem of the optimal sizing, economic, energy management and planning expansion for a hybrid renewable energy system designed to satisfy the loads in a stand-alone area in Brittany, France. The hybrid system consists of wind/tidal/PV/battery, therefore, the solar radiation, ambient temperature, tidal speed, wind speed, location and electrical load are taken into consideration. The economic problem was represented by several scenarios depending on variables such as weather data and electric load demand. According to the results, the best configuration in the area under study is a wind turbine with batteries.

- *Reactive optimization*: Being the “future” unknown, or predictable with a degree of uncertainty, the optimal solution to apply is determined at every calculation step (not necessarily in real-time) based on the present system state. Another way to perform reactive optimization is by readjusting a global solution based on the difference between the forecasts and the real values of the variables. Dynamic problems in which the plant is subject to system state variations, as the optimization occurs, are solved by this type of methods. Two examples of reactive optimization problems are the power dispatch of an isolated MicroGrid to meet a load varying at every instant, and the operation of a hybrid RES-storage plant to meet the different hourly power injection levels defined in its commitment profile, as the renewable energy resources vary. The authors in [113] apply an optimization technique to the management of a storage system in a generation facility coupling renewable power sources with energy storage. Thus, for the sake of smoothing the power produced from ocean waves, the storage system is controlled using a dynamic programming (DP) algorithm.

The power dispatch of the wind-storage HPP is a problem without *a priori* knowledge of future events in the environment. Indeed, the instant wind turbine production and other measurements of the hybrid plant are input information received at every calculation instant for the resolution of the optimization problem. Therefore, the problem treated requires reactive optimization. The literature review of energy management strategies presented in the following section is mainly focused on reactive optimization schemes. Some global optimization examples are included though.

2.5.2 Control and optimization of wind-storage hybrid systems

Recent research addressing the dispatch of grid-connected MicroGrids and hybrid power plants integrating wind turbines and an energy storage system has given rise to various publications. Below are presented several energy management strategies identified in the

literature. The description begins with energy management schemes based on control and decision-making approaches not optimizing a performance index, hereinafter referred to as cost function.

2.5.2.1 Approaches not optimizing a cost function

EMS strategies based on these methods do not optimize numerical cost functions. This category of approaches covers heuristic methods and predictive control.

a) *Heuristic methods*

Methods that present low computational cost and allow quick results. However, this is achieved by trading optimality and accuracy for speed. Some examples of heuristic methods are rule-based and fuzzy logic:

- Rule-based programming: strategies based upon rule-sets of the “if-then/else” form, that are defined starting from the expertise or the knowledge of the system. In [114], to facilitate the integration of a PV system production into the grid, the authors propose peak shaving at the minimal cost. For guaranteeing peak shaving, a set of rules is defined for the PV-BESS system to operate with the storage system at maximum SoC. This power management strategy is compared with a global, day-ahead approach of power management based on dynamic programming. The simulation results showed that both the fluctuations and the cost obtained were reduced through the latter strategy. In [115], a rule-based energy management algorithm is proposed for the power supply of the load in an isolated MicroGrid. As represented in Fig. 2.11, the algorithm makes decisions about the use of the different sources, storage system or even the possibility to import energy from the main grid while, maintaining the battery system’s state-of-charge between 20% and 80%.

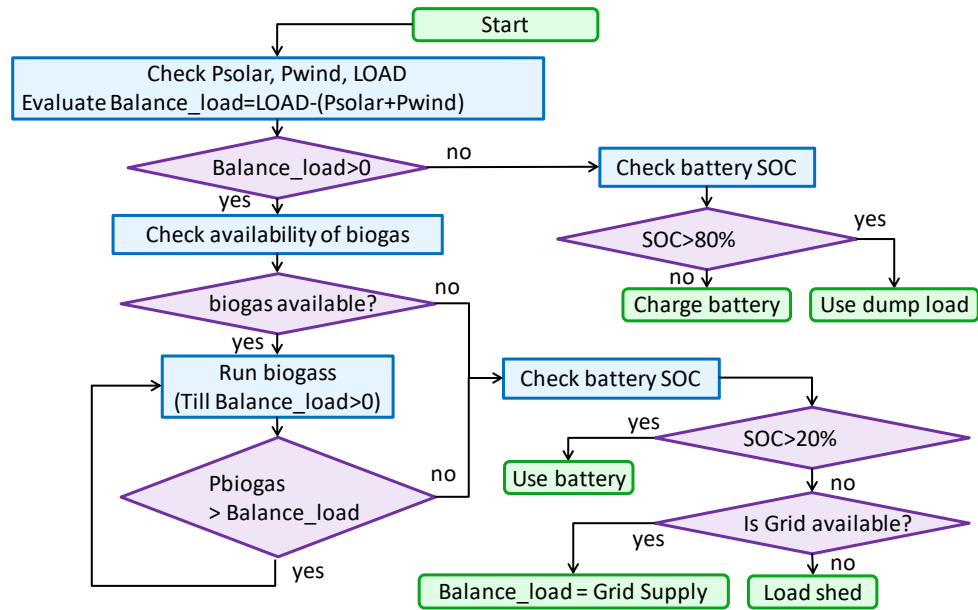


Fig. 2.11. Flowchart of rule-based EMS algorithm implemented in [115].

The authors in [116] employ a rule-based algorithm implementing five operation modes depending on time and weather conditions to reduce the user electricity price and to reduce the voltage variations in a PV-BESS system. The authors in [117], propose an energy management strategy for an isolated grid-connected wind-Li-ion BESS system in order to fulfill a power production commitment to the utility grid. Two classes of energy management strategies are compared: one capable of providing a global optimum of the power flow planning based on a linear programming approach assuming *a priori* knowledge on the future events; and another, based on rule-based control without any *a priori* knowledge on the future, therefore applicable in real-time. As the comparison shows that the heuristic method can be improved, a second rule-based algorithm is developed based on LP behavior showing major performance improvements.

- **Fuzzy logic:** these methods are based upon transition rules between states each of which are associated with a degree of truth (real value between 0 and 1). Human expertise is the basis for the assignation of the mentioned degrees of truth. In [94], a fuzzy logic controller is used to modify the storage units active power references calculated by the supervisory control system of a wind-BESS-SC hybrid system. The fuzzy rules specified allow maintaining the SoC of the storage units inside the margins desired. According to the simulation results, fuzzy logic allowed better compared to other control techniques (state machine, and the same structure without the fuzzy logic compensator). In [118], a fuzzy self-adjusting filter-based SoC controller regulates the state-of-charge

of a BESS according to a pre-calculated *SoC* optimal range in a wind-BESS system. The approach also keeps the WECS output smooth in real-time. The method is tested through simulation. In [119], a control management strategy is proposed for a hybrid PV-diesel generator-BESS-PHS system. The strategy aims at ensuring the water volume in need, while maximizing the use of the PV panels, and limiting the utilization of the diesel generator. For this, a fuzzy logic controller is dedicated to ensuring the maximum power point tracking of the PV system.

b) Model predictive control

MPC relies on a plant model used for the prediction of future states. The method uses information about the current system state as well as a trajectory of future references which spans over a finite time horizon. From that information MPC outputs at each calculation step a sequence of future control actions of which only the first element is applied to the physical system. The process is repeated at the next calculation step with a new set of measurements, and so on. The main advantages of MPC are the handling of constraints as well as multi-variable and nonlinear models. Also, it integrates the disturbances and future variations in the references in the optimization problem. However, MPC main disadvantage is its reliance on the accuracy of the physical system model [120]. Rather than an optimization algorithm, model predictive control is a family of control methods that can be used in real-time implementations [121], [122]. Nonetheless, it is frequently combined with optimization methods such as quadratic programming [123] or brute-force search [120]. In [124], a MPC scheme is proposed for the interlinking converter in a hybrid AC/DC MicroGrid. The scheme allows the local power and voltage control and is connected to a second control stage, in charge of maintaining the power balance under varying generation and consumption conditions. Compared to traditional cascade linear, the strategy requires less tuning work. Often, the method is used to include the RES production forecasts in the optimization problem, either in terms of the expected generation or in terms of the primary source, (wind speed, solar irradiance, etc) [121], [122]. In [123] QP is used to minimize a quadratic cost function fed at every calculation step by an MPC-based algorithm developed for the optimal operation of several converters in a DC-grid connected wind-BESS MicroGrid. The design concept has been verified through simulation. However, further experimental validation is required because measurement and modeling errors in the parameters of the actual system affect the controller performance in practical implementation.

2.5.2.2 Approaches optimizing a cost function

This second group of methods permits the definition of EMS schemes based on the optimization of a cost function. The methods are divided into deterministic, metaheuristic search techniques, and artificial intelligence approaches.

a) *Deterministic approaches*

Approaches that taking advantage of the analytical properties of the problem, generate a sequence of points that converge to a global optimal solution. They can provide a global optimum or an approximate global optimum [125]. These techniques can be used in the resolution of global or reactive optimization problems. Some examples are:

- *Linear programming (LP)*: the problem of maximizing or minimizing a linear cost function subject to a set of linear equality or inequality constraints. In [126], a formulation is proposed for the energy management of grid-connected wind-PV-microturbine- BESS-FC MicroGrid using LP optimization jointly with artificial intelligence techniques. Hence, a LP-based multi-objective energy management strategy is proposed to minimize both the operational expenses and the CO₂ emissions of the sources in the MicroGrid. Also, a neural network ensemble (NNE) is developed to predict 24-hours- ahead PV generation and 1-hour-ahead wind power generation and load demand. This strategy is implemented in a MicroGrid simulation model and validated using experimental data. In [127] is addressed the optimal management of a BESS supplied by a PV system in a grid-connected PV-BESS microgrid. The main contribution of the work is the consideration given to uncertainty in the electricity price while managing the storage. Hence, the optimal operation of the BESS is determined by solving a linear cost function comprising the conditional value at risk. The cost function is the difference among the power sold and bought, subject to constraints limiting both the charging and discharging rates for the battery, and the state-of-charge desired range. Simulation confirms that risk consideration has a significant impact on the results obtained.

Integer linear programming (ILP) optimization problems contain linear cost function and constraints. MILP is a variant of ILP in which some of the variables must be integers whereas the others can be non-integers. The authors of [128] formulated an online EMS for a grid-connected hybrid wind-PV-diesel-BESS system. The EMS proposed solves in real-time an optimization problem in the form of a MILP framework with the objectives of minimizing the operating cost and minimizing the pollutant gas emissions. To do that, a rolling optimization algorithm is established to schedule operation based

on forecast data using MPC. The rolling dispatch scheduling is then adjusted through feedback intrasample correction, that reschedules BESS, renewable production and grid imports to minimize the operation cost.

- *Quadratic programming (QP)*: QP is the problem of maximizing or minimizing a quadratic cost function, meaning that it has terms with the decision variable squared, subject to a set of linear equality or inequality constraints.

The simplest possible function which has a minimum is $f(x) = x^2$, which has a minimum in $x = 0$. Shifting the function into $f(x) = ax^2 + bx$, leads to a more general function whose minimum is located at $x = b/2a$ is generated. That means that $f(x) = (1/2)ax^2 + bx$ has a minimum in $x = b/a$, leading to the standard form of QP problems, that can be represented as

$$\min_x \frac{1}{2} \mathbf{x}^T \mathbf{H} \mathbf{x} + \mathbf{f}^T \mathbf{x} \quad \text{Eq. 2.1}$$

where \mathbf{x} is the decision variable, \mathbf{f} is a vector and \mathbf{H} is a squared matrix. A constant term could be added in the equation affecting its minimum. However, in essentially all the applications of optimization in the framework of natural phenomena, the aim in solving this kind of problems is focused in finding where the minimum occurs in opposition to what is the value of the function at that minimum. Another important aspect of Eq. 2.1, that if the matrix \mathbf{H} is positive definite, the problem is a special case of convex optimization. In minimization problems, a convex objective function ensures that all local minimums are global minimums, allowing local search algorithms to find optimal solutions. The same can be applied to concave objective functions and maximization. Without convexity, local search algorithms may converge to local minimums.

An optimization strategy for the optimal scheduling of an island microgrid with high penetration of wind and PV generation is proposed in [129]. A two-stage robust model predictive control (RMPC) based optimization approach is used for obtaining a robust operation schedule for the MicroGrid. Uncertainties related to RES and loads are considered through interval forecasting methods. Robust linear methods are used for transforming the robust optimization method into a mixed-integer quadratic programming model.

- *Dynamic programming (DP)*:

According to Richard Bellman's principle of optimality, on which DP is based, optimal solutions can be found by breaking the problems into simpler sub-problems and then sequentially finding optimal solutions to those sub-problems. As an example, Fig. 2.12 shows a multi-stage weighted graph that has costs (or distances) between the nodes, usually useful for representing resources allocation. The graph's nodes are divided into stages such that the edges are connecting nodes from one stage to the next stage only.

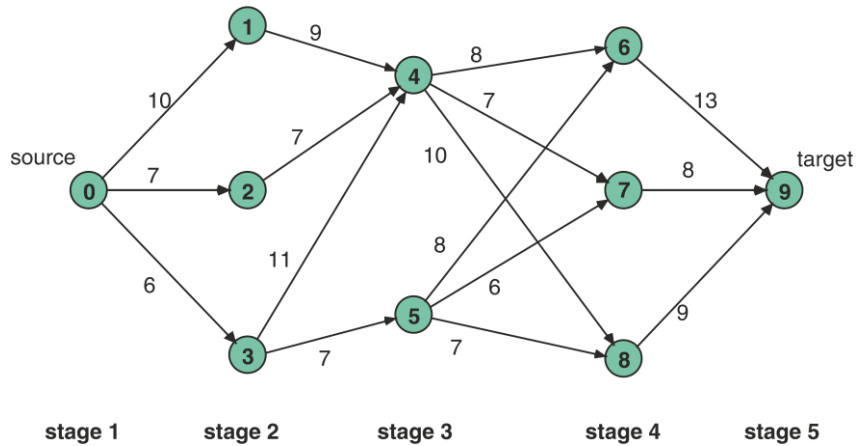


Fig. 2.12. Weighted graph with distances between the nodes [130].

The first stage (source) and last stage (target) have a single node each. As there are various paths from source to target, the objective of the problem is finding the path that gives minimum cost. This optimization problem can be solved by applying a dynamic programming strategy.

Let $F(x)$ be the minimum distance required to reach node 9 from a node x .

Starting at stage 5 (backward recursion-DP), $F(9)$ is equal to zero because there is no path cost to get to itself.

Going back a level, $F(6)$, $F(7)$ and $F(8)$ are respectively 13, 8 and 9, simply based on the weighting edges. A knowledge base is filled in with the costs of the functions, and

Table 2.3 Knowledge base for stage 5 of example problem, backward recursion.

N	0	1	2	3	4	5	6	7	8	9
F	-	-	-	-	-	-	13	8	9	0
d	-	-	-	-	-	-	9	9	9	9

the information of the sub-path with the minimum cost for each node (see Table 2.3). In the table, N represents the nodes (0 to 9), F the sub-path costs, and d the minimum cost for each stage.

Now for the third stage, $F(4)$ is calculated as the minimum cost between 3 options, or:

$$F(4) = \min[8 + F(6), 7 + F(7), 10 + F(8)]$$

Where $F(6)$, $F(7)$ and $F(8)$ are known and available in memory. Hence $F(4) = 15$ and this minimum cost is obtained by going through node 7. The same for node 5, resulting in a cost of 14 and node 7 as optimum path.

By repeating this procedure for the remaining stages, the knowledge base is filled with the next information:

Table 2.4 Knowledge base filled.

N	0	1	2	3	4	5	6	7	8	9
F	27	24	22	21	15	14	13	8	9	0
D	3	4	4	5	7	7	9	9	9	9

Now, based on the data available, the sequence of decisions is going to be determined starting from the source node. According to the resulting table, the first decision consists in going from the source node to node 3. Then, starting from node 3 the optimal decision is going to node 5. From node 5, the decision retained is going to node 7, and finally, the last step in the sequence is going from node 7 to the target node. Hence, the optimal path that minimizes this problem is 0-3-5-7-9.

The DP global strategy proposed in [114] allows the scheduling of the battery use from 24-hours ahead forecasting data for helping a PV system to provide peak shaving at the lowest cost in a grid-connected PV-BESS system. A multi-stage optimization approach is employed to find the optimal sequence of the battery system SoC from the initial time to the final time. The transition between two stages is the SoC variation written ΔSoC , a constrained variable. For each ΔSoC , the battery use (P_{BAT}) and the power exchanged with the grid (P_{GRID}) are calculated according to the a priori knowledge base of the loads consumption (P_{LOADS}) and the PV availability (P_{PV}). The authors in [131] employ DP for the energy management problem of a PV-diesel-BESS MicroGrid. The DP strategy is an extended version of Bellman's principle applied in the optimization of switching times for the on/off modes of the diesel generator. The time it takes to the strategy to find global optimal solutions is less than a second. This is important as the energy management problem is formulated as an optimal control problem.

b) *Meta-heuristic search techniques*

Metaheuristic techniques sample a set of solutions which is too large to be completely sampled. They provide a sufficiently good solution to an optimization problem [132]. These techniques are more commonly applied to the resolution of global optimization problems. Some examples are:

- Genetic algorithms (GA): iterative search inspired by Charles Darwin's theory of natural evolution. The process begins with an initial population of individuals (chromosomes filled by genes). Each one of those individuals is a solution to the optimization problem. Every generation of parents gives origin to new chromosomes for their children through the crossover. Such genetic recombination results in variations and adaptations. If an adaptation makes an individual more fit, it will increase its chances to survive and pass on its genes. Typically, fitness is the value of the cost function obtained by evaluating each individual. Least satisfactory individuals are thrown out while the more fit ones are recombined to produce a new generation. The algorithm stops either after a maximum number of generations or when reaching a satisfactory fitness level.

A global management strategy is presented in [133] for the optimal operation of a MicroGrid, based on power forecasting inputs. It is composed of a power forecasting module, an ESS management module and an optimization module. The forecasting module is used for the hourly prediction of the PV panels power generation according to weather forecast inputs. Meanwhile, as energy storage needs to be optimized over multiple time steps to fulfill the load, the matrix real-coded genetic algorithm (MRC-GA) optimization module coordinates the optimal operation schedule in terms of economic dispatch (energy prices reduction for consumers and daily MicroGrid operational cost reduction).

- Particle swarm optimization (PSO): approach that iteratively optimizes a problem. Similar to the case of genetic algorithms, the method starts with an initial population and searches for solutions by updating generations. In PSO, candidate solutions are particles whose position and velocity depend on each particle's best-known position, which is also refreshed in every iteration by better positions found by other particles. In [134], an optimal EMS strategy based on PSO is proposed for a grid-connected MicroGrid including generation units and energy storage devices. Uncertainties of the wind turbines and PV panels energy production, as well as load demand and market prices, are introduced using a point estimate method. The proposed method is tested through simulation under different operational scenarios. Moreover, the results obtained using the PSO algorithm are found to be either better or comparable to those obtained using other methods reported in the literature such as GA, fuzzy self-adaptive particle swarm optimization (FSAPSO), combinatorial particle swarm optimization (CPSO), and adaptive modified particle swarm optimization (AMPSO).

c) *Artificial intelligent approaches:*

Artificial intelligence is an area of computer science that aims at creating computational entities that act intelligently. Under this definition, acting intelligently, implies that the entity does what is appropriate given the circumstances and goals, is flexible to changing environments and goals, learns from experience, and makes appropriate choices given its perception and computational limitations [135]. Multi-agent system is one example of artificial intelligent methods:

- *Multi-agent system (MAS)*: the multi-agent approach is broad and not necessarily used for optimization. MAS is a computer-based system that comprises several interacting agents each of which has a certain degree of intelligence. An agent is a computerized system able to carry out a task on behalf of a user by determining the actions required to satisfy design objectives, as opposed to regularly receiving orders. To solve complex problems, rather than employing a single agent (generally implying more computational power or time), multiple (simpler) agents can be implemented to interact with each other and collaborate to solve the problem based on locally accessible information. There exist several methods for MAS to intelligently tend to find the best solution without intervention. However, the search policies that the agents ought to follow are sometimes unobvious and optimality is practically impossible to attain. An energy management scheme for an islanded microgrid based on the MAS approach is proposed in [136]. The PV system, wind energy conversion system, FC system, BESS and loads with their corresponding breakers, are the strategy's agents. Following a global optimization approach, the energy management system manages the utilization of power among the agents based on predicted renewable powers and load demand. A STATCOM is used for reactive power compensation to mitigate the voltage fluctuations and harmonics. The simulation model of the agents and the central controller were implemented and tested through simulation.

Fig. 2.13 summarizes the optimization methods considered in the literature review of EMS strategies. According to the review, the management strategies are based on: non-optimal control strategies, optimization algorithms (implying the optimization of a cost function), or the association of methods from the two groups to build more advanced control-optimization schemes.

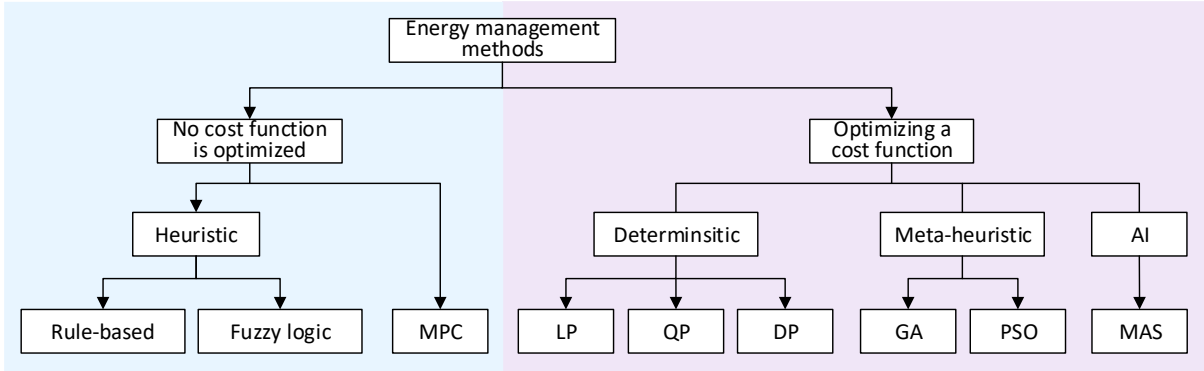


Fig. 2.13. Optimization methods considered.

2.6 Chapter conclusions

The present Chapter defined and dressed a state of the art related to the operation of wind energy-based HPPs. First, hybrid power plants were defined as systems closely related to MicroGrids with the difference that the latter could operate connected or isolated to the main grid. Apart from that, both are hybrid systems accommodating generation equipment (conventional and/or renewable sources, and energy storage devices), interfaced through an energy management system.

The attention has been on wind power, one of the primary energy resources available in islands and overseas territories. Due to the intermittency and variation of wind resources, hybridization (i.e. combination with other forms of generation, and with energy storage means) was presented as the adapted solution to allow a dispatchable supply.

Regarding the energy storage, according to their discharge time storage technologies were classified into long-term and short-term storage. While long-term storage (minutes or hours) is more adapted to energy dispatch and frequency regulation, short-term technologies are usually employed in voltage stability improvement applications.

The storage technologies used with wind turbines or WECSs, while offering a long discharge time are pumped hydro, batteries, compressed air, and hydrogen energy storage. Conversely, some short-term technologies employed in wind power facilities are flywheel, supercapacitor and superconducting magnetic storage. Among those, several stood out for being more suitable for HPPs in non-interconnected islands (PHS, BESS, and FES). To illustrate the existing hybrid power systems, some application examples of storage systems implemented in demonstrator projects testing wind power in isolated islands have also been depicted.

After discussing production and storage, the architectures of wind-storage HPPs were put under the spotlight. Because of the smoothing effects of distributed wind turbines,

centralized storage was found to be more suitable for wind farms with a capacity of the order of hundreds of MW. In the same way, distributed storage tends to be more adapted for facilities integrating only a few wind turbines.

The last part of the Chapter dealt with the energy management of hybrid systems, which is attained through optimization. Several optimization methods there exist yet there is no specific one able to solve a particular problem.

On the other hand, the power dispatch of an HPP consists in the dynamic search for the values of the degrees of freedom either optimizing a performance index or at least providing a result which is good enough. In the problem of managing the power flows of an island grid-connected wind-storage HPP, the handling of production forecasts is a key aspect.

The energy dispatch of RES-storage hybrid systems has inspired numerous research works in the last years. Diverse groups of strategies were reviewed. Among those groups, deterministic optimization methods are both compatible with reactive optimization problems and allow for optimal or approximately optimal solutions. QP is one of the several deterministic methods examined. It presents the advantage of assuring the existence of a global optimum when the cost function is convex. On the other side, model predictive control is not an optimization method *per se*, however, it is commonly associated with optimization algorithms to produce optimal outputs. MPC outstands for being a common way to integrate forecasts in optimization problems related to the energy management of RES-storage system hybrid plants.

Given the nature of the system and the complexity of the revenue optimization problem dealt with, it seems appropriate to focus on methods capable of finding optimal solutions combined with control strategies handling the forecasting aspects, rather than heuristic strategies.

CHAPTER

3

Electrical grid and hybrid power plant modeling and validation

Summary

3.1 Introduction	64
3.2 Guadeloupe electrical grid: current state description	64
3.2.1 Transmission system.....	65
3.2.2 Electricity consumption.....	66
3.2.2.1 Evolution of the demand	66
3.2.2.2 Seasonality	66
3.2.2.3 Load curve	67
3.2.3 Existing capacity.....	67
3.2.3.1 Base and semi-base thermal production facilities.....	69
3.2.3.2 Peaking and emergency thermal production facilities	69
3.2.3.3 Renewable energies.....	70
3.2.3.4 Evolution of renewables share in production.....	71
3.2.3.5 Current energy mix	71
3.2.3.6 Daily balance	72
3.3 PowerFactory Modeling	73
3.3.1 Modeled grid.....	73
3.3.1.1 Grid description	73
3.3.1.2 Evolution of the demand	75
3.3.2 PowerFactory grid model	78
3.3.3 Grid model validation.....	80
3.3.3.1 Static validation	80

3.3.3.2 Dynamic validation	83
3.3.4 Hybrid power plant model.....	88
3.3.4.1 Wind generation system modeling and validation	89
3.3.4.2 Energy storage system modeling and validation	95
3.4 Model for control	105
3.4.1 Linear model for control.....	105
3.4.2 Control model validation	108
3.5 Chapter conclusions	108

Chapter overview

This Chapter establishes the models for the main grid and the hybrid power plant systems. The software tools employed for the modeling implementation and validation are DIgSILENT PowerFactory and Matlab.

3.1 Introduction

Even though wind energy is one of the most promising renewable energy sources (RES) for non-interconnected island territories, such as Guadeloupe island, the energy mix of this French overseas department is still mainly based on fossil fuels.

This Chapter begins with a description of the current state of the electrical system of Guadeloupe island, where the hybrid power plant (HPP) studied is implemented. After describing the main features of the infrastructure and exploitation of the electrical system, the validation of the modeled network's static and dynamic behavior is presented.

3.2 Guadeloupe electrical grid: current state description

The archipelago of Guadeloupe is a French insular region and overseas department located in the eastern Caribbean Sea. Guadeloupe counts with a land area of 1 628 km² and an estimated population of 394 100 inhabitants as of June of 2018. The two main islands, commonly referred to as the main island, Basse-Terre (848 km²) and Grande-Terre (586.7 km²) are separated by a narrow strait and are connected by bridges. The other three islands in the archipelago are the Dependencies of the Department: Les Saintes, Marie-Galante and La Désirade. Even though its enormous potential for renewable energies development, Guadeloupe's energy mix depends predominantly upon power plants producing electricity from imported petroleum-based fuels.

3.2.1 Transmission system

Guadeloupe's electrical grid comprises three different levels:

- The transmission network (presented in Fig. 3.1), which is operated at 63 kV (high-voltage level).
- The 20 kV network (medium-voltage), allowing the electricity to be transmitted to the distribution network.
- The distribution network at 220/380 V (low-voltage), through which energy is delivered to customers.

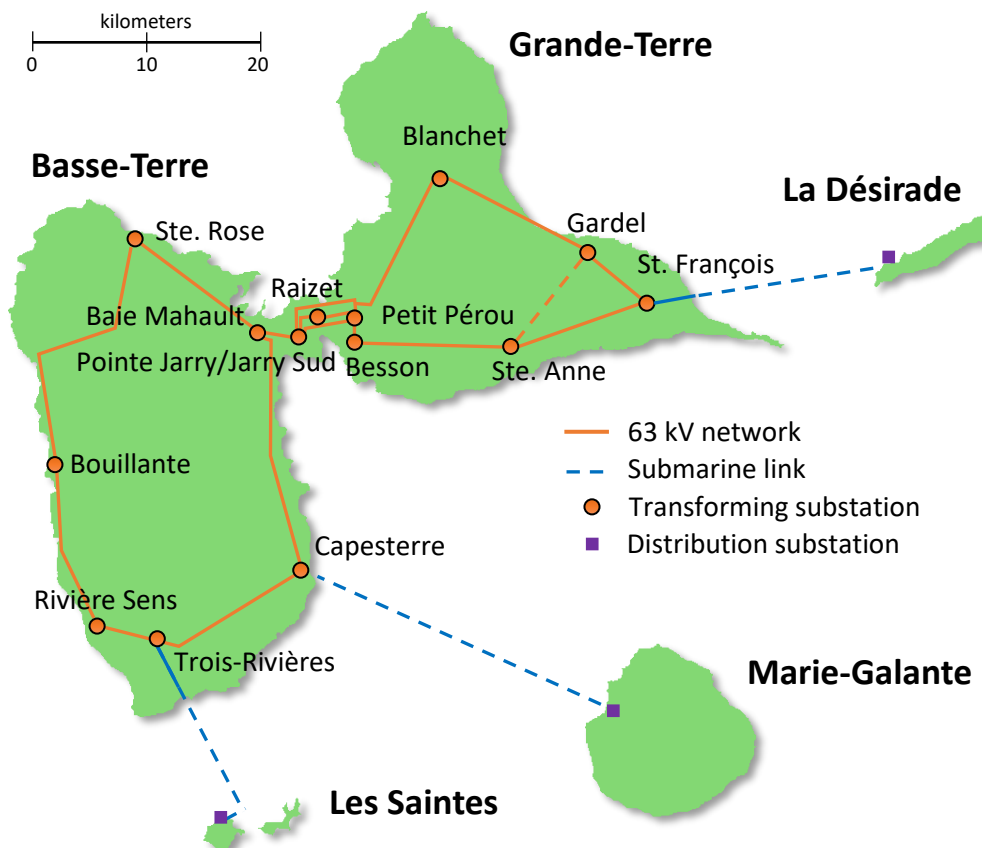


Fig. 3.1. Guadeloupe transmission network and substations.

Several transforming and distribution substations are installed between the voltage levels mentioned. 15 transforming substations (63 kV/ 20 kV) are also represented in Fig. 3.1. The main production sites as well as the 20 kV distribution network, are connected to these substations.

The Guadeloupean transmission system is composed of two big loops of overhead lines. The loop covering Basse-Terre is interconnected at the Jarry Sud substation with Grande-Terre's loop. Submarine cables at 20 or 30 kV interconnect the distribution substations located

in the islands Les Saintes, Marie-Galante and La Désirade to the 63 kV network covering Basse-Terre and Grande-Terre.

3.2.2 Electricity consumption

In the present section, the main features of Guadeloupe's gross consumption (not considering transportation and distribution losses) are described.

3.2.2.1 Evolution of the demand

The total generation delivered to the island system of Guadeloupe in 2018 reached 1 704 GWh. An average annual gross per capita consumption of 4,32 MWh was registered that year versus 6,5 MWh at the whole of France in 2017 [137].

Whereas from 2005 to 2010, the electricity delivered to the island system of Guadeloupe grew more than 15%, the consumption was stable between 2010 and 2014, and presented a growth exceeding 3,3% between 2014 and 2016. Later on, a downward trend begun in 2017 and was confirmed in 2018 with a decrease of 3% (see Fig. 3.2).

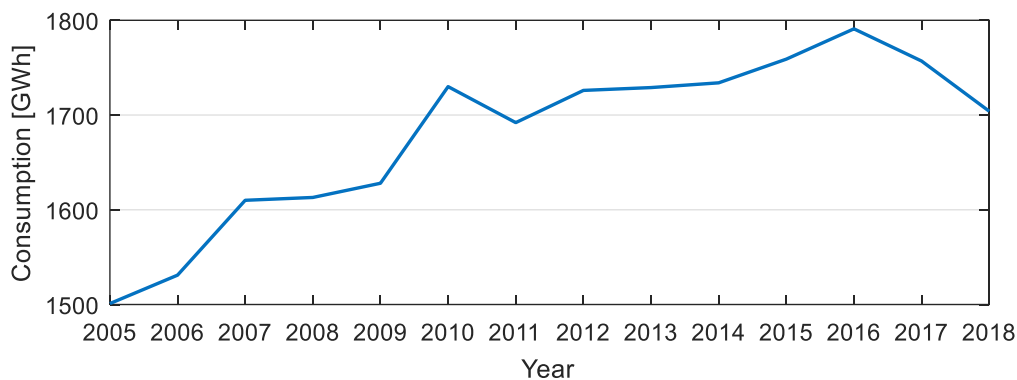


Fig. 3.2. Electricity consumption starting from 2005.

The economic crisis, but also the implementation of administrative measures promoting energy demand management and increased energy efficiency of the equipment of buildings and industrial facilities, could explain the tendency change in the demand pattern [138].

3.2.2.2 Seasonality

In 2018 the monthly gross electricity consumption in the archipelago averaged 142 GWh. In comparison with other months, February exhibited an atypical behavior, as shown in Fig. 3.3. This is explained by the fact the month only counted 28 days. As can be seen, the energy demand is relatively stable over the year, and therefore the demand seasonality is low. However, there seem to be a correlation among the monthly consumption and the evolution of the temperature throughout the year [139].

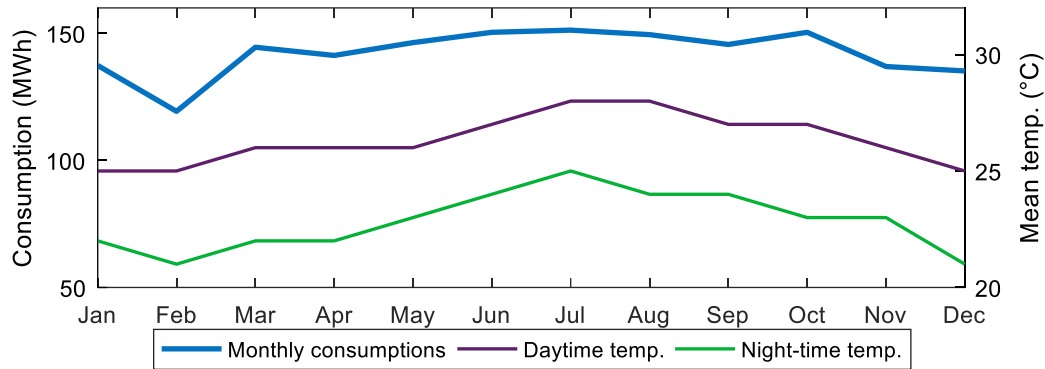


Fig. 3.3. 2018 monthly consumptions and mean temperature measured at the substation Raizet.

3.2.2.3 Load curve

Daily consumptions are characterized by two peaks. The first one occurs at 12h and is attributed to the services sector (private and public). Attributed to consumptions in the residential sector, the remaining one is the most important and takes place at 20h.

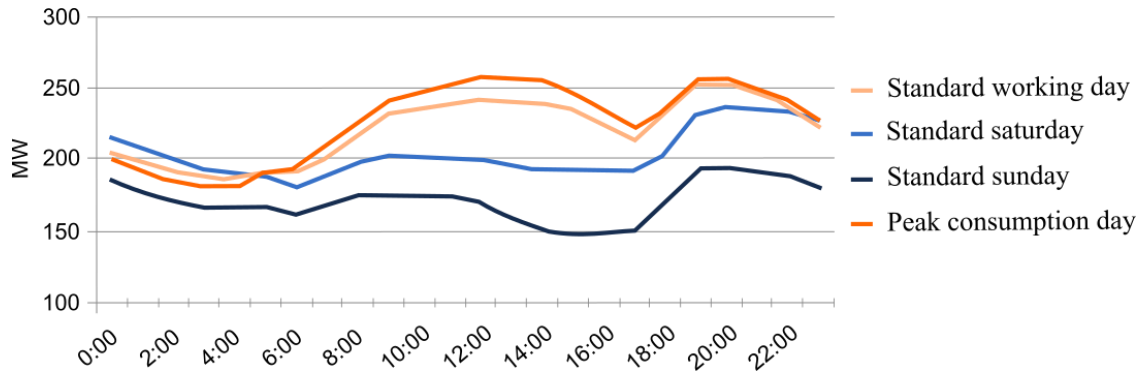


Fig. 3.4. 2016 standard and peak days representative load curves.

As an example, Fig. 3.4 displays daily load curves for three standard days and for the peak consumption days in 2016. From the figure, the evening peaks in 2016 resulted in demands ranging from 200 MWh and more than 250 MWh during the evening. The gaps between the evening and noon peaks were of around 10 MWh in the case of the standard working day profile while no difference is observed for the peak consumption day. This difference was more marked for the standard weekend days. Thus, the gaps associated to standard Sunday and standard Saturday consumptions are of a 25 MWh and 40 MWh, respectively.

Conversely, the profiles reveal low consumption periods happening at 7h30 and 16h, in the case of standard weekend days, and at 4h and 17h30 for the remaining types of days.

3.2.3 Existing capacity

In the French overseas departments, among which is Guadeloupe, the tasks of the public service of the supply of electricity are carried out by EDF's (Électricité de France) insular power

systems department (EDF SEI). EDF SEI is responsible for the following tasks on the Guadeloupean territory:

- Supply of electricity at regulated sale tariffs,
- purchase all the electricity generated within the insular territory,
- balancing electricity supply and demand continuously, and
- ensure the transmission, distribution and supply of electricity to all the costumers.

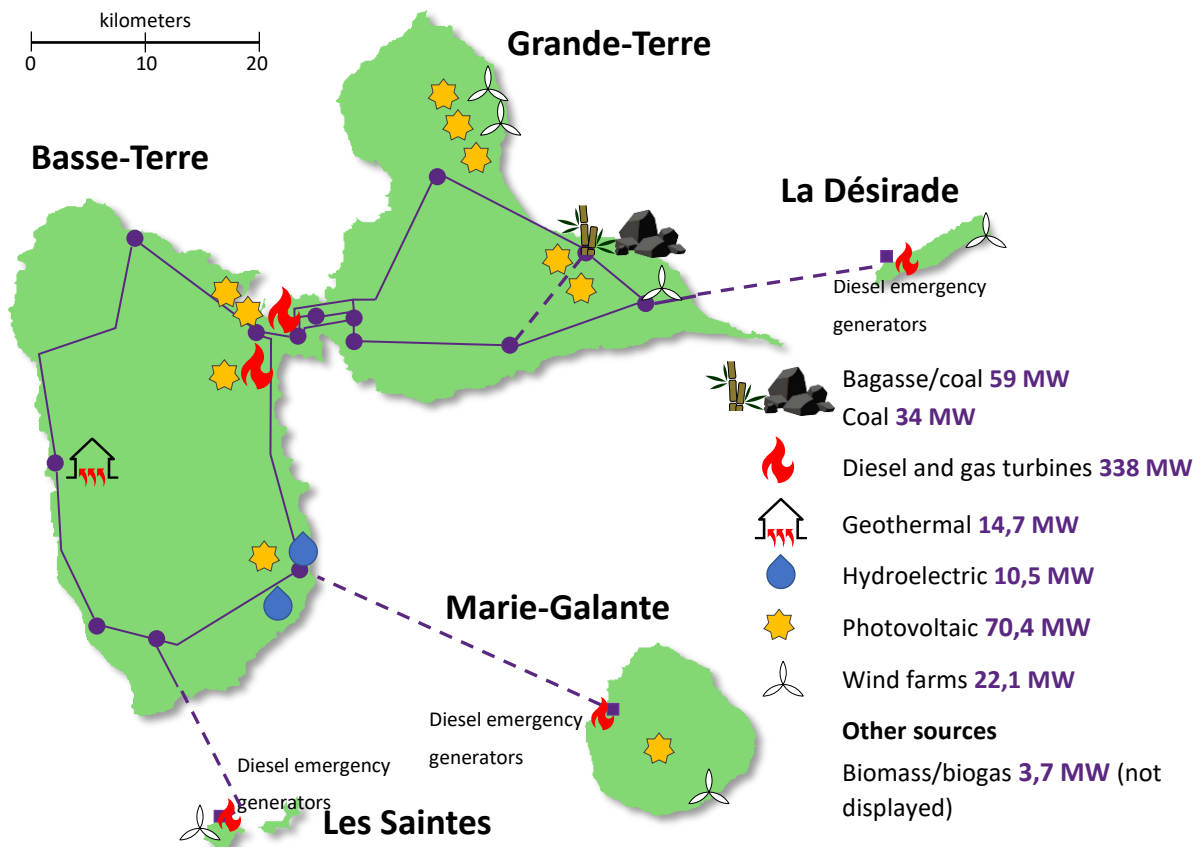


Fig. 3.5. Available power in Guadeloupe's power grid by type of primary energy in 2018.

However, EDF is not granted a monopoly on generating electricity, meaning that other actors can also own and/or operate power generating facilities on Guadeloupe.

A particular feature of the archipelago is the diversity of its energy sources, particularly renewables. Thus, apart from coal, diesel and fuel (the latter two are here referred to as thermal production means), several renewable sources are being exploited to produce electricity on the island territory: solar (photovoltaic), geothermal, wind, hydroelectric and biogas.

The geographical distribution of the main generation facilities according to their primary source, is represented in Fig. 3.5.

3.2.3.1 Base and semi-base thermal production facilities

- Bagasse/coal power plant (Albioma): the Le Moule power plant was put in service in 1998. It is composed of two units totaling 59,5 MW. It runs using sugarcane bagasse and coal as sources of fuel during the sugarcane harvest season (between February and June), and using coal the rest of the year. In 2018 Le Moule produced 55 755 MWh from bagasse, thereby constituting the third renewable energy source after geothermal and solar PV.

The thermal plant Caraïbes Energie, with an installed capacity of 34 MW, is a coal-fired power station. These two power stations belong to the group Albioma.

- Pointe Jarry diesel power station (EDF-PEI): between 2014 and 2015, the formerly known Jarry Nord diesel station (eight 20,9 MW diesel engines for a total capacity of 167 MW), was gradually replaced by the new EDF-PEI Pointe Jarry (EDF Production Electrique Insulaire, subsidiary of EDF). The power station is now composed by the twelve 17,6 MW diesel engines (total capacity of 210 MW).
- Energies Antilles diesel power station (Contour Global): with a capacity of 18 MW, the station is constituted of four diesel engines. Energies Antilles runs at Baie-Mahaut since 2000 and is currently operated by Contour Global.

3.2.3.2 Peaking and emergency thermal production facilities

- Jarry-Sud combustion turbines (EDF): composed of four combustion turbine generators located at Jarry-Sud, the installed capacity of this production plant is of 100 MW. Units 2, 3 and 4 have a generation capacity of 20 MW each, whereas the unit 5 has a capacity of 40 MW. Some of these units are not equipped with proper flue gas denitrification systems, therefore their use is constrained to no more than 500 hours per year.

If compared to other types of generators in the system, combustion turbines present the shortest starting times. However, producing energy from these units is more expensive (generation based on fuel oil), consequently they are employed to meet peak demands.

- Southern islands diesel emergency generators (EDF): southern islands (Marie-Galante, les Saintes, la Désirade) are fed through submarine cables from Guadeloupe. These islands are provided with small diesel emergency plants (7,1 MW at Marie-Galante, 1,5 MW at les Saintes, and 1,6 MW at la Désirade) which produce power in case the corresponding relying line is unavailable or on the occasion of periodic tests. The emergency generators can also be used in case of production outages on the main island. In total, 10,2 MW can be made available.

3.2.3.3 Renewable energies

Within the archipelago context, two kinds of renewable sources can be distinguished: stable and intermittent renewables. The former, interfaced with the grid through synchronous generators and the most of the times relied to the 20 kV network due to their significant generation capacity (Biomass, geothermal, hydroelectric power), while the latter are interfaced through power electronic converters and are often relied to either medium or low voltage busbars, like is the case for PV and wind power.

The integration of these intermittent and unpredictable production means into the island systems poses several challenges. Their power output being variable, it is necessary to ensure adjustment margins so that they can contribute to maintaining the balance between production and consumption. Energy storage but also the spatial distribution of the sources can contribute to the smoothing of the output fluctuations.

On the other side, as intermittent RES power sources inject power in the medium or low-voltage level (feeders supplying end-users), the imposition of specific behaviors seeking the protection of persons and goods is made necessary. Also, high penetration of power electronic interfaced power sources without contribution to inertia is known to be associated with excessive frequency rate of change, particularly when sudden power imbalances occur while total system inertia is low within the synchronous area [140].

For this, Ministerial Order of 23 April 2008 limits the intermittent RES use whenever the addition of the power injected by those sources reaches 30 % of the active power passing over the network. Moreover, according to decree No 2017-570 of 19 April 2017, the trend is for this limitation to evolve in the years to come. In order to maintain the quality of the electricity service while increasing the coverage of intermittent RES, solutions must to the devised to the above-mentioned impacts. Both system operator and renewable energy producers are called to apport the remedial actions required [141].

- *Geothermal*: the Bouillante plant is composed of two units (4,4 MW and 10,25 MW) put into service in 1986 and 2004, respectively. Fed by the heat from the earth which escapes as steam, the plant produced power taking advantage of Basse-Terre's cluster of composite volcanoes. The plant was formerly operated by Géothermie Bouillante, subsidiary of BRGM, the *French geological* survey, but since 2016 it is owned by the group ORMAT. Bouillante generated 106 794 MWh in 2018, more than any other renewable energy source in the archipelago.
- *Small hydroelectric plants*: there are several mini-hydroelectric power stations that take advantage of the mountainous terrain and water potential in Basse-Terre. In total, those

power stations combined add around 10,5 MW. The existing sites are operated either by FHA (Force Hydraulique Antillaise), or by EDF.

- Wind: wind production started on the island in 1992. The first wind farm with storage was commissioned end of 2016 at Marie-Galante with an installed capacity of 2,5 MW. In 2018, wind turbines represented a production capacity of 22,1 MW and generated 3 % of the total production.

The farms operators are Quadran, Société d’Eolienne Caribéenne or EDF Energies Nouvelles. In 2018 wind turbines produced 52 424 MWh.

- Photovoltaic: as of 2018, the Guadeloupean system counts 70,4 MW of PV panels. That year the panels produced 94 836 MWh. On the other hand, wind turbines represent a production capacity of 22,1 MW. The first wind farm with storage was commissioned end of 2016 at Marie-Galante with an installed capacity of 2,5 MW.

3.2.3.4 Evolution of renewables share in production

Renewable energies allowed producing 21,2% of the total production in 2018, that is 361 895 MWh. After a first decrease from 2008 to 2010, the increment of geothermal and photovoltaic power meant a change in the tendency until a new decrease took place in 2015. Together, geothermal and photovoltaic represent today more than 55 % of energy from renewable sources (see Fig. 3.6).

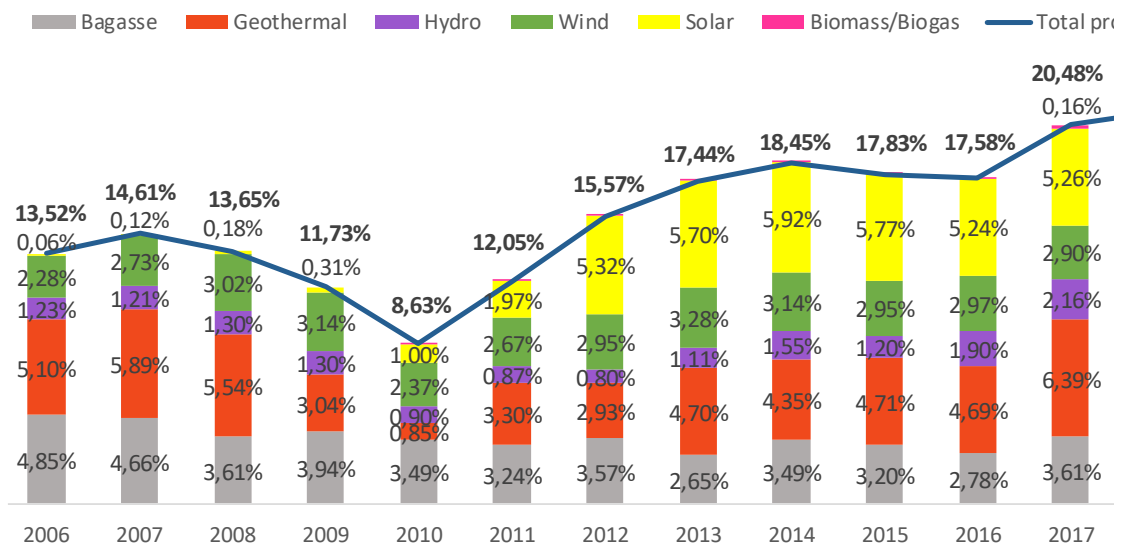


Fig. 3.6. Guadeloupe distribution of RES shares from 2006 to 2018.

3.2.3.5 Current energy mix

- Non-renewable sources (coal-fired power stations, diesel generators and natural gas turbines) are predominant in Guadeloupe’s electrical system. In Fig. 3.7 is depicted the

distribution of the electricity production depending on the primary energy source for the year 2018.

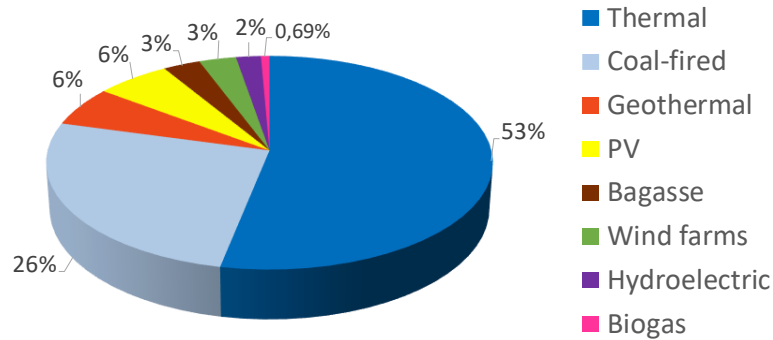


Fig. 3.7. Guadeloupe 2018 energy mix.

3.2.3.6 Daily balance

Guadeloupe’s power generation park is marked by an overcapacity situation. In fact, the generating capacity of base production facilities is such that often the evening peak can be handled without the combustion turbines of Jarry-Sud. As an example, Fig. 3.8 depicts the generating means stacking for a working in Guadeloupe. At this day, the noon/evening peaks present similar levels. The use of the combustion turbines is avoided by the PV production at

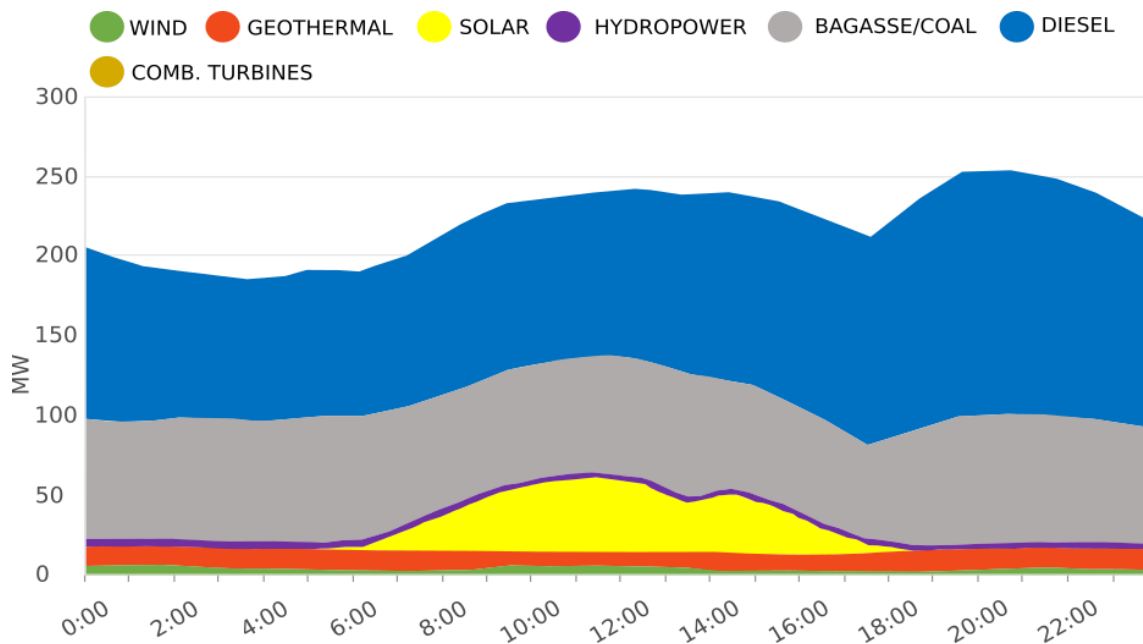


Fig. 3.8. Example of generating means stacking.

noon, and by the diesel Pointe Jarry power station, which covers for the consumption increment at the evening. Moreover, in the example the average demanded power and peak consumption are respectively 205 MW and 261 MW while the dispatchable base production facilities (PEI Jarry, Albioma Caraïbes, Albioma le Moule and Contours Global) can supply a close to 320 MW [141], [142].

3.3 PowerFactory Modeling

The first part of the present section describes the situation of the island's electrical network represented by the grid model. Then, the grid model allowing the simulation of the wind-storage hybrid power plant operation, is explained. After presenting the modeling in PowerFactory, the static and dynamic validation of the grid model is dealt with.

3.3.1 Modeled grid

As the aim of this research work is to assess the impact of a new wind-storage hybrid power plant injecting power into the node Saint-Rose of the Guadeloupean electrical grid, a grid model representing the grid's dynamics has been investigated. The current situation of the transmission grid was presented in section 3.2.1. While the node Saint-Rose, in which is located the point of connection of the hybrid plant has not been impacted by grid evolutions in the last years, the transforming substation Trois-Rivières and the underground line relying the substations Sainte Anne and Gardel, as well as the evolution of installed capacity and consumption, most recent modifications, are not considered in the modeling.

3.3.1.1 Grid description

The model set up contains 13 nodes that correspond to transforming substations each comprising two 63 kV/20 kV step down transformers each feeding one 20 kV busbars to which are connected loads and, in some cases, loads and reactive compensation stations. An additional node that corresponds to Jarry Nord generation site (composed of five 28,5 MVA synchronous machines) is also part of the model. The generation stations located in the islands Les Saintes, Marie-Galante and La Désirade, as well as the interconnection through submarine links and step-up transformers of those stations to the 63 KV overhead lines transmission network covering the main island, are not part of the grid model.

The electrical network of Guadeloupe has been subject to different studies, especially concerning the participation of wind energy conversion systems in the grid frequency regulation and grid stability [5, 22, 143-148]. Using the data reported in [5], a simulation model of the Guadeloupean grid has been implemented and validated in the present thesis using the PowerFactory tool.

The installed capacity reported for the generation facilities in the electricity grid is of 439 MW. Because of the following reasons, such installed capacity cannot be considered the instantaneous available power [5]:

- The efficiency of the machines, some which were at the end of their useful life by the time at which the grid data collection took place, presenting thereby particularly small efficiencies.
- The consumption of ancillary services within the generation sites, meaning a part of the production is not available to be transmitted to the consumption side.
- The technical losses.
- The availability of the generation units which are subject to maintenance schedules and can experience failures.
- The operating conditions of the generation units, some of which are sensitive to air temperature conditions (e.g. the combustion turbines).

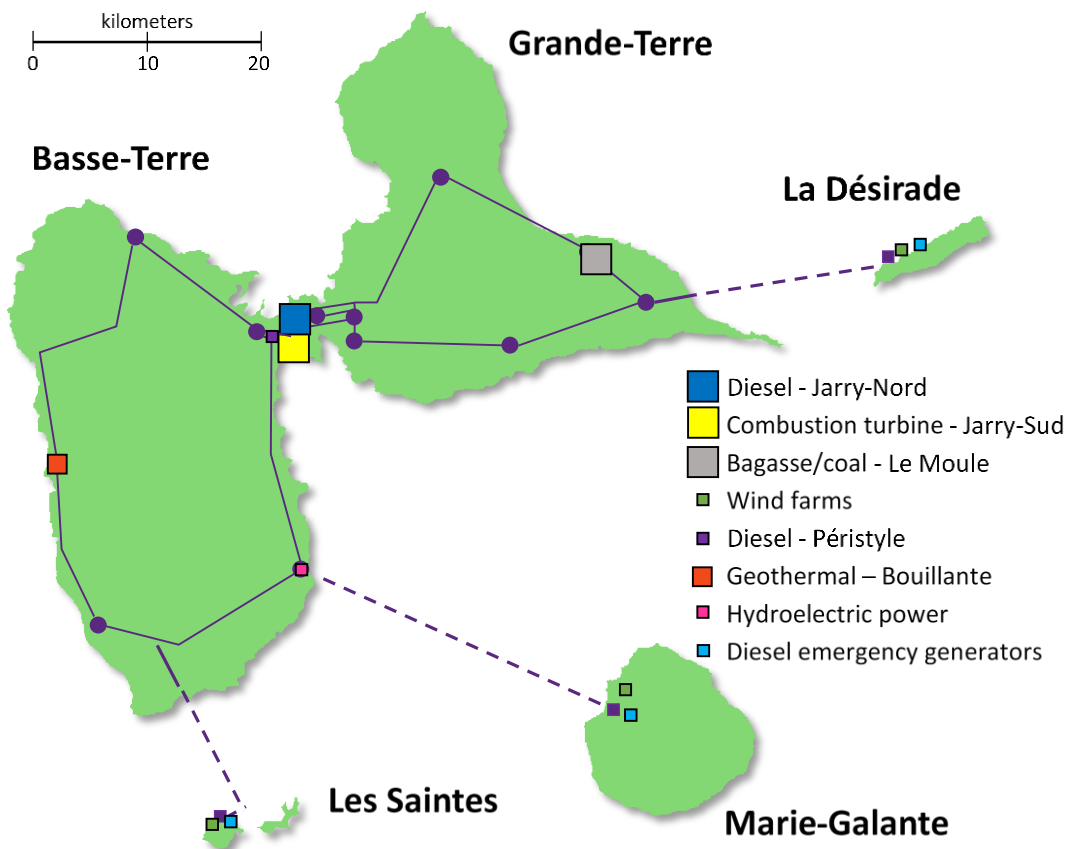


Fig. 3.9. Guadeloupe's main generation centers as of 2006.

Fig. 3.9 shows the energy production in the archipelago that involves diverse primary sources. The different types of sources are:

- ***Diesel***: several diesel-fueled generators can be found at the generation sites Jarry-Nord and Péristyle. In 2006, 52,5 % of the total energy generated came from Jarry-Nord station.
- ***Combustion turbines***: Jarry-Sud generation site comprises several combustion turbine generation units. This power station is only used during consumption peaks or when a

backup is required. The power produced by the generation site in 2006 corresponded to 3,5 % of the total consumption that year.

- ***Bagasse/coal***: the Le Moule thermal power plant runs using sugarcane bagasse and coal as sources of fuel. For this, about 18 % of the yearly production in the power station is considered renewable. In 2006 Le Moule delivered 26,7% of the total production.
- ***Geothermal***: the Bouillante plant is fed by the heat from the earth which escapes as steam. 5,1% of the production was attributed to this plant in 2006.
- ***Hydroelectric***: several run-of-river mini-hydroelectric power stations using synchronous machines to generate power. Mini-hydro stations supplied for 1,2 % of the total consumption in 2006.
- ***Wind***: wind turbines represent a small production capacity in the archipelago. Such generation units are mainly exploited on the islands Les Saintes, Marie-Galante and La Désirade. The share of wind turbines in the total production of 2006 is of 2,3 %.
- ***Photovoltaic***: photovoltaic production is also small even though the proper conditions in the archipelago. The power delivered by PV panes in the archipelago in 2006 is estimated in 0,3 %.
- ***Southern islands diesel emergency generators (EDF)***: Other than the wind turbines, Marie-Galante, les Saintes and la Désirade islands have small diesel emergency plants used only in exceptional cases. The production of those plants in 2006 was 0,1 % of the total production.

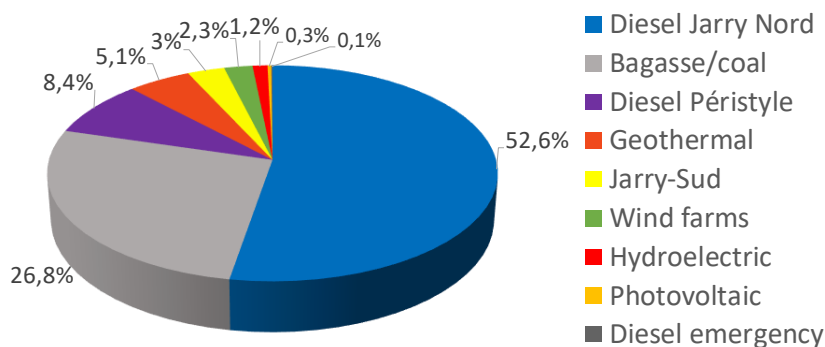


Fig. 3.10. Partitioning of power generation in 2006.

Fig. 3.10 depicts the partitioning of the generation sources described above.

3.3.1.2 Power system control components

Next, the main features of frequency and voltage control are briefly exposed. Depending on the period of the day, Guadeloupe’s primary frequency control policies establish a primary reserve ranging between 20 MW and 26 MW. This corresponds approximately to the size of

the largest generation unit connected to the power system (located at Le Moule thermal power station).

Frequency and active power control

The power plants in the energy system are called according to the following order [5]:

1. Renewable power plants benefit from an obligation on the part of EDF to purchase the power they generate. For this reason, they are the first to be brought online to meet demand. However, these sources (in exception of the geothermal station) are not dispatchable because of their intermittency and stochastic behavior. For that, renewable energy plants do not contribute to the frequency control in the archipelago.
2. The diesel generation units of Péristyle are operated most of the times close to their nominal power. In the case of consumption troughs, their power setpoints are slightly reduced. The share in the frequency control of these diesel units is low.
3. The thermal units of Le Moule are operated between 20 MW and 28 MW, depending on the time of the day. Those generators participate in the primary frequency regulation. As the two generation units are dimensioned for 30 MW, they are in charge of a part of the primary reserve.

These three first-generation sources in the generation ordering are exploited by independent operators and their operation is subject to contractual agreements.

4. The diesel generators of Jarry Nord are operated by EDF to ensure the system's production-consumption balance while participating in the constitution of the primary reserve. Lastly in the production order are the combustion turbines connected at the peaking station Jarry-Sud. These generators are used eventually during peak periods or when other generators are at a stop.

Given the size of the system, secondary frequency control is ensured by the generators of Jarry Nord station. Adjustments are made manually by the power-station operator. Tertiary frequency control is also ensured manually but by the system operator, according to the availability of the generator units in the system.

Fig. 3.11 presents the evolution of the generating fleet production over a typical day as well as the ordering system described.

The Guadeloupean grid is operated with a primary reserve which is close to the rating power of the largest generation unit in the system. This can lead to the need for shedding loads during power shortfalls. According to [5], the degree of load-shedding depends on the system frequency level: 48,5 48,2 47,9 47,6 and 47,2 Hz.

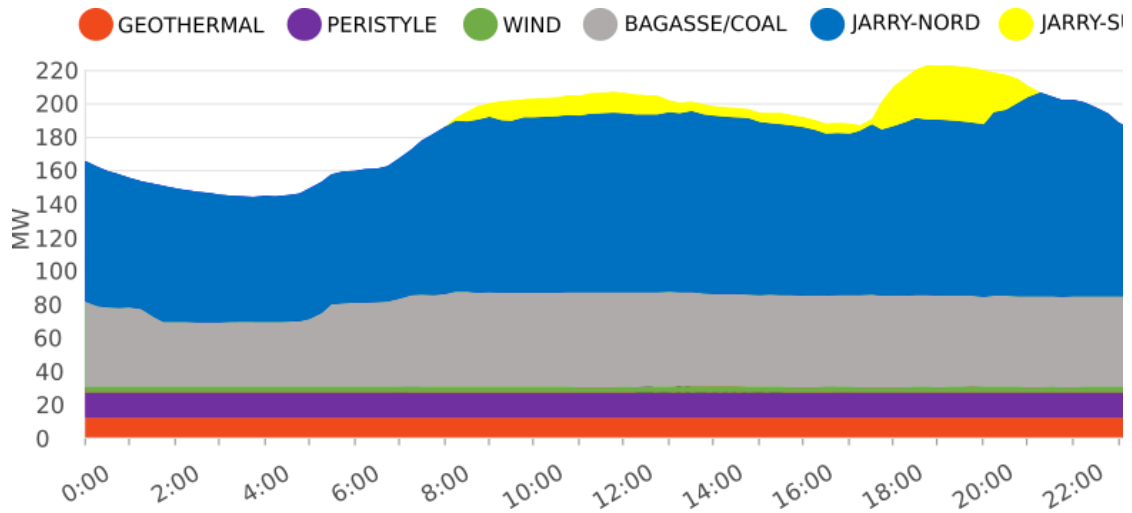


Fig. 3.11. Energy production distribution.

Control of voltage and reactive power

The first level of compensation of the reactive power demanded by the loads is done through the static var compensators installed at the 63 kV/20 kV transforming substations. The number of capacitors switched on is controlled manually from the dispatch center based on the consumption level. The capacitors that allow the consumption compensation during low-consumption periods are switched on all the time. Other capacitors are activated in the morning when the consumption increases and remain connected to produce a part of the reactive power demand of the nearby loads during peak hours.

The excitation current of the conventional generator units is controlled so that the setpoint of the voltage at their terminals is a little higher than the rated values. This allows the precise control of the voltage at medium-voltage busbars while dynamically providing the grid with reactive power balance.

In addition, the 63 kV/20 kV transformers are equipped with automatic on-load tap changers that adjust the voltages at the 20 kV side by shifting the number of turns on the 63 kV side winding. Typically, high settings are applied in order to keep the distribution level voltages at around 20,5 kV. This allows obtaining voltages within the required ranges for busbars where loads are connected.

3.3.2 PowerFactory grid model

The PowerFactory model of Guadeloupe island electrical system shown in Fig. 3.12 was implemented from data presented in [5]. The shaded area corresponds to the point of common coupling located within the node Sainte-Rose, where the hybrid power plant is connected.

A zoom of Fig. 3.12 at the Sainte-Rose substation is presented in Fig. 3.13. As shown, Sainte-Rose comprises a 63 kV busbar connected through 63 kV/20 kV transformers with two 20 kV busbars (Terminals 1 and 2). Sainte-Rose transformers comprise 17 tap changer positions (the minimum position is -8, the maximum is 8 and the neutral is position 0) with 1,75 % additional voltage per tap. The terminal 1 relies a local load and serves as the PCC for the hybrid plant. Meanwhile, the terminal 2 relies a load and a static var system.

Sainte-Rose's main busbar is connected to the main busbars of the neighboring substations Bouillante and Baie-Mahault through transmission lines at 63 kV.

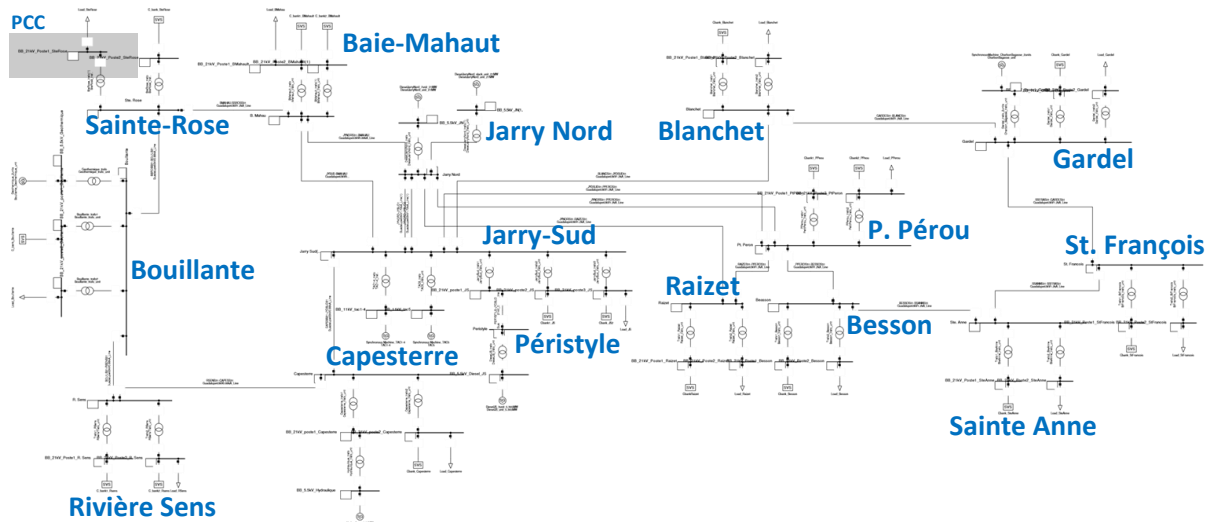


Fig. 3.12. PowerFactory Guadeloupe grid investigated model.

The grid model described in PowerFactory contains the different synchronous generators with their respective transformers, 63 kV/20 kV transformers with static loads and static var compensators, as well as overhead power lines connecting the different substations. A particularity of PowerFactory is that the description of the transmission lines must be implemented through the unit resistance and reactance (both in Ohm/km). Consequently, the transmission lines length must be known. As the total resistance and reactance for every transmission line were available while the line lengths were unknown, it was necessary to estimate the line lengths. For that, the web mapping service of the French government [geoportail³](http://www.geoportail.gov.fr/) was employed. The service allows seeing the transportation lines in the French

³ www.geoportail.gov.fr/

territories. Also, a distance measurement tool permitted approximating the transmission lines lengths.

Diverse DSL models are available in the library of PowerFactory that can be equipped on power system components being part of a grid. Attached to the generator components are automatic voltage controller, and governor and turbine DSL models. The latter containing the primary controller and the prime mover unit.

The IEEE1 model, one of many standard types of voltage regulators existing, is the AVR model equipped on the generators. In Annex A are described the governors of the diesel generators of Jarry Nord and Péristyle stations, as well as those of the steam generators of Le Moule, all participating in the primary frequency control, that were defined using DSL models. For the remaining generators in the system, built-in PowerFactory governors were used.

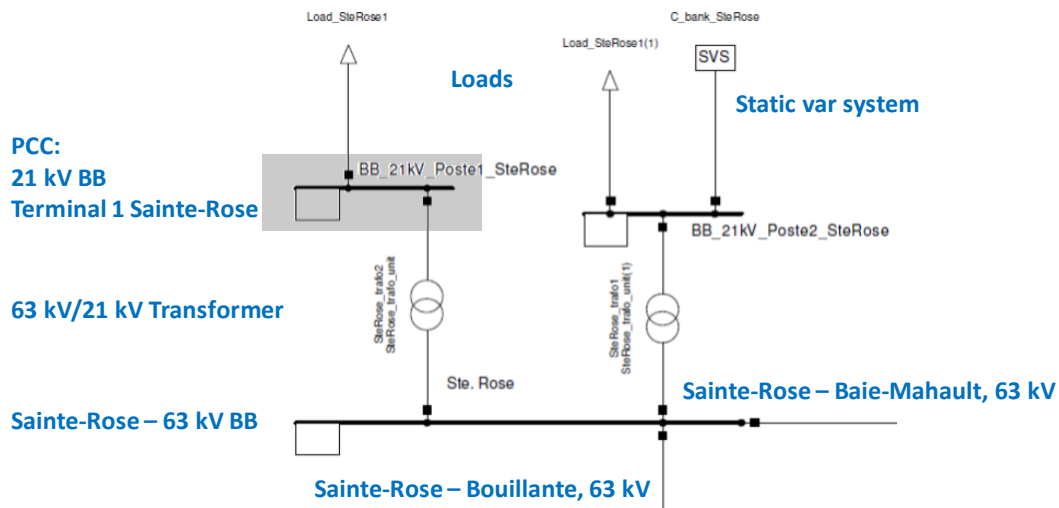


Fig. 3.13. Sainte-Rose substation.

According to the data collection work presented in [5], 53% of the load in Guadeloupe can be considered static, representing mainly home appliances which do not have an electric engine, while the remaining 47% are dynamic loads based on induction motors. For the sake of simplicity, in the implemented grid model, all the loads were assumed static and invariant with respect to the frequency and voltage changes

The system is composed by 3 types of buses:

- **Slack bus**: specifies the reference magnitude and phase angle of the voltage. The generator connected to this bus (known as the slack generator) is in charge of balancing the system active and reactive production with the consumption and the losses. The diesel generator unit 1 at the substation Jarry Nord is the slack generator.
- **PQ buses**: at which active and reactive powers are specified. In the grid model, PQ buses integrate static loads and var compensators. The latter allow the voltage control at the

directly connected busbars, depending on the load situation, injecting reactive power in response to reactive power demand.

- *PV buses*: production nodes fixing the active power and adjusting the reactive power production in order to keep a given voltage magnitude. In the investigated grid model, PV nodes are composed of generators, loads, and or generators, loads and var compensators.

3.3.3 Grid model validation

- The aim here is verifying the data used in the grid model description, such as the transportation lines impedances and reactances, and the transformers reactances and time constants. For that, the model validation presented is separated into static and dynamic validation. The static validation requires controlling the grid model by the imposition of an operation point or scenario. In the present case, such scenario is determined by the following conditions: The slack bus voltage and angle setpoints.
- The distribution of the consumption (active and reactive) and reactive power compensation among the different PQ nodes in the system.
- The active power setpoints of the generators, as well as the setpoints for the voltages at their relying busbars, in the case of PV nodes.

Then, the repartition of power flows obtained by the run of a load flow⁴ can be validated through comparison with respect to a valid reference. Typically, telemetry data collected from the real power grid is used as the basis for the definition of validation scenarios.

The dynamic validation will consider the disconnection of a generator during the most restrictive operating conditions, that is, during off-peak hours, when the grid's inertia is at its lowest level [5].

3.3.3.1 Static validation

The scenario implemented for the static validation of the grid model is similar to the one proposed by [5]. Such an operation point corresponds to a time of peak consumption for which the telemetry data is available for comparison.

Definition of the validation scenario

⁴ Power flow study that consists in determining the magnitudes and phase angle of voltages at each bus, and active and reactive power flow in each line. In solving a power flow problem, balanced system operations are assumed, and a single-phase model is employed.

The scenario is described in the following paragraphs. In Table 3.1 are displayed the setpoints for the reference voltage and angle established by means the slack generator.

Table 3.1. Slack generator setpoints (generator convention).

Slack generator	V [kV]	Angle [°]
Diesel - Jarry Nord unit 1	5,53	0

The power injections into the 63 kV grid are detailed in the second column of Table 3.2. Finally, the system's consumption (active and reactive power) is presented in Table 3.3.

Table 3.2. Distribution of the production (generator convention).

Generator units	P [MW]	Voltage [kV]
Diesel - Jarry Nord units 2 - 8	106,46	5,56
Geothermal - Bouillante	10,01	5,41
Combustion turbine - Jarry Sud	16,64	11
Hydroelectric - Capesterre	0	6,2
Bagasse/coal - Le Moule	51,17	10,96
Diesel - Péristyle	14,9	5,5
Total	199,18	-

These values correspond to power flows at the high-voltage feeders, therefore the losses in step-down transformers and injections from reactive compensators are considered. Given the lack of measurements for the nodes Raizet and Petit Pérou, the values shown were estimated in [5].

Table 3.3. Distribution of the consumption (load convention).

Consumption nodes	Consumption	
	P [MW]	Q [Mvar]
Sainte-Rose	13,41	3,84
Bouillante	4,72	1,86
Rivière Sens	19,6	-5,50
Capesterre	18,1	3,9
Jarry-Sud	22,54	-1,48
Raizet	14,04	2,26
Besson	26,2	9,70
Petit Pérou	20,65	-4,64
Sainte-Anne	10,7	0,7
Saint-François	8,8	-2,8
Gardel	6,31	3,39
Blanchet	18,3	10,1
Baie-Mahault	19,61	-3,67
Total	203,0	17,16

Load flow results

A load flow was run from the scenario described. The reactive power injections that result from the active power dispatch and the voltage targets defined above are displayed in Table 3.5. The values are compared with the telemetry data of the system operator (EDF SEI).

Table 3.5. Reactive power injected into HTB busbars at generation nodes (generator convention).

Generation site	Reactive injection [Mvar]	
	Q_{simu}	Q_{telem}
Diesel - Jarry Nord 1	12,12	2,17
Diesel - Jarry Nord units 2 - 8	-0,85	8,94
Géothermal - Bouillante	18,19	0
Combustion turbine - Jarry Sud	-30,31	3,16
Bagasse/coal - Le Moule	11,20	6,31
Diesel - Péristyle	13,54	8,94
Total reactive injection into HTB network	23,9	29,52

Also, the active and reactive power production of the slack generator is detailed in Table 3.4.

Table 3.4. Slack generator active power injection into the 63 kV network (generator convention).

Slack generator	Active injection [MW]	
	P_{simu}	P_{telem}
Diesel - Jarry Nord unit 1	5,38	17,28

This means a total injection of active power into the high-voltage network of:

$P_{inj_{simu}} = \text{production of slack generator} + \text{other generation units} = 5,38 + 199,18 = 204,56 \text{ MW.}$

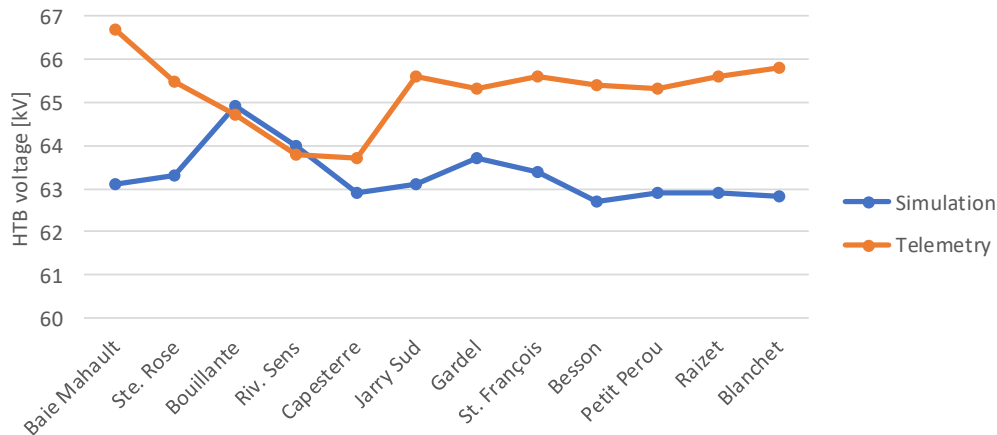


Fig. 3.14. High-voltage busbars comparison.

Meanwhile, according to the telemetry data the active injection is:

$$P_{inj_{telem}} = 17,28 + 199,18 = 216,5 \text{ MW.}$$

In closing, Fig. 3.14 presents the voltages for the different transmission network busbars in the system obtained both from simulation and measurements. Even though the transmission network nominal voltage is of 63 kV, the network is operated with a normal range of variation of 55 kV to 72 kV.

Comparative analysis

- The total injected active power obtained from simulation is 204,4 MW. The active injection obtained from telemetry is 216,5 MW. This means a difference of 12,1 MW (5,6 %). This error is big and can be explained by the difference among the telemetry data corresponding to production and consumption (216,5 and 203 MW, respectively). Considering that according to simulation the active power losses amount 3,01 MW, it appears unlikely that losses are the only explanation to the gap in the measurements. Incorrect or missing consumption data would be the source of the difference.
- According to simulation, the total reactive injections comes to 25,8 Mvar. Meanwhile, the telemetry data amounted 29,5 Mvar. Thus, the difference among the Mvar obtained through simulation and those measured on the grid is of 3,7 Mvar (12,7 %). Even though the difference is smaller than that obtained in the earlier case, the percentage error is bigger as the total injection of reactive power is between seven and eight times smaller than that of active power.
- It seems that the gap between the reactive power injections can be related to the differences obtained in terms of voltages in high-voltage busbars. As a matter of fact, simulation results present not only smaller reactive injections but also smaller voltages. Removing the voltage measurement data for Sainte Anne busbar, which seems to be incorrect, the voltages obtained from simulation are 2,8 % smaller. Yet, all voltages at load busbars are between 20,4 kV and 20,6 kV.

To sum up, the total production (active and reactive) obtained for the scenario introduced through simulation appears to be consistent with the real data even though the production distributions throughout the generator units are not identical. As for the voltages, simulation results show smaller values at high-voltage busbars. Nonetheless, the voltages at the connection points of the users are within the right interval. After the run of a load flow without the hybrid power plant, it is found that the match between the results obtained and the data of the SO is good enough, which validates the static behavior of the model.

3.3.3.2 Dynamic validation

The scenario implemented for the dynamic validation of the grid model reproduces real telemetry and is also inspired by [5].

Definition of the scenario for dynamic validation

It is during off-peak periods that the variability in the frequency of an electrical system tends to be more important. Indeed, because of the limited number of generation units in operation, both the kinetic energy stored in the rotating masses and the primary reserve,

allocated on fewer generators, are close to their minimum. In any case, the production-consumption imbalance caused by the failure of a generator is more or less important depending mainly on the generator’s share in the total island production [146].

Some aspects determining whether an imbalance leads or not in a certain level of load-shedding are the available primary reserve, the failure of a generator participating in the primary reserve, and the dynamic behavior of both the loads and the generation facilities within the system [146]. That said, a candidate for validation scenario can be found via the analysis of recordings of production-related incidents.

Based on EDF SEI’s production incidents data collected at the Guadeloupean archipelago during the period 2006-2008, in [146] is presented an analysis of the relationship among the total production before an incident and the resulting amount of load shed (in MW). Next are summarized the elements emerging from that analysis:

- Production-consumption unbalances inferior to 15 MW seemed not to represent any risk for the supply of the consumers.
- The system’s dynamics appears to be weakened whenever the consumption is lower (as expected). Hence, production failures in the 15 – 25 WM range leded to greater levels of load-shedding when the system’s consumption was smaller. This can be seen in Table 3.6.
- The occurrence of load-shedding beyond 25-30 MW fault incidents was less common and rather related to the simultaneous failure of several generation units. Events of this kind are, in general, rare (yet likely to happen).

Table 3.6. Production-consumption imbalances within 15 – 25 WM and load-shedding according to the consumption level.

Consumption level range	% of incidents leading to load-shedding	
120-160 MW	~66 %	
160-200 MW	~50 %	
200-240 MW	~33 %	

The situation of loads and reactive compensators in the consumption nodes is described in Table 3.7 (load convention is applied). These values take into account the losses in 63 kV/20 kV transformers.

As it can be seen, the total consumption under this scenario is of 146,3 MW, (i.e. within the 120-160 MW range). Moreover, the usual nighttime (off-peak hours) consumptions in the archipelago at the period mentioned above were smaller than 150 MW [5], [146].

At the operation point considered, the active power dispatch of each of the generators in Le Moule is set at 20 MW. A participation of 4 MW per generation unit in the primary frequency reserve is also considered.

Meanwhile, the geothermal station and the hydroelectric plant are operated at 15 MW and 3 MW, respectively. These generation units do not participate in the primary reserve.

The diesel generators located at the station Péristyle are operated at 14 MW, which is its typical production during off-peak periods. A participation of 2,2 MW in the primary reserve is considered for this power station. Besides, the combustion turbines, which are peaking resources, are not injecting power into the system as the operation point represented, corresponds to an off-peak period.

Table 3.7. Consumption nodes (load convention).

Substation	Consumption and static compensation	
	P [MW]	Q [Mvar]
Sainte-Rose	11,2	1,8
Bouillante	3,48	-0,05
Rivière Sens	13,44	-0,8
Capesterre	7,47	0,1
Jarry-Sud	24,89	1,9
Raizet	14,93	1,3
Besson	17,42	0,11
Petit Perou	11,2	-3,2
Sainte-Anne	7,47	1
Saint-François	8,71	2,3
Gardel	3,73	1,2
Blanchet	12,44	-0,1
Baie-Mahault	9,96	-1,5
Total	146,3	4,06

Next, the number of generation units to be connected at the station of Jarry Nord is going to be calculated. For this off-peak condition, the total primary reserve must be of around 22 MW and the active power losses around 3 MW.

Total consumption:

$$Load + losses = 146,3 + 3 = 149,3 \text{ MW}$$

Total production without Jarry Nord:

$$Le \text{ Moule} + geoth. + hydro + Péristyle = 20 \times 2 + 15 + 3 + 14 = 72 \text{ MW}$$

Remaining reserve to be allocated:

$$Total \text{ reserve} - (Le \text{ Moule} + Péristyle) = 22 - (4 \times 2 + 2,2) = 11,8 \text{ MW}$$

Now, the number of generators to turn on at Jarry Nord is determined as to ensure the balance production-consumption.

Generation required at Jarry Nord:

$$\text{Consumption} + \text{remaining res.} - \text{other stations} = 149,3 + 11,8 - 72 = 89,1 \text{ MW}$$

Hence, four diesel generators operated at 20,9 MW and one more operated at 12,6 MW are connected at Jarry Nord.

Table 3.8 summarizes the power dispatch as well as primary and secondary frequency control settings for the production nodes in the system. The transformers losses are considered. As can be seen, there is a difference of 2,2 MW among the total production and consumption. Such a difference corresponds to the estimated system losses. The information displayed in Table 3.8 corresponds to the situation of the grid prior to the fault of the generation unit 2 of Le

Table 3.8. Validation scenario: PV nodes settings (generator convention).

Generation units	[MW]		Sec. frequency control [%]
	Active power	Prim. reserve	
Diesel - Jarry-Nord 1-5	76,5	19,7	100
Géothermal - Bouillante	15	0	-
Hydroelectric - Capesterre	3	0	-
Bagasse/coal – Le Moule 1	20	4	-
Bagasse/coal – Le Moule 2	20	4	-
Diesel – Péristyle 1-3	14	2,2	-
Total	148,5	29,1	100

Moule station (highlighted in the table). It must be noticed that the generator failure is within the 15 – 25 MW range mentioned above.

As shown in the third column, before the incident the primary reserve allocated by the SO is of 29,1 MW. This reserve is very close to the maximum capacity of the generation unit being disconnected.

Moreover, the droop of the generation units participating in the primary frequency reserve is of 4 %.

Simulation results

A load flow was run from the scenario described. The active and reactive losses obtained from simulation are shown in Table 3.9. The results achieved in PowerFactory are compared with those of the reference modeling.

Table 3.9. P and Q values obtained at slack bus (generator convention).

Generation site	Active losses [MW]		Reactive losses [Mvar]	
	Simu PF	Simu ref. scen.	Simu PF	Simu ref. scen.
Diesel - Jarry-Nord 1	1,18	2,16	17,8	16

Fig. 3.15.a-c presents the grid frequency, the dynamics of Jarry Nord station generation units and the voltage at the point of common coupling of the HPP, respectively, according to the modeling of reference.

In Fig. 3.16.a-c are presented the dynamic evolutions of grid frequency, active power production at one of the generation units in Jarry Nord station, and voltage at the PCC, obtained for the same scenario with the model implemented in PowerFactory.

And according to the results shown in Fig. 3.15 and Fig. 3.16:

- The frequency dynamic of the PowerFactory model is slower than that of the reference scenario. The times to get to a new steady-state were 11 s and 8 s, respectively.

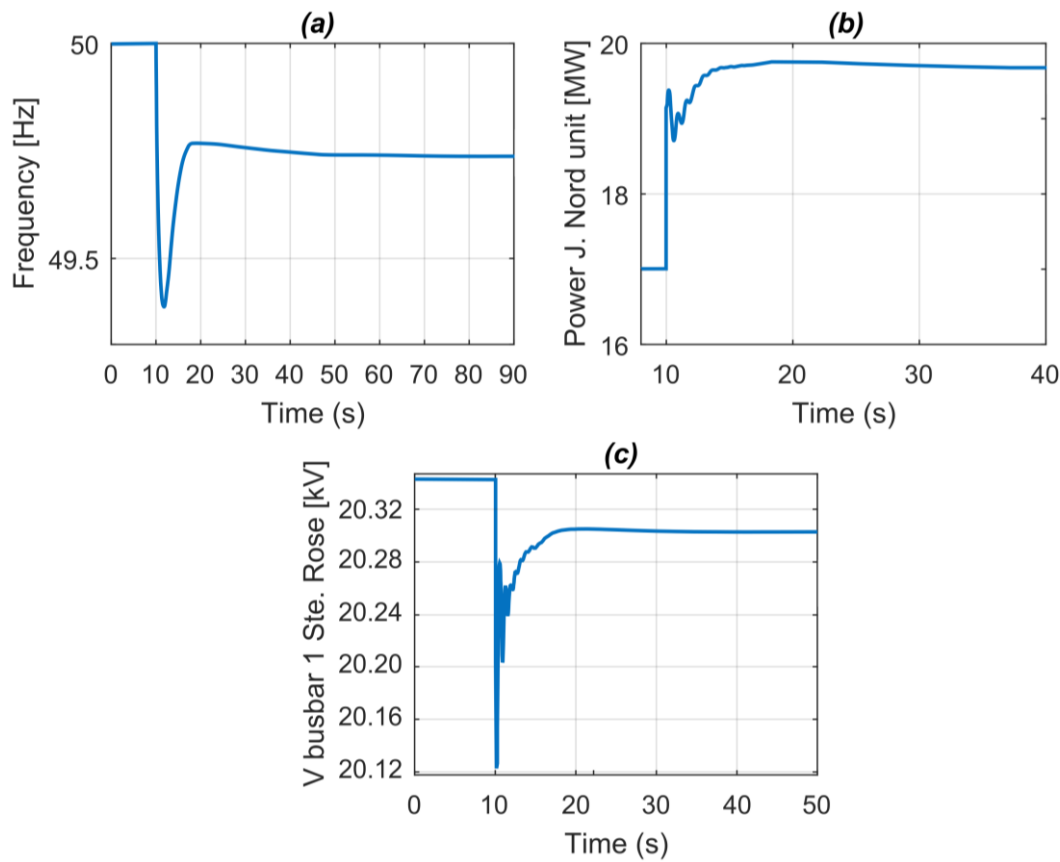


Fig. 3.15. Reference scenario dynamics: (a) grid frequency, (b) dynamic behavior generation units of Jarry nord, and (c) voltage at HPP connection busbar.

The Δf achieved in the steady-state was 0.24 Hz in PowerFactory, whereas in the reference scenario the frequency deviation was 0.25 Hz.

The droop in this case can be computed as:

$$K = \frac{1}{\partial f} \sum P = \frac{1}{0,04} \frac{20,9 \times 4 + 12,6 + 32 + 5,4 \times 3}{50} = 72,2 \frac{MW}{Hz}$$

Thus, with

$$P - P_0 = -K(f - f_N),$$

the disconnection of a machine delivering 20 MW, produces a frequency deviation of:

$$f - f_N = \frac{124,4 - 144,4}{-72,2} = 0,28 \text{ Hz}$$

which is the expected frequency variation. Hence, the result obtained (0.24 Hz) presents a 40 mHz difference which can be attributed to the parameters of the governors and turbine models.

Even if there is an important gap among the voltages obtained, a similarity can be observed between the dynamics from the two models.

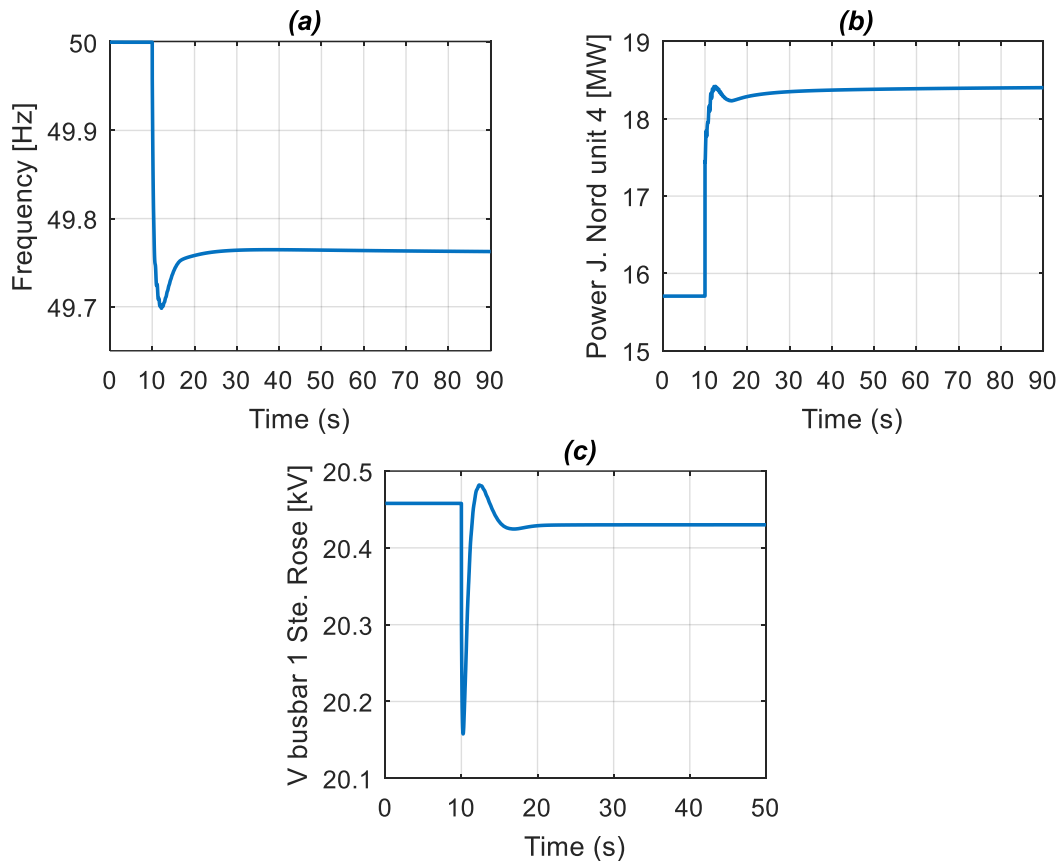


Fig. 3.16. Dynamic behavior of PowerFactory model: (a) grid frequency, and (b) Active power production of unit 4 Jarry Nord, and (c) voltage at HPP connection busbar.

3.3.4 Hybrid power plant model

The wind-BESS hybrid power plant is depicted Fig. 3.17. As shown, the 20 kV busbar 1, at Sainte Rose substation serves as a point of common coupling for the HPP. The wind generation system comprises four 2 MW wind turbines with their respective converters and transformers. Meanwhile, the BESS consists of four 1 MW 580 kWh Li-ion storage devices, with their respective converters and transformers.

As mentioned in Chapter 1, not only the HPP sizing but also the selection of Li-ion as storage technology took place during the pre-study conducted in the context of the Insul'Grid

project. For that, the study carried out in the present thesis considers the HPP configuration shown in Fig. 3.17.

Next, the modeling of the HPP is introduced by the modeling of the WECS and followed by that of the ESS.

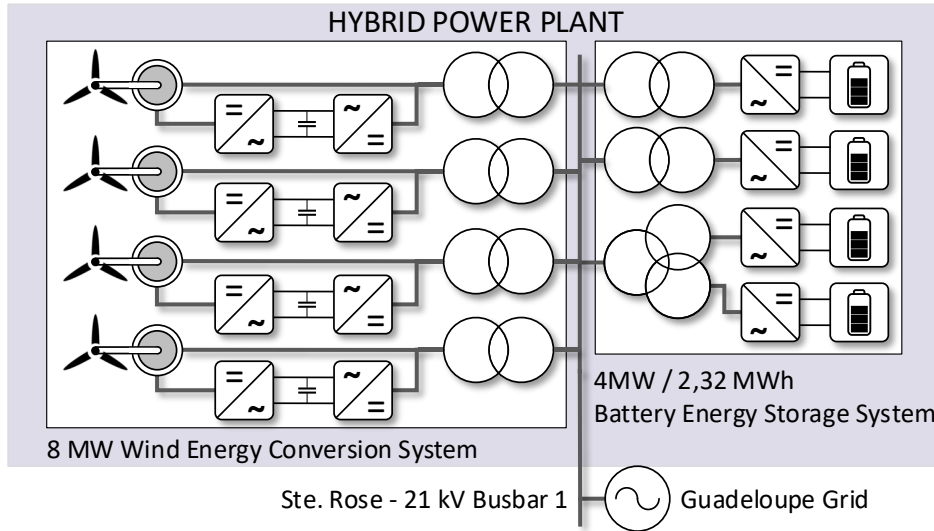


Fig. 3.17. Hybrid power plant.

3.3.4.1 Wind generation system modeling and validation

Fig. 3.18 presents the wind generation system single line diagram described in PowerFactory. The system consists of four 2 MW DFIG generators connected to the point of common coupling at 20 kV through underground lines, medium and low voltage busbars and transformers.

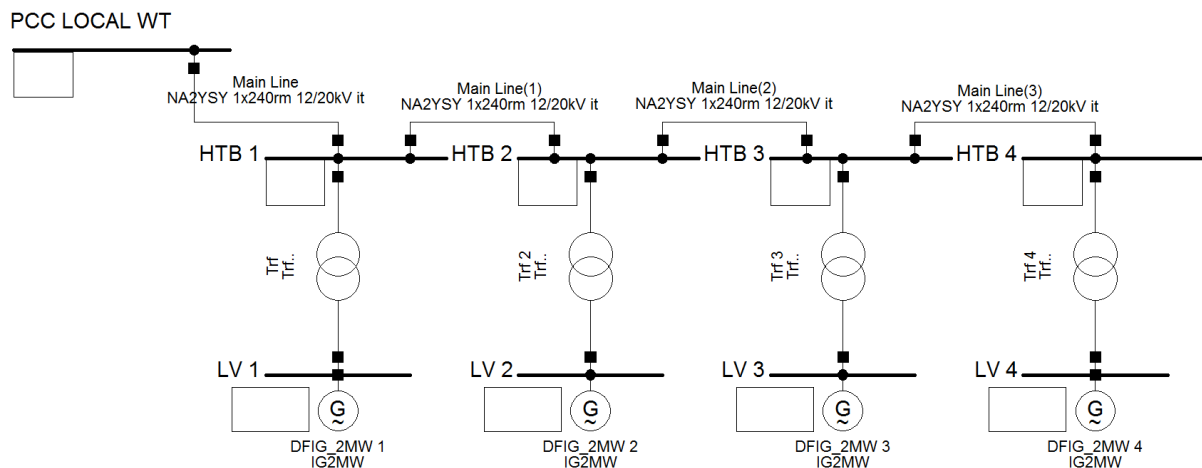


Fig. 3.18. Wind generation system implemented in PowerFactory.

Wind turbines

In the wind generation system shown in Fig. 3.18, a built-in wind turbine template representing the turbines as induction machine electrical grid components configured as a DFIG

is utilized. Conceived for low voltage ride through simulation, the wind turbine modeling comprises DSL blocks defining the behavior of the different modeled aspects: the electrical component (doubly-fed induction machine), the mechanical system, the aerodynamic system, the control system, and the protection system. Those aspects are briefly described below.

- *Modeling of the DFIG*: Fig. 3.19 shows the doubly-fed induction machine model, that integrates a rotor side converter (RSC), and is a model with AC and DC terminals.

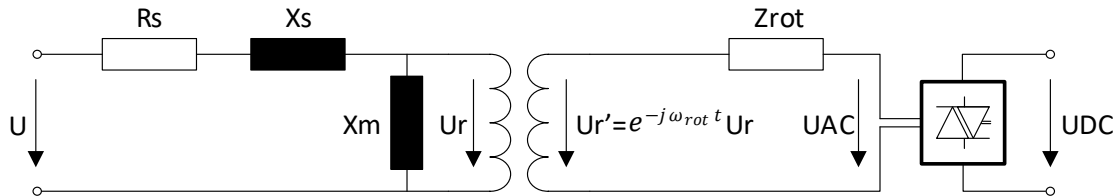


Fig. 3.19. Doubly-fed induction machine with rotor-side converter.

The PWM converter allows for a flexible and fast control of the machine by modifying the magnitude and phase of the output voltage U_{AC} on the rotor-side. This is achieved by adjusting a modulation factor. On the basis of the power balance between the AC and DC sides of the converter, the DC voltage and DC current can be calculated. The following equation defines the AC-DC relationship of the converter (the AC voltage is expressed as line-to-line voltage):

$$U_{ACr} = \frac{\sqrt{3}}{2\sqrt{2}} PWM_r \cdot U_{DC} \quad \text{Eq. 3.1}$$

$$U_{ACi} = \frac{\sqrt{3}}{2\sqrt{2}} PWM_i \cdot U_{DC}$$

where PWM_r and PWM_i are the real and imaginary components of the modulation factor.

It is assumed that a standard bridge consisting of six transistors builds the converter.

The relationship between AC and DC currents can be established by:

$$P_{AC} = \text{Re}(U_{AC} \cdot I_{AC}^*) = U_{DC} \cdot I_{DC} = P_{DC} \quad \text{Eq. 3.2}$$

Equation Eq. 3.2 assumes an ideal, loss-less PWM-converter.

During time domain simulations the converter is controlled via the pulse width modulation factors PWM_d and PWM_q that define the the ratio between DC voltage and AC voltage at the slip rings.

The model equations of the doubly-fed machine are:

$$\mathbf{u}_s = R_s \mathbf{i}_s + j \frac{\omega_{syn}}{\omega_n} \boldsymbol{\psi}_s + \frac{1}{\omega_n} \frac{d\boldsymbol{\psi}_s}{dt} \quad \text{Eq. 3.3}$$

$$\mathbf{u}_r \cdot e^{-j(\omega_{syn}-\omega_{gen})t} = R_r \mathbf{i}_r + j \frac{(\omega_{syn}-\omega_{gen})}{\omega_n} \boldsymbol{\psi}_r + \frac{d\boldsymbol{\psi}_r}{dt},$$

where the vectors \mathbf{u} , \mathbf{i} and $\boldsymbol{\psi}$ are voltage, current and flux. Also, ω_{syn} is the synchronous speed, ω_{gen} is the generator rotor speed, and ω_n , the nominal electrical frequency of the grid.

The per unit rotor voltage that appears in Eq. 3.3 is related to the DC voltage as follows:

$$\mathbf{u}_{rd} = \frac{\sqrt{3}}{2\sqrt{2}} PWM_d \cdot \frac{U_{DC}}{U_{rnom}} \quad \text{Eq. 3.4}$$

$$\mathbf{u}_{rq} = \frac{\sqrt{3}}{2\sqrt{2}} PWM_q \cdot \frac{U_{DC}}{U_{rnom}}$$

where U_{rnom} is the nominal rotor voltage.

- Mechanical model: On the drive train side, the shaft is modeled as a two-mass model representing the two major sources of inertia: the wind rotor with a larger inertia J_{rot} and the generator rotor with a smaller inertia J_{gen} , which is part of the induction machine grid component. In other words, besides the electromagnetic description, the generator model also contains the generator inertia J_{gen} . While the low-speed side of the shaft is modeled by a stiffness k and a damping coefficient c , the high-speed shaft is assumed stiff. Also, an ideal gear-box with ratio $1:n_{gear}$ is included. Below are the equations describing the mechanical model of the wind turbine:

$$\dot{\theta}_{rot} = \omega_{rot} \quad (\text{rad/s})$$

$$\dot{\theta}_k = \omega_{rot} - \frac{\omega_{gen}}{n_{gear}} \quad (\text{rad/s}) \quad \text{Eq. 3.5}$$

$$\dot{\omega}_{rot} = (T_{rot} - T_{shaft})/J_{rot} \quad (\text{rad/s}^2)$$

where $\theta_k = \theta_{rot} - \theta_k/n_{gear}$ is the angular difference between the two ends of the shaft. The mechanical torque on the low-speed side and the mechanical power of the generator are:

$$T_{shaft} = c \left(\omega_{rot} - \frac{\omega_{gen}}{n_{gear}} \right) + k\theta_k \quad (\text{Nm})$$

$$P_t = \omega_{gen} \frac{T_{shaft}}{n_{gear}} \quad (\text{W}) \quad \text{Eq. 3.6}$$

where P_t is the mechanical power (W) of the wind turbine. The damping coefficient c is given by:

$$c = 2\xi\sqrt{kJ_{rot}} \quad \text{Eq. 3.7}$$

where ξ represents the damping ratio can be expressed as:

$$\xi = \frac{\delta_s}{\sqrt{\delta_s^2 + 4\pi^2}} \quad \text{Eq. 3.8}$$

with δ_s , the logarithmic ratio between the amplitude at the beginning of the period and the amplitude at the end of the next period of oscillation:

$$\delta_s = \ln\left(\frac{a(t)}{a(t + t_p)}\right) \quad \text{Eq. 3.9}$$

where a represents the amplitude of the signal.

- Aerodynamic model: the aerodynamic torque developed on the main shaft of the turbine is modelled by the equation:

$$T_{rot} = \frac{P_{rot}}{\omega_{rot}} = \frac{1}{2\omega_{rot}} \rho A_{rot} C_p(\theta, \lambda) v_w^3 \quad \text{Eq. 3.10}$$

where ρ is the air density in kg/m^3 , A_{rot} is the area covered by the wind turbine rotor in m^2 , C_p is the power coefficient, which is a function of the pitch angle θ and the tip-speed ratio λ , and v_w (m/s) is the wind speed. On the other side, the tip-speed ratio is computed as:

$$\lambda = \frac{\omega_{rot} R}{v_w} \quad \text{Eq. 3.11}$$

where R (m) is the radius of the rotor.

C_p is obtained by the aerodynamic model through a look up table using θ and λ as inputs, allowing the maximization of the power generated. Originally, the model generates an equivalent wind speed v_w at the hub height of the wind turbine that considers the effect of rotational turbulence and the effect of tower shadow influence [149]. Nevertheless, a block was added allowing the variable v_w to be an input to the model defined through a time series of wind speed measurements.

- Control system: Fig. 3.20 presents a generic control scheme for the DFIG generator model. The rotor side converter is part of the DFIG model which is a d-q built-in model with predefined inputs and outputs. DFIG and rotor side converter are modeled in rotor reference frame (RRF) rotating at generator speed. Nonetheless, the controller of the RSC is expressed in the stator flux reference frame (SFRF) rotating at grid synchronous

speed. Different coordinate transformations are performed to interconnect these blocks. The output of the generator model is expressed in RRF, so it has to be transformed to SFRF in order to be used by the RSC's controller.

RSC control modifies the stator active (P) and reactive (Q) power by regulating the q and d-axis rotor currents $I_{q,rotor}^{SFRF}$ and $I_{d,rotor}^{SFRF}$, respectively. The control of active and reactive power is decoupled. The induced controlled rotor voltage is modulated with pulse-width factor PWM and is expressed in SFRF. This modulation factor is PWM_{rotor}^{SFRF} and is the output of the rotor side converter.

Similarly, to the RSC, the grid side converter is current regulated. The DC-voltage is controlled indirectly through the control of the grid side converter current. The converter current control operates in the voltage-oriented reference frame (GCVRF). Reference frame transformation in the framework of wind generators modeling is treated in reference [150].

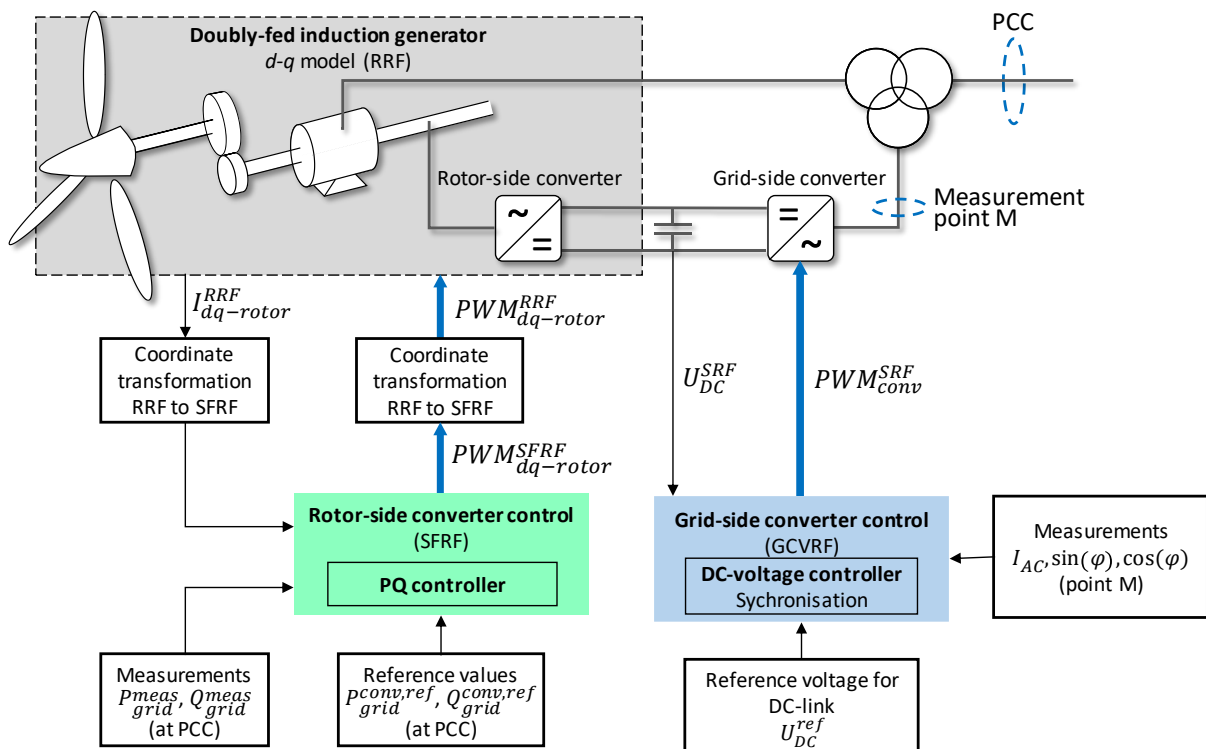


Fig. 3.20. Generic control model scheme for DFIG template.

- **Protection system:** The protection of the DFIG comprises a crowbar, the possibility to disconnect the DFIG and the possibility to re-synchronize it. If the speed, the voltage or the rotor current exceeds the limits for a certain time the DFIG is disconnected. The crowbar is an additional inductance inserter in case of overcurrent [151]. Some of parameter values of the protection model where modified so that the modeled wind

turbine starts to produce power at a windspeed of 3 m/s, instead of 6 m/s with the default configuration. In Annex B are listed the settings used for the protection system.

Performance of the DFIG and rotor-side converter model

The power curve of the wind turbine whose modeling was discussed in the earlier section is displayed in Fig. 3.21. The curve presents the steady-state electrical power obtained from simulation. As noted, the modeled wind turbine produces power for wind speeds between 3 m/s and 29 m/s.

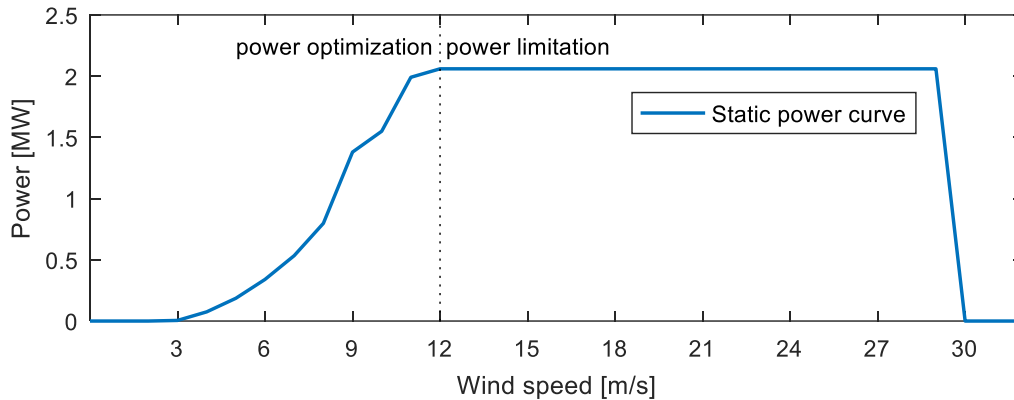


Fig. 3.21. Calculated power curve of the modeled DFIG wind turbine.

Two operation modes can be observed in Fig. 3.21: power limitation and power optimization. The power output is limited to nominal power (2,06 MW) when speed is between nominal wind speed (12 m/s as indicated by the dashed line) and 29 m/s. In this operation mode, in order to get a constant power output above nominal speed the pitch angle β is adjusted accordingly to control the stall effect.

On the other side, between 3 m/s and 12 m/s the power output is maximized. In this operation mode, the pitch angle β is adjusted to optimize the power coefficient C_p and this way maximize the power output.

In Fig. 3.22.a is presented an available dataset of wind speed measurements. The wind data comprise 86,400 measurement points of wind speed (m/s) with timestamps that were collected every second during a 1-day period. The readings were received from an anemometer mounted on a 2 MW DFIG Gamesa G87 wind turbine. The data is considered as if it had been obtained from an anemometer mounted at the top of a measuring mast (i.e., the influence of the wind turbine rotor on the wind data measured is considered negligible).

Fig. 3.22.b plots the output power obtained from the wind profile through the DFIG PowerFactory model as well as the power obtained by application of the power curve shown in Fig. 3.21.

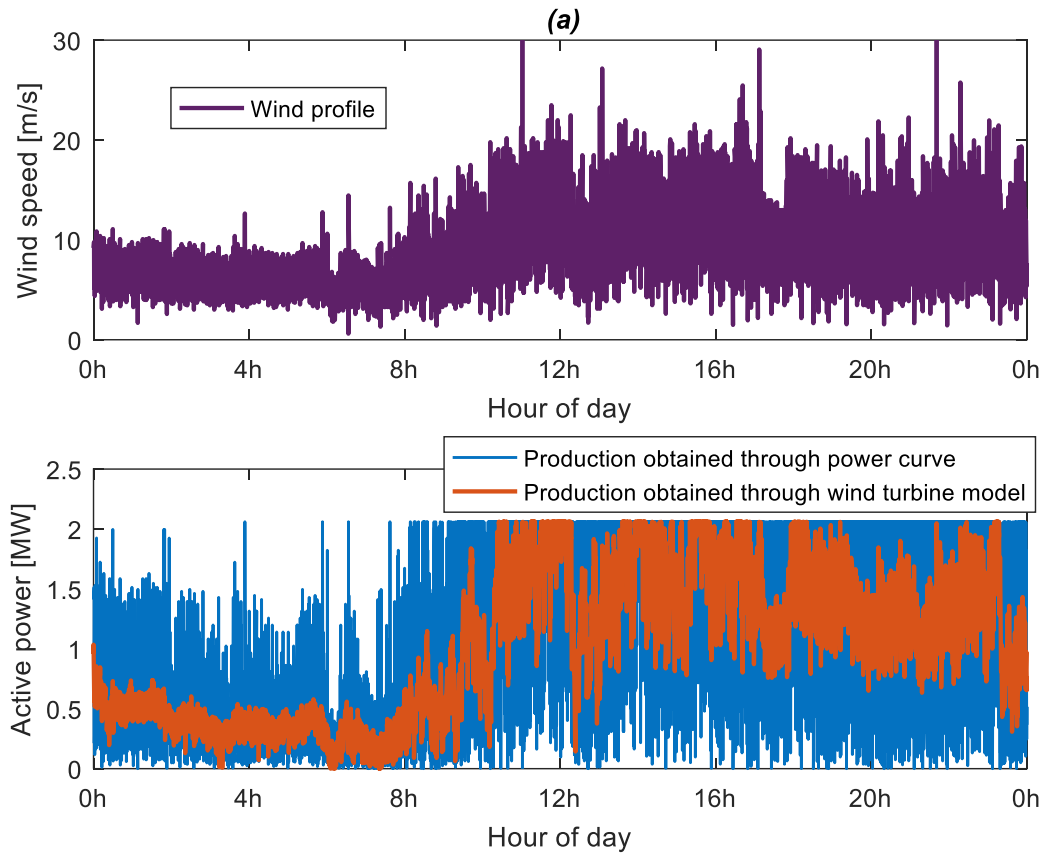


Fig. 3.22. (a) wind profile, and (b) production obtained from the profile with both power curve and DFIG model.

3.3.4.2 Energy storage system modeling and validation

Fig. 3.23 presents the ESS implemented in PowerFactory. The model of the battery system is based on the commercial storage solution Intensium Max 20M of Saft. The IM20M

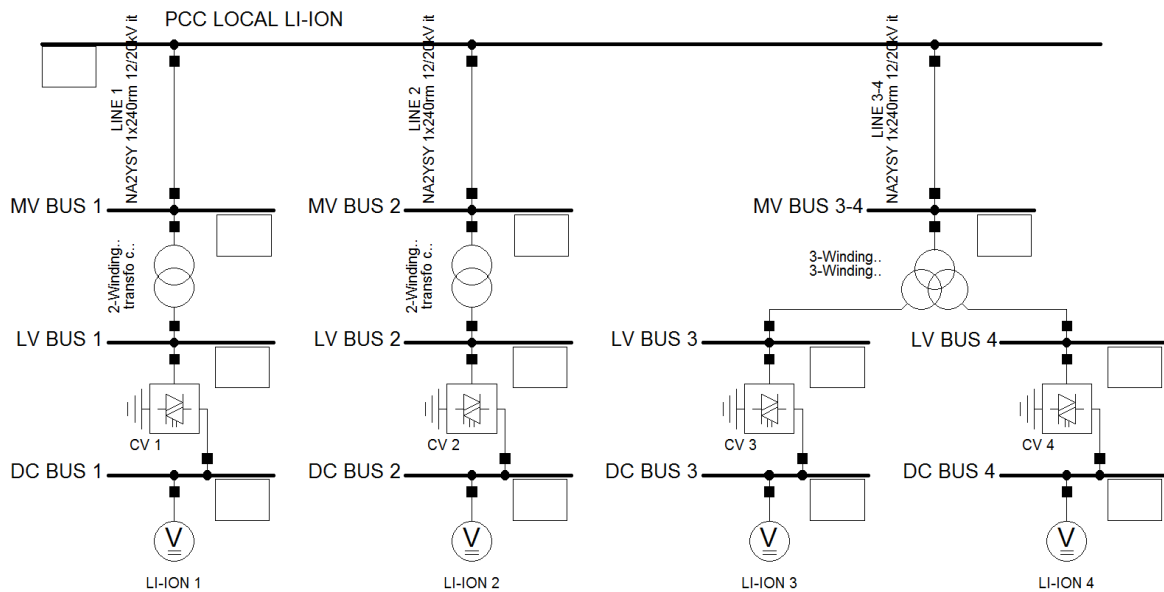


Fig. 3.23. ESS implemented in PowerFactory.

is composed of 20 parallel branches and 174 series of the VL41M cell (3,6V and 41 Ah) and allows a nominal power of 1 MW for a capacity of 580 kWh.

Next, the modeling of the storage units is dealt with. The configuration used for converters, transformers and lines in the ESS is described in Annex C.

Battery storage units modeling

In the present thesis, the Tremblay battery model is employed for the modeling of the storage units. This model, on which the battery block available in Simulink is based, is a modification of the widely known Shepherd model [152].

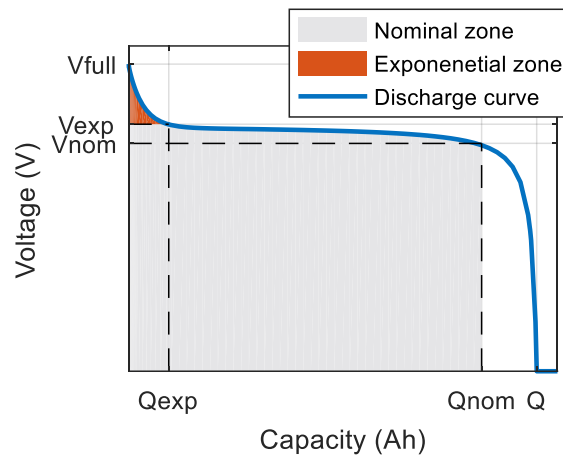


Fig. 3.24. Battery discharge characteristic.

The Shepherd model describes the output voltage of a cell as a function of the capacity in ampere-hours (Ah) obtained from it. Fig. 3.24 shows the evolution of the battery voltage with the capacity at a constant discharge current.

The discharge characteristic shown in Fig. 3.24 is composed of three sections: exponential zone, nominal zone, and end of discharge. The first section represents the exponential voltage drop that takes place when the battery is discharged from its fully charged voltage (V_{full}). The second section indicates the charge that can be extracted from the battery before the voltage drop below its nominal value (V_{nom}). Within this almost linear region the battery state-of-charge ranges between 80 % and 20 % of the nominal capacity. Lastly, in the section below V_{nom} (i.e. SoC under 20%) the battery voltage drops rapidly [107, 152].

Under this model, the battery cell is represented by a voltage source with variable magnitude in series with a resistance. The battery cell terminal voltage is calculated through Eq. 3.12:

$$V_{batt} = E_0 - R \cdot i_{batt} - K \frac{Q_{max}}{Q_{max} - it} i_{batt} - A \cdot e^{\left(\frac{-B \cdot it}{Q_{max}}\right)} \quad \text{Eq. 3.12}$$

where E_0 is the open-circuit voltage constant (V), R is the battery cell internal resistance (Ω), i_{batt} is the battery current (A), K is the polarization resistance (Ω) or polarization constant (V/Ah), $it = \int i_{batt} dt$ is the battery cell extracted capacity (Ah), Q_{max} is the maximum battery cell capacity (Ah) (as shown in Fig. 3.24), A is the exponential zone amplitude (V), and B is the exponential zone time constant inverse (Ah) $^{-1}$. i_{batt} is negative during the battery cell charging and positive during the discharging, and the parameters E_0 , R , K , A and B are known as the Shepherd model parameters. Finally, the term $K \frac{Q_{max}}{Q_{max}-it} i_{batt}$ describes a non-linearity in the terminal voltage that depends on the battery cell current and extracted capacity, and the term $A \cdot e^{\left(\frac{-B \cdot it}{Q_{max}}\right)}$ is used to approximate the exponential part of the discharge curve.

Tremblay's model main contribution is extending the validity of the model described above for variable charging and discharging currents [153]. The model consists of an internal resistance in series with a controlled voltage source. Eq. 3.13 allows the computation of the terminal voltage for a Lithium-ion battery:

$$\begin{aligned} V_{charge} &= E_0 - R \cdot i_{batt} - K_{cr} \frac{Q_{max}}{it + 0.1Q_{max}} i^* - K_{cv} \frac{Q_{max}}{Q_{max} - it} it + A \cdot e^{(-B \cdot it)} \\ V_{discharge} &= E_0 - R \cdot i_{batt} - K_{dr} \frac{Q_{max}}{Q_{max} - it} i^* - K_{dv} \frac{Q_{max}}{Q_{max} - it} it + A \cdot e^{(-B \cdot it)} \end{aligned} \quad \text{Eq. 3.13}$$

where the term concerning the polarization resistance in the previous model, $K \frac{Q_{max}}{Q_{max}-it}$, is replaced by $K_{cr} \frac{Q_{max}}{it+0.1Q_{max}}$ and $K_{dr} \left(\frac{Q_{max}}{Q_{max}-it}\right)$, polarization resistance for charge and discharge, respectively. Also, the term $K_{cv} \frac{Q_{max}}{Q_{max}-it} it$, called the polarization voltage, allows the open-circuit voltage varying with the SoC.

The filtered current (i^*) is the one flowing through the polarization resistance. Experimental results show a slow voltage dynamic for a current step response. i^* solves algebraic loop problems in Simulink and is equal to i_{batt} when the current is in steady-state. This filtered current can be expressed as the first order step response of the battery current:

$$i^* = i_{batt} (1 - e^{-\Delta t / \tau}) \quad \text{Eq. 3.14}$$

where τ is the filter time constant (in seconds), and Δt is the simulation step time (in hours). Lastly, the term $A \cdot e^{(-B \cdot it)}$ is exclusive for describing the exponential zone in Li-ion batteries.

Given that the polarization resistances and constants for charge and discharge have similar values with an order of magnitude of 10^{-4} , one simplification on Eq. 3.13 consists in

assuming K_{cr} , K_{dr} , K_{cv} and K_{dv} to be equal [154]. The replacement of those parameters by the constant K (while keeping the corresponding units), giving:

$$\begin{aligned} V_{charge} &= E_0 - R \cdot i_{batt} - K \frac{Q_{max}}{it + 0.1Q_{max}} i^* - K \frac{Q_{max}}{Q_{max} - it} it + A \cdot e^{(-B \cdot it)} \\ V_{discharge} &= E_0 - R \cdot i_{batt} - K \frac{Q_{max}}{Q_{max} - it} i^* - K \frac{Q_{max}}{Q_{max} - it} it + A \cdot e^{(-B \cdot it)} \end{aligned} \quad \text{Eq. 3.15}$$

Fig. 3.25 shows the discharge model of the battery.

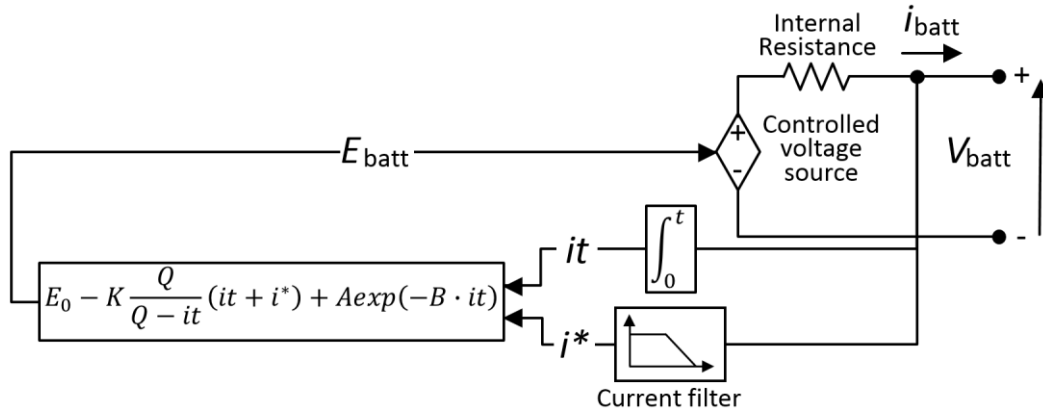


Fig. 3.25. Discharge battery model.

Battery model parameters values

A method for the identification of the parameters A , B , E_0 , K and R is described in [153] that does not require to take experimental measures on the battery. According to this, with the three points on the battery manufacturer's discharge curve $(0, V_{full})$, (Q_{exp}, V_{exp}) , and (Q_{nom}, V_{nom}) , as well as the internal resistance and maximum capacity, the following equations (Eq. 3.16, Eq. 3.17 and Eq. 3.18) can be solved, using Eq. 3.13.

For the fully charged voltage, the extracted charge is 0 ($it = 0$) and the filtered current (i^*) is 0 as the current step has just begun, giving:

$$V_{full} = E_0 - R \cdot i_{batt} \quad \text{Eq. 3.16}$$

At the end of the exponential zone, the factor B can be approximated to $3/Q_{exp}$ as the energy of the exponential term is almost 0 after 3 time constants. The filtered current i^* is equal to i_{batt} given the current is in steady-state:

$$V_{exp} = E_0 - K \frac{Q_{max}}{Q_{max} - Q_{exp}} (Q_{exp} + i_{batt}) - R \cdot i_{batt} + A \cdot e^{\left(\frac{-3}{Q_{exp}} \cdot Q_{exp}\right)} \quad \text{Eq. 3.17}$$

The nominal zone voltage is given by:

$$V_{nom} = E_0 - K \frac{Q_{max}}{Q_{max} - Q_{nom}} (Q_{nom} + i_{batt}) - R \cdot i_{batt} + A \cdot e^{\left(\frac{-3}{Q_{exp}} \cdot Q_{nom}\right)} \quad \text{Eq. 3.18}$$

The level of accuracy of this approach depends on the precision of the points extracted from the discharge curve. However, those points are found via observation of the discharge curve in the battery datasheet, which is not straightforward, especially when it comes to (Q_{exp}, V_{exp}) , and (Q_{nom}, V_{nom}) [155].

In [154], the Tremblay model parameters are approximated for the IM20M, selected in the present work for the modeling of the storage system. As the manufacturer does not specify the internal resistance of the VL41M cell, the aforementioned approximation approach does not suffice to describe fully describe the model. For that, the authors employed the method proposed in [107], which consists of varying the Tremblay parameters to adjust the resulting discharge curves to those available for several C-rates⁵ in the manufacturer's datasheet. The method applies optimization techniques to find the values of the \mathbf{X} vector, subject to \mathbf{X}^{min} and \mathbf{X}^{max} :

$$\begin{aligned} \mathbf{X} &= [E_0 \quad A \quad B \quad K \quad R] \\ \mathbf{X}^{min} &= [E_0^{min} \quad A^{min} \quad B^{min} \quad K^{min} \quad R^{min}] \\ \mathbf{X}^{max} &= [E_0^{max} \quad A^{max} \quad B^{max} \quad K^{max} \quad R^{max}] \end{aligned} \quad \text{Eq. 3.19}$$

that minimize the cost function $f_{obj}(\mathbf{X})$ for the discharge currents I_1, \dots, I_n :

$$f_{obj}(\mathbf{X}) = \sqrt{\sum_{i=1}^{i=n} \sum_{Q=0}^{Q_{nom}} (V_{mes}(Q, I_i) - V(Q, I_i))^2}, \quad \text{Eq. 3.20}$$

so that the quadratic error among the manufacturer's voltage V_{mes} and the model estimations V is minimized. For that, the amperes-hour delivered Q and the discharge current I are varied. In that sense, the method identifies simultaneously i discharge curves.

Long simulation times (several years) were considered in [154] allowing battery capacity degradation analysis. Good accuracy was achieved at reduced computational costs through sampling periods ranging from 1 minute up to 60 minutes.

Nonetheless, in the context of the energy management of the wind/battery storage HPP, a step time of 1 minute would be too long. Assuming the maximum frequency for the reception of wind farm production measurements is 1 second, the BESS model (and in general all the models employed to describe the hybrid plant) need to be used with a simulation sample time

⁵ Discharge current is usually expressed as a C-rate which is a measure of the rate at which a battery is discharged with respect to its maximum capacity. Thus, a 1-C rate refers to the discharge current that will discharge the battery in 1 hour. Other C-rates can be defined that are multiples and submultiples of the unitary C rate (e.g. 5C, C/2, etc.).

small enough to allow the energy management strategy to generate and apply control actions every second.

Table 3.10. VL41M cell parameters values [154].

Symbol	Description	Unit	Value
V_{full}	Fully charged voltage	V	3,95
V_{nom}	Nominal voltage	V	3,6
V_{exp}	Exponential voltage	V	3,9
Q_{nom}	Nominal capacity	Ah	39
Q_{max}	Maximum cell capacity	Ah	41
Q_{exp}	Exponential capacity	Ah	1
I	Nominal discharge current	A	13,67
V_{chlim}	Cell charge voltage limit	V	4
V_{dchlim}	Cell cut-off voltage	V	2,7

To describe the IM20M storage system through the Tremblay model equations in Matlab, the VL41M battery parameters values shown in Table 3.10 were used along with the following values given to the Tremblay model parameters: $E_0=3,2399$ V, $R=0,00197367$ Ω , $K=0,00010415$ V/Ah, $A=0,7541$ V, and $B=0,0348$ (Ah)⁻¹ [154]. Also $SoC^{max}=80$ %, $SoC^{min}=20$ %, $\tau=1,8$ s⁶, $\Delta t=1/3600$ h, and 20 parallel cells as well as 174 cells in row.

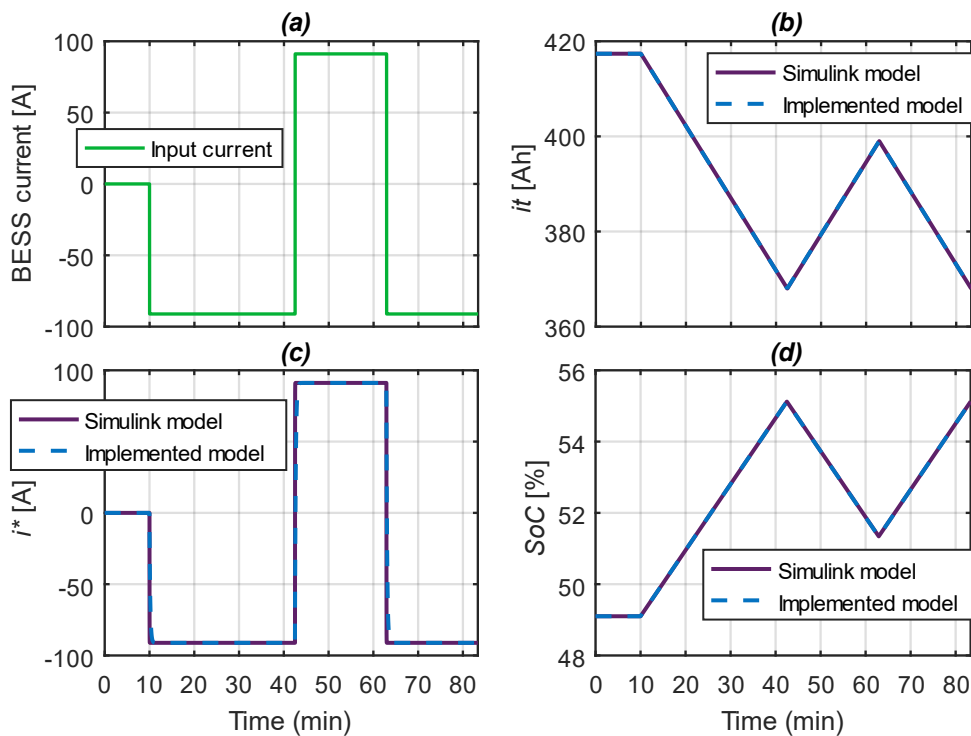


Fig. 3.26. Validation of Matlab implementation: (a) input current. In (b), (c) and (d) the signals obtained for i_t , i^* and SoC are compared.

⁶ According to VL41M battery specification.

For validating this nonlinear model, the current signal displayed in Fig. 3.26.a was applied to both the implemented model and the Simulink battery block, the latter configured to represent the 1 MW / 580 kWh storage system (using the values in Table 3.10 and the numbers

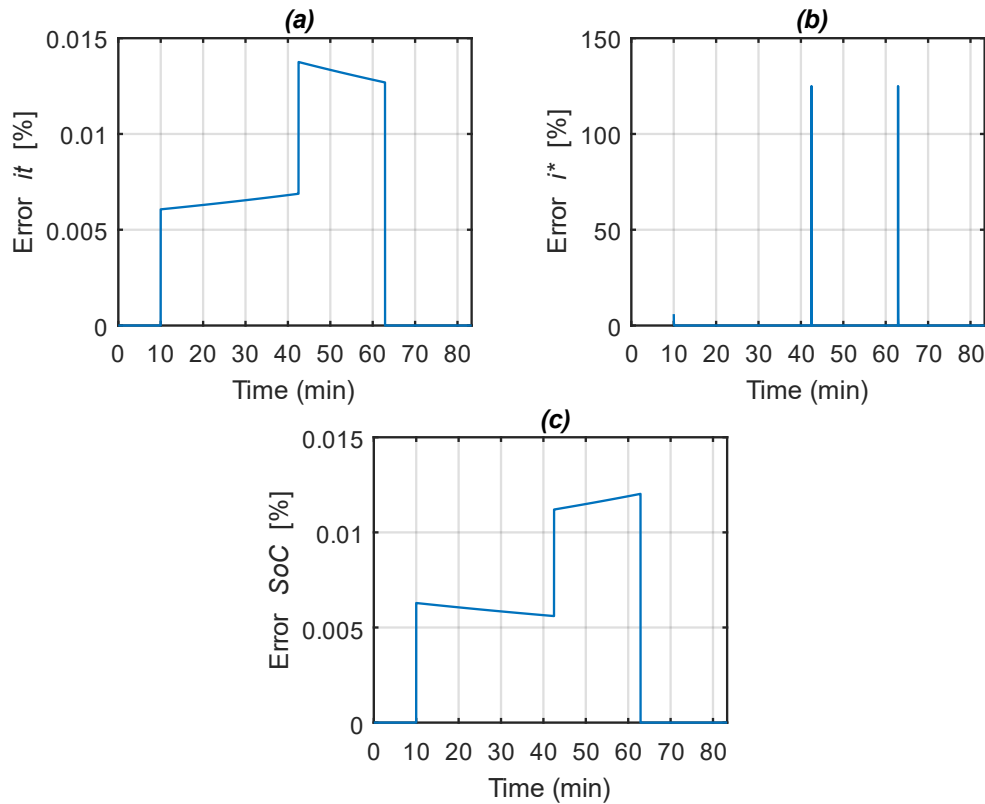


Fig. 3.27. Percentage errors of: (a) i_t , (b) i^* , and (c) SoC signals obtained.

of parallel and series cells). An initial state-of-charge of 50 % was chosen for the test. Fig. 3.26.b-d show the signals obtained for i_t , i^* and SoC . As can be seen in Fig. 3.26.d, at the beginning of the simulation the initial SoC is slightly lower than the value declared. A look-up table was used so that the SoC value for the first iteration of the script describing the IM20M could follow the Simulink battery.

On its turn, Fig. 3.27 depicts the percentage errors obtained when the Simulink signals are taken as theoretical values and the implemented model signals, as approximated values.

The errors in the model for the signals i_t and SoC are close to zero (Fig. 3.27.a and Fig. 3.27.c). Meanwhile, Fig. 3.27.b reveals an error caused by a delay between the i^* signals obtained. Error peaks take place during several seconds when the input current changes (see Fig. 3.28.a and Fig. 3.28.b). As can be noted from Fig. 3.28.b the implemented model presents a dynamic which is a bit faster (of the order of 4 seconds) than that of the Simulink model. In that sense, the model implemented is less realistic

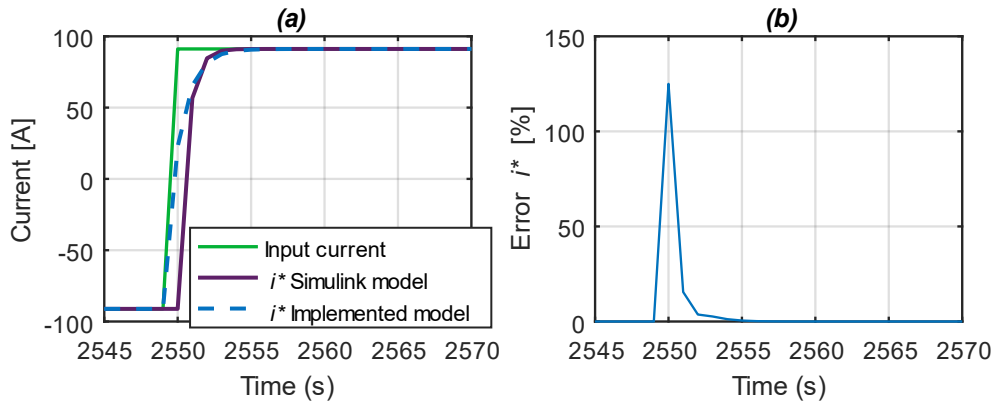


Fig. 3.28. Zoom in on time axis around the second change in the input current signal: (a) input current and i^* signals obtained (b) i^* error.

Fig. 3.29 presents the discharge of the modeled 1 MW / 580 kWh storage system (Fig. 3.29.a). For this test, the initial state-of-charge was set at 100 % and the minimum and maximum *SoC* limits, at 0 and 100 % (Fig. 3.29.b). Furthermore, the power reference was defined to withdraw 580 kW from the battery for one hour. As can be seen, the power followed

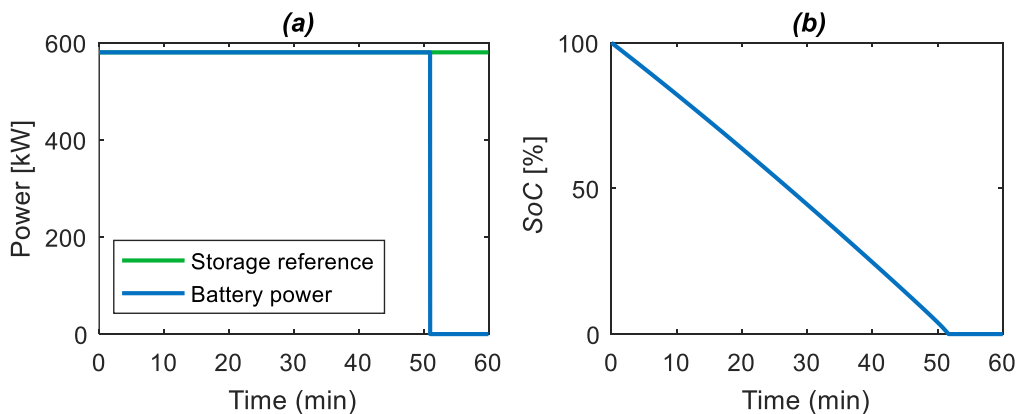


Fig. 3.29. Discharge of IM20M storage system model.

the reference until the *SoC* reached 0 % after 52 minutes.

PowerFactory model validation

A step taken before the battery nonlinear model implementation in PowerFactory, was the validation of a standalone storage unit in the same software through comparison with the Matlab battery block. To do so, the setup shown in Fig. 3.30 was employed. The IM20M modeling was based on the battery template available in the library of PowerFactory. Such a battery template implements a static generator grid element with several DSL models. A DPL (DIgSILENT Programming Language) script with the Tremblay model equations was added. The validation setup also contains a PowerFactory external grid element, used to represent external networks, a 4,6 MVA, 0,9 lagging power factor PowerFactory synchronous motor

element configured to consume 2 MW and 2 Mvar, and a 10 kV busbar linking the three first elements.

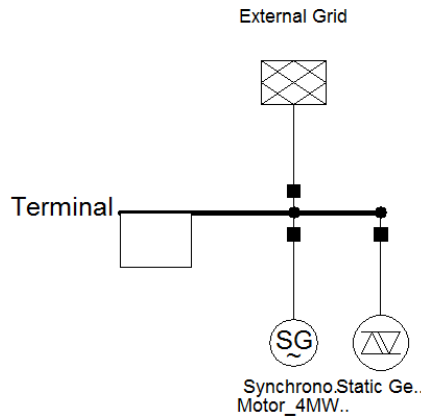


Fig. 3.30. System employed to test the battery model in PowerFactory.

The frequency control and the voltage support feature, originally present in the template, were removed. With this modification, the battery active power reference is no longer calculated depending on the frequency but imposed through an external file. Fig. 3.31 shows the resulting DSL frame on which the battery modeling is based. The DSL models, measurement devices and PowerFactory elements of which the frame is composed are [156]:

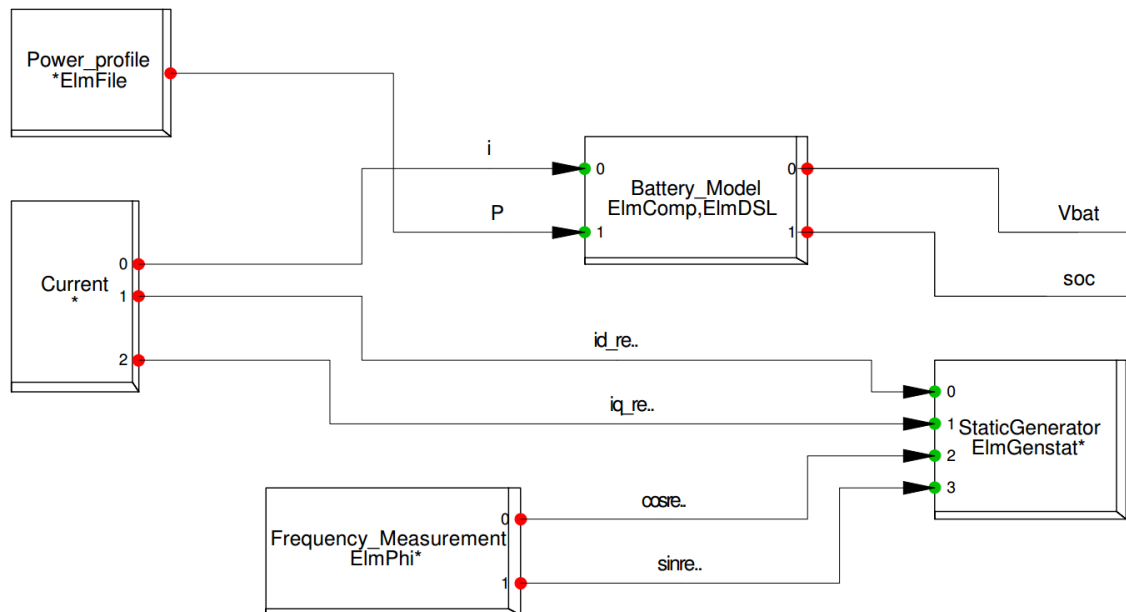


Fig. 3.31. DSL frame for integrating the battery model and an external file.

- Power profile: link to external file with timestamped active power data. The data is used as reference for the battery active power.
- Current: current signals required by the battery model and the static generator block.
- Battery Model: Model of the battery.
- Static generator: Link to a static generator, representing the battery and the inverter.
- Frequency Measurement: Frequency measurement for frequency control.

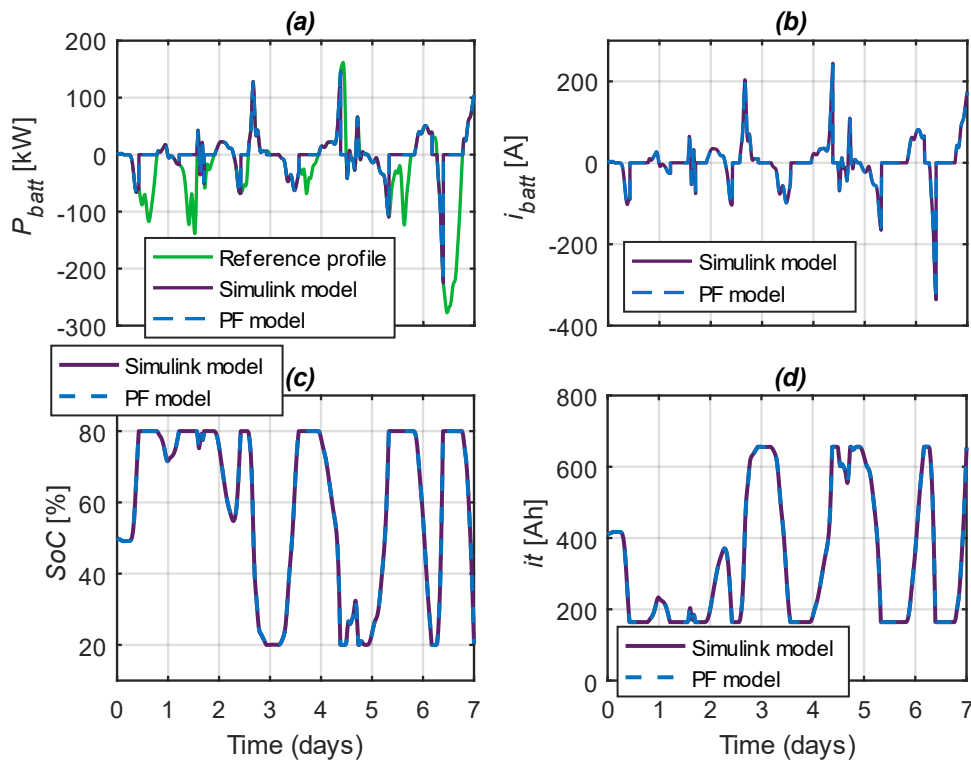


Fig. 3.33. Simulation results of BESS modeling in PowerFactory in comparison to Matlab: (a) power reference profile and active power obtained, (b) battery current, (c) SoC, (d) it .

Fig. 3.33 presents the validation test results of the BESS modeling. Fig. 3.33.a shows the reference power profile as well as the battery power signals obtained from the Simulink battery bloc and the PowerFactory implementation. Given a power reference was used as input, the battery current in Matlab was calculated by dividing the target power by the battery voltage (Fig. 3.33.b). The state-of-charge (SoC) and integral current (it) signals obtained are presented in Fig. 3.33.c-d. The simulation time is of seven days and the minimum and maximum state-of-charge limits are set at 20 % and 80 %. A sampling time of 1 second was employed in the simulations.

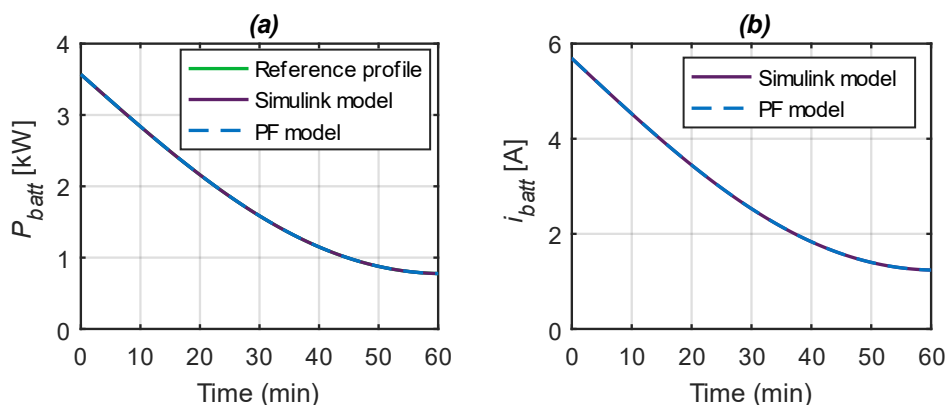


Fig. 3.32. Simulation results of BESS modeling in PowerFactory in comparison to Matlab, zoom around the first simulation hour: (a) power reference profile and active power obtained, (b) battery current.

Fig. 3.32 and Fig. 3.34 take up the signals from Fig. 3.33, zooming around the first hour of simulation.

As can be seen, the power signals are superposed indicating the Matlab and PowerFactory implementations models produce similar results.

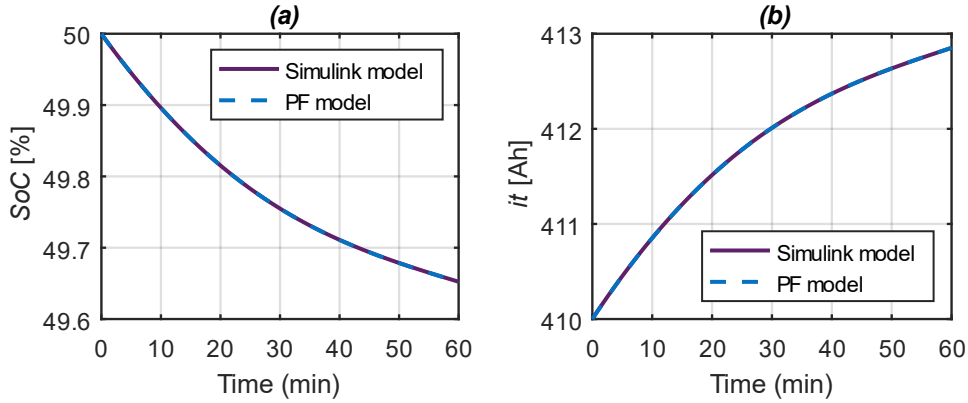


Fig. 3.34. Simulation results of BESS modeling in PowerFactory in comparison to Matlab, zoom around the first simulation hour: (a) SoC, (b) it .

3.4 Model for control

A control-oriented linear model is required by the controller to generate optimal control actions. A linear time-invariant (LTI) system described by the following state-space representation is used:

$$\begin{aligned} \mathbf{x}(k+1) &= \mathbf{A}_d \cdot \mathbf{x}(k) + \mathbf{B}_d \cdot \mathbf{u}(k) \\ \mathbf{y}(k) &= \mathbf{C}_d \cdot \mathbf{x}(k) \end{aligned} \quad \text{Eq. 3.21}$$

where k represents the sampling time, $\mathbf{x}(k) \in \mathbb{R}^n$ represents the system states, $\mathbf{u}(k) \in \mathbb{R}^{n_u}$ the decision variable or input, and $\mathbf{y}(k) \in \mathbb{R}^{n_r}$, the controlled output.

The linear model for control presented next is founded on the BESS model, whose input is the storage system current.

3.4.1 Linear model for control

In the discrete-time implementation, the BESS actual storage system charge it is calculated as [154]:

$$it(k+1) = it(k) + \Delta_t \cdot i_{BESS}(k+1) \quad \text{Eq. 3.22}$$

i^* is calculated through filtering the BESS current as:

$$i^*[k+1] = (1 - \alpha) \cdot i^*[k] + \alpha \cdot i_{BESS}(k+1) \quad \text{Eq. 3.23}$$

where the mitigating factor α is defined as [154]:

$$\alpha = \frac{\Delta_t}{(\tau + \Delta_t)} \quad \text{Eq. 3.24}$$

The SoC in percent is calculated from the storage system extracted capacity (it) as:

$$SoC(k+1) = 100 \left(1 - \frac{it(k)}{Q} \right) - \frac{\Delta_t}{Q} u(k+1) \quad \text{Eq. 3.25}$$

Rewriting Eq. 3.22 - Eq. 3.25 in the form of state-space representation gives:

$$\begin{bmatrix} it(k+1) \\ i^*(k+1) \\ SoC(k+1) \\ 100 \end{bmatrix} = \begin{bmatrix} 1 & 0 & 0 & 0 \\ 0 & (1-\alpha) & 0 & 0 \\ -100/Q & 0 & 0 & 1 \\ 0 & 0 & 0 & 1 \end{bmatrix} \begin{bmatrix} it(k) \\ i^*(k) \\ SoC(k) \\ 100 \end{bmatrix} + \begin{bmatrix} \Delta_t \\ \alpha \\ -\Delta_t/Q \\ 0 \end{bmatrix} u(k+1) \quad \text{Eq. 3.26}$$

Eq. 3.26 describes the ESS model used in this thesis to approximate the storage system extracted capacity it , filtered current i^* , and state-of-charge SoC . As can be seen, it , i^* , SoC and a constant used in the SoC calculation, conform the state vector in the representation.

The model input and storage system active power is given by

$$\begin{aligned} u &= i_{BESS} \\ P_{BESS} &= v_{BESS} \cdot i_{BESS} \end{aligned} \quad \text{Eq. 3.27}$$

where the subscript ‘‘BESS’’ in the variables names indicates the storage model considers four IM20M units. Also, the injected power is calculated according to:

$$P_{INJ} = P_{WECS} + P_{BESS} \quad \text{Eq. 3.28}$$

where P_{BESS} is the power absorbed or delivered by the storage system. Its sign is negative during charging and positive during discharging cycles of the battery.

As stated in Eq. 3.28, by means of P_{BESS} can be controlled the power injection into the grid (P_{INJ}), which as said is one of the problem outputs.

Eq. 3.15, used for computing the output battery voltage, presents two non-linearities:

1. The exponential zone on the discharge curve (Fig. 3.24).
2. The non-linear terms containing the parameter K .

Instead of considering v_{BESS} among the output variables of the HPP model for control, the proposed implementation uses a measurement of the voltage coming from the plant. It is assumed that the voltage measurement signal is available at every calculation step.

Also, in order to decouple the control of the output P_{INJ} from the model input, it is necessary to define among the regulated variables a current signal that is equivalent to i_{BESS} . In section 3.3.4.2 was mentioned that the filtered current i^* and i_{batt} have the same magnitude in steady state.

To compare these signals, the linear model equations were implemented in Matlab. Fig. 3.35.a illustrates the stepped exciting current i_{BESS} used as input to the BESS model along with the filtered current i^* signal obtained. The relative error obtained by comparing these two

signals: i_{BESS} as the theoretical or reference signal, and i^* as the measured signal, is depicted in Fig. 3.35.b.

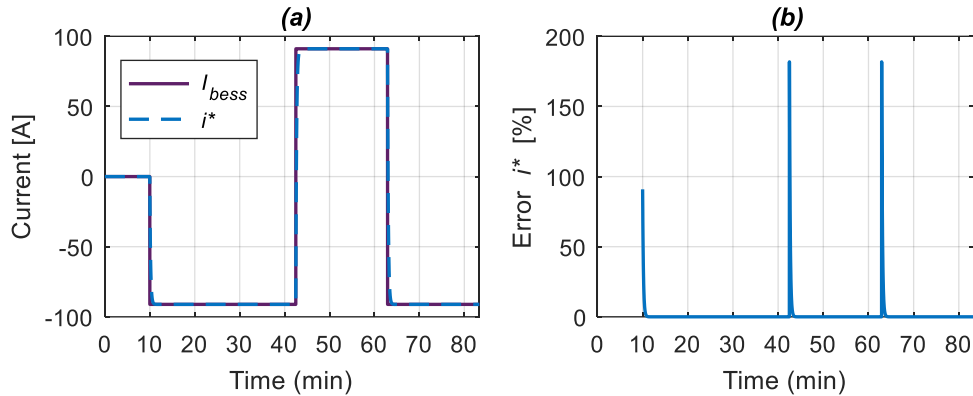


Fig. 3.35. i_{BESS} and i^* : (a) current plots, (b) error function.

The instantaneous variations in the input current are nonrealistic yet allow to appreciate the difference among the two signals. As evidenced in the figures, i^* presents a slight delay with respect to the storage system current. As in the calculation of the variable it (employed to compute the variable SoC), this implementation uses i^* instead of i_{BESS} (see Eq. 3.22), the delay in i^* implies that the linear modeling presents a dynamic which is a bit slower than that of the system. Such a dynamic is expected not to affect the control strategy though.

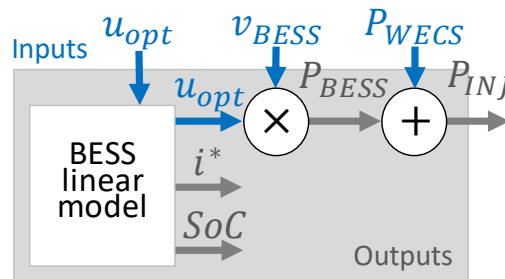


Fig. 3.36. Model for control and output calculation.

Other than i^* , another signal to regulate is the state-of-charge. Thus, Eq. 3.29 describes the model output vector y containing the regulated variables.

$$y[k] = \begin{bmatrix} i^*(k) \\ SoC(k) \end{bmatrix} = \begin{bmatrix} 0 & 1 & 0 & 0 \\ 0 & 0 & 1 & 0 \end{bmatrix} \begin{bmatrix} it(k) \\ i^*(k) \\ SoC(k) \\ 100 \end{bmatrix} \quad \text{Eq. 3.29}$$

Later, the model for control will allow the optimal control effort calculation and with it, the estimation of states and output. For that, the knowledge of the storage system voltage (v_{BESS}) and instant wind farm production (P_{WECS}) is required, as sketched in Fig. 3.36.

3.4.2 Control model validation

The model for control which is based on the storage system linear model described in Matlab is next validated by comparison with the nonlinear BESS model implemented in PowerFactory. The PowerFactory configuration is the one depicted in Fig. 3.23.

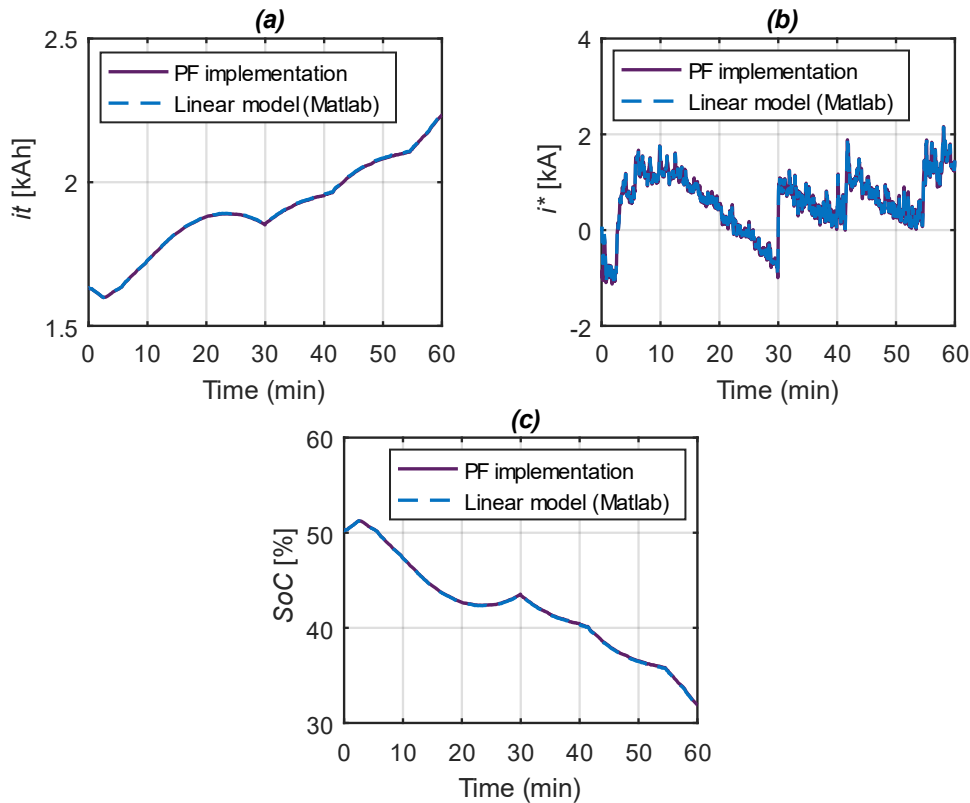


Fig. 3.37. Validation test signals comparison: (a) integral current, (b) filtered current, (c) state-of-charge, (d) BESS power.

Fig. 3.37.a-c present the integral current, the filtered current, and the state-of-charge, respectively. Under the simulation conditions studied, it can be said that the linear model behaved as the more detailed description of the BESS implemented in PowerFactory.

3.5 Chapter conclusions

In this third Chapter, the models developed for simulation and control have been described.

Power flow and dynamic simulations have allowed analyzing static and dynamic behavior of the grid model with respect to two operation scenarios for which real data was available for comparison. In the static case, power flows throughout the grid obtained via simulation seem consistent with respect to the telemetry data. Even though HTB-level busbars voltages from simulation were on average 2,8 % smaller than the measured ones, the voltages at load busbars were inside the desired limits and consistent with the telemetry.

Control models in DIgSILENT simulation language were used to represent the wind turbines and the storage units within the hybrid power plant using. The wind turbines modeling considers electrical, mechanical, aerodynamic and control system aspects. The energy storage elements modeling was based on the Tremblay model equations. A simulation was performed that allowed to follow up the evolution of several signals as the IM20M, commercial storage solution retained, was charged and discharged over a seven days period.

A discrete-time and linear version of the ESS model was the basis for the HPP model for control. Comparison with the more detailed representation of the BESS implemented in PowerFactory showed similar results when the state-of-charge was within the 20 % - 80 % range, where the variation of the output voltage with respect to the charge is approximately linear.

(This page is intentionally left blank)

CHAPTER

4

Model predictive control & quadratic programming-based energy management strategy

Summary

4.1 Introduction	112
4.2 Control strategy design.....	113
4.2.1 Plant description	114
4.2.2 Problem definition	114
4.2.2.1 Objectives	114
4.2.2.2 Design variables	115
4.2.2.3 Constraints	117
4.2.3 Control and optimization: application to the hybrid power plant.....	118
4.2.3.1 Deterministic optimization problems.....	119
4.2.3.2 MPC feedback control design	120
4.2.3.3 Quadratic cost function	124
4.2.4 Prediction and optimization using MPC and Matlab QP solver.....	127
4.2.4.1 Unconstrained MPC/QP prediction and optimization	128
4.2.4.2 Constraints handling	130
4.3 Chapter conclusions	133

Chapter overview

This Chapter presents the design of the MPC control strategy for the energy management of the hybrid power plant. For this purpose, several steps are followed comprising the problem definition, the optimization method selection and, the cost function definition, which converge in a global mathematical description of the strategy.

4.1 Introduction

Several criteria can be used to figure out an optimization problem. Indeed, the type of an optimization problem can be identified depending features like the presence and type of constraints, the “nature” of the system model variables, the problem physical structure, the allowed values for the decision variables, or the number of quantities to minimize or maximize (objectives) in the cost function.

Accordingly, considering the presence and type of constraints, optimization problems subject to one or more constraints are said constrained problems. Meanwhile, problems with no constraints are called unconstrained problems. Otherwise, if the constraints depict restrictions in the system behavior, the problem is said to have functional constraints whilst those with constraints representing physical limitations on the system variables are problems with geometric or side constraints [157]. If the system variables in the optimization problem do not change over time, the variables are said to be static and the problem is a static optimization problem. Conversely, if the variables are function of the time, the problem is known as a dynamic optimization problem [157].

In static optimization problems, the values of the system variables are considered for a specific instant, hence the optimal corresponds only to one instant. In dynamic problems the system variables represent the phenomena over a period of time, that is, system change over time is considered. Also, dynamic problems implicate a number of calculation stages. Several other types of optimization problems can be found considering the system modeling strategy (discrete, continuous, linear, nonlinear, etc.).

By taking into account the allowed values for the decision variables, two ways to classify them can be depicted: first, as integer or real-valued and second, as deterministic or stochastic [157]. According to the first classification, if some or all the decision variables in the problem only can take integer (or discrete) values, the problem is referred to as an integer programming problem. On the other hand, if the problem consists of choosing values of real variables to minimize or maximize a real function, the problem is said real-valued. Under the second classification, deterministic problems are those in which a given starting point and

parametrization produce a unique result [107]. Finally, in stochastic problems, some or all variables are probabilistic (also termed non-deterministic or stochastic).

Optimization problems can also be classified into optimal control problems or non-optimal control problems. Optimal control problems are mathematical programming problems defined by two types of variables: control or decision variables (controlled by the decision-maker), and state variables (describing the mathematical state of the system) [157]. A key aspect in understanding optimal control is that solving an optimal control problem means finding the set of control variables minimizing the cost function (not present in non-optimal control problems) to achieve the desired performance.

One last criterion to identify optimization problems is the number of optimization objectives (variables to minimize or maximize). Under this classification, problems having only one objective are called single-objective programming problems. Consequently, problems having two or more are called multi-objective programming problems [157].

Considering this, the next section focuses on the design of a control strategy that at every timeslot solves the energy dispatch problem of controlling the HPP, so its output complies a power injection commitment. The design process is explained step-by-step starting at the problem definition and ending at the equations leading to finding the optimal solutions.

4.2 Control strategy design

The present section deals with the design of the control strategy for the energy management of the hybrid power plant. For that, the HPP's operating conditions and mathematical representation are reviewed to identify the quantitative measures to optimize, the controllable variables that affect the state of the system, and the problem restrictions limiting the set of feasible solutions. After that, a short description of different optimization problem types precedes both the selection of an optimization method and the definition of the cost function.

The algorithm selection, done according to the nature of the constraints and the equations involved, as well as to the permissible values for the decision variables, affects the mathematical form of the cost function defined in this section. Finally, the algorithm to obtain optimal outputs taking into consideration both wind production forecasts and the system state, is developed.

4.2.1 Plant description

The transmission of power from the wind power generation-battery energy storage system HPP towards the Guadeloupe island grid is coordinated by an EMS. Fig. 4.1 depicts a simplified version of the hybrid power plant considered.

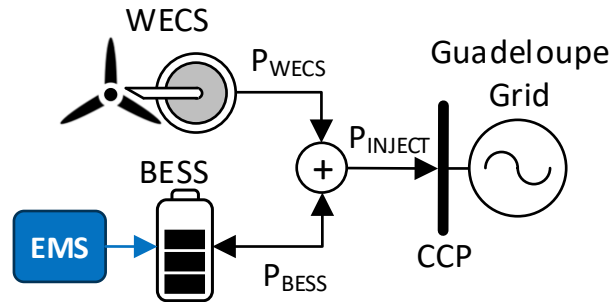


Fig. 4.1. Simplified representation of the hybrid wind-storage power plant.

The hybrid plant is composed of 4 DFIG wind turbines for a total of 8 MW and 4 Intensium Max 20M battery storage units connected in parallel for a total capacity of 4 MW / 2,32 MWh. In such a generation facility, the power injected into the island power system P_{INJ} is the addition of the power coming from the wind energy conversion energy system P_{WECS} and the storage system power P_{BESS} (negative in case of discharge), or:

$$P_{INJ} = P_{WECS} + P_{BESS} \quad \text{Eq. 4.1}$$

4.2.2 Problem definition

The problem definition consists in the identification of control objectives, decision variables, and problem constraints. These steps precede the development of an optimization strategy adapted to the problem dealt with. Below, the control objectives identification process starts with a recall of the contractual hybrid power operating conditions.

4.2.2.1 Objectives

The aim of the hybrid power plant EMS is ensuring that the power supplied to the main grid respect the operating rules, defined at the Insul'Grid project specification, while maximizing the plant's profit. Below are described the functioning rules taken into consideration in the definition of the EMS.

- *State-of-charge*: the storage system must be operated with its *SoC* (in %) limited to within the range $[SoC^{max}, SoC^{min}]$.
- *Forecasts and power injection band*: the plant operation is based on 24 hours of wind speed forecasts for the period 0h00 – 23h59 of the day D+ 1 (i.e. the next day, when the

actual production is taking place). A scheduling algorithm represents the forecasted production in the form of a half-hourly stepped profile. Such a profile is taken here as daily day-ahead electricity commitment generation schedule (P_{SCHED}).

The tolerated injection region determines how far the power transferred towards the grid (P_{INJ}) can get from the commitment profile (P_{SCHED}) without triggering a penalty condition (see Fig. 1.9). As the output power of the WECS is limited at 8 MW (P_{MAX}), by setting the tolerance at 25 % of the installed capacity, the upper and lower limit are 2 MW above and below P_{SCHED} (see the example presented in section 1.4.1.2):

$$\begin{aligned} P_{upper\ limit} &= P_{SCHED} + 0.25 \cdot 8 \times 10^6 \\ P_{lower\ limit} &= P_{SCHED} - 0.25 \cdot 8 \times 10^6 \end{aligned} \tag{Eq. 4.2}$$

- Power variation speed limits: during the positive or negative step changes of the generation schedule, the injected power variation (MW/s) must respect the following rate of change limitations: during upward steps, the passing from 0 to P_{MAX} must happen between 30 seconds and 5 minutes. Also, during downward steps, the passing from P_{MAX} to 0 must take place between 1 and 10 minutes.
- Plant revenues and penalty system: the plant revenues are determined via a penalty system. According to this, power injections with excursions of 60 consecutive seconds outside the limits are penalized with non-payment of the power supplied to the grid for the next 10 minutes. The plant revenue during the simulation time can then be calculated considering the energy selling price (SP in /c per kWh) as:

$$PR = \sum_{t=0}^{sim.\ time} P_{INJ}(t) \times SP(t) \times \partial(t)$$

where

$$\partial(t) = \begin{cases} 0 & \text{when a penalty condition is active} \\ 1 & \text{In other cases,} \end{cases} \tag{Eq. 4.3}$$

The hybrid plant operating conditions having been explained, the attention shall focus now on the model design variables.

4.2.2.2 Design variables

A model is a mathematic representation of the interactions between the system variables and its environment [158]. Different elements in the system model play a role in the definition of the cost function and constraints, e.g. the number of independent variables and equations it

is composed, or the decision variables, which are controllable parameters that affect the state of the system. The definition of the latter is another step in the problem definition phase preceding the problem's cost function definition and control strategy development.

A model for the wind-storage HPP was introduced in Chapter 3. Such a model, is based on the Li-ion battery state-space representation presented in the same Chapter, as represented in Fig. 3.36, and defined by Eq. 3.22 – Eq. 3.29.

The hybrid plant's ESS consists of a Li-ion 4 MW / 2.32 MWh battery system comprising four units of the Saft's IM20M (1 MW / 580 kWh). The latter is composed by packs of VL41M cells. This is described in the BESS state-space representation which implements the parameters of that cell (described in Table 3.11) and the corresponding series and parallel branches required to reach the power and energy ratings mentioned.

The state-space representation considers as state variables the BESS actual charge measured in Ah, the filtered current in Amperes and the state-of-charge in percent, as follows:

$$\begin{bmatrix} x_1 \\ x_2 \\ x_3 \end{bmatrix} = \begin{bmatrix} it \\ i^* \\ SoC \end{bmatrix} \quad \text{Eq. 4.4}$$

Meanwhile, the model input u is the BESS current.

$$u = i_{BESS} \quad \text{Eq. 4.5}$$

Also, the model outputs are P_{INJ} and SoC , or

$$\mathbf{y} = \begin{bmatrix} P_{INJ} \\ SoC \end{bmatrix}, \quad \text{Eq. 4.6}$$

namely the storage system state-of-charge and power transferred to the grid. The SoC is the third state variable (x_3), whereas P_{INJ} can be computed through Eq. 4.7 via the BESS voltage (considered a measurable variable) and the battery current, which is part of the state-space representation model.

$$P_{BESS} = v_{BESS} \cdot i_{BESS} \quad \text{Eq. 4.7}$$

However, i_{BESS} is also the decision variable of the model, i.e. the signal used to control the hybrid power plant ESS. In sections 3.4.1 and 3.4.2 it was demonstrated that the filtered current (i^*) can be assumed equal in magnitude to i_{BESS} for the calculation of the BESS power. In line with this, Eq. 4.7 can be rewritten as

$$P_{BESS} = v_{BESS} \cdot i^* \quad \text{Eq. 4.8}$$

Finally, the storage system is used to compensate for the lacking power required to meet the commitment. The amount of battery power required at any instant is given by:

Until now, the system design variables have been stated and discussed. In order to

$$P_{BESS_{ref}} = P_{SCHED} - P_{WECS} \quad \text{Eq. 4.9}$$

complete the problem definition, in the following section, the problem constraints will be defined.

4.2.2.3 Constraints

According to the description of the system operation presented, the following are the problem constraint variables introduced in the form of inequalities. The constraints allow the definition of “forbidden” operating regions with respect to the constrained quantities. Therefore, they also limit the set of feasible values for the decision variable in the search for an optimal solution.

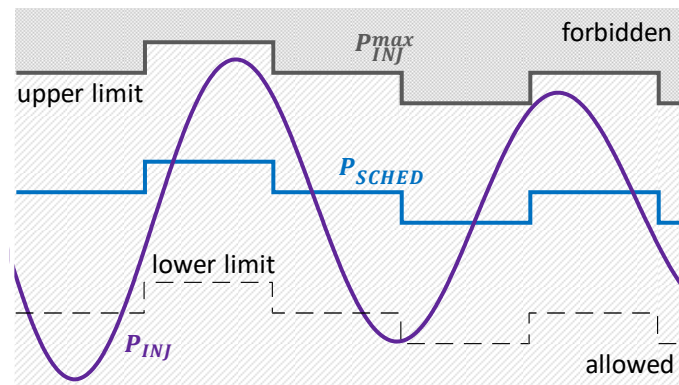


Fig. 4.2 Power injection constraint: forbidden and allowed injections regions.

- **Maximal power injection:** the power injected into the utility grid is subject to excursions outside the injection band whose boundaries are those defined in Eq. 4.2. Those excursions are undesired as they can trigger penalty conditions reducing the hybrid plant profit. As sketched in Fig. 4.2, the maximal power injection constraint is given by:

$$P_{INJ} \leq P_{INJ}^{max} \quad \text{Eq. 4.10}$$

With this, injections above the band ceiling are forbidden, making available extra power for charging the ESS.

This constraint is implemented via the current, by translating the instant upper power injection limit in terms of current. In inequality form, the constraint is given by:

$$i^* \leq i^{*max} \quad \text{Eq. 4.11}$$

- Rate of change of power injected: in the proposed strategy, given an instantaneous wind turbine production level, the power injection is controlled through the storage system power which in turn is controlled through the input $u = i_{BESS}$ (Eq. 3.28 and Eq. 4.1). This means that the rate of change of the power transferred to the utility grid (dP_{INJ}/dt) can be limited by restricting the derivative of the storage system current. Expressing the power variation bounds as current variation bounds gives in inequality form:

$$\frac{di_{BESS}^{min}}{dt} \leq \frac{di_{BESS}}{dt} \leq \frac{di_{BESS}^{max}}{dt} \quad \text{Eq. 4.12}$$

where the set-point signal for $u = i_{BESS}$ at any calculation instant k is computed as follows:

$$i_{BESS_{ref}}(k) = \frac{P_{INJ_{ref}}(k)}{v_{BESS}(k)} = \frac{P_{SCHED}(k)}{v_{BESS}(k)} \quad \text{Eq. 4.13}$$

- State-of-charge: the ESS must be operated in accordance with the recommendations of the manufacturer in terms of depth-of-discharge (DoD) and charging rates as to avoid premature aging. DoD and SoC are related terms giving an idea of current storage system capacity in percentage. The first, measures the ESS capacity that has been discharged starting from the maximum capacity while the second, measures the present ESS capacity as a percentage of maximum capacity. The relation among DoD and SoC is as follows [122]:

$$SoC = 100 \% - DoD \quad \text{Eq. 4.14}$$

According to Eq. 4.14, a 100 % SoC is a 0 % DoD , and so on. The depth-of-discharge recommendations can thus be translated into SoC bounds. In inequality form, the SoC constraints are expressed as follows:

$$SoC^{min} \leq SoC \leq SoC^{max} \quad \text{Eq. 4.15}$$

4.2.3 Control and optimization: application to the hybrid power plant

After the problem definition phase, previously presented, the remaining steps in the control strategy design are the optimization algorithm selection and the cost function formulation. Firstly, the deterministic problem types are discussed. An algorithm is then selected from among those types, and in conformity with the problem definition, a compatible cost function is defined.

4.2.3.1 Deterministic optimization problems

A general form of optimization problems is presented as follows:

$$\min_x f_0(\mathbf{x}) \text{ subject to } f_i(\mathbf{x}) \leq 0 \quad \text{Eq. 4.16}$$

where $\mathbf{x} \in \mathbb{R}^n$ is the vector of decision variables or the control input, $f_0 : \mathbb{R}^n \rightarrow \mathbb{R}$ is the cost function, and $f_i : \mathbb{R}^n \rightarrow \mathbb{R}, i = 1, \dots, m$ represent the constraints. The set $\{\mathbf{x} : f_i(\mathbf{x}) \leq 0, i = 1, \dots, m\}$ is known as the feasible set or search space and contains all the possible points that satisfy the constraints of the problem. An \mathbf{x}_{opt} is defined as the optimal solution to the problem if $f_0(\mathbf{x}_{opt})$ gives the optimal cost and if \mathbf{x}_{opt} is inside the feasible set [157].

On the basis of the equations describing the cost function and constraints, optimization problems can be divided into linear, nonlinear, geometric, and quadratic problems [157]. For instance, given $\mathbf{A} \in \mathbb{R}^{m \times n}$ and $\mathbf{b} \in \mathbb{R}^m$, finding the vector $\mathbf{x} \in \mathbb{R}^n$ that minimizes the cost function

$$\min_x \|\mathbf{Ax} - \mathbf{b}\|^2 \quad \text{Eq. 4.17}$$

is a least-squares problem or a linear least-squares problem. In other case, if the problem consists in finding a n -vector,

$$\mathbf{x} = \begin{pmatrix} x_1 \\ \vdots \\ x_n \end{pmatrix} \quad \text{Eq. 4.18}$$

to solve

$$\min_x \mathbf{c}^T \mathbf{x} = \mathbf{a}_i^T \mathbf{x} \leq \mathbf{b}_i, i = 1, \dots, m, \quad \text{Eq. 4.19}$$

given $\mathbf{c} \in \mathbb{R}^n$, $\mathbf{a}_i \in \mathbb{R}^n$ and $\mathbf{b}_i \in \mathbb{R}^n$, where \mathbf{c}^T denotes the transpose of \mathbf{c} , the problem is called a linear programming (LP) problem. When the objective or at least one of the constraints is nonlinear, the problem is said to be a nonlinear programming (NLP) problem.

Problems of the form:

$$g(\mathbf{x}) = \sum_{k=1}^m \mathbf{c}_k x_1^{a_{1k}} x_2^{a_{2k}} \dots x_n^{a_{nk}} \quad \text{Eq. 4.20}$$

in which the cost function and constraints are polynomials of the decision variable \mathbf{x} are called geometric programming problems.

In like manner, quadratic programming (QP) problems are a type of NLP problems containing a quadratic objective function and linear constraints. The standard form of a QP problem can be represented as:

$$\min_{\mathbf{x}} \frac{1}{2} \mathbf{x}^T \mathbf{H} \mathbf{x} + \mathbf{f}^T \mathbf{x} \quad \text{Eq. 4.21}$$

where \mathbf{f} is a vector and \mathbf{H} is a squared matrix. To consider an objective function to be convex (condition for the existence of a global minimum) the H matrix must be positive definite (in addition to symmetric) [157], [159].

4.2.3.2 MPC feedback control design

Model Predictive Control (MPC), also known as Receding Horizon Control (RHC) [160-163], refers to a family of control methods which use the model of the controlled system to obtain a control signal by minimizing an objective function [161]. MPC allows the incorporation of constraints as part of the control design requirements, enabling their systematic handling. The ability to handle constraints is important as real-life applications are subject to several kinds of restrictions that should be considered in the search for optimal solutions. Compared to classical linear unconstrained methodologies such as PID techniques, MPC has proven to produce much better results as it permits operating the systems near their constraint boundaries [164]. Other features of MPC are the handling of multi-variable and nonlinear systems.

Predictive control is an intuitive strategy. It consists of planning over a finite time window the future control actions that would lead to the predicted and desired outcome, like humans do every day. The cost function is a scalar function that evaluates the future control actions in the search for those minimizing the cost. Low values of cost imply good closed-loop performance. In general, a closed-loop system is the one taking a measurement of the output and using it for comparison with a reference signal, in order to estimate the states. In this dissertation, MPC control law is considered a closed-loop process because it uses the state-feedback to compute control actions stepwise [164].

Once a cost function has been defined, the MPC strategy implements the following steps [163]:

- Measure the state at time k .
- Calculate the trajectory of control actions that minimize the cost function.
- Apply the first control action in the trajectory during the timeslot $[k, k + 1]$.
 $k + 1$ refers to the timestep one sample interval after the timestep k .

Measure the state at time $k + 1$ and restart the process.

In an MPC algorithm, all the input dynamics take place within the time horizon selected and the assumption is done that the control inputs remain constant all along the prediction window. Long horizons tend to allow better closed-loop behavior and stability but add more complexity to the optimization problem resolution due to the growth in the matrices sizes they involve [164]. To calculate the best trajectory of control actions at each step, the strategy needs to predict the consequences on the cost function of every possible control sequence. The state-space representation of linear time-invariant (LTI) systems

$$\mathbf{x}(k + 1) = \mathbf{A}\mathbf{x}(k) + \mathbf{B}\mathbf{u}(k) \quad \text{Eq. 4.22}$$

is a one-step-ahead prediction map as it gives the state $\mathbf{x}(k + 1)$ from the current state vector $\mathbf{x}(k) \in \mathbb{R}^n$ and the input or control action $\mathbf{u}(k) \in \mathbb{R}^{n_u}$, where the matrices \mathbf{A} and \mathbf{B} have dimensions $n \times n$ and $n \times n_u$, respectively.

A multi-step ahead map is then required to apply the predictive control agenda mentioned above. The state trajectory vector containing estimates for the next N_p sampling instants is described by:

$$\tilde{\mathbf{x}}(k) = \begin{pmatrix} \mathbf{x}(k + 1) \\ \vdots \\ \mathbf{x}(k + N_p) \end{pmatrix} \quad \text{Eq. 4.23}$$

which means that the N_p state vector estimates $\mathbf{x}(k + 1), \dots, \mathbf{x}(k + N_p)$ are piled up in $\tilde{\mathbf{x}}(k) \in \mathbb{R}^{N_p n}$. The parameter N_p is the length of the optimization window, or the prediction horizon.

The future control sequence is composed of the N_c elements $\mathbf{u}(k), \dots, \mathbf{u}(k + N_c - 2), \mathbf{u}(k + N_c - 1)$, where N_c is called the control horizon. For simplicity, in the present work the control horizon size is defined as equal to the length of the optimization window ($N_c = N_p$). Thus, the future control trajectory $\tilde{\mathbf{u}}(k) \in \mathbb{R}^{N_p n_u}$ is a vector composed by the concatenation of N_p vectors:

$$\tilde{\mathbf{u}}(k) = \begin{pmatrix} \mathbf{u}(k) \\ \vdots \\ \mathbf{u}(k + N_p - 2) \\ \mathbf{u}(k + N_p - 1) \end{pmatrix} \quad \text{Eq. 4.24}$$

This is represented in Fig. 4.3, in which $\tilde{\mathbf{x}}(k|\tilde{\mathbf{u}}(k))$ denotes the fact that the state trajectory $\tilde{\mathbf{x}}(k)$ calculation takes place at the current timestep k and results from the control actions sequence $\tilde{\mathbf{u}}(k)$ [163].

Applying the one-step-ahead prediction map between the time samples for the instants $k + 1$ and $k + 2$ leads to

$$\begin{aligned} \mathbf{x}(k+2) &= \mathbf{A}\mathbf{x}(k+1) + \mathbf{B}\mathbf{u}(k+1) \\ &= \mathbf{A}[\mathbf{A}\mathbf{x}(k) + \mathbf{B}\mathbf{u}(k)] + \mathbf{B}\mathbf{u}(k+1) \\ &= \mathbf{A}^2\mathbf{x}(k) + \mathbf{A}\mathbf{B}\mathbf{u}(k) + \mathbf{B}\mathbf{u}(k+1) \end{aligned} \quad \text{Eq. 4.25}$$

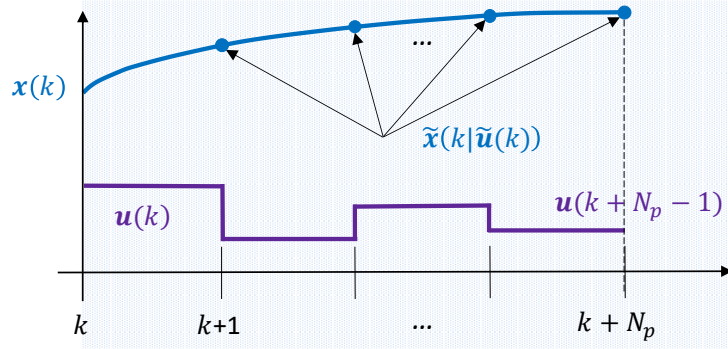


Fig. 4.3. N_p -step-ahead map to calculate for each possible control sequence $\tilde{\mathbf{u}}(k)$, the trajectory of predicted states $\tilde{\mathbf{x}}(k|\tilde{\mathbf{u}}(k))$ with $\mathbf{x}(k)$ as the initial state.

And more generally, for any $i \in \{1, \dots, N_p\}$:

$$\mathbf{x}(k+i) = \mathbf{A}^i\mathbf{x}(k) + [\mathbf{A}^{i-1}\mathbf{B}, \dots, \mathbf{A}\mathbf{B}, \mathbf{B}] \cdot \begin{pmatrix} \mathbf{u}(k) \\ \vdots \\ \mathbf{u}(k+i-2) \\ \mathbf{u}(k+i-1) \end{pmatrix} \quad \text{Eq. 4.26}$$

The matrix $\mathbf{\Pi}_i^{n_u, N_p}$ is defined allowing the selection of the i -th vector of dimension n_u from the N_p elements of $\tilde{\mathbf{u}}$ [163]:

$$\begin{pmatrix} \mathbf{u}(k) \\ \vdots \\ \mathbf{u}(k+i-2) \\ \mathbf{u}(k+i-1) \end{pmatrix} = \begin{pmatrix} \mathbf{\Pi}_1^{n_u, N_p} \\ \vdots \\ \mathbf{\Pi}_{i-1}^{n_u, N_p} \\ \mathbf{\Pi}_i^{n_u, N_p} \end{pmatrix} \tilde{\mathbf{u}} \quad \text{Eq. 4.27}$$

Here, every $\mathbf{\Pi}_i^{(n_u, N_p)}$ is computed as an identity matrix concatenated with a zero matrix whose sizes change with i , i.e.:

$$\mathbf{\Pi}_i^{(n_u, N_p)} = (\mathbb{I}_{n_u i \times n_u i} \quad \mathbb{O}_{n_u i \times (N_p - 1) \cdot n_u}) \quad \text{Eq. 4.28}$$

With this, Eq. 4.26 can then be rewritten as

$$\mathbf{x}(k+i) = \mathbf{A}^i\mathbf{x}(k) + ([\mathbf{A}^{i-1}\mathbf{B}, \dots, \mathbf{A}\mathbf{B}, \mathbf{B}] \cdot \mathbf{\Pi}_i^{n_u, N_p}) \tilde{\mathbf{u}}(k) \quad \text{Eq. 4.29}$$

and the prediction of future states can be written in a compact form as

$$\mathbf{x}(k+i) = \mathbf{\Phi}_i\mathbf{x}(k) + \mathbf{\Psi}_i\tilde{\mathbf{u}}(k) \quad \text{Eq. 4.30}$$

where Φ_i and Ψ_i are constant matrices given for every value of i and depend on A and B , the state and input matrices, respectively:

$$\begin{aligned}\Phi_i &= A^i \\ \Psi_i &= [A^{i-1}B, \dots, AB, B] \cdot \Pi_i^{n_u N_p}\end{aligned}\quad \text{Eq. 4.31}$$

On the other hand, the cost function was defined in Eq. 4.16 as a function of the decision variable used in the calculation of the optimal sequence of actions $\tilde{\mathbf{u}}_{opt}(x(k))$. One among several ways to define a cost function reflecting the control objectives and the time horizon is to choose an output vector containing linear combinations of the state vector. This means that the output \mathbf{y}_r is defined from a matrix \mathbf{C}_r with dimension $n_r \times n$, where n_r is the number of variables that the control designer wants to regulate [163]. In Eq. 4.32, the output equation is presented including the feedthrough matrix \mathbf{D} with dimension $n_r \times n_u$, allowing for more general systems.

$$\mathbf{y}_r(k+i) = \mathbf{C}_r \mathbf{x}(k+i) + \mathbf{D} \mathbf{u}(k) \quad \text{Eq. 4.32}$$

Two more vectors are introduced at this point:

$$\tilde{\mathbf{y}}_r(k) = \begin{pmatrix} \mathbf{y}_r(k+1) \\ \vdots \\ \mathbf{y}_r(k+N_p) \end{pmatrix} \quad \text{Eq. 4.33}$$

and

$$\tilde{\mathbf{y}}_{ref}(k) = \begin{pmatrix} \mathbf{y}_{ref}(k+1) \\ \vdots \\ \mathbf{y}_{ref}(k+N_p) \end{pmatrix} \quad \text{Eq. 4.34}$$

where $\tilde{\mathbf{y}}_r(k)$ represents the sequence of the predictions for the regulated outputs whereas $\tilde{\mathbf{y}}_{ref}(k)$ is the future references (or desired outputs) sequence.

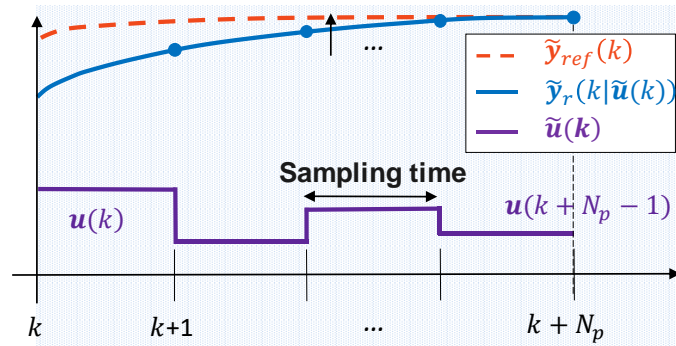


Fig. 4.4. MPC strategy. Future references $\tilde{\mathbf{y}}_{ref}(k)$, outputs predictions $\tilde{\mathbf{y}}_r(k)$, and control sequence $\tilde{\mathbf{u}}$.

As seen, the system model allows the prediction of future states and hence the estimation of the future outputs. Fig. 4.4 illustrates the fact that the tracking error (the difference among a regulated output and a corresponding set-point signal) is minimized through the application of the “right” sequence of future control actions. Such a sequence is the solution² to an optimization problem which considers the future tracking of error and the problem constraints.

Until here, a generic description of the equations of the prediction phase has been presented. An optimizer, in charge of generating stepwise the optimal sequence of inputs from the prediction stage result while considering the constraints and cost function is also part of the strategy (see Fig. 4.5).

As the output to the optimization problem $\tilde{\mathbf{u}}$ is part of the prediction equations (see Eq. 4.30), the selection matrix $\mathbf{\Pi}_i$ introduced above allows pointing to the different $u(k+i-1)$ elements of the control sequence (undefined at the moment the prediction takes place), is used in the calculation of the prediction matrices received by the optimizer. Next, the cost function is

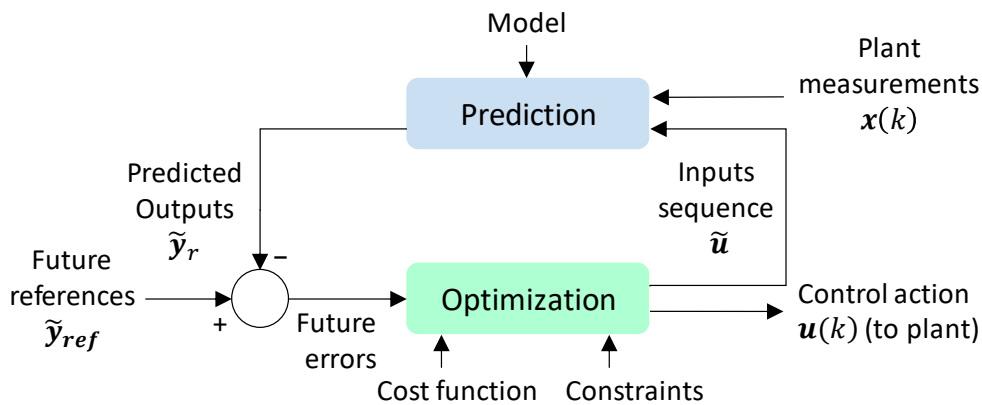


Fig. 4.5. Structure of an MPC: prediction and optimization.

discussed, followed by the adaptation of the prediction to a form compatible with the optimizer utilized.

4.2.3.3 Quadratic cost function

In the previous section, the predictive control principle and equations were presented using the generic state-space representation of an LTI system.

When an optimization problem is formulated using MPC, it is important that it can be solved in a time not bigger than the sampling interval. For this, linear programming and quadratic programming are typical formulations employed in combination with MPC. While LP may sometimes be advantageous for very large optimization problems, in general QP formulations lead to smoother control actions and more intuitive effects of changes in the tuning parameters [165].

The present section is based on the QP and predictive control strategy for LTI systems presented by the author in [163]. The fact that the strategy uses QP induces a cost function that is quadratic in the decision variable. In this section, a cost function derived from the MPC control law presented above is adapted to the problem of the energy management of the hybrid power plant by considering the problem control objectives.

The quadratic function to be minimized is a scalar function of the form:

$$\min_{\tilde{\mathbf{u}}} \frac{1}{2} \tilde{\mathbf{u}}^T \mathbf{H} \tilde{\mathbf{u}} + \mathbf{f}^T \tilde{\mathbf{u}} + c \quad \text{Eq. 4.35}$$

where c is a constant not affecting the position of the minimum solution on the parabola associated to Eq. 4.35. Also, the control effort $\tilde{\mathbf{u}}$ is the variable to minimize, $\tilde{\mathbf{u}}^T$ denotes the transpose of $\tilde{\mathbf{u}}$, and the matrix $\mathbf{H} \in \mathbb{R}^{N_p n_u \times N_p n_u}$, called the *Hessian matrix*, must be positive definite according to the following condition to ensure the optimal solution is finite and uniquely defined, and therefore that a global minimum exists:

$$\tilde{\mathbf{u}}^T \mathbf{H} \tilde{\mathbf{u}} \geq a \cdot \|\tilde{\mathbf{u}}\|^2 \text{ for some } a > 0 \quad \text{Eq. 4.36}$$

If $\tilde{\mathbf{u}}^T \mathbf{H} \tilde{\mathbf{u}} \geq 0$, the matrix \mathbf{H} is said to be positive semidefinite (or non-negative).

Based on Eq. 4.33 and Eq. 4.34, a general quadratic cost function reflecting the predictive control goal of minimizing the errors between predicted output and set-point is given by:

$$\Gamma(k) = \sum_{i=1}^{N_p} \|\mathbf{y}_r(k+i) - \mathbf{y}_{ref}(k+i)\|_{\mathbf{Q}_y}^2 \quad \text{Eq. 4.37}$$

with the subscript \mathbf{Q}_y , a positive diagonal matrix giving a weight to the tracking of errors of the control objectives, and the superscript 2, an exponent. Thus, the norm delimiters $\|\cdot\|$ employed to define the cost function, are applied considering:

$$\|\mathbf{x}\mathbf{A}\|_{\mathbf{Q}}^2 = [\mathbf{x}\mathbf{A}]^T \mathbf{Q} \mathbf{A} \mathbf{x} \quad \text{Eq. 4.38}$$

where $\mathbf{A} \in \mathbb{R}^{n \times n}$ and $\mathbf{x} \in \mathbb{R}^n$.

By injecting Eq. 4.30 in Eq. 4.32, the prediction of future outputs results in

$$\mathbf{y}_r(k+i) = \mathbf{C}_r \Phi_i \mathbf{x}(k) + \mathbf{C}_r \Psi_i \tilde{\mathbf{u}} + \mathbf{D} \tilde{\mathbf{u}} \quad \text{Eq. 4.39}$$

which leads to a cost function given by:

$$\Gamma(k) = \sum_{i=1}^{N_p} \|\mathbf{C}_r \Phi_i \mathbf{x}(k) + (\mathbf{C}_r \Psi_i + \mathbf{D}) \tilde{\mathbf{u}} - \mathbf{y}_{ref}(k+i)\|_{\mathbf{Q}_y}^2 \quad \text{Eq. 4.40}$$

and the Hessian of Γ is obtained by developing Eq. 4.40:

$$\mathbf{H} = 2 \sum_{i=1}^{N_p} (\mathbf{C}_r \boldsymbol{\Psi}_i + \mathbf{D})^T \mathbf{Q}_y (\mathbf{C}_r \boldsymbol{\Psi}_i + \mathbf{D}) = 2 \sum_{i=1}^{N_p} \|\mathbf{C}_r \boldsymbol{\Psi}_i + \mathbf{D}\|_{\mathbf{Q}_y}^2 \quad \text{Eq. 4.41}$$

Even if \mathbf{Q}_y is positive definite, if the number of rows in \mathbf{C}_r is smaller than the number of states (or $n_r < n$), the Hessian matrix can violate the condition described by Eq. 4.36 [163]. Clearly, \mathbf{H} is nonnegative because

$$\tilde{\mathbf{u}}^T \mathbf{H} \tilde{\mathbf{u}} = \tilde{\mathbf{u}}^T \left[2 \sum_{i=1}^{N_p} \|\mathbf{C}_r \boldsymbol{\Psi}_i + \mathbf{D}\|_{\mathbf{Q}_y}^2 \right] \tilde{\mathbf{u}} \quad \text{Eq. 4.42}$$

This non negativity does not allow to ensure \mathbf{H} is always positive, meaning there is a risk that the optimal solution is not appropriately defined.

For the condition Eq. 4.36 to be respected in the resulting \mathbf{H} matrix, a term taking into consideration the control effort employed in keeping \mathbf{y}_r close to \mathbf{y}_{ref} can be added to the cost function Γ . Using the definition of control effort from Eq. 4.27, Γ results in

$$\Gamma(k) = \sum_{i=1}^{N_p} \|\mathbf{C}_r \boldsymbol{\Phi}_i \mathbf{x}(k) + (\mathbf{C}_r \boldsymbol{\Psi}_i + \mathbf{D}) \tilde{\mathbf{u}} - \mathbf{y}_{ref}(k+i)\|_{\mathbf{Q}_y}^2 + \sum_{i=1}^{N_p} \|\boldsymbol{\Pi}_i^{n_u, N_p} \tilde{\mathbf{u}}\|_{\mathbf{Q}_u}^2 \quad \text{Eq. 4.43}$$

where the control actions weighting design parameter $\mathbf{Q}_u \in \mathbb{R}^{n_u \times n_u}$ is a positive diagonal matrix for weighting and adjusting the control effort of the inputs. \mathbf{Q}_u is chosen to give the right tradeoff between minimizing the tracking error $\sum (\mathbf{y}_r - \mathbf{y}_{ref})^2$ and keeping $\sum \tilde{\mathbf{u}}^2$ not too big. Also, and the second term in the equation can alternatively be expressed as:

$$\|\boldsymbol{\Pi}_i^{n_u, N_p} \tilde{\mathbf{u}}\|_{\mathbf{Q}_u}^2 = [\boldsymbol{\Pi}_i^{n_u, N_p} \tilde{\mathbf{u}}]^T \mathbf{Q}_u [\boldsymbol{\Pi}_i^{n_u, N_p} \tilde{\mathbf{u}}] \quad \text{Eq. 4.44}$$

Thus, \mathbf{H} becomes

$$= 2 \left[\sum_{i=1}^{N_p} \|\mathbf{C}_r \boldsymbol{\Psi}_i + \mathbf{D}\|_{\mathbf{Q}_y}^2 + \sum_{i=1}^{N_p} \|\boldsymbol{\Pi}_i^{n_u, N_p} \tilde{\mathbf{u}}\|_{\mathbf{Q}_u}^2 \right] \quad \text{Eq. 4.45}$$

Then, adding a positive definite matrix to a non-negative matrix allowed to obtain a positive definite Hessian.

Eq. 4.43 represents a quadratic function in the variable $\tilde{\mathbf{u}}$. Moreover, Γ can be interpreted as the cost obtained by the evaluation of the future control actions function $\tilde{\mathbf{u}}$ given the future references $\mathbf{y}_{ref}(k)$ and the present system state $\mathbf{x}(k)$ within the time horizon $[k, k + N_p]$.

During the problem definition phase, the operational objectives of maximizing the plant's profit and respecting the SO's conditions were presented. Besides, Eq. 4.3 defined the plant revenue through the function $\partial(t)$ which changes between zero and one according to whether the penalty is active or inactive. However, the description of if-else-then conditions is incompatible with the predictive control scheme described. It is for this reason that, the revenue maximization is treated indirectly by minimizing the commitment failures occurrence. Moreover, P_{INJ} and SoC are chosen as regulated quantities. With this, tuning parameters allow to act on both the transferred power and the storage system usage while the commitment failures are minimized.

P_{SCHED} and SoC_{ref} are defined as the references for the transfer of power to the grid and for the SoC variable. In this thesis, the SoC set-points definition does not consider the storage system ageing.

The integration of both the control objectives and the control effort into Eq. 4.40 gives rise to the following cost function:

$$\Gamma(k) = \sum_{i=1}^{N_p} \left\{ \lambda_1 \|P_{INJ} - P_{SCHED}\|^2 + \lambda_2 \|SoC - SoC_{ref}\|^2 + [\boldsymbol{\pi}_i^{n_u, N_p} \tilde{\mathbf{u}}]^T \mathbf{Q}_u [\boldsymbol{\pi}_i^{n_u, N_p} \tilde{\mathbf{u}}] \right\} \quad \text{Eq. 4.46}$$

where λ_1 and λ_2 are the control objective weights introduced through the diagonal matrix \mathbf{Q}_y .

In the next section, optimization problem solving tools will be described and then the cost function depicted in Eq. 4.46 will be adapted so that the at every calculation instant the MPC predictor may feed the QP solver with the adequate matrices.

4.2.4 Prediction and optimization using MPC and Matlab QP solver

The cost function described in Eq. 4.46 was derived based on MPC control law while considering the control objectives. An appropriate optimization algorithm is required to reduce future errors based on such a quadratic function and in the presence of linear constraints. For that, a parametric prediction is proposed which is compatible with *quadprog*, the quadratic programming solver provided by Matlab's optimization toolbox.

This solver finds the minimum \mathbf{x} for problems specified by [166]

$$\begin{aligned} & \min_{\mathbf{x}} \frac{1}{2} \mathbf{x}^T \mathbf{H} \mathbf{x} + \mathbf{f}^T \mathbf{x} \\ & \text{Subject to } \mathbf{A}_{ineq} \mathbf{x} \leq \mathbf{b}_{ineq} \\ & \mathbf{A}_{eq} \mathbf{x} = \mathbf{b}_{eq} \\ & \mathbf{l} \leq \mathbf{x} \leq \mathbf{u} \end{aligned} \quad \text{Eq. 4.47}$$

where \mathbf{H} , \mathbf{A}_{ineq} , and \mathbf{A}_{eq} are squared matrices whereas \mathbf{x} , \mathbf{f} , \mathbf{b}_{ineq} , \mathbf{b}_{eq} , \mathbf{l} and \mathbf{u} are vectors and the above cost function is convex if \mathbf{H} is positive definite. Also, \mathbf{A}_{ineq} and \mathbf{b}_{ineq} allow defining inequality constraints whereas \mathbf{A}_{eq} and \mathbf{b}_{eq} are used to define equality constraints.

To use MPC with *quadprog*, the prediction information given to the optimizer must be defined by $(\mathbf{H}, \mathbf{f}, \mathbf{A}_{ineq}, \mathbf{b}_{ineq}, \mathbf{A}_{eq}, \mathbf{b}_{eq}, \mathbf{l}, \mathbf{u})$, where \mathbf{H} and \mathbf{f} are required terms and the others are optional. In the applied strategy, the *quadprog* function is called with the input variables \mathbf{H} , \mathbf{f} , \mathbf{A}_{ineq} and \mathbf{b}_{ineq} . Further, $\mathbf{A}_{ineq}\mathbf{x} \leq \mathbf{b}_{ineq}$ implies that the inequality is taken element-wise over $\mathbf{A}_{ineq}\mathbf{x}$ and \mathbf{b}_{ineq} . As the problem formulation must be conform to the above form, the mathematical operator \geq can be declared by rewriting the inequality as $-\mathbf{A}_{ineq}\mathbf{x} \leq -\mathbf{b}_{ineq}$.

4.2.4.1 Unconstrained MPC/QP prediction and optimization

With the power injected into the island grid P_{INJ} and the ESS state-of-charge SoC as the regulated quantities, an adapted cost function was derived in Eq. 4.46.

The matrix \mathbf{C}_r is now defined as to include the regulated quantities i^* and SoC (x_2 and x_3) in the problem output. Recalling that P_{INJ} is controlled through P_{BESS} as in Fig. 3.36. Hence, according to Eq. 4.1 and Eq. 4.8, the regulated output is given by

$$\mathbf{y}_r = \begin{bmatrix} \mathbf{c}_{r1} \\ \mathbf{c}_{r2} \end{bmatrix} \mathbf{x}(k) + \mathbf{D}\tilde{\mathbf{u}} = \begin{bmatrix} i^* \\ SoC \end{bmatrix} \mathbf{x}(k) + \mathbf{D}\tilde{\mathbf{u}} = \begin{bmatrix} 0 & 1 & 0 \\ 0 & 0 & 1 \end{bmatrix} \mathbf{x}(k) + \mathbf{D}\tilde{\mathbf{u}} \quad \text{Eq. 4.48}$$

Also, the term related to the size of the control effort in Eq. 4.46 is not considered in the formulation for the search of optimal solutions of the *quadprog* solver (see Eq. 4.47). Indeed, what is being searched is the u whose image is the vortex of the parabola (the global minimum) resulting of the combination of the parabolas $\|P_{INJ} - \mathbf{P}_{SCHED}\|^2$ and $\|SoC - \mathbf{SoC}_{ref}\|^2$. The neglected term only affects the parabola's vertical position on the 2-d plane

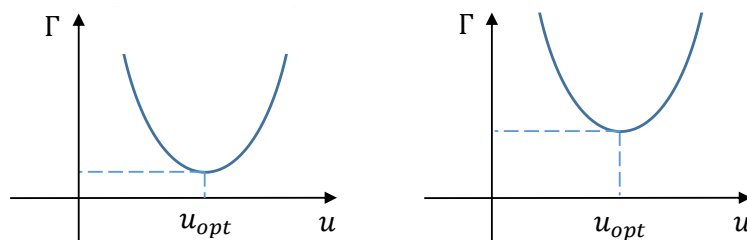


Fig. 4.6. Other terms that $\|P_{INJ} - \mathbf{P}_{SCHED}\|^2$ and $\|SoC - \mathbf{SoC}_{ref}\|^2$ introduce offsets in the parabola vortex searched.

without changing the value that minimizes the cost function, as represented in Fig. 4.6.

The application of the definition of output trajectory prediction defined on the term $\|P_{INJ} - \mathbf{P}_{SCHED}\|^2$ produces:

$$[\mathbf{c}_{r1} \Phi_i \mathbf{x}(k) + (\mathbf{c}_{r1} \Psi_i + \mathbf{D}) \tilde{\mathbf{u}} - \mathbf{P}_{SCHED}]^T \cdot [\mathbf{c}_{r1} \Phi_i \mathbf{x}(k) + (\mathbf{c}_{r1} \Psi_i + \mathbf{D}) \tilde{\mathbf{u}} - \mathbf{P}_{SCHED}] \quad \text{Eq. 4.49}$$

Developing Eq. 4.49:

$$[\mathbf{c}_{r1} \Phi_i \mathbf{x}(k) + (\mathbf{c}_{r1} \Psi_i + \mathbf{D}) \tilde{\mathbf{u}}]^T \cdot [\mathbf{c}_{r1} \Phi_i \mathbf{x}(k) + (\mathbf{c}_{r1} \Psi_i + \mathbf{D}) \tilde{\mathbf{u}}] + \mathbf{P}_{SCHED}^2 - 2[\mathbf{c}_{r1} \Phi_i \mathbf{x}(k) + (\mathbf{c}_{r1} \Psi_i + \mathbf{D}) \tilde{\mathbf{u}}] \mathbf{P}_{SCHED} \quad \text{Eq. 4.50}$$

As in finding $\min_x ax^2 + bx + c$, the first derivative is $2ax + b$ (meaning the minimum is $x = -b/2a$ and the minimization is independent of c), the constant term \mathbf{P}_{SCHED}^2 is not considered. With that modification, the development of Eq. 4.50 yields

$$[\mathbf{c}_{r1} \Phi_i \mathbf{x}(k)]^T \cdot \mathbf{c}_{r1} \Phi_i \mathbf{x}(k) + [(\mathbf{c}_{r1} \Psi_i + \mathbf{D}) \tilde{\mathbf{u}}]^T \cdot (\mathbf{c}_{r1} \Psi_i + \mathbf{D}) \tilde{\mathbf{u}} + 2(\mathbf{c}_{r1} \Phi_i \mathbf{x}(k) \cdot (\mathbf{c}_{r1} \Psi_i + \mathbf{D}) \tilde{\mathbf{u}}) - 2(\mathbf{c}_{r1} \Phi_i \mathbf{x}(k) + (\mathbf{c}_{r1} \Psi_i + \mathbf{D}) \tilde{\mathbf{u}}) \mathbf{P}_{SCHED} \quad \text{Eq. 4.51}$$

Finally, with the application of the vector operations property of Eq. 4.44, the Eq. 4.51 can be rewritten as:

$$\mathbf{c}_{r1} \Phi_i \mathbf{x}(k) \cdot \mathbf{c}_{r1} \Phi_i \mathbf{x}(k) + \tilde{\mathbf{u}}^T (\mathbf{c}_{r1} \Psi_i + \mathbf{D}) \tilde{\mathbf{u}} + 2\mathbf{c}_{r1} \Phi_i \mathbf{x}(k) \cdot (\mathbf{c}_{r1} \Psi_i + \mathbf{D}) \tilde{\mathbf{u}} - 2(\mathbf{c}_{r1} \Phi_i \mathbf{x}(k) + (\mathbf{c}_{r1} \Psi_i + \mathbf{D}) \tilde{\mathbf{u}}) \mathbf{P}_{SCHED} \quad \text{Eq. 4.52}$$

Repeating the same procedure on term $\|SoC - SoC_{ref}\|^2$ gives:

$$\mathbf{c}_{r2} \Phi_i \mathbf{x}(k) \cdot \mathbf{c}_{r2} \Phi_i \mathbf{x}(k) + \tilde{\mathbf{u}}^T (\mathbf{c}_{r2} \Psi_i + \mathbf{D}) \tilde{\mathbf{u}} + 2\mathbf{c}_{r2} \Phi_i \mathbf{x}(k) \cdot (\mathbf{c}_{r2} \Psi_i + \mathbf{D}) \tilde{\mathbf{u}} - 2(\mathbf{c}_{r2} \Phi_i \mathbf{x}(k) + (\mathbf{c}_{r2} \Psi_i + \mathbf{D}) \tilde{\mathbf{u}}) SoC_{ref} \quad \text{Eq. 4.53}$$

Factoring out $\tilde{\mathbf{u}}$ and coupling the similar terms together from Eq. 4.52 and Eq. 4.53 (once again, the terms independent of $\tilde{\mathbf{u}}$ do not affect the minimization), gives:

$$\left[\underbrace{2\mathbf{c}_{r1} \Phi_i \cdot (\mathbf{c}_{r1} \Psi_i + \mathbf{D}) \mathbf{x}(k)}_{\mathbf{F}_1} \quad \underbrace{-2(\mathbf{c}_{r1} \Psi_i + \mathbf{D}) \mathbf{P}_{SCHED}}_{\mathbf{F}_2} \right] \tilde{\mathbf{u}} + \left[\underbrace{2\mathbf{c}_{r2} \Phi_i \cdot (\mathbf{c}_{r2} \Psi_i + \mathbf{D}) \mathbf{x}(k)}_{\mathbf{F}_1} \quad \underbrace{-2(\mathbf{c}_{r2} \Psi_i + \mathbf{D}) SoC_{ref}}_{\mathbf{F}_2} \right] \tilde{\mathbf{u}} \quad \text{Eq. 4.54}$$

where \mathbf{F}_1 and \mathbf{F}_2 matrices contain information of future outputs predictions. By doing:

$$\mathbf{f}^T = \mathbf{F}_1 \cdot \mathbf{x}(k) + \mathbf{F}_2 \cdot \tilde{\mathbf{y}}_{ref}(k) \quad \text{Eq. 4.55}$$

is obtained the vector \mathbf{f}^T , which is compatible with the formulation of the optimization subroutine used to solve the QP problem (see Eq. 4.47).

Moreover, coupling the $\tilde{\mathbf{u}}^T (\mathbf{c}_r \Psi_i + \mathbf{D}) \tilde{\mathbf{u}}$ terms gives the *Hessian matrix*, \mathbf{H} ,

$$\tilde{\mathbf{u}}^T \underbrace{\begin{bmatrix} \mathbf{c}_{r1} \Psi_i + \mathbf{D} \\ \mathbf{c}_{r2} \Psi_i + \mathbf{D} \end{bmatrix}}_{\mathbf{H}} \tilde{\mathbf{u}} \quad \text{Eq. 4.56}$$

which is part of Eq. 4.47 as well as is \mathbf{f}^T . Given \mathbf{H} , \mathbf{F}_1 and \mathbf{F}_2 are independent of both the current state $\mathbf{x}(k)$ and the reference output trajectory $\tilde{\mathbf{y}}_{ref}(k)$, they can be defined off-line. This

means that they can be computed once and stored to be invoked when necessary to obtain new optimal solutions.

With this unconstrained formulation, optimal solutions can be obtained at every instant over a given simulation time. For that, a closed loop including an MPC/QP controller composed by prediction and optimization stages like the one depicted in Fig. 4.7 can be used to control the hybrid plant. In that case, the optimization subroutine must receive at every timeslot the input (\mathbf{H}, \mathbf{f}) with the prediction information. As said \mathbf{H} is constant whereas \mathbf{f} value is updated at every calculation step. Future references in Fig. 4.7 and current state measurements appear

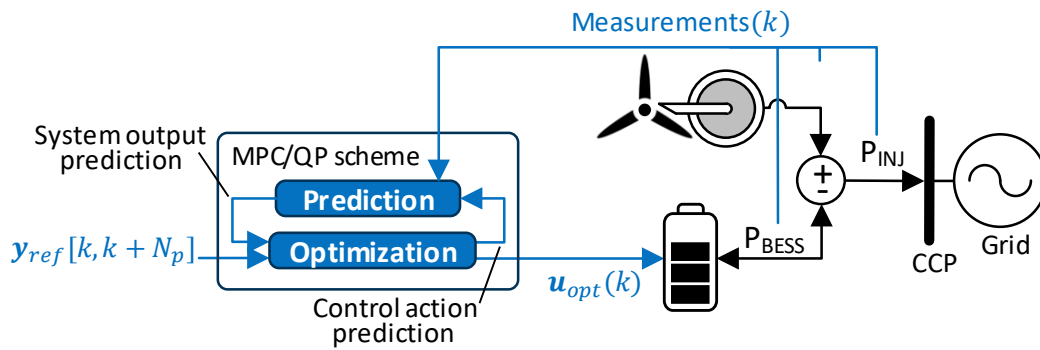


Fig. 4.7 MPC/QP strategy structure.

in the controller input. Furthermore, the first element from the control action optimal sequence is sent to the BESS so as to indirectly control the power transferred to the grid P_{INJ} .

Now that the unconstrained version of the control strategy has been detailed, the constrained case, this is, calculations for filling \mathbf{A}_{ineq} and \mathbf{b}_{ineq} at every calculation instant are the subject of the next section.

4.2.4.2 Constraints handling

This last part deals with the constraint's inclusion in the optimization problem. Three main kinds of operational constraints can be classified as:

- Trajectory constraints (on the outputs or states): supposing that the future outputs trajectory has lower and upper limits \mathbf{y}_c^{min} and \mathbf{y}_c^{max} , these constraints can be represented in the form:

$$\mathbf{y}_c^{min} \leq \mathbf{y}_c(k+i) \leq \mathbf{y}_c^{max} \quad \text{Eq. 4.57}$$

where \mathbf{y}_c contains the outputs with constraints. In the context of predictive control, those limits must be defined for all the instants in the moving time window $[k, k + N_p]$.

Moreover, Eq. 4.57 can be expressed with two lower than-like inequalities as:

$$\begin{aligned} \mathbf{y}_c(k+i) &\leq \mathbf{y}_c^{max} \\ -\mathbf{y}_c(k+i) &\leq -\mathbf{y}_c^{min} \end{aligned} \quad \text{Eq. 4.58}$$

By applying the definition of output trajectory of Eq. 4.37, Eq. 4.58 becomes:

$$\begin{aligned} \mathbf{C}_c \Phi_i \mathbf{x}(k) + (\mathbf{C}_c \Psi_i + \mathbf{D}) \tilde{\mathbf{u}} &\leq \tilde{\mathbf{y}}_c^{max} \\ -(\mathbf{C}_c \Phi_i \mathbf{x}(k) + (\mathbf{C}_c \Psi_i + \mathbf{D}) \tilde{\mathbf{u}}) &\leq -\tilde{\mathbf{y}}_c^{min} \end{aligned} \quad \text{Eq. 4.59}$$

where $\mathbf{C}_c \in \mathbb{R}^{N_p n_c \times N_p n_c}$ contains the variables with constraints and n_c is the problem's number of variables with trajectory constraints. This can be written in the form:

$$\underbrace{\begin{pmatrix} +\mathbf{C}_c \Psi_1 + \mathbf{D} \Pi_1^{n_u, N_p} \\ -\mathbf{C}_c \Psi_1 - \mathbf{D} \Pi_1^{n_u, N_p} \\ \vdots \\ +\mathbf{C}_c \Psi_{N_p} + \mathbf{D} \Pi_{N_p}^{n_u, N_p} \\ -\mathbf{C}_c \Psi_{N_p} - \mathbf{D} \Pi_{N_p}^{n_u, N_p} \end{pmatrix}}_{\mathbf{A}_{ineq}^{traj} \in \mathbb{R}^{N_p n_c \times N_p n_c}} \tilde{\mathbf{u}} \leq \underbrace{\begin{pmatrix} +\mathbf{y}_c^{max} \\ -\mathbf{y}_c^{min} \\ \vdots \\ +\mathbf{y}_c^{max} \\ -\mathbf{y}_c^{min} \end{pmatrix}}_{\mathbf{b}_{ineq}^{traj} \in \mathbb{R}^{N_p n_c}} + \underbrace{\begin{pmatrix} -\mathbf{C}_c \Phi_1 \\ +\mathbf{C}_c \Phi_1 \\ \vdots \\ -\mathbf{C}_c \Phi_{N_p} \\ +\mathbf{C}_c \Phi_{N_p} \end{pmatrix}}_{N_p n_c \times n} \mathbf{x}(k) \quad \text{Eq. 4.60}$$

where \mathbf{A}_{ineq}^{traj} and \mathbf{b}_{ineq}^{traj} contain the information of the problem's trajectory constraints.

In the case of the hybrid plant management, the matrix $+\mathbf{C}_c$ and $-\mathbf{C}_c$ are given by:

$$\begin{aligned} +\mathbf{C}_c &= \begin{bmatrix} \mathbf{c}_{c1} \\ \mathbf{c}_{c2} \end{bmatrix} = \begin{bmatrix} i^* \\ SoC \end{bmatrix} \\ -\mathbf{C}_c &= [-\mathbf{c}_{c2}] = [-SoC] \end{aligned} \quad \text{Eq. 4.61}$$

And the references are:

$$\begin{aligned} +\mathbf{y}_c^{max} &= \begin{bmatrix} P_{INJ}^{max} / v_{BESS} \\ SoC^{max} \end{bmatrix} \\ -\mathbf{y}_c^{min} &= [-SoC^{min}] \end{aligned} \quad \text{Eq. 4.62}$$

where P_{INJ}^{max} is equal to $P_{upper\ limit}$, calculated as stated in Eq. 4.2. Also, in the hybrid plant problem $n_c=3$ as the variables with trajectory constraints are i^* , SoC and $-SoC$.

- Constraints on the amplitude of the decision variable: let \mathbf{u}^{min} and \mathbf{u}^{max} denote control amplitude lower and upper bounds due to operational conditions. In that case, the constraints are represented in the form given by

$$\mathbf{u}^{min} \leq \mathbf{u}(k+i-1) \leq \mathbf{u}^{max} \quad \text{Eq. 4.63}$$

Again, the constraints can be separated into the two inequalities:

$$\begin{aligned} \mathbf{u}(k+i-1) &\leq \mathbf{u}^{max} \\ -\mathbf{u}(k+i-1) &\leq -\mathbf{u}^{min} \end{aligned} \quad \text{Eq. 4.64}$$

which can also be written as

$$\begin{pmatrix} \mathbb{I}_{N_p n_u} \\ -\mathbb{I}_{N_p n_u} \end{pmatrix} \tilde{\mathbf{u}} \leq \begin{pmatrix} \tilde{\mathbf{u}}^{max} \\ -\tilde{\mathbf{u}}^{min} \end{pmatrix} \quad \text{Eq. 4.65}$$

or

$$\underbrace{\begin{pmatrix} +\mathbf{\Pi}_1^{n_u, N_p} \\ \vdots \\ +\mathbf{\Pi}_{i-1}^{n_u, N_p} \\ +\mathbf{\Pi}_i^{n_u, N_p} \\ -\mathbf{\Pi}_1^{n_u, N_p} \\ \vdots \\ -\mathbf{\Pi}_{i-1}^{n_u, N_p} \\ -\mathbf{\Pi}_i^{n_u, N_p} \end{pmatrix}}_{\mathbf{A}_{ineq}^{ampl} \in \mathbb{R}^{2N_p \times N_p}} \tilde{\mathbf{u}} \leq \underbrace{\begin{pmatrix} \mathbf{u}^{max} \\ \vdots \\ \mathbf{u}^{max} \\ \mathbf{u}^{max} \\ -\mathbf{u}^{min} \\ \vdots \\ -\mathbf{u}^{min} \\ -\mathbf{u}^{min} \end{pmatrix}}_{\mathbf{b}_{ineq}^{ampl} \in \mathbb{R}^{2N_p}} \quad \text{Eq. 4.66}$$

- Constraints on rate of change of the decision variable: with δ_{min} and δ_{max} as bounds, the limitation of the incremental variation of the control actions, is expressed as

$$\delta_{min} \leq \mathbf{u}(k) - \mathbf{u}(k-1) \leq \delta_{max} \quad \text{Eq. 4.67}$$

Which can be rewritten as the inequalities:

$$\begin{aligned} \mathbf{u}(k) - \mathbf{u}(k-1) &\leq \delta_{max} \\ -(\mathbf{u}(k) - \mathbf{u}(k-1)) &\leq -\delta_{min} \end{aligned} \quad \text{Eq. 4.68}$$

Putting Eq. 4.68 into a more detailed form, gives:

$$\underbrace{\begin{pmatrix} \Delta \\ -\Delta \end{pmatrix}}_{\mathbf{A}_{ineq}^{rate} \in \mathbb{R}^{4N_p \times N_p}} \tilde{\mathbf{u}} \leq \underbrace{\begin{pmatrix} \delta_{max} \\ \delta_{max} \\ \vdots \\ \delta_{max} \\ -\delta_{min} \\ -\delta_{min} \\ \vdots \\ -\delta_{min} \end{pmatrix}}_{\mathbf{b}_{ineq}^{rate} \in \mathbb{R}^{4N_p}} + \begin{pmatrix} \mathbb{I} \\ \mathbb{O} \\ \vdots \\ \mathbb{O} \\ -\mathbb{I} \\ \mathbb{O} \\ \vdots \\ \mathbb{O} \end{pmatrix} \mathbf{u}(k-1) \quad \text{Eq. 4.69}$$

where \mathbf{A}_{ineq}^{rate} is formed by piling $\Delta \in \mathbb{R}^{N_p n_u \times N_p n_u}$ over $-\Delta$. At the beginning of its calculation the matrix Δ is filled with zeros. Then, as i increases between 1 and N_p , the i -th row of Δ is replaced by the difference $\mathbf{\Pi}_k^{n_u, N_p} - \mathbf{\Pi}_{k-1}^{n_u, N_p}$, as:

$$\Delta = \begin{pmatrix} \mathbf{\Pi}_1^{n_u, N_p} \\ \mathbf{\Pi}_2^{n_u, N_p} - \mathbf{\Pi}_1^{n_u, N_p} \\ \vdots \\ \mathbf{\Pi}_{N_p}^{n_u, N_p} - \mathbf{\Pi}_{N_p-1}^{n_u, N_p} \end{pmatrix} \quad \text{Eq. 4.70}$$

In the hybrid plant EMS, the bounds for the incremental variation of the battery current (δ_{min} and δ_{max}) are calculated from the power variation speed limits and the voltage of the BESS.

The strategy proposed uses a control action variable considering both the ESS charge and discharge, rather than separated control action variables (e.g. u_{charge} and $u_{discharge}$). This means that the strategy cannot integrate individual change rate constraints for charging and discharging, therefore a simplification of the variation speed limits stipulated in the HPP contractual operation requirements specified in Chapter 1, is required. The simplification consists in assuming the same minimal and maximum times for upward and downward variations in dP_{INJ}/dt . The definition of the limits for the constraints described is left for Chapter 5 where the strategy is application is dealt with.

Finally, the three types of constraints explained above are piled up to form \mathbf{A}_{ineq} and \mathbf{b}_{ineq} according to the *quadprog* solver form (see Eq. 4.47), giving:

$$\underbrace{\begin{pmatrix} \mathbf{A}_{ineq}^{traj} \\ \mathbf{A}_{ineq}^{ampl} \\ \mathbf{A}_{ineq}^{rate} \end{pmatrix}}_{\mathbf{A}_{ineq}} \tilde{\mathbf{u}} \leq \underbrace{\begin{pmatrix} \mathbf{b}_{ineq}^{traj} \\ \mathbf{b}_{ineq}^{ampl} \\ \mathbf{b}_{ineq}^{rate} \end{pmatrix}}_{\mathbf{b}_{ineq}} \quad \text{Eq. 4.71}$$

where $\mathbf{A}_{ineq} \in \mathbb{R}^{N_p(n_c+6) \times N_p}$ can be computed off-line, whereas $\mathbf{b}_{ineq} \in \mathbb{R}^{N_p(n_c+6)}$ changes dynamically as it depends on $\mathbf{x}(k)$ and $\mathbf{u}(k-1)$.

In this manner, the solutions to the hybrid power plant energy management constrained problem can be found through using the input $(\mathbf{H}, \mathbf{f}, \mathbf{A}_{ineq}, \mathbf{b}_{ineq})$ when calling the subroutine that computes $\tilde{\mathbf{u}}_{opt}$.

The publications [167-171], dealing with to the use of MPC/QP strategies for the management of the hybrid power plant where produced during the thesis work. Other publications that were co-published in the context of the PhD are [172-174].

4.3 Chapter conclusions

Chapter 4 is devoted to the control and optimization strategy on which the EMS for the hybrid power plant is based. The optimization problem definition was the first of three steps performed for the control strategy design. This step consisted in the identification of problem objectives, hybrid plant model design variables and operation constraints.

The problem objectives are strictly related to the hybrid plant operating conditions. Those conditions are part of a contractual agreement among the SO and the energy producer. A penalty system punishes the excursions outside the injection band built around the day-ahead engaged generation plan. For this, the EMS' task is to ensure the transfer of as much power as possible towards the distribution grid of the island while considering the ESS lifetime protection and the injection band respect.

While the aims of the EMS are the maximization of the power plant revenue and the respect of the technical conditions, optimal use of the BESS is the key to achieve that. The BESS state-space representation, working with discrete systems at a timestep of 1 second, is the backbone of the power plant modeling. The BESS current is considered as input to the power plant model, and as the main assumption, the voltage is considered linear which implies that voltage small variations can be despised.

In the control strategy, the regulated variables are the BESS filtered current and state-of-charge, two of the system states, whereas the constrained ones are the decision variable and the state-of-charge. As the representation is an LTI representation and the constraints are linear, the selection of an appropriate optimization method was focused on linear approaches.

Optimization problem types were classified into linear, nonlinear, geometric, and quadratic problems. The concepts of decision variables, cost function, optimal solution and convexity were discussed along with a short description of the problem types. In this manner, Model Predictive Control schemes were introduced, that are characterized by being independent of any particular optimization method. Another important feature of MPC is that it implements a feedback control scheme over a finite horizon, where the closed-loop performance is usually better as the horizon size tends to the infinite.

Some advantages of MPC are highlighted, for example, it allows a relatively simple design framework, enables the systematic handling of constraints, and permits generation forecasts in the optimization problem. Even though MPC is not in itself an optimization method, it can be coupled with mathematical optimization-based methods.

A quadratic cost function was proposed based on the problem definition and the description of the predictive control law. The instant wind power generation is an input for the controller.

A predictive algorithm was developed on the assumption that the wind production is the same at future instants inside the prediction horizon, which is probably the strongest of the assumptions done. At the same time, with the aim of reducing the amount of on-line calculations, a prediction strategy in which certain calculations can be done off-line and stored for their later use is adapted to the problem. According to the philosophy of predictive control, the optimal solution issued by the optimizer is a trajectory of optimal control actions of which only the first element is sent to the system.

Weighting parameters allow adapting the EMS controller to the user's needs by giving more importance to certain control objectives than others. Also, the application of positive or negative offsets on the references set-points was established as a way to introduce modifications in the strategy. This capacity to adjust the relative levels of satisfaction of the control objectives added to the fact that the strategy does solve at every calculation instant a constrained, multi-objective optimal problem considering the wind production forecasts, are the aspects making the present EMS strategy remarkably better than classical PID or heuristic decision-making approaches.

Rather than minimizing the cost function, the optimal solution found through this MPC/QP strategy searches the operation point located on the vortex of the parabola formed by adding the two quadratic objectives present in the cost function. After calculating the matrices and vectors allowing to connect the prediction stage with the QP subroutine *quadprog*, in the last section of the Chapter, the problem constraints are put in a form compatible with the selected solver.

(This page is intentionally left blank)

CHAPTER

5

Control strategy validation under Matlab/Simulink

Summary

5.1 Introduction	138
5.2 Energy management of the HPP with respect to a 24h commitment profile	139
5.2.1 Admissible thresholds, performance indicators and commitment profiles	139
5.2.2 Economic optimization of the HPP operation with respect to a 24 hours commitment profile.....	147
5.2.2.1 Profit maximization strategy 1	147
5.2.2.2 Profit maximization strategy 2	158
5.2.3 Technical optimization of the HPP operation.....	161
5.2.3.1 Profit maximization strategy 1	161
5.2.4 Impact of Q_u and N_p on the results	166
5.2.4.1 Impact of Q_u	166
5.2.4.2 Impact of N_p	168
5.3 Energy management of the HPP during a month	170
5.3.1 Rule-based strategy description.....	170
5.3.2 Simulation results	171
5.4 Chapter conclusions	174

Chapter overview

This Chapter presents the validation of the proposed control and optimization strategy through simulations conducted in Matlab/Simulink. A rule-based algorithm is employed for comparison.

5.1 Introduction

The optimization problem described in this thesis consists of deciding on the storage system usage (i.e. which part of the production is used to charge the BESS or how much power is to be discharged) as the wind turbines output instantly varies, so as to inject power into the island grid fulfilling a committed generation schedule. As outlined in Chapter 1, the commitment profile is generated based on day-ahead forecast data. Also, the disrespect of the tolerated injection region may lead to commitment failures (triggered by injection band overtakes lasting 60 seconds) that are associated with economic penalties. Fig. 5.1 illustrates the commitment schedule (P_{SCHED}) and power injection (P_{INJ}) signals, as well as the tolerated injection region, determined by upper and lower limits $P_{SCHED} + tolerance$ and $P_{SCHED} - tolerance$. The aim being the plant revenues maximization, an EMS is required to reduce the occurrence of commitment failures while considering the BESS lifespan.

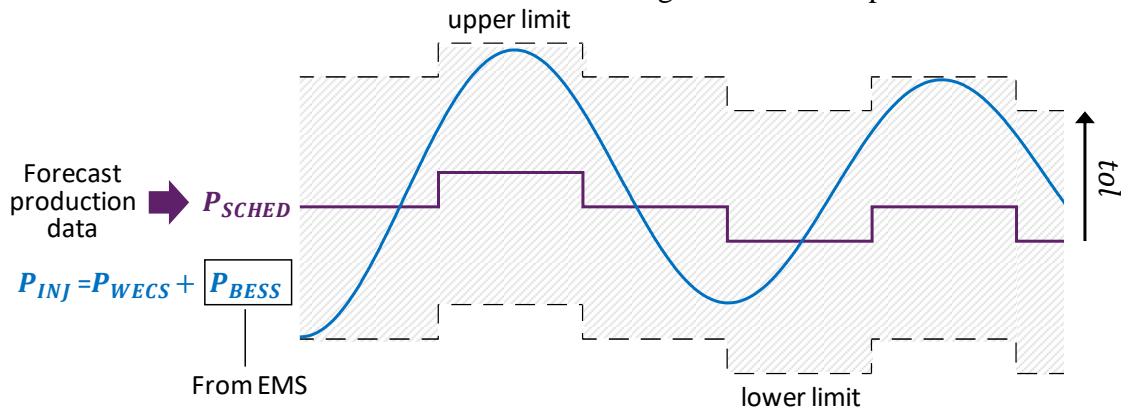


Fig. 5.1. Power injection tolerance region.

Fig. 5.2 sketches the setup implemented in Matlab/Simulink for testing the proposed energy management approach. The Simulink battery block is configured to represent the BESS (nonlinear model). It is remembered that the output of the optimization process are the N_p elements of the sequence of current control actions $\mathbf{u}(k), \mathbf{u}(k+1), \dots, \mathbf{u}(k+N_p-2), \mathbf{u}(k+N_p-1)$ from which only the first element $\mathbf{u}(k)$ is applied. As represented in the figure, at every calculation step k the controller receives the information of the instantaneous wind-generated power $P_{WECS}(k)$ along with the elements $k+1, k+2, \dots, k+N_p$ of the vectors of future references P_{SCHED} and \mathbf{SoC}_{ref} .

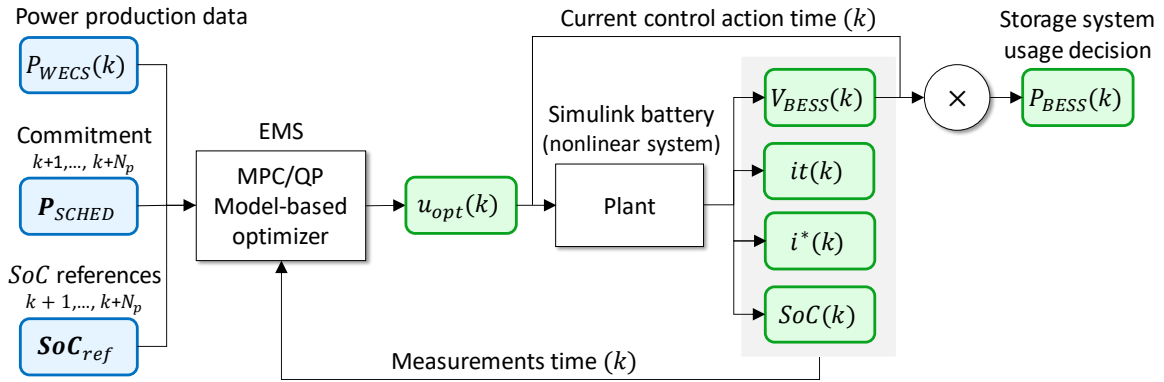


Fig. 5.2. Diagram of the setup utilized for Matlab/Simulink simulation.

The first part of this Chapter deals with the definition of the problem inputs, thresholds and performance indicators. Then is tackled the validation of the proposed control and optimization algorithm with the system connected to an infinite bus in Matlab/Simulink. Several runs of the algorithm employing different management strategies allow testing the approach. The aim of those simulations is determining the approach's most adequate parameters set and management strategy to be implemented in PowerFactory environment in part Chapter 6.

5.2 Energy management of the HPP with respect to a 24h commitment profile

This section presents the definition the optimization problem input signals, variables thresholds and performance indicators to be employed in the Matlab/Simulink tests of the strategy. Those tests are the subject of the subsequent sections.

5.2.1 Admissible thresholds, performance indicators and commitment profiles

Next are defined the optimization problem inputs and variables limitations, as well as the indicators proposed to allow the comparison of results.

Constraints limitations

Eq. 5.1 presents the quadratic cost function that was defined in Chapter 4 to optimize the HPP operation.

$$\Gamma(k) = \sum_{i=1}^{N_p} \left\{ \lambda_1 \|P_{INJ} - P_{SCHED}\|^2 + \lambda_2 \|SoC - SoC_{ref}\|^2 + \tilde{\mathbf{u}}^T \mathbf{Q}_u \tilde{\mathbf{u}} \right\} \quad \text{Eq. 5.1}$$

The first and second terms in Eq. 5.1 are linked to the minimization of the errors between predicted outputs and set-point trajectories for P_{INJ} and SoC , respectively, while the third term reflects the consideration given to the size of the control action in making $\Gamma(k)$ as small as

possible. It is also recalled that λ_1, λ_2 and \mathbf{Q}_u are tuning parameters for adding relative weights to the three terms. It is reminded that the role of the optimizer is finding the sequence \mathbf{u} of N_p elements minimizing Γ .

Such cost function is subject to a set of constraints whose limits are discussed below together with the plant limits. To start with, the power transferred to the grid is delimited by the HPP size, or:

$$0 \leq P_{INJ} \leq P_{MAX} + P_{BESS_{max_disch}} \quad \text{Eq. 5.2}$$

where the limits represent the following cases in which:

- no power is delivered by the wind turbines nor discharged from the BESS, and
- the wind turbines deliver nominal power while the storage system is discharged at maximum discharge current.

Besides, the plant model limits the state-of-charge variable to the range:

$$20 \% \leq SoC \leq 80 \% \quad \text{Eq. 5.3}$$

These limitations are saturations of the controlled hybrid system.

In more traditional control strategies using simple saturation, if a variable exceeds a limit the limit value is implemented, and no consideration is given to the impact of the current control action over the future performance of the algorithm. In contrast, MPC algorithms including proper systematic knowledge of the constraints within the optimization, propose trajectories satisfying the constraints and can improve the closed-loop performance where constraints are active [160].

Below is the definition of the numerical values for those constraints:

- Maximal power injection: as explained in Chapter 4, the power injection is constrained with a limit equal to the upper band boundary. With this, the algorithm will not consider possible solutions that drive the power injection above the mentioned boundary in the search for optimal solutions. In line with this, P_{INJ}^{max} , the upper limit for the power transfer is computed according to the evolution of the commitment profile, as follows:

$$P_{INJ}^{max}(k) = P_{SCHED}(k) + tolerance \quad \text{Eq. 5.4}$$

where the tolerance is of 2 MW (25 % of P_{MAX}).

This constraint is implemented by means of the current i^* :

$$i^*(k) \leq \frac{P_{SCHED}(k) + tolerance}{v_{BESS}(k)} \quad \text{Eq. 5.5}$$

- Rate of change of power injected: according to the contractual specifications of the HPP operation, the speed at which P_{INJ} varies (in MW/s) must be limited, so that: 1), the time it takes passing from 0 to P_{MAX} is in the range [30 s – 5 min], and 2), the time it takes passing from P_{MAX} to 0 is in the range [1 min – 10 min]. However, as it was explained in the last part of section 4.2.4.2, one single range is applied for the increasing and decreasing changes of P_{INJ} . The range retained is [1 min – 5 min], that is a mix of the original time ranges. Also, as the constrained variable is the controller model input, $u = i_{BESS}$, the limits are expressed in terms of current:

$$\begin{aligned} \text{Lower limit} & \quad \frac{[0 - (\mathbf{P}_{SCHED}(k) + tolerance)]/300}{v_{BESS}(k)} \left[\frac{W/s}{V} \right] \\ \text{Upper limit} & \quad \frac{[(\mathbf{P}_{SCHED}(k) + tolerance) - 0]/60}{v_{BESS}(k)} \left[\frac{W/s}{V} \right] \end{aligned} \quad \text{Eq. 5.6}$$

where the use of absolute value indicates that the equation is valid for both the passing from P_{MAX} to 0 and vice versa. As noted, the lower limit is associated to the larger time

$$-\frac{1}{300} \cdot \frac{\mathbf{P}_{SCHED}(k) + tol}{v_{BESS}(k)} \leq \frac{du(k)}{dt} \leq \frac{1}{60} \cdot \frac{\mathbf{P}_{SCHED}(k) + tol}{v_{BESS}(k)} \quad \text{Eq. 5.7}$$

in the range (5 minutes or 300 seconds), whereas the upper limit is related to the case where the passing takes place in 1 minute (60 s). The reason for this is a shorter passing time implies a steepest slope, or a bigger rate of change limit. Putting the limits for the rate of change of vi_{BESS} in inequality form, gives:

where the bounds are in $[W/V \cdot s]$ or $[A/s]$.

- State-of-charge: as mentioned, the *SoC* is constrained as follows:

$$20 \% \leq SoC \leq 80 \% \quad \text{Eq. 5.8}$$

This range corresponds to the storage solution manufacturer recommendation for achieving 20 years design life [175].

- ESS maximum charge/discharge current: considering the sign convention defined for BESS charge and discharge, the maximum continuous recharge and discharge currents are 3280 and -6400 Amperes, respectively [175]. Hence, the battery current is constrained as

$$-6400 A \leq u \leq 3280 A \quad \text{Eq. 5.9}$$

Table 5.1 recapitulates the constraints limits explained.

Performance indicators

Table 5.1. Limitations assigned to the constraints.

Parameter	Description	Unit	Value
i^{*max}	Filtered current upper bound	A	$\frac{P_{SCHED}(k) + tol}{v_{BESS}(k)}$
u^{min}	Control amplitude lower bound	A	-6400
u^{max}	Control amplitude upper bound	A	3280
SoC^{min}	State-of-charge upper limitation	%	20
SoC^{max}	State-of-charge lower limitation	%	80
$\frac{du^{min}}{dt}$	Control actions rate of change lower bound	[A/s]	$-\frac{1}{300} \cdot \frac{P_{SCHED}(k) + tol}{v_{BESS}(k)}$
$\frac{du^{max}}{dt}$	Control actions rate of change upper bound	[A/s]	$\frac{1}{60} \cdot \frac{P_{SCHED}(k) + tol}{v_{BESS}(k)}$

To solve the issue of handling the power produced during strong wind periods and the energy storage system is not available to be charged, curtailment of wind power is assumed to happen if the production is above the band upper limit with the BESS fully charged.

Hence, whenever $P_{WECS} > P_{SCHED} + tolerance$ with $SoC = 80\%$, the lost power due to curtailment is calculated as

$$\text{(if } P_{WECS} > \text{upper limit and } SoC \text{ is max): } P_{curt} = P_{WECS} - (P_{SCHED} + tol) \quad \text{Eq. 5.10}$$

Then, the percentage of the power produced that was curtailed is obtained from

$$P_{curt} \% = 100 \cdot \frac{P_{curt}}{P_{WECS}} \quad \text{Eq. 5.11}$$

Meanwhile, the commitment failures are calculated as the percentage of the time during which the penalty condition was active (overtakes of the injection band upper threshold lasting 60 seconds with $SoC = 80\%$ are not considered in this calculation but in P_{curt}), or

$$CF \% = 100 \cdot \frac{\text{Number of minutes with penalty triggered}}{\text{Total simulation time in minutes}} \quad \text{Eq. 5.12}$$

Also, whenever a commitment failure has been triggered, the unbilled power is computed as

$$\text{(if } CF = ON): P_{unbilled} = P_{WECS} + P_{BESS} \quad \text{Eq. 5.13}$$

This means that the total remunerated power injected is given by

$$P_{INJ} = P_{WECS} + P_{BESS} - P_{curt} - P_{unbilled} \quad \text{Eq. 5.14}$$

The energy injected (E_{INJ} in MWh) is computed from the injected power by considering the time. Finally, the percent of the production non-remunerated due to commitment failures is obtained from

$$P_{unbilled} \% = 100 \cdot \frac{P_{unbilled}}{P_{WECS}} \quad \text{Eq. 5.15}$$

Also, to keep track of the storage system usage, the account of the partial charging and discharging cycles is kept:

$$\begin{aligned} chg &= chg + \Delta SoC, \text{ if } \Delta SoC > 0 \\ dchg &= dchg + \Delta SoC, \text{ if } \Delta SoC < 0 \end{aligned} \quad \text{Eq. 5.16}$$

with $\Delta SoC = SoC(k) - SoC(k - 1)$. Then, the number of cycles of the storage system is given by:

$$BESS \text{ cycles} = (chg + dchg)/120 \quad \text{Eq. 5.17}$$

where a maximal depth-of-discharge (DoD) of 60 % is considered. The BESS cycles counting method here employed is based on the approach introduced in [176].

The error of the injected power is given by the mean of the absolute value of the relative error with respect to the reference P_{SCHED} :

$$P_{INJ} \text{ error \%} = mean \left| 100 \cdot \frac{P_{INJ} - P_{SCHED}}{P_{SCHED}} \right| \quad \text{Eq. 5.18}$$

Finally, the absolute value of the state-of-charge relative error is computed as

$$SoC \text{ error \%} = mean \left| 100 \cdot \frac{SoC - SoC_{ref}}{SoC_{ref}} \right| \quad \text{Eq. 5.19}$$

The above-described indicators P_{curt} , $P_{not \ billed}$, E_{INJ} , CF , $BESS \text{ cycles}$, $P_{INJ} \text{ error}$ and $SoC \text{ error}$ will be used as comparison criteria of the simulation results obtained from the application of the proposed algorithm with respect to different strategies.

Next, the power production data and generation of the day ahead power commitment are discussed. The profile with the power production information (P_{WECS}) is obtained from real wind data, whereas the commitment data is generated by applying a simple stochastic approach.

Presentation of the production data and commitment profiles generation

The 27 days of wind measurements shown in Fig. 5.3.a were collected every minute using a measurement tower at Guadeloupe during February of 2016. The associated wind power profile is plotted in Fig. 5.3.b. The latter was generated by a WECS operator by applying the power curve of a 2 MW Gamesa G90 wind turbine. The total energy produced by the WECS

during that time period amounts to 1,817 GWh. According to the average of both the wind speeds and the productions obtained, these are classed as:

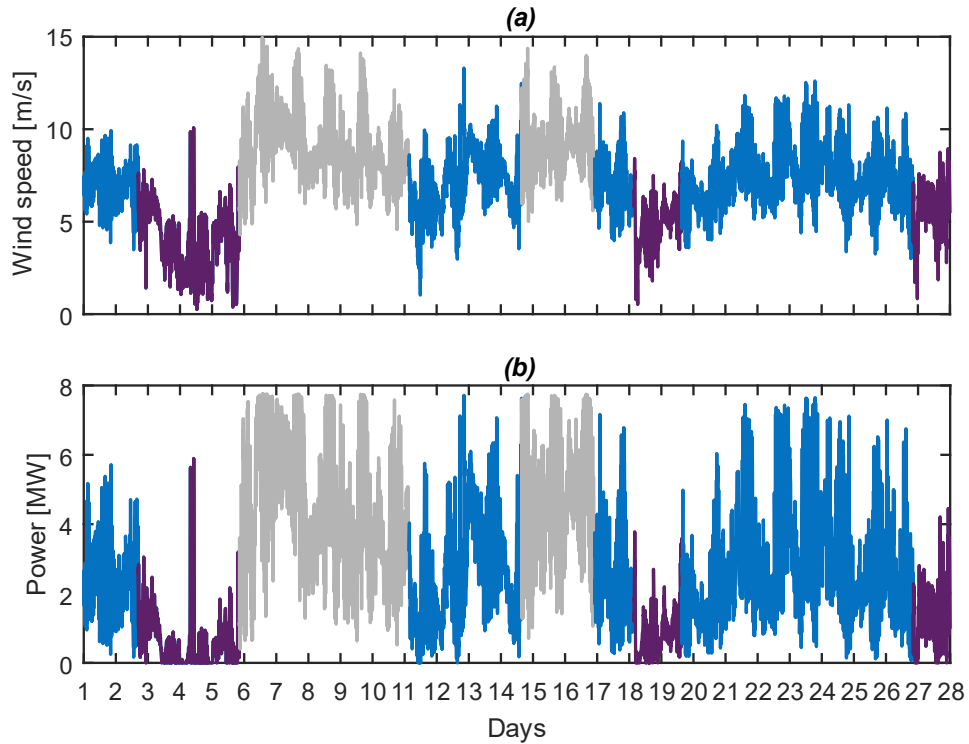


Fig. 5.3. (a) Wind measurements profile, and (b) associated power production profile.

- weak wind zones (displayed in Fig. 5.3 in violet). The average wind speeds and power productions are 4,8 m/s and 0,83 MW,
- medium wind zones (in blue), average speeds of 7.2 m/s and average productions of 2,50 MW, and
- strong wind zones (in gray), average speeds of 9,2 m/s and average productions of 4,71 MW.

It is reminded that at every timestep k , a sample of \mathbf{P}_{WECS} is provided to the energy management strategy. The prediction is made under the assumption that such sample, received at the beginning of the prediction window, will stay constant all through the instants $k + 1, k + 2, \dots, k + N_p$, which is one of the assumptions on which the algorithm is based.

The test of the energy management algorithm requires a firm injection commitment (\mathbf{P}_{SCHED}), associated with the production data. In the absence of wind speed or power prediction data (and having no access to a forecasting tool), a stochastic approach is followed to generate the day-ahead commitment profile. Under this approach, the commitment is obtained from the production data by adding a given amount of synthetic random error.

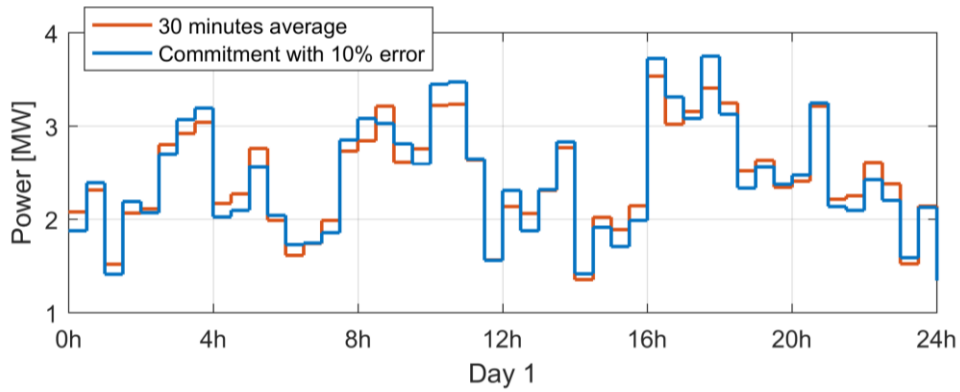


Fig. 5.4. Production average with 30 minutes steps and injection commitment with maximum 10 % error, day 1.

The proposed method requires inputs being received every second. For this, the production data is modified by replicating every measurement 59 times. Starting from the 30 minutes average of the production profile, random errors were added within the $\pm 10\%$ range, giving a first commitment profile shown in Fig. 5.4 for the first day.

Fig. 5.5 plots the error of this commitment profile with respect to the profile of averages.

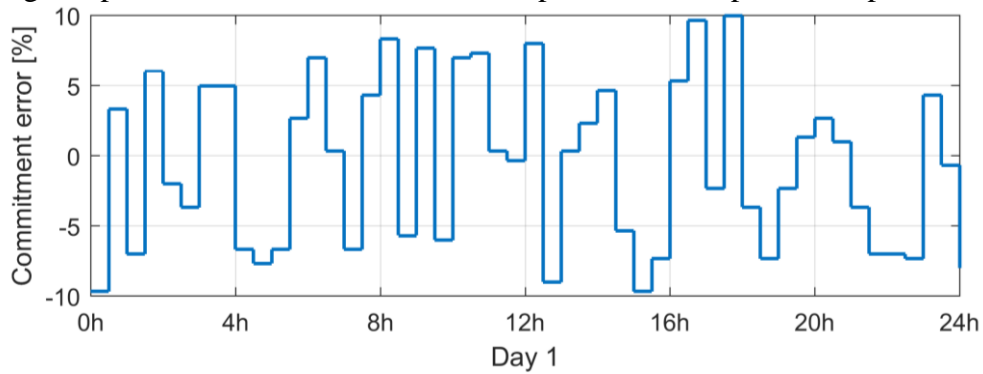


Fig. 5.5. Error of commitment profile.

Two more commitment profiles were created based on the latter by adding up to $\pm 20\%$ and $\pm 30\%$ errors, respectively. The resulting commitment profiles for the first simulation day are shown in Fig. 5.6. whereas in Fig. 5.7 are shown the commitments for the 27 days period.

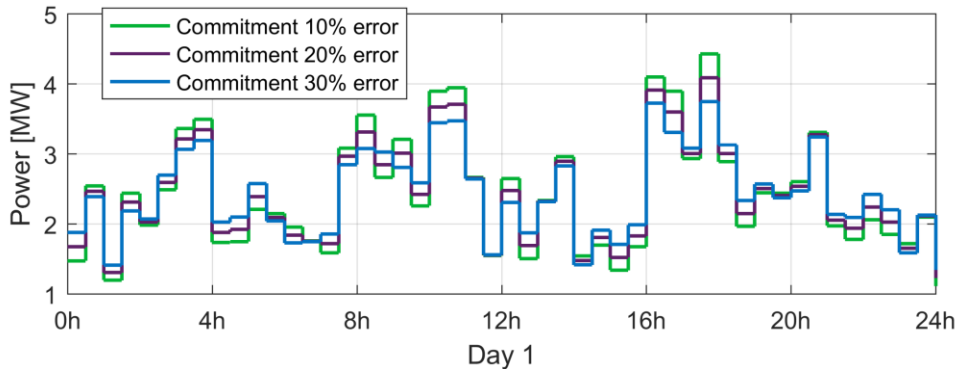


Fig. 5.6. Commitment profiles, first day.

In Fig. 5.8 is displayed the tolerated injection zone for the commitment profile with maximum 20 % error. The retained tolerance of $0.25P_{MAX}$ implies the injection band bounds are 2 MW up and down the committed profile P_{SCHED} .

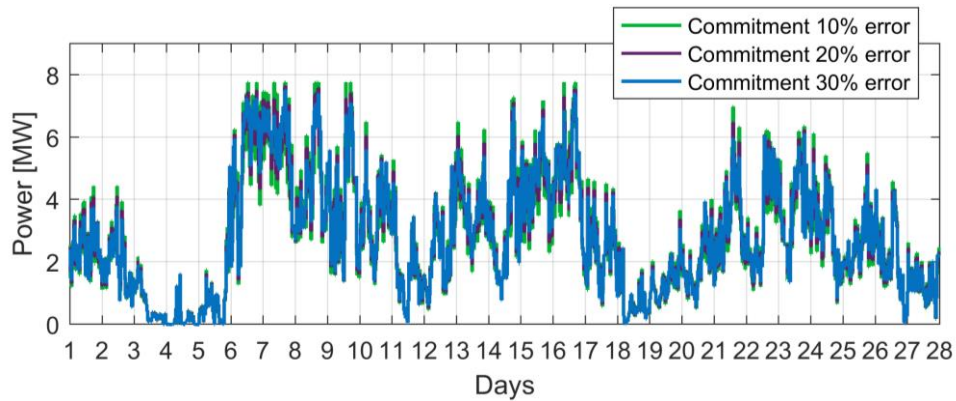


Fig. 5.7. Commitment profiles, 27 days period.

Along with the commitment signals P_{SCHED} defined, the production profile from Fig. 5.3.b is used as input to the simulations, representing the production (P_{WECS}).

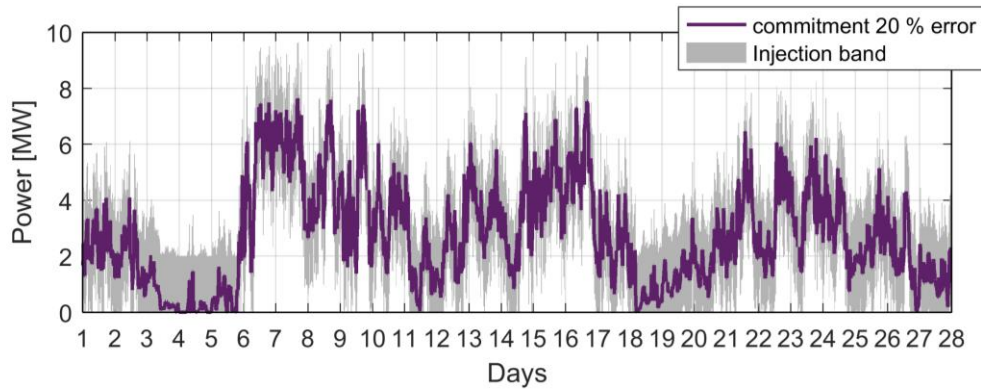


Fig. 5.8. Commitment with 20 % error and corresponding tolerated region, 27 days period.

A simulation sample time (T_s) of 1 second has been defined for the validation tests in Matlab/Simulink. On the other side, as the commitment failures are triggered by the disrespect of the injection band during 60 consecutive seconds, the parameter N_p is given values smaller than 1 minute.

Table 5.2. Simulation settings for tests in Matlab/Simulink.

Parameter	Description	Unit	Value
T_s	Simulation sample time	s	1
N_p	Optimization window length	s	10, 15, 30, 45
Tolerance	Injection band tolerance	MW	2
SoC_{init}	Initial state-of-charge	%	50

During a first part of the tests, N_p will be fixed at 10 seconds, implying that at every timestep the samples from the vector of future references corresponding to the 10 seconds following the current calculation instant are received by the controller. Later, N_p values of 15,

30 and 45 seconds will also be considered. All the simulations have been run with an initial state-of-charge of 50 %. Table 5.2 summarizes the values for these simulation settings. For their part, the constraints are defined as in Table 5.1.

5.2.2 Economic optimization of the HPP operation with respect to a 24 hours commitment profile

The aim of the proposed algorithm is to maximize the plant revenues via the minimization of the commitment failures. As more transferred energy means an increased plant turnover, the algorithm settings allowing to act on the amount of power injected to the main grid need to be adjusted. The settings influencing on the power injection are λ_1 , λ_2 , Q_u (see Eq. 5.1), and the positive or negative offset that can be added to the commitment P_{SCHED} (see Fig. 5.9).

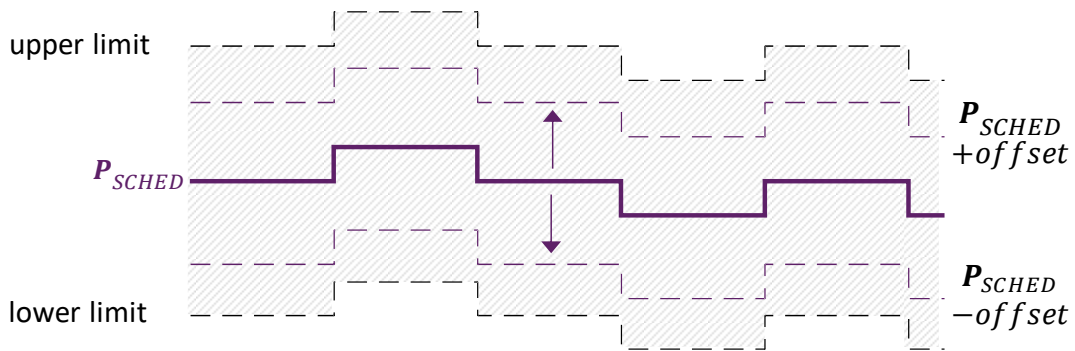


Fig. 5.9. The power injection set-point can be modified to increase (positive offset) or decrease (negative offset) the transfer of power to the grid.

Q_u is tuned by the user and can be assumed a fixed parameter. The influence of the control objectives weights and the vertical offset are next studied separately. Other than plant revenues maximization, other strategies may focus on maximizing the energy stored in the ESS, while the commitment failures are minimized. These strategies are explored below.

5.2.2.1 Profit maximization strategy 1

To start with, a strategy with greater weight attributed to the minimization of the tracking error of the power injection (or sub-cost of the optimization objective related to the injection) with respect to the minimization of the SoC tracking error (or SoC -related objective sub-cost), is considered (Eq. 5.1). Table 5.3 introduces the controller parameter values used in this first strategy. The sub-costs' weights λ_1 and λ_2 are non-negative and are defined to add up 100 ($\lambda_1 + \lambda_2 = 100$). Meanwhile, a value for Q_u is chosen to adjust the control effort so that the amplitude of P_{BESS} is equivalent to the difference $P_{SCHED} - P_{WECS}$, this is, the amount

power provided by or transferred to the storage system that allows holding the firm injection commitment.

As the variables in the cost function present different magnitudes, scale factors are

Table 5.3. Profit maximization strategy 1: algorithm parameters values.

Parameter	Description	Unit	Value
λ_1	Injection sub-cost	-	100, 50 and 0
SF_1	Injection sub-cost scale factor	A^2	$[(u^{min} - u^{max})/2]^2$
λ_2	SoC sub-cost	-	0, 50 and 100
SF_2	SoC sub-cost scale factor	$\%^2$	50^2
Q_u	Parameter for adjustment of the control effort	-	0,5
SF_u	Control effort scale factor	A^2	$[(u^{min} - u^{max})/2]^2$
<i>offset</i>	Vertical displacement of P_{SCHED}	MW	0
SoC_{ref}	SoC set-point level	%	50
N_p	Optimization window length	s	10

applied to $(i^* - P_{SCHED}/v_{BESS})^2$, $(SoC - SoC_{ref})^2$ and u^2 . These scale factors are typical values dividing the respective sub-costs. The injection sub-cost in the optimization problem is expressed in terms of the regulated variable i^* which is a current signal. Thus, the scale factors for the injection objective and control effort are similar.

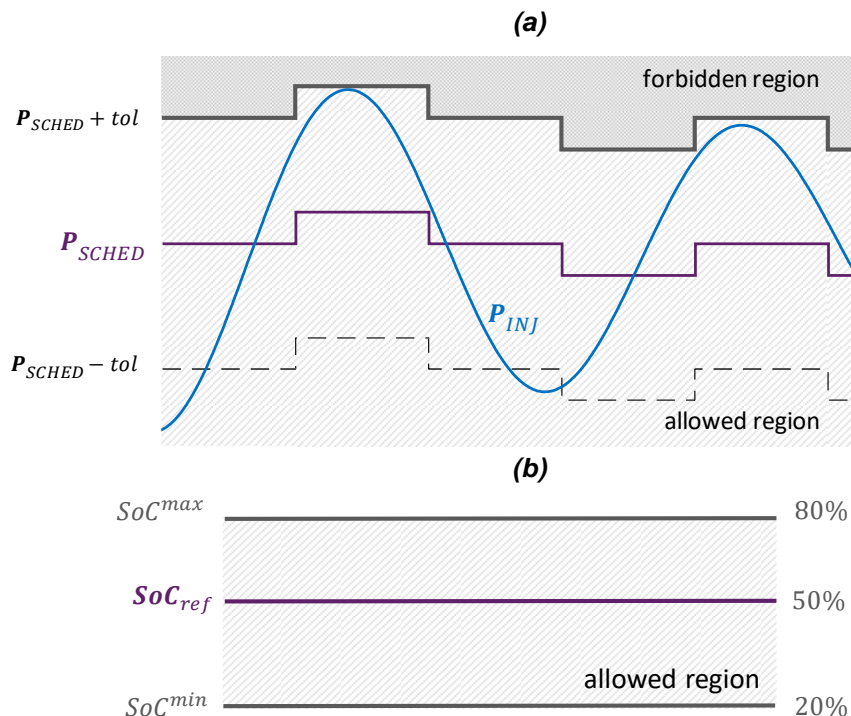


Fig. 5.10. Approach to act on the transfer of power through the weights λ_1 and λ_2 (Strategy 1). Set-points and allowed regions for the evolution of: (a) power injection, and (b) state-of-charge.

As explained in Chapter 4, the power transferred to the grid is limited so that injections beyond the band ceiling are avoided. In the current strategy, the commitment is kept in the middle of the band and the SoC reference is set at the 50 % level, as sketched in Fig. 5.10.a and Fig. 5.10.b. The capacity of the strategy to influence the power injection (and thus, the plant turnover) is to be established through simulation.

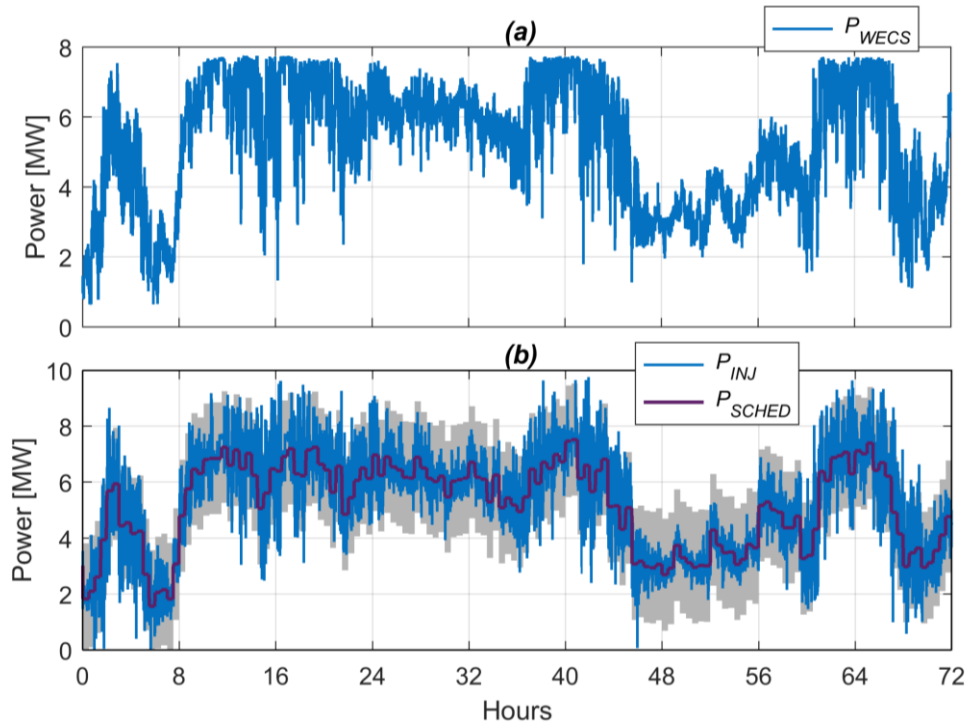


Fig. 5.11. Profit maximization strategy 1: (a) wind generated power data for 3 days period, and (b) resulting injection with $\lambda_1=100$, $\lambda_2=0$, initial SoC of 50 % and P_{SCHED} with maximum 10 % error.

A sample of the production profile shown in Fig. 5.3.b is selected for testing the capacity of the MPC/QP algorithm to maximize the injection. The sample is shown in Fig. 5.11.a and consists of the data for the 5th, 6th and 7th days of the dataset. The total production during those 3 days amounts 380,1 MW. A simulation run with the algorithm using the commitment profile with maximum 10 % error and $\lambda_1=100$, $\lambda_2=0$ (interest focused on the respect of the injection reference), results in the injection profile shown in Fig. 5.11.b. Several overtakes of the band (gray region in the figure) can be observed, some of which trigger commitment failures. Indeed, under the present conditions, during 1,4 % of the time commitment failures were active. Because of the penalties, 0,6 % of the total production was unbilled. Also, 0,006 % of the power produced was curtailed. As it was said earlier in the Chapter, curtailments happen when the production is above the upper band limit and the BESS is fully charged ($SoC=80\%$). A total of 376,9 MWh are injected into the grid and the injection error (absolute value of the relative error) totals 2,9 %.

As the algorithm controls the storage system power through current control actions, the dynamic behavior of the ESS power is similar to that of the calculated storage system current, as can be seen in Fig. 5.12.a and Fig. 5.12.b which present the evolutions of P_{BESS} and I_{BESS} during the 3-day period. In Fig. 5.12.a, the signal P_{BESS} is compared with $P_{SCHED} - P_{WECS}$, reference signal indicating what is the instant power the storage system must compensate for according to the commitment. As shown, the P_{BESS} follows closely its set-point. On several occasions the storage system's maximum discharge capacity is reached, as indicated by the saturation in the positive side of both the power and current plots. It is reminded that the maximum discharge current is equal to 3,28 kA whereas the storage system maximum charge

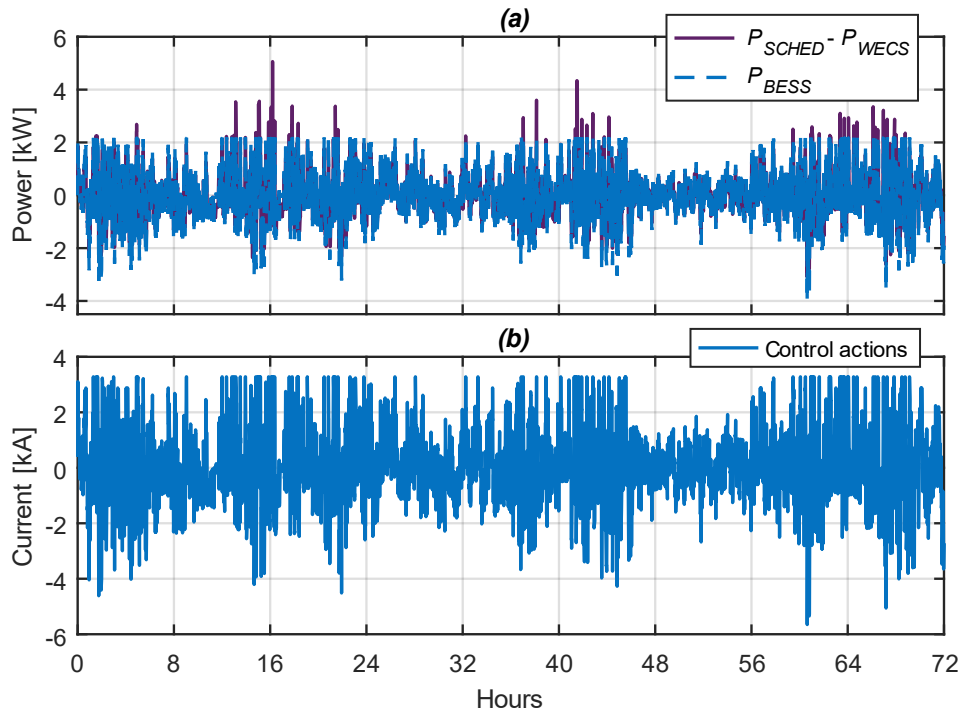


Fig. 5.12. Profit maximization strategy 1: (a) storage system power, and (b) storage system current with $\lambda_1=100$, $\lambda_2=0$, initial SoC of 50 % and P_{SCHED} with maximum 10 % error.

current is -6,4 kA. The current signal is the optimized variable in the energy management scheme proposed.

Fig. 5.13 presents the evolution of the state-of-charge. Several times the upper SoC limitation is attained which gives explanation to the occurrence of curtailments in this case. The number of charging cycles (8,6) is slightly bigger than the number of discharge cycles (8,3). Consequently, a total of 16,9 cycles during the 3 days is registered. Meanwhile, the state-of-charge error totals 31,8 %.

In Fig. 5.14.a a zoom is made around the first time the upper SoC limit is reached. Fig. 5.14.b displays the control actions corresponding to the same time period taking place the 5th

day between 11h and 12h. As can be appreciated in the control actions plot, the instants during which the constraint SoC^{max} is activated the control actions are essentially null.

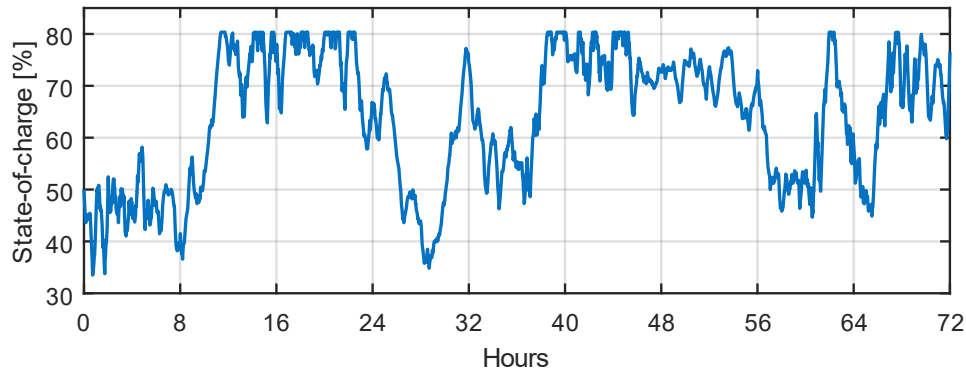


Fig. 5.13. Profit maximization strategy 1: state-of-charge with $\lambda_1=100$, $\lambda_2=0$, initial SoC of 50 % and P_{SCHED} with maximum 10 % error.

Now the ponderation of the power injection objective is decreased by a half ($\lambda_1=50$). Following the condition $\lambda_1 + \lambda_2 = 100$ defined for the weights, the same value is assigned to λ_2 . In Fig. 5.15 are superposed the plotted the SoC signals obtained when $\lambda_1=100$, $\lambda_2=0$ and $\lambda_1=\lambda_2=50$. In the latter case, less importance is given to the respect of the reference P_{SCHED} while the weight given to the tracking of SoC_{ref} is increased. Consequently, the EMS optimizes the injection whilst allowing smaller variations in the state-of-charge. Thus, the number of charging and discharging cycles with $\lambda_1=\lambda_2=50$ is 6,6 and 6,4 for a total of 13 cycles, smaller than the 16,9 cycles obtained with $\lambda_1=100$ and $\lambda_2=0$.

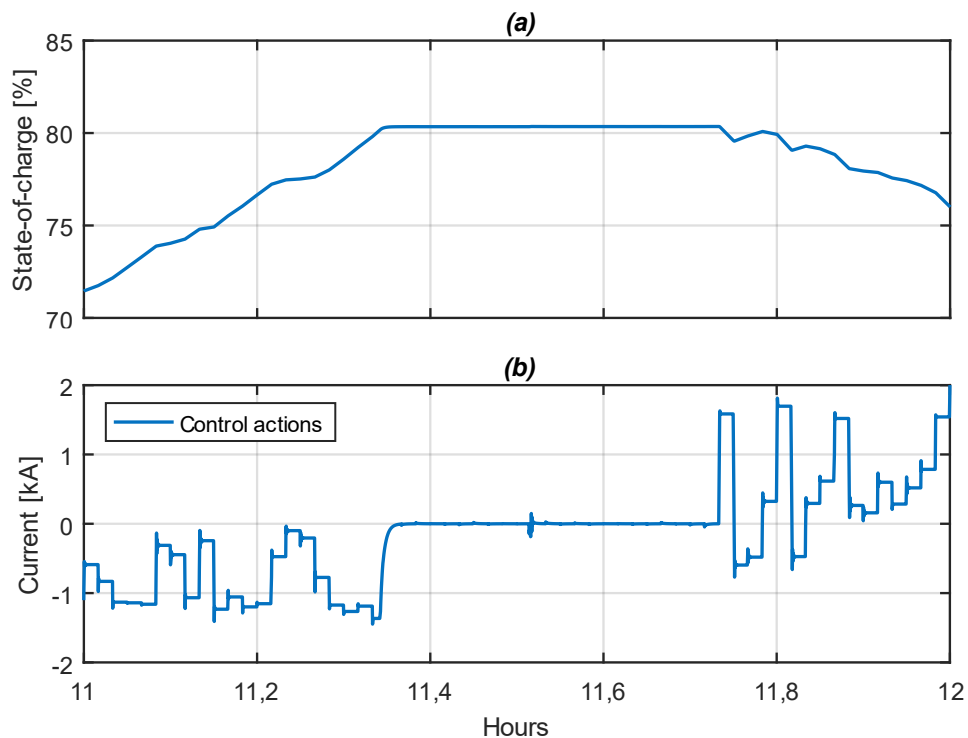


Fig. 5.14. Zoom around the first period with SoC^{max} restriction activated: (a) state-of-charge, and (b) storage system current, $\lambda_1=100$, $\lambda_2=0$, initial SoC of 50 % and P_{SCHED} with 10 % error

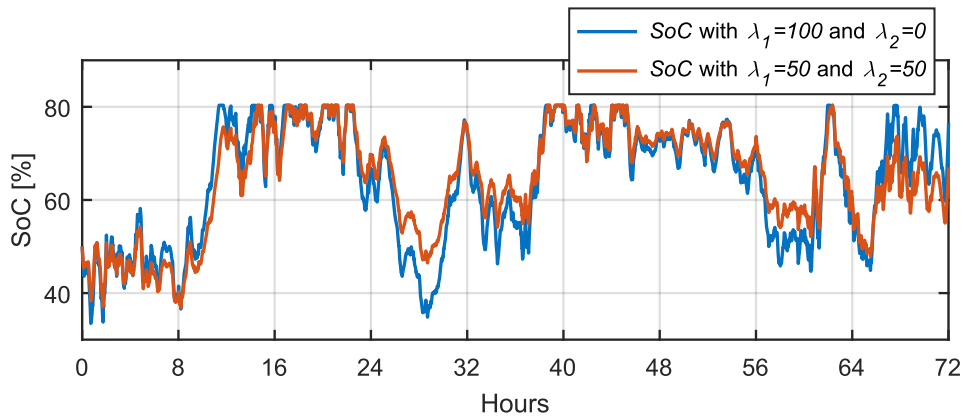


Fig. 5.15. Profit maximization strategy 1: state-of-charge signals with $\lambda_1=100$, $\lambda_2=0$ and $\lambda_1=\lambda_2=50$, initial SoC of 50 % and P_{SCHED} with 10 % error.

Fig. 5.16 compares the control actions resulting from these two situations. With a higher value of λ_1 , I_{BESS} evolves with bigger amplitudes during both the BESS charging and discharging, which explains why the storage system usage is bigger when $\lambda_1=100$ and $\lambda_2=0$. In both cases it can be appreciated that the BESS current reaches several times the upper

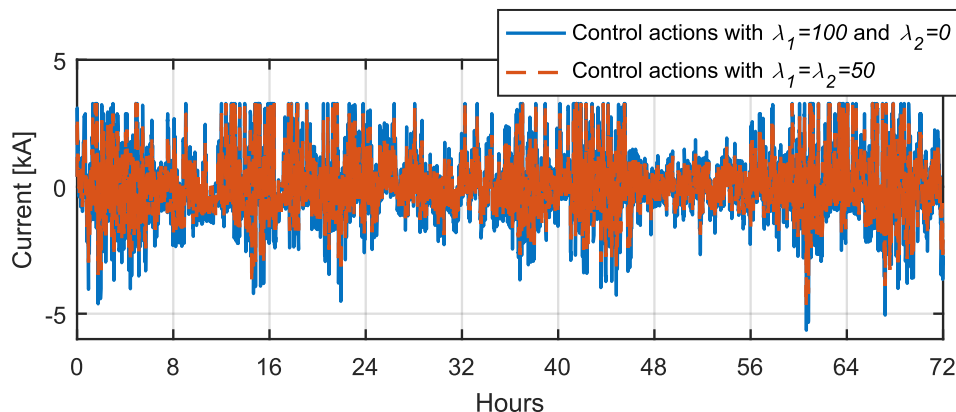


Fig. 5.16. Profit maximization strategy 1: comparison of storage system current with $\lambda_1=100$, $\lambda_2=0$ and $\lambda_1=\lambda_2=50$, initial SoC of 50 % and P_{SCHED} with maximum 10 % error.

boundary (u^{max}) leading to the activation of the control action amplitude constraint.

While the number of cycles changed when the ponderations were modified, the percentage of time during which commitment failures were active was the same (1,4 % in both situations). After considering unbilled power and curtailments, the total injection is slightly higher when $\lambda_1=\lambda_2=50$ (377,3 MW and 376,9 MW in the other case). Fig. 5.17 displays the power injection plots. With $\lambda_1=100$, $\lambda_2=0$ the BESS usage is less limited, and the amplitude of the resulting power injection signal is higher.

In Fig. 5.18 are presented the resulting cost plots. The scales were modified so that the addition of the sub-costs is within the [0,2] range and the control effort sub-cost within [0,1], for a total cost between 0 and 3. Even though the total injection is higher when $\lambda_1=\lambda_2=50$, the

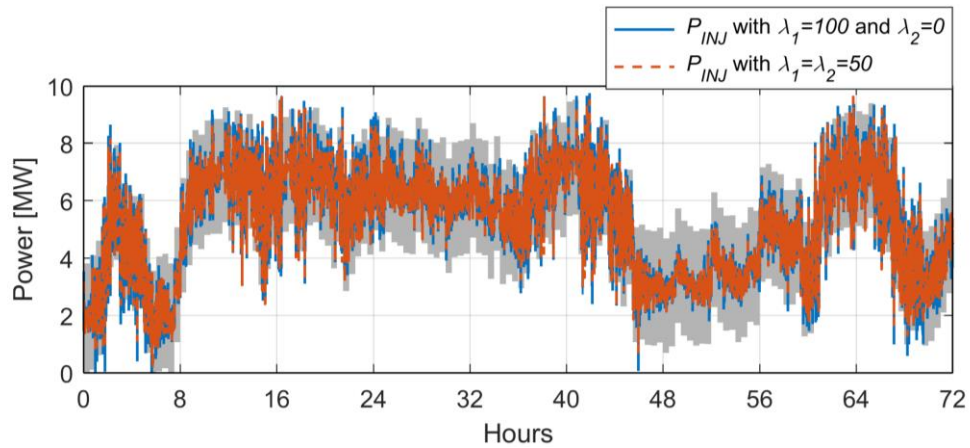


Fig. 5.17. Profit maximization strategy 1: injected power signals with $\lambda_1=100$, $\lambda_2=0$ and $\lambda_1=\lambda_2=50$, initial SoC of 50 % and P_{SCHED} with 10 % error.

injection and state-of-charge errors are bigger in this case. Then, the mean cost is also higher. Indeed, the mean cost is 0,13 with $\lambda_1=\lambda_2=50$, and 0,06 in the case where $\lambda_1=100$ and $\lambda_2=0$.

It is reminded that the total cost is the addition of the injection, state-of-charge and control effort sub-costs, presented in Fig. 5.19-Fig. 5.21. $\lambda_2=0$ implies the optimizer does not consider the SoC cost in the search for optimal solutions. Fig. 5.20 show this cost is zero when $\lambda_2=0$ and reaches 25 % of its highest value with $\lambda_1=\lambda_2=50$. In Fig. 5.21, the values beyond the saturation region in the control effort plots correspond to the charge peaks in the current plots presented in Fig. 5.16.

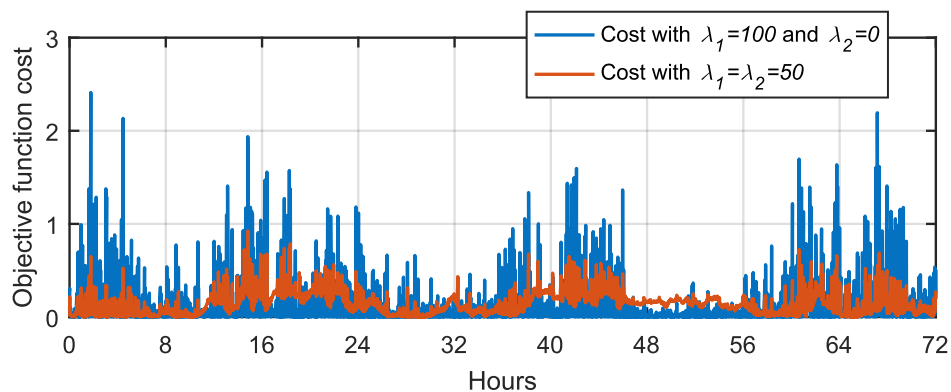


Fig. 5.18. Profit maximization strategy 1: comparison of the total costs with $\lambda_1=100$, $\lambda_2=0$ and $\lambda_1=\lambda_2=50$, initial SoC of 50 % and P_{SCHED} with maximum 10 % error.

Table 5.4 recapitulates the results obtained from the present strategy with several combinations of λ_1 and λ_2 in terms of the proposed performance indicators. Whenever using only one value after the comma was not enough to understand the effect on a given indicator of varying the ponderation of the control objectives, the number of values was augmented.

Apart from the atypical results obtained with $\lambda_1=0$, $\lambda_2=100$ and $\lambda_1=10$, $\lambda_2=90$ a certain uniformity can be observed among the remaining results shown in the table.

Apart from the atypical results obtained with $\lambda_1=0, \lambda_2=100$ and $\lambda_1=10, \lambda_2=90$ a certain

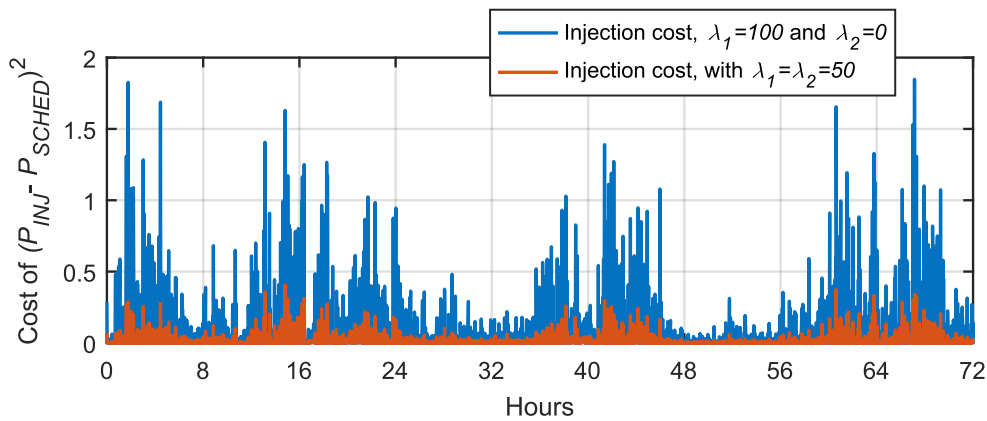


Fig. 5.19. Profit maximization strategy 1: comparison of the injection costs with $\lambda_1=100, \lambda_2=0$ and $\lambda_1=\lambda_2=50$, initial SoC of 50 % and P_{SCHED} with maximum 10 % error.

uniformity can be observed among the remaining results shown in the table.

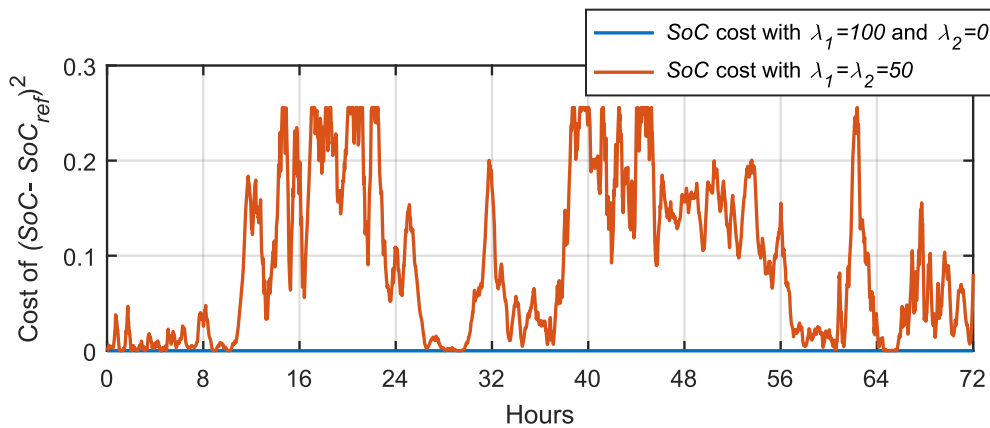


Fig. 5.20. Profit maximization strategy 1: comparison of the SoC costs with $\lambda_1=100, \lambda_2=0$ and $\lambda_1=\lambda_2=50$, initial SoC of 50 % and P_{SCHED} with maximum 10 % error.

The obtained amounts of commitment failures and unbilled power were similar among those results with 0,5 % and 0,6 %, respectively.

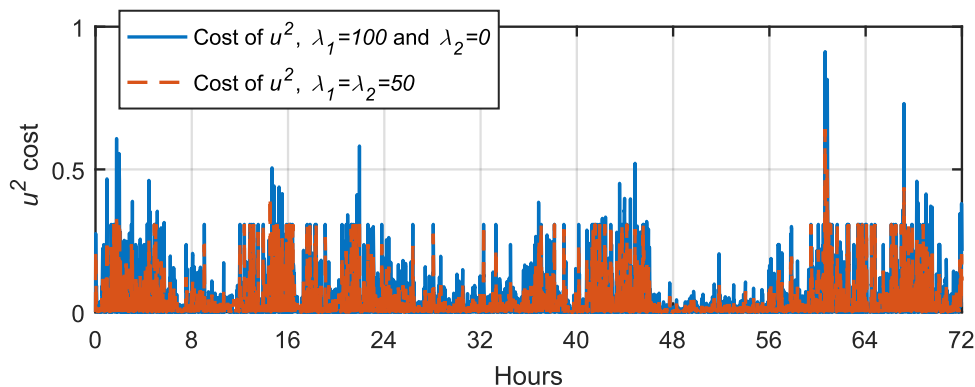


Fig. 5.21. Profit maximization strategy 1: comparison of the control effort costs with $\lambda_1=100, \lambda_2=0$ and $\lambda_1=\lambda_2=50$, initial SoC of 50 % and P_{SCHED} with maximum 10 % error.

While low levels of production curtailments took place in these cases (the maximum curtailment level is 0,006 %), the range of values of energy injected obtained was narrow (745

Table 5.4. Several results obtained from strategy 1 by varying the weights relation.

Indicator	$\lambda_1 - \lambda_2$ ponderation						
	0-100	10-90	20-80	50-50	60-40	80-20	100-0
CF [%]	13,9	7,4	0,5	0,5	0,5	0,5	0,5
$P_{unbilled}$ [%]	14,9	8,2	0,6	0,6	0,6	0,6	0,6
P_{curt} [%]	0,000	0,000	0,001	0,004	0,004	0,004	0,006
E_{INJ} [MWh]	323,4	348,7	377,7	377,3	377,5	377,0	376,9
BESS cycles [-]	0,005	2,8	6,6	13,0	11,4	15,8	16,9
P_{INJ} error [%]	13,4	11,2	8,3	3,4	4,6	2,3	2,9
SoC error [%]	1,0	18,5	34,1	32,2	32,0	31,8	31,8
Mean cost [-]	0,00	0,11	0,17	0,13	0,19	0,09	0,06

kW difference among the minimum and maximum values). The storage system cycles increase with λ_1 while the relation among the λ values and both the injection errors and mean costs is less obvious

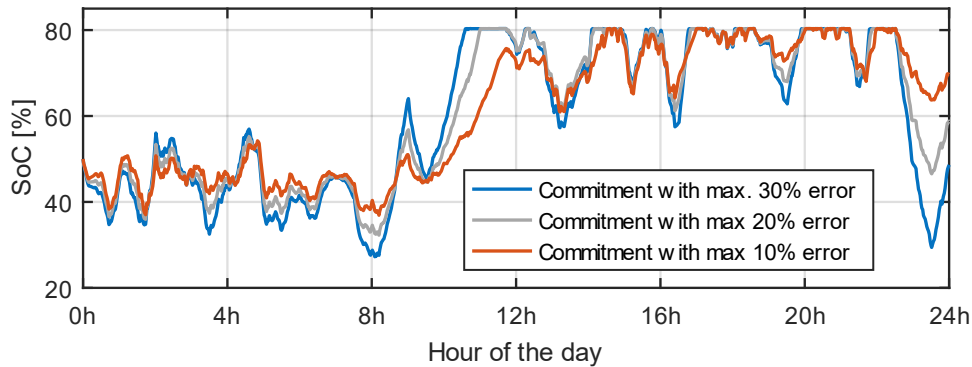


Fig. 5.22. Profit maximization strategy 1: state-of-charge signals comparison with P_{SCHED} with maximum 10, 20 and 30 % error, $\lambda_1=\lambda_2=50$ and initial SoC of 50 %

Fig. 5.22 compares the state-of-charge plots when the firm injection commitments are those with maximum 10 %, 20 % and 30 % maximum error, with $\lambda_1=\lambda_2=50$. The production data from day 5 is used in this test. As shown in the figure, with a bigger forecast error, more

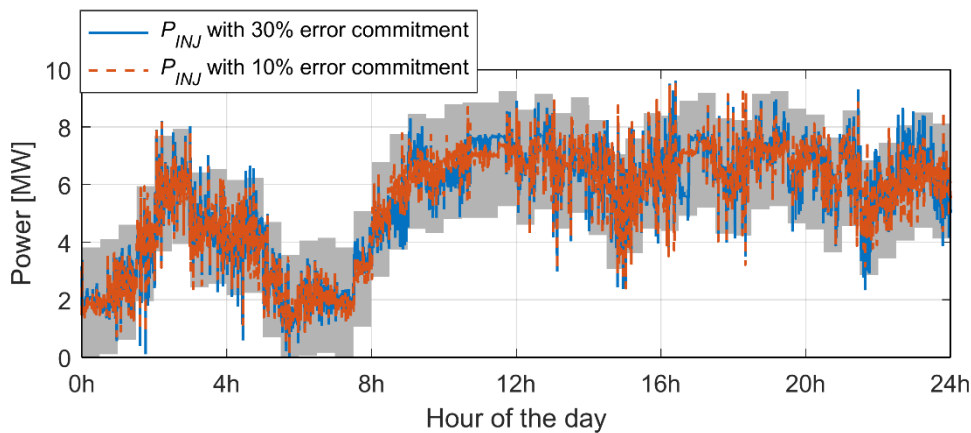


Fig. 5.23. Profit maximization strategy 1: comparison of the power injections with P_{SCHED} with maximum 10 % error and 30 % error, $\lambda_1=\lambda_2=50$ and initial SoC of 50 %.

BESS usage is required to accomplish the injection schedule. This leads to bigger P_{INJ} and SoC sub-costs, and ultimately the increment of the resulting cost

Fig. 5.23 presents the power injection signals with the first and third commitment profile. As in the earlier case, the amplitude of the injection signal increases with the commitment error.

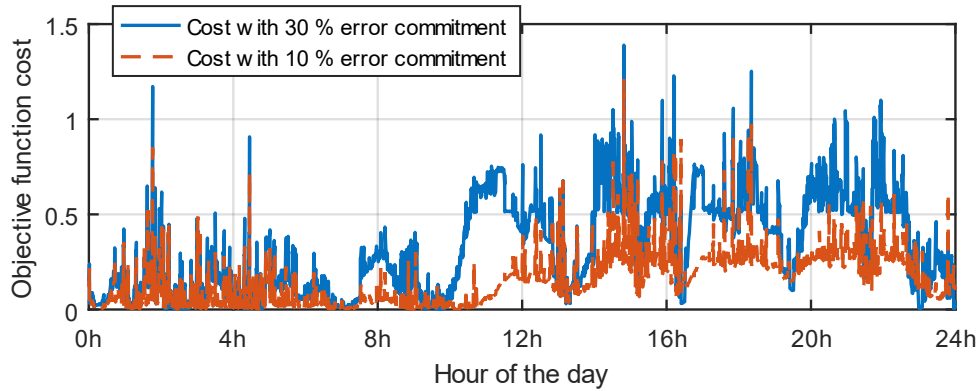


Fig. 5.24. Profit maximization strategy 1: comparison of the objective function costs with P_{SCHED} with maximum 10 % error and 30 % error, $\lambda_1=\lambda_2=50$ and initial SoC of 50 %.

Fig. 5.24 shows the comparison of the resulting costs for the commitments with 10 % and 30 % error and Table 5.5 summarizes the results obtained using the proposed comparison indicators.

Table 5.5. Summary of the results obtained from strategy 1 with P_{SCHED} with maximum 10 % error and 30 % error, $\lambda_1=\lambda_2=50$ and initial SoC of 50 %

Indicator	P_{SCHED} with maximum error		
	10 %	20 %	30 %
CF [%]	0,69	0,69	0,69
$P_{unbilled}$ [%]	0,79	0,80	0,83
P_{curt} [%]	0,01	0,09	0,38
E_{INJ} [MWh]	129,0	129,0	128,8
$BESS$ cycles [-]	4,8	5,0	5,6
P_{INJ} error [%]	4,0	6,0	8,6
SoC error [%]	30,9	33,1	35,2
Mean cost [-]	0,14	0,28	0,31

While close amounts of commitment failures and unbilled power are achieved in the three cases, some indicators increase with the commitment error. Such is the case of production curtailment, number of cycles, injection and SoC errors, and mean cost. It is noted that the number of cycles increment between the second and third columns is more than two times bigger than the increment between the first and second columns. This non-linearity among the variations is due to the upper limit of the SoC variable (Fig. 5.22).

As mentioned, the injection errors and mean costs obtained also grow with the commitment error. The values for these indicators with the commitment profile with the 30 % error are more than two times bigger than those obtained with commitment with 10 % error. The curtailment is particularly big with the commitment profile having a maximum 30 % error compared to the other two cases.

Next, to understand the effect on the results of the constraints defined, the strategy is tested with $\lambda_1=\lambda_2=50$, $Q_u=0.25$ and initial SoC of 50 %, without considering the constraints in resolving the optimization problem. The production data for the period starting on the fifth day and ending at the end of the seventh day is employed in the tests.

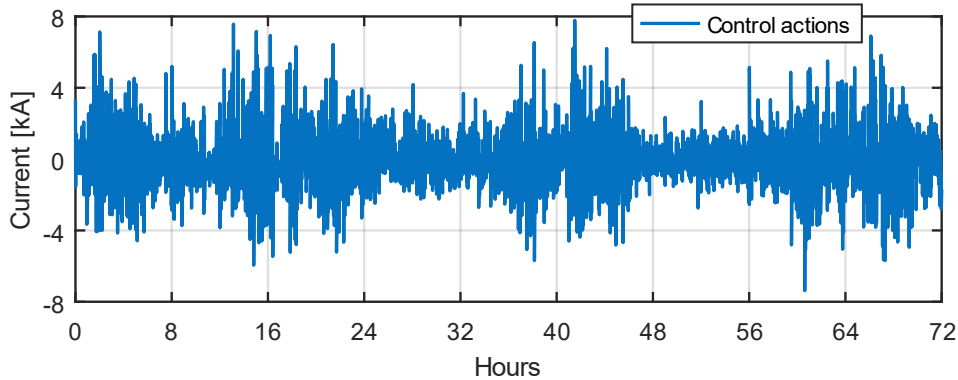


Fig. 5.25. Profit maximization strategy 1 - constraints deactivated: control actions with $\lambda_1=\lambda_2=50$, P_{SCHED} with maximum 10 % error and initial SoC of 50 %.

In the absence of constraints, only the plant saturations impose limits to the variables. Fig. 5.25 plots the control actions determined by the controller and applied to the plant. Meanwhile, in Fig. 5.26 is shown the evolution of the SoC. If the state-of-charge stays inside the [0 %,100 %] SoC range when the constraints are turned off is because of the saturations imposed by the storage system controlled.

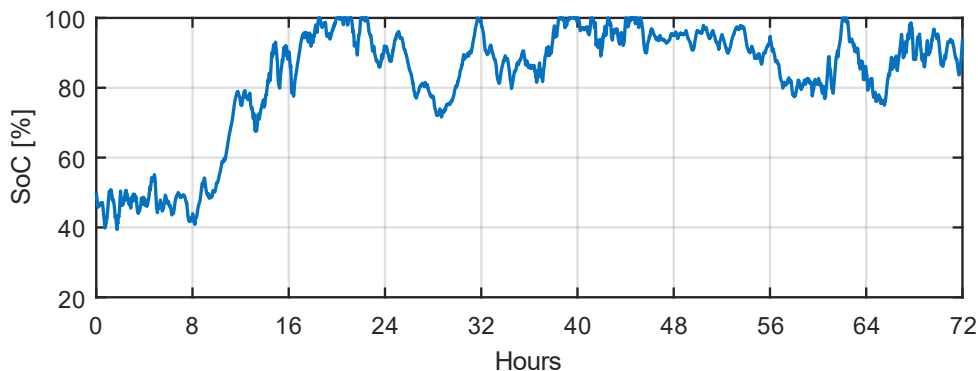


Fig. 5.26. Profit maximization strategy 1 - constraints deactivated: state-of-charge with $\lambda_1=\lambda_2=50$, P_{SCHED} with maximum 10 % error and initial SoC of 50 %.

Other than an important increment in the amplitude of the control actions oscillations (in Fig. 5.16 is presented the constrained current plot for the same period with $\lambda_1=\lambda_2=50$), it

can be observed that during periods in which the storage is not available, e.g. around 32 simulation hours (Fig. 5.26), the BESS current is not zero like happened in the presence of constraints, meaning that in those situations bigger control actions are employed to manage the BESS.

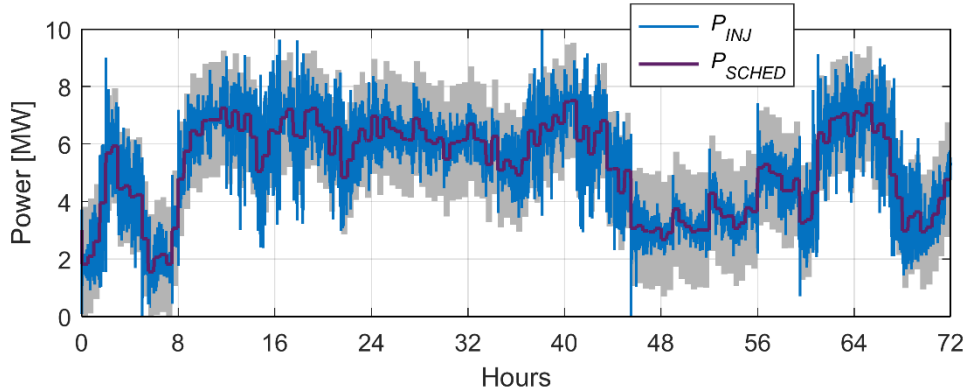


Fig. 5.27. Profit maximization strategy 1 - constraints deactivated: injected power with $\lambda_1=\lambda_2=50$, P_{SCHED} with maximum 10 % error and initial SoC of 50 %.

Fig. 5.27 plots the resulting profile of injection which presents oscillations with a bigger amplitude than those observed in the presence of constraints (compare with power injection signal with $\lambda_1=\lambda_2=50$ presented in Fig. 5.17). In this case using constrained control allowed obtaining a smoother output while employing smaller control actions.

5.2.2.2 Profit maximization strategy 2

It was mentioned that other than the relative weight λ_1 , the vertical offset that can be added to the signal P_{SCHED} has an influence on the power injection. Strategy 2 is a modification of Strategy 1 in which an offset is added to P_{SCHED} . Table 5.6 summarizes the values of the parameters employed in the strategy. Two values for the vertical displacement are utilized in simulation giving results presented in Fig. 5.28 - Fig. 5.30. On the other hand, the weights λ_1 and λ_2 as well as the other remaining parameters are fixed.

Table 5.6. Profit maximization strategy 2: algorithm parameters values.

Parameter	Description	Unit	Value
λ_1	Weight of injection sub-cost	-	50
λ_2	Weight of SoC sub-cost	-	50
Q_u	Control effort adjustment parameter	-	0,5
$offset$	Vertical displacement of P_{SCHED}	MW	-0,5, 0
SoC_{ref}	SoC set-point level	%	50
N_p	Optimization window length	s	10

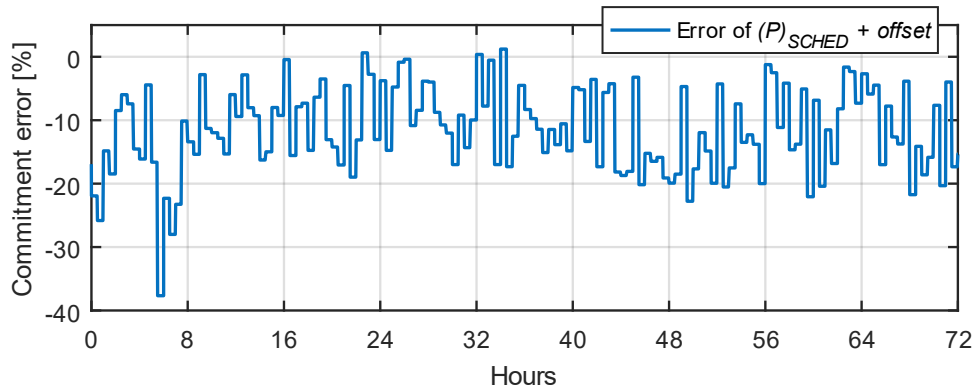


Fig. 5.28. Error of commitment profile with maximum 10 % error with -0,5 MW offset and initial SoC of 50 %.

With a vertical displacement of -0,5 MW the commitment is moved downwards by the same amount. With this modification the commitment profile error is inferior to 23 % during 96 % of the simulation time and bigger the rest of the time, with a maximum of 37,7%. Such error is displayed in Fig. 5.28.

Fig. 5.29 shows the resultant state-of-charge signal. Because of the decrement in the scheduled injection set-point, a surplus of power is made available to be stored. To mobilize the power required to follow the power injection set-point, the BESS is charged from the beginning of the simulation. With this, the SoC increases until reaching 80 % after 1,9 hours. At that moment, the constraint SoC^{max} gets activated and the algorithm forbids any charging of the BESS. From there, the injection follows the production ($P_{INJ} = P_{WECS}$) until there is not enough power production meet the commitment, that is $P_{WECS} < P_{SCHED}$ and the storage system is discharged. When P_{WECS} becomes greater than P_{SCHED} the storage system is charged again and so on. 6,2 cycles of the storage units were registered in the present test (without modification of the commitment the number of cycles was of 13,0 cycles).

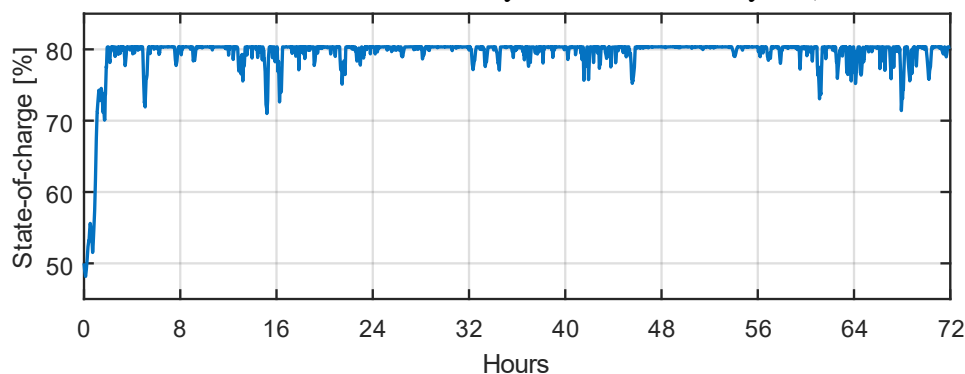


Fig. 5.29. Profit maximization strategy 2: state-of-charge with -0,5 MW offset, $\lambda_1=\lambda_2=50$, commitment with maximum 10 % error and initial SoC of 50 % .

Fig. 5.30 shows the resultant injection profile plot. In this case, the injection reference is followed from close the BESS units are fully charged. With the storage system unavailable

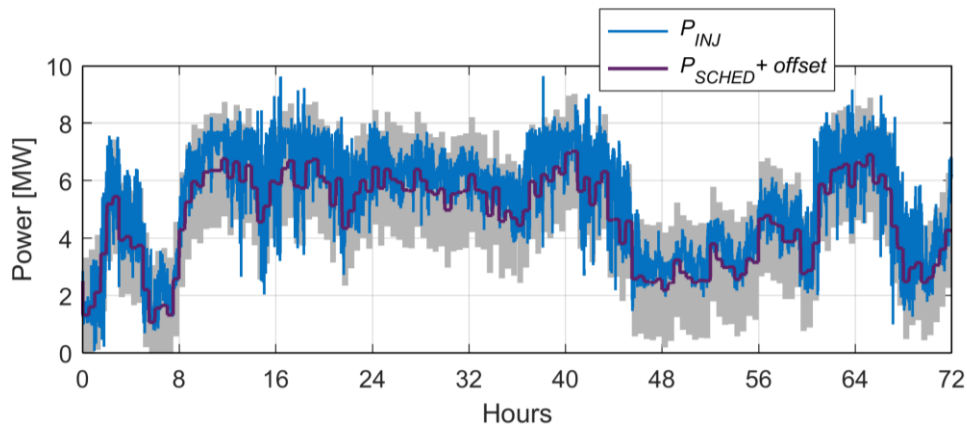


Fig. 5.30. Profit maximization strategy 2: power injection with $-0,5$ MW offset, $\lambda_1=\lambda_2=50$, commitments with maximum 10 % error and initial SoC of 50 %.

to store much power, the injection takes place most of the time between the commitment profile and the upper threshold of the tolerated injection region. With commitment failures occurring during 0,5 % of the simulation time, 0,5 % of the total power produced is unbilled. 0,03 % of the production is curtailed, and a total of 377,3 MWh are injected into the grid.

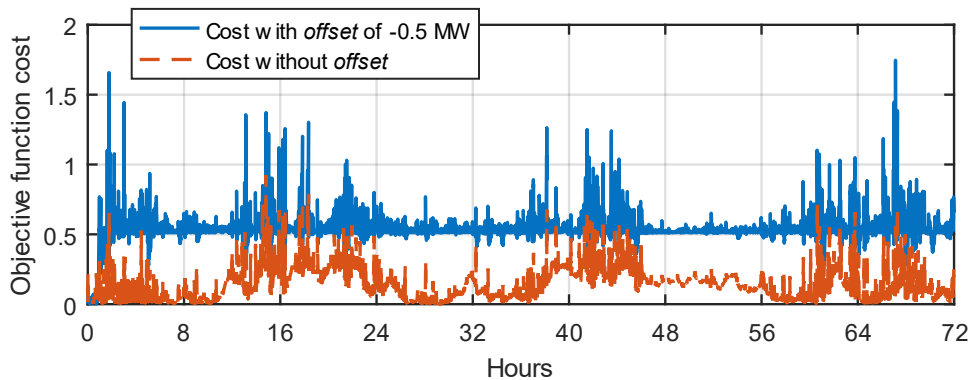


Fig. 5.31. Profit maximization strategy 2: comparison of the objective function costs with $-0,5$ and 0 offset, $\lambda_1=\lambda_2=50$, commitment with maximum 10 % error and initial SoC of 50 %.

In Fig. 5.31, the objective function costs resulting from using a vertical offset of $-0,5$ MW is compared to the cost without vertical displacement of the commitment profile. With the vertical displacement a constant cost was added because of the disrespect of the SoC reference.

Moreover, this strategy tends to rely heavily on the storage system which is frequently charged. Thus, the BESS units tend to be fully charged and therefore unavailable. This is inconvenient as implies a lack of storage capacity during strong wind periods when the BESS must store the surplus so that the injection can be flattened. In Table 5.7 are presented the indicators values obtained using offsets between -1 MW and $+1$ MW. According to these results, the strategy performs better with small offset values (such as $-0,2$ MW) or no offset.

Table 5.7. Results summary of strategy 2. Several offset values, $\lambda_1=\lambda_2=50$, commitment with maximum 10 % error and initial SoC of 50 %.

Indicator	offset [MW]						
	-1	-0,5	-0,2	0	+0,2	+0,5	+1
CF [%]	0,5	0,5	0,5	0,5	3,7	7,9	10,4
$P_{unbilled}$ [%]	0,5	0,5	0,5	0,6	3,8	8,7	11,8
P_{curt} [%]	0,03	0,03	0,02	0,00	0,00	0,00	0,00
E_{INJ} [MWh]	377,4	377,3	377,2	377,3	365,9	347,4	335,6
BESS cycles [-]	3,1	6,2	9,7	13,0	10,0	6,2	2,3
P_{INJ} error [%]	31,1	14,2	7,0	3,4	5,9	9,7	16,6
SoC error [%]	59,9	58,8	54,7	32,182	51,0	57,9	59,5
Mean cost [-]	0,5	0,5	0,2	0,1	0,1	0,5	0,5

5.2.3 Technical optimization of the HPP operation

While the commitment failures are minimized, another objective that can be prioritized is the maximization of the stored energy. Such maximization can be achieved by fixing the set-point SoC_{ref} to attract the SoC signal towards the highest admissible value, 80 %, as portrayed in Fig. 5.32. The relative weights λ_1 and λ_2 also play a role in the achievement of this objective.

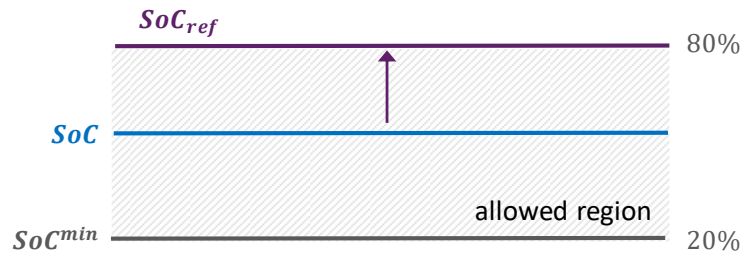


Fig. 5.32. Approach to maximize the SoC through the parameter λ_2 : set-point and allowed regions for the state-of-charge.

Before checking the effect of λ_2 in the SoC maximization in section 5.2.3.1, SoC_{ref} is given the values 20 %, 50 % and 80 % while fixing λ_1 and λ_2 .

5.2.3.1 Strategy focused on the storage system state-of-charge maximization

In Table 5.8 are presented the algorithm's parameter values used in a first set of tests in which the set-point SoC_{ref} is varied.

The data of the 11th day is employed in this part. Fig. 5.33 presents the corresponding production and commitment data. That day the wind park production totals 57,1 MW.

Fig. 5.34.a shows the storage system state-of-charge when $\lambda_1=0$ and $\lambda_2=100$ and the SoC variable references are set at the 20 %, 50 % and 80 % levels. Under these conditions, it

Table 5.8. SoC maximization strategy: algorithm parameters values.

Parameter	Description	Unit	Value
λ_1	Weight of injection sub-cost	-	0
λ_2	Weight of SoC sub-cost	-	100
Q_u	Control effort adjustment parameter	-	0,5
$offset$	Vertical displacement of P_{SCHED}	MW	0
SoC_{ref}	SoC set-point level	%	20, 50, 80
N_p	Optimization window length	s	10

takes a little more than 24 hours for the SoC to reach 20 % or to 80 % when the initial value is 50 %. In the case where the reference is set at 50 %, the variations in the SoC during the day are minimal. In the three cases, the BESS usage is minimum

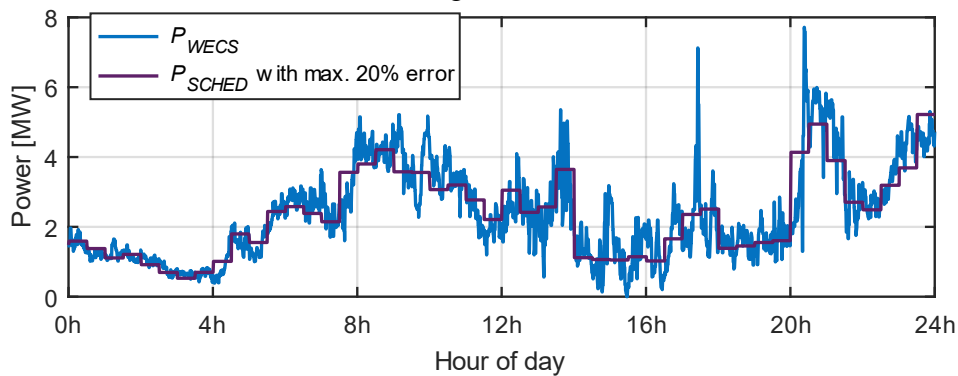


Fig. 5.33. SoC maximization strategy: wind generated power data for day 11 and commitment profile.

The corresponding control actions generated by the optimizer are presented in Fig. 5.34.b. As can be noted, when the optimization problem is solved focusing only on the minimization of the tracking error of the SoC variable, the current variations are very limited. Therefore, the power charged into or discharged from the BESS is also limited and therefore, insufficient to compensate the forecast errors. Table 5.9 presents the performance indicators obtained for the three tests. In all of them, an important injection error (superior to 22 %) can be observed.

 Table 5.9. Results summary of strategy 2. SoC_{ref} of 20 %, 50 % and 80 %.

Indicator	$SoC_{ref}=20$	$SoC_{ref}=50$	$SoC_{ref}=80$
CF [%]	2,8	4,2	4,2
$P_{unbilled}$ [%]	4,0	4,9	4,8
P_{curt} [%]	0	0	0
E_{INJ} [MWh]	55,2	54,3	53,8
$BESS$ cycles [-]	0,2	0,0	0,2
P_{INJ} error [%]	22,6	22,4	22,3
SoC error [%]	35,1	0,7	37,3
$Mean$ cost [-]	0,03	0,00	0,05

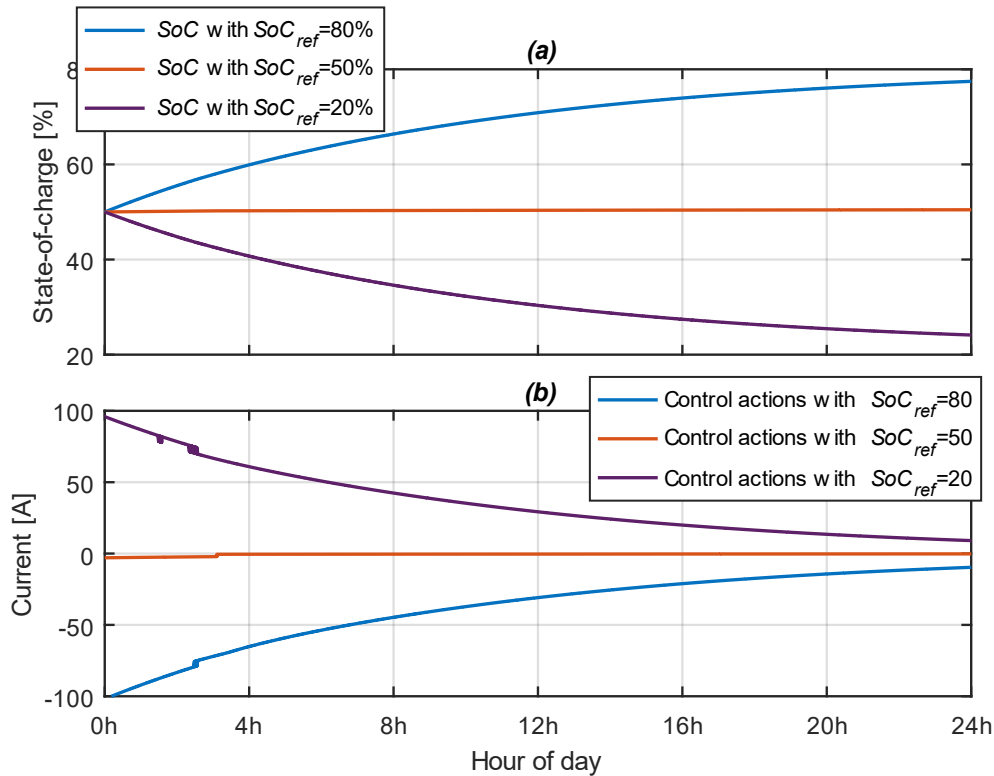


Fig. 5.34. SoC maximization strategy: (a) SoC signals, and (b) control actions with set-point levels 20 %, 50 % and 80 %, commitment with maximal 20 % error, $\lambda_1=0$ and $\lambda_2=100$ and initial SoC of 50 %.

In Fig. 5.35 are compared the SoC signals resulting of using the ponderations $\lambda_1=0$, $\lambda_2=100$ and $\lambda_1=100$, $\lambda_2=0$ when the SoC set-point is set at 80 %. As can be seen, the bigger λ_2 the bigger the attraction effect of the state-of-charge towards the set-point SoC_{ref} . With this bigger attraction the BESS usage decreases. With $\lambda_1=0$, $\lambda_2=100$ the total cycles are 0,2 and 4,2 cycles with $\lambda_1=100$, $\lambda_2=0$.

Table 5.10 presents the parameters employed for several tests done with the data of the 11th day, and Table 5.11 summarizes the results obtained with several ponderations of the control objectives with the data of the 11th day.

In the cases where λ_1 was equal or greater than λ_2 , no commitment failures or unbilled injections were registered. Also, in those cases the injection errors were significantly smaller.

Table 5.10. SoC maximization strategy: algorithm parameters values.

Parameter	Description	Unit	Value
λ_1	Weight of injection sub-cost	-	0, 10, 20, 60, 80, 100
λ_2	Weight of SoC sub-cost	-	100, 90, 80, 50, 40, 20, 0
Q_u	Control effort adjustment parameter	-	0,5
<i>offset</i>	Vertical displacement of P_{SCHED}	MW	0
SoC_{ref}	SoC set-point level	%	50
N_p	Optimization window length	s	10

According to these results, the pursuit for the technical objective of reducing the BESS usage lead to an increment in the commitment failures. In this thesis, the decision was made to define relative weights λ_1 and λ_2 that add up 100. This was done to highlight the fact that the user of the algorithm can give a quantitative value to the importance of each of the control objectives. The range [0,100] is straightforward but, as shown above, when λ_1 and λ_2 are 0 and 100, the SoC can go from 20 % or 80 % level towards 50 % within nearly 24 hours while the control actions are minimal.

Table 5.11. Results summary of strategy 2. Several ponderations λ_1 , λ_2 , commitment with maximum 20 % error, initial SoC and SoC_{ref} of 50 %..

Indicator	$\lambda_1 - \lambda_2$ weights						
	0-100	10-90	20-80	50-50	60-40	80-20	100-0
CF [%]	4,2	1,4	0,7	0,0	0,0	0,0	0,0
$P_{unbilled}$ [%]	4,9	2,5	0,8	0,0	0,0	0,0	0,0
P_{curt} [%]	0,0	0,0	0,0	0,0	0,0	0,0	0,0
E_{INJ} [MWh]	54,3	55,4	56,2	56,6	56,6	56,7	56,7
BESS cycles [-]	0,0	0,7	1,6	3,2	3,4	3,9	4,2
P_{INJ} error [%]	22,4	18,7	13,9	5,5	4,0	2,8	3,2
SoC error [%]	0,7	5,7	11,7	21,0	22,4	22,9	22,8
Mean cost [-]	0,00	0,02	0,07	0,13	0,07	0,08	0,03

Seeking that the BESS can be either charged or discharged at the beginning of every day, a user of the algorithm can be interested in ensuring that a certain amount of power (e.g. a SoC of 50 %) is stored in the battery units at the end of the day.

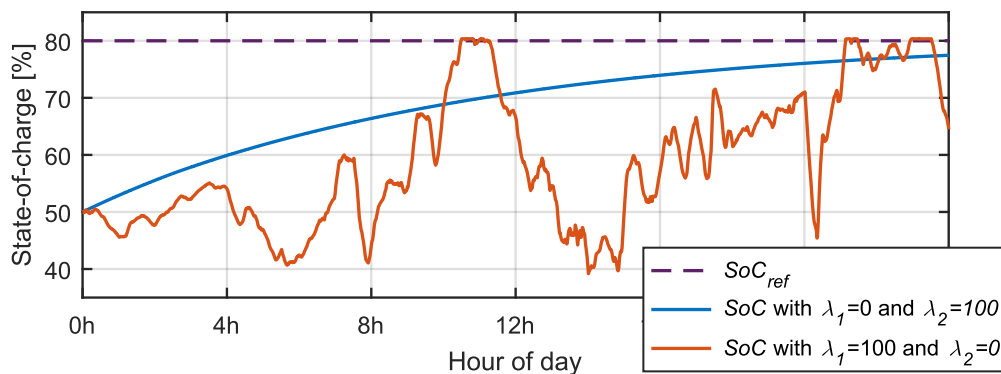


Fig. 5.35. SoC maximization strategy: state-of-charge with $\lambda_1 = \lambda_2 = 50$, commitment with maximum 20 % error, initial SoC of 50 % and SoC set-point at 80 %.

For achieving this, other couples of values λ_1 , λ_2 can be explored. As an example, in Fig. 5.36.b are compared the SoC signals obtained with $\lambda_1 = \lambda_2 = 50$, $\lambda_1 = 50$ and $\lambda_2 = 10\ 000$, and $\lambda_1 = 50$ and $\lambda_2 = 100\ 000$ with the SoC set-point at 50 %. For this test, the power data used corresponds to the period starting the day 11 and ending at the end of the 17th day. Fig. 5.36.a

presents the production and commitment profiles used as simulation inputs whereas in Fig. 5.36.b are presented the corresponding *SoC* signals.

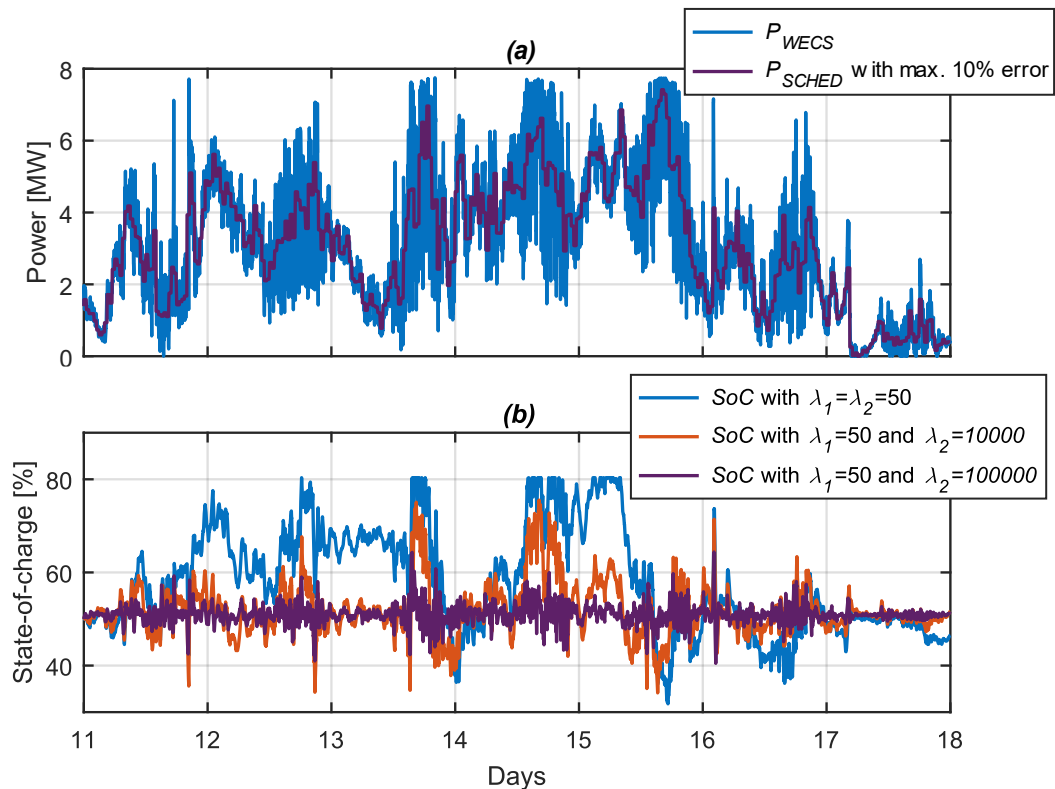


Fig. 5.36. *SoC* maximization strategy: (a) wind generated power for days 11-18 and commitment profile and (b), state-of-charge with λ_1 - λ_2 weights: 50-50, 50-10 000 and 50-100 000, commitment with maximum 20 % error, initial *SoC* of 50 % and 50 % as *SoC* set-point.

Of course, the bigger λ_2 , the closer to the 50 %, reference level the *SoC* will evolve. Thus, with increasing λ_2 the *SoC* error should decrease. λ_2 values of 50, 10 000 and 100 000 produce *SoC* errors of 21,1 %, 8,3 % and 3,3 %, respectively. It is because of several activations of the *SoC* constraint that the number of cycles with $\lambda_2=50$ is not the biggest, as indicated in

Table 5.12. Results summary of strategy 2. Other ponderations λ_1 , λ_2 , commitment with maximum 20 % error, initial *SoC* and SoC_{ref} of 50%.

Indicator	$\lambda_1 - \lambda_2$ weights		
	50-50	50-10 000	50-100 000
<i>CF</i> [%]	0,4	0,1	0,7
$P_{unbilled}$ [%]	0,2	0,2	0,2
P_{curt} [%]	0,01	0,00	0,00
E_{INJ} [MWh]	523,5	523,5	523,7
<i>BESS</i> cycles [-]	25,1	25,7	23,7
P_{INJ} error (RPD) [%]	0,06	0,06	0,11
<i>SoC</i> error [%]	21,1	8,3	3,3
Mean cost [-]	0,1	4,1	2,9

Table 5.12. From the table, the total injections resulting from the bigger λ_2 values considered are in the same order as in the case with $\lambda_1=\lambda_2=50$. Even so, the mean costs are greater.

As the commitment is equal to 0 MW for several hours during the 17th day, the injection error cannot be calculated using relative error (Eq. 5.18). For this, the injection error in Table 5.12 was calculated using the relative percent difference (RPD), a common alternative to the relative error used in laboratory quality control procedures. The RPD is defined as the difference of P_{INJ} and P_{SCHED} to their average magnitude:

$$RPD \% = mean \left| \frac{P_{INJ} - P_{SCHED}}{(|P_{INJ}| + |P_{SCHED}|)/2} \right| \quad \text{Eq. 5.20}$$

The value of the RPD always lies between -2 and 2.

SoC levels of 20 % or 80 % correspond to the maximum and minimum admitted values. Therefore, pursuing *SoC* references defined at or close to those levels may lead to conditions in which the BESS is unavailable (storage units depleted or fully charged). From thereon, seeking to favor the BESS availability while not penalizing the objective of respecting the injection target, SoC_{ref} is set at 50 %.

5.2.4 Impact of Q_u and N_p on the results

In the following are considered the impacts of the control effort parameter and the optimization horizon size on the performance of the strategy.

5.2.4.1 Impact of Q_u

In order to test the influence of the control actions size on the performance of the algorithm, the parameter Q_u is now given the values 0 and 0,1 while fixing the remaining parameters, as indicated in Table 5.13.

Table 5.13. Influence of Q_u on the results: parameters values.

Parameter	Description	Unit	Value
λ_1	Weight of injection sub-cost	-	50
λ_2	Weight of <i>SoC</i> sub-cost	-	50
Q_u	Control effort adjustment parameter	-	0, 1
<i>offset</i>	Vertical displacement of P_{SCHED}	MW	0
SoC_{ref}	<i>SoC</i> set-point level	%	50
N_p	Optimization window length	s	10

The plots of the resulting control actions are superposed in Fig. 5.37. With $Q_u=0$, no consideration is given to the size of the control actions in resolving the optimization problem. Hence, the algorithm may use as much control action as required to ensure the regulated

variables set-points are closely respected accordingly to the relative weights assigned. As can be seen, with a greater value of Q_u , the control actions amplitude decreases.

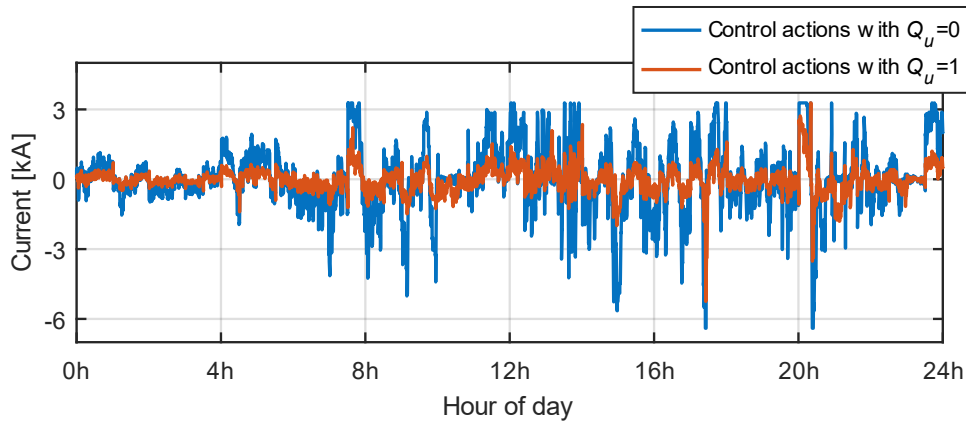


Fig. 5.37. Influence of Q_u on the results: control actions with $Q_u=0$, and 1, commitment with maximum 30 % error, initial SoC of 50 % and 50 % as SoC set-point.

The state-of-charge signals are plotted in Fig. 5.38. With $Q_u=0$ the SoC present more variations. With $Q_u=0$ and $Q_u=1$ the storage system cycles amounted 5,9 and 2,2 cycles, respectively.

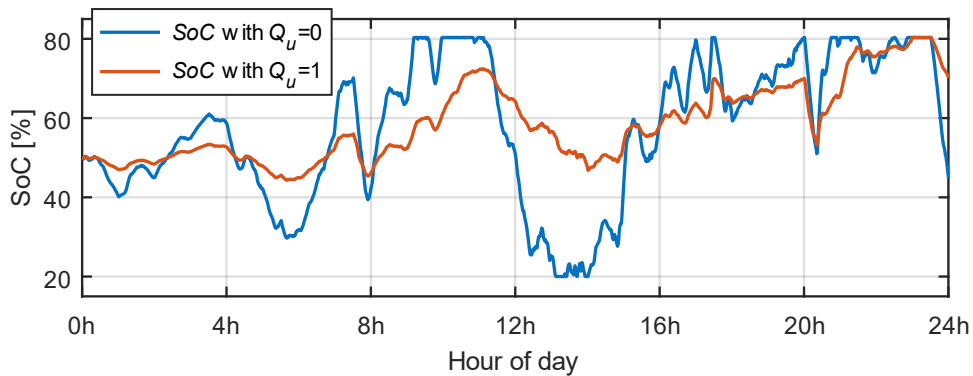


Fig. 5.38. Influence of Q_u on the results: state-of-charge with $Q_u=0$, and 1, commitment with maximum 30 % error, initial SoC of 50 % and 50 % as SoC set-point.

Fig. 5.39 presents the power injections obtained with both Q_u values. Considering the commitment failures, unbilled power and production curtailment, that are zero when $Q_u=1$, the

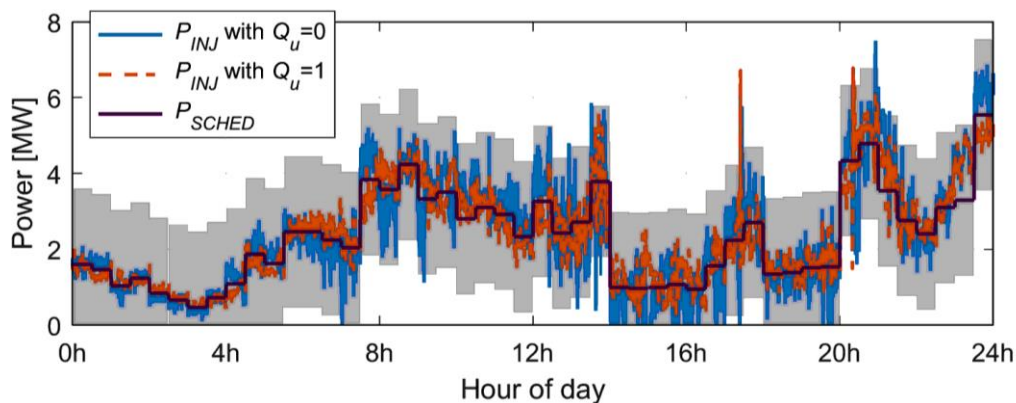


Fig. 5.39. Influence of Q_u on the results: power injection with $Q_u=0$ and 1, commitment with maximum 30 % error, initial SoC of 50 % and 50 % as SoC set-point.

total injection is bigger in that case. These indicators totaled 1,4 %, 0,6 % and 0,05 % with $Q_u=0$. The energy injections totaled 56,65 MWh and 56,58 MWh, with $Q_u=1$ and $Q_u=0$.

Table 5.14 summarizes these results obtained with the Q_u values 0, 0,5 1 and 10.

As can be noted from the last column ($Q_u=10$), a bigger Q_u is associated to more attenuated control actions, less storage system cycles, a smaller injection and a bigger injection error.

Table 5.14. Results summary of tests with different Q_u values. Initial SoC of 50 %.

Indicator	Q_u			
	0	0,5	1	10
CF [%]	1,4	0,0	0,0	5,6
$P_{not\ billed}$ [%]	0,6	0,0	0,0	8,1
P_{curt} [%]	0,05	0,00	0,00	0,00
E_{INJ} [MWh]	56,58	56,75	56,65	52,45
$BESS\ cycles$ [-]	5,9	3,5	2,2	0,1
$P_{INJ\ error}$ [%]	16,8	6,8	14,0	25,7
$SoC\ error$ [%]	32,8	23,0	19,5	0,4
$Mean\ cost$ [-]	0,27	0,15	0,06	0,00

5.2.4.2 Impact of N_p

To gain insight into the consequences of modifying the prediction and optimization window size, the algorithm is tested utilizing the parameters from Table 5.15.

Table 5.15. Influence of N_p on the results: parameters values.

Parameter	Description	Unit	Value
λ_1	Weight of injection sub-cost	-	50
λ_2	Weight of SoC sub-cost	-	50
Q_u	Control effort adjustment parameter	-	0,5
$offset$	Vertical displacement of P_{SCHED}	MW	0
SoC_{ref}	SoC set-point level	%	50
N_p	Prediction and optimization window length	s	10, 15, 30, 45

Fig. 5.40 presents the power injections when the number of samples of the control and optimization window N_p is set at 10 s and 45 s. These are the smallest and biggest optimization window sizes considered. A smaller optimization windows means predicting the future system states over a shorter number of timesteps. With N_p of 45 s more information is used at time k to calculate estimates over the period $x(k+1) \dots x(k+N_p)$. However, the assumption done that $P_{WECS}(k)$ stays invariant over that period becomes less truthful as N_p increases. Thus, with N_p of 10 s, the total energy injection is bigger (218,0 MWh and 189,3 MWh with N_p of 45 s).

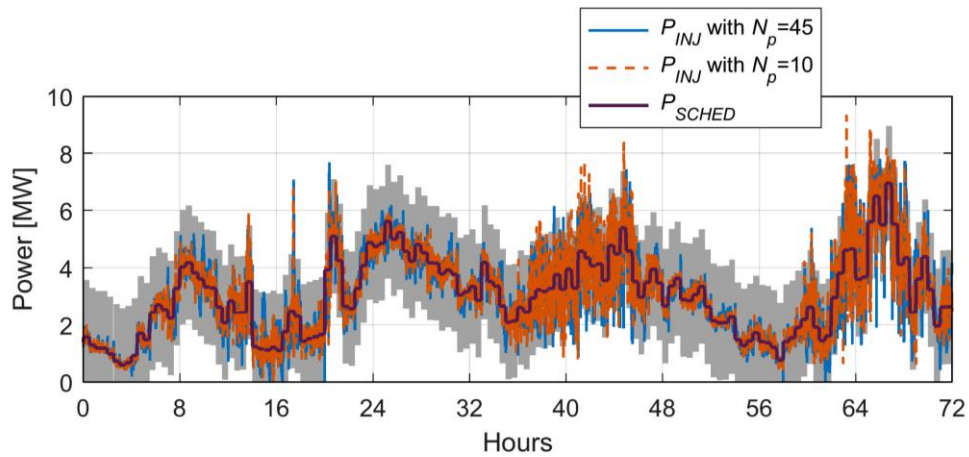


Fig. 5.40. Control horizon size influence on the results: power injection with $N_p=10$, and 45, commitment with maximum 10 % error, initial SoC of 50 % and 50 % as SoC set-point.

The SoC evolution for the four N_p values considered, namely 10 s, 15 s, 30 s and 45 s, is presented in Fig. 5.41. According to the figure, increasing the N_p values appear to be associated with a narrower range of variations for the state-of-charge variable (or a smaller number of cycles). Thus, the biggest number of cycles obtained is 11,2 with an optimization window of 10 s. Meanwhile, with 15 s, 30 s and 45 s, the cycles were 6,1, 0,9, and 0,2, respectively.

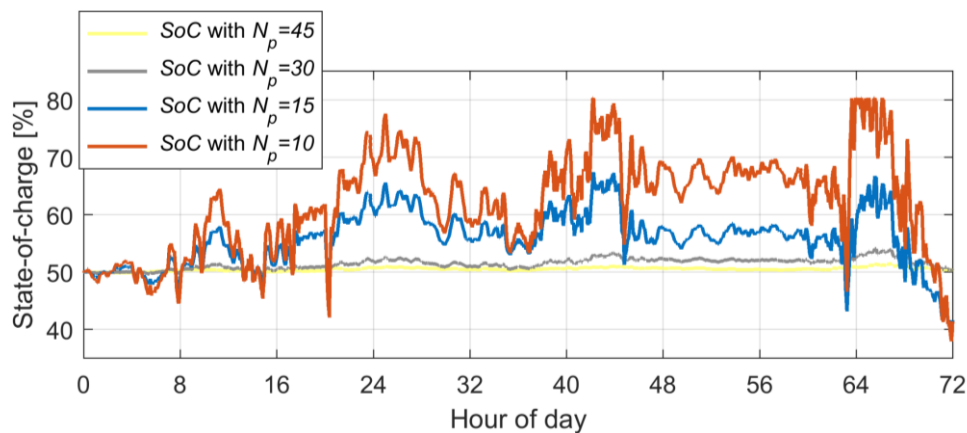


Fig. 5.41. Control horizon size influence on the results: SoC with $N_p=10$, 15, 30, 45 commitment with maximum 10 % error, initial SoC of 50 % and 50 % as SoC set-point.

In Table 5.16 are displayed the indicators found through simulation when using time windows of 10 s, 15 s, 30 s and 45 s as prediction and optimization horizon with the data of the 11th day. From the observation of these results, the obtained performance with a time horizon of 10 s is the best with respect to several of the indicators (commitment failures, unbilled power, energy injection and injection error).

Until here, several tests with a duration of one or three days were done with the aim of figuring out the impact of the elements in the cost function described in Eq. 5.1 on the algorithm performance. Next, the algorithm is tested during a month.

Table 5.16. Results summary of tests with different N_p values. Initial SoC of 50 %.

Indicator	Time horizon [s]			
	10	15	30	45
CF [%]	0,2	0,5	8,3	9,5
$P_{unbilled}$ [%]	0,5	0,7	11,9	13,7
P_{curt} [%]	0,02	0,00	0,00	0,00
E_{INJ} [MWh]	218,0	218,0	193,1	189,3
$BESS$ cycles [-]	11,2	6,1	0,9	0,2
P_{INJ} error [%]	4,2	10,7	17,3	18,3
SoC error [%]	25,1	12,7	3,0	1,1
$Mean$ cost [-]	0,09	0,04	0,02	0,02

5.3 Energy management of the HPP during a month

The proposed algorithm is now applied to manage the hybrid plant during a 27-days period. In Table 5.17 are displayed the algorithm parameter values to be employed.

Table 5.17. Retained parameters values.

Parameter	Description	Unit	Value
λ_1	Weight of injection sub-cost	-	50
λ_2	Weight of SoC sub-cost	-	50
Q_u	Control effort adjustment parameter	-	0,5
$offset$	Vertical displacement of P_{SCHED}	MW	0
SoC_{ref}	SoC set-point level	%	50
N_p	Optimization window length	s	10

A rule-based energy management technique used in the Insul'Grid project during the HPP design phase is chosen as a benchmark. After defining the principle of the technique are presented some simulation results obtained from the two energy management algorithms.

5.3.1 Rule-based strategy description

Fig. 5.42 shows the different cases considered by the strategy with respect to the current production P_{WECS} .

The same convention for the storage system is used with this basic rule-based strategy: the power is assumed negative for discharge and positive for charge. In this manner, the amount of power discharged from or provided by the storage system required to fulfill the commitment profile is as described in Eq. 4.10.

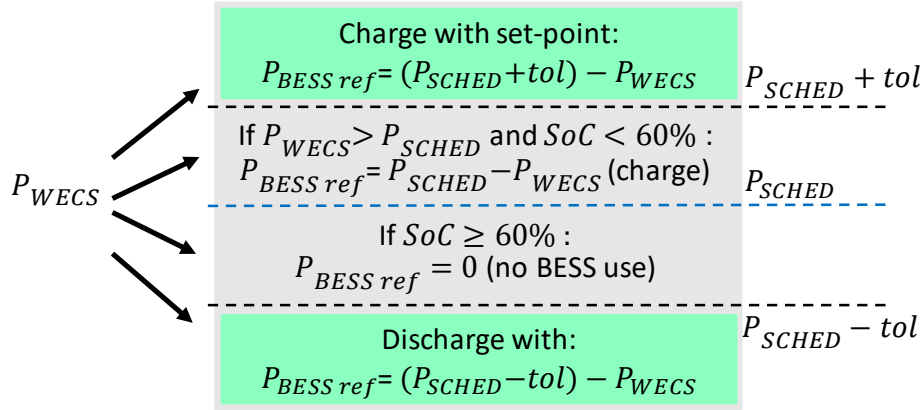


Fig. 5.42. Simple energy management algorithm.

According to this strategy, for productions exceeding the band ceiling ($P_{WECS} > P_{SCHED} + tol$), the target injection is the upper value of the band ($P_{SCHED} + tol$) and the difference is stored in the BESS. If due to the storage system limits a part of the oversupply of power cannot be stored, this excess in the wind turbines production is considered curtailed. On the contrary, if the power production is below the band floor ($P_{WECS} < P_{SCHED} - tol$), the target injection is the lower value of the band ($P_{SCHED} - tol$) and the BESS is discharged. Commitment failures are triggered in the same way as in the case of the optimal management strategy, namely when the power transferred to the grid is outside of the tolerated region for 1 minute.

As for the case when P_{WECS} is within the tolerance band, two possibilities are considered:

- If $P_{SCHED} < P_{WECS} < P_{SCHED} + tol$ and $SoC < 60\%$, the targeted injection is the commitment (P_{SCHED}) and the power excess is stored.
- If $P_{SCHED} - tol < P_{WECS} < P_{SCHED} + tol$ but $SoC \geq 60\%$, the ESS is not charged or discharged

5.3.2 . Simulation results

The injection profiles resulting from simulation using the MPC/QP and rule-based management schemes for the 27-days period (Fig. 5.3.b) with $\lambda_1 = \lambda_2 = 50$, are presented in Fig. 5.43. The injection band upper limit overshooting is higher in the case of the MPC/QP algorithm, for which the curtailment is bigger in this case (0,007 %, against 0 % of the

production curtailed with the rule-based algorithm). On the other hand, the commitment failures and unbilled power totals associated to the proposed strategy are smaller (1,8 % and 0,4 %) than those obtained with the rule-based scheme (8,5 % and 13,6 %). Consequently, the total injection with the MPC/QP controller is 16,6 % higher (MPC/QP : 1 807,3 MWh and rule-based:

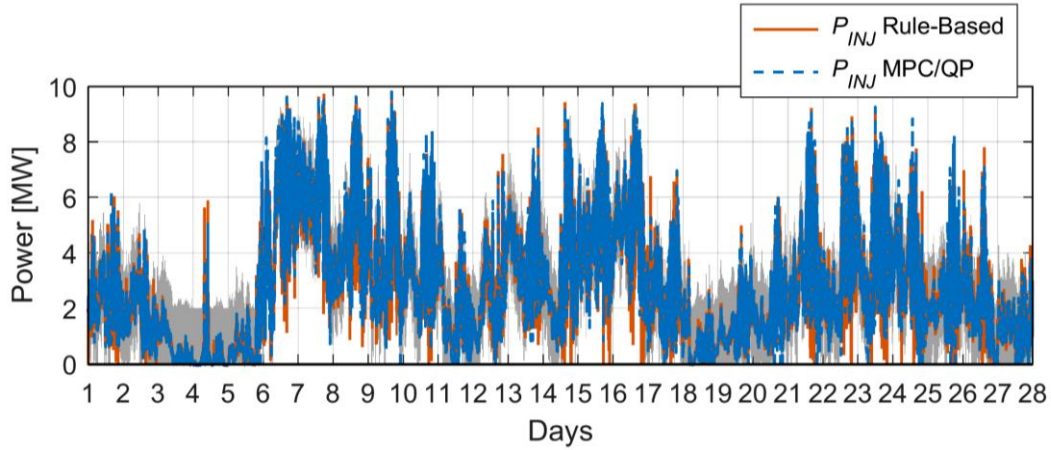


Fig. 5.43. MPC/QP and rule-based algorithms: injection profiles with $\lambda_1=\lambda_2=50$, commitment with maximum 10 % error, initial SoC of 0 % and 50 % as SoC set-point.

1 504,5 MWh).

Fig. 5.44 plots the resulting BESS power signals. The time of no use of the storage system is longer in the case of the scheme based on rules, as can be seen in the figure. The more recurrent non-availability of the ESS translates into lesser filtering of the wind turbine production lacks and excesses and ultimately the smaller injection of power. While the MPC algorithm calls upon the BESS whenever the SoC is not at its maximum or minimum threshold, the rule-based strategy tends to use the BESS at maximum power either during charging or discharging. Thus, the plot of the resulting power obtained from the latter strategy suggests an on/off-like behavior.

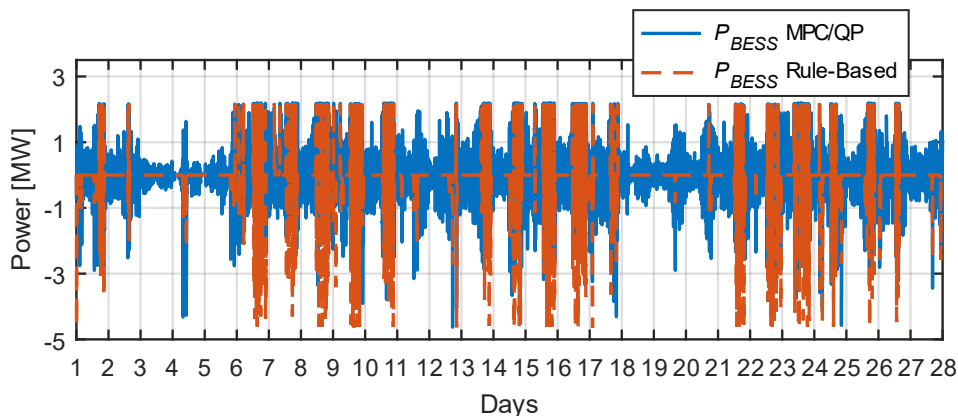


Fig. 5.44. MPC/QP and rule-based algorithms: storage system power with $\lambda_1=\lambda_2=50$, commitment with maximum 10 % error, initial SoC of 50 % and 50 % as SoC set-point.

Fig. 5.45 plots the state-of-charge charts obtained from the algorithms. It is remarked from the figures that the MPC/QP activates several times the constraints SoC^{min} and SoC^{max} , that is, minimum and maximum allowed levels. Under the rule-based algorithm, the SoC evolves between the 40 % and 80 % levels. The cycles accounted are 91,2, for MPC/QP and 15,8, for the strategy based on rules.

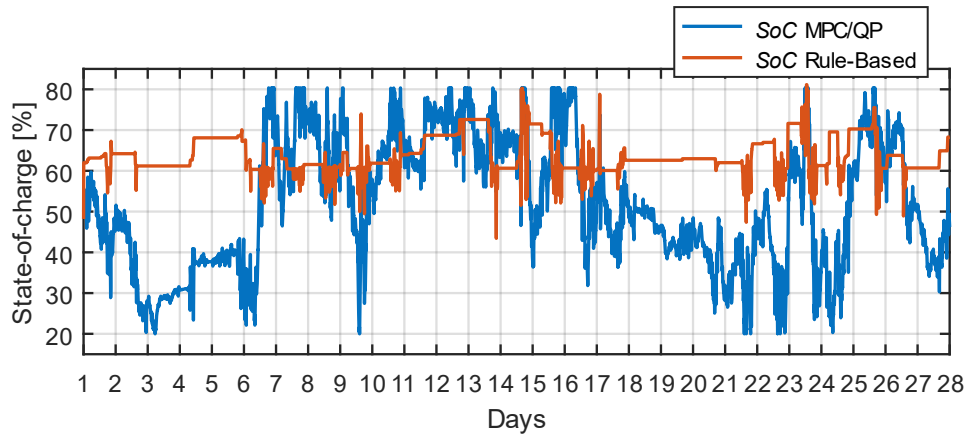


Fig. 5.45. MPC/QP and rule-based algorithms: state-of-charge with $\lambda_1=\lambda_2=50$, commitment with maximum 10 % error, initial SoC of 50 % and 50 % as SoC set-point.

Finally, in Fig. 5.46 are compared to the resulting costs. In this case, the mean of the cost resulting from the control actions calculated by the MPC/QP strategy is higher than the mean cost of the rule-based strategy.

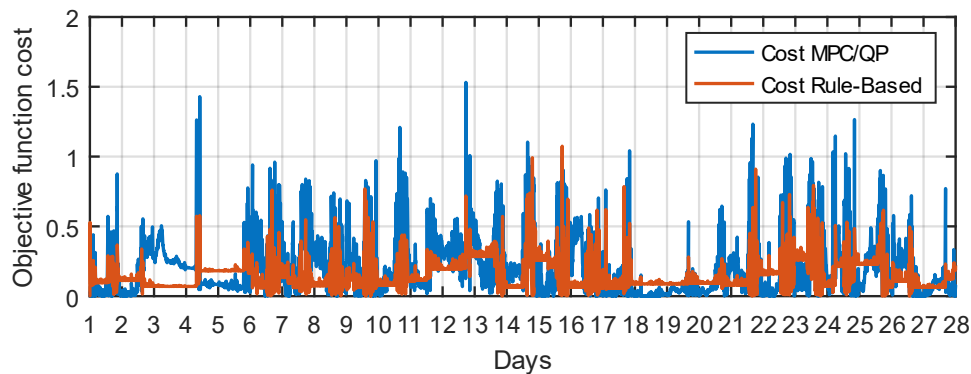


Fig. 5.46. MPC/QP and rule-based algorithms: objective function cost with $\lambda_1=\lambda_2=50$, commitment with maximum 10 % error, initial SoC of 50 % and 50 % as SoC set-point.

In Table 5.18 are included the results obtained from runs of the algorithms using four different ponderations of the control objectives defined.

An additional line was included in the table to account the additional injection obtained through the MPC proposed strategy.

Table 5.18. Results summary 27 days simulation, commitment with maximum 10 % error, initial SoC of 50 % and 50 % as SoC set-point.

Indicator	20-80			50-50		60-40		80-20	
	MPC	RB		MPC	RB	MPC	RB	MPC	RB
CF [%]	1,7	8,5		1,8	8,5	1,7	8,5	1,7	8,5
$P_{not\ billed}$ [%]	0,3	13,6		0,4	13,6	0,4	13,6	0,4	13,6
P_{curt} [%]	5×10^{-4}	0		7×10^{-3}	0	9×10^{-3}	0	1×10^{-2}	0
E_{INJ} [MWh]	1811,2	1504,5		1807,3	1504,5	1806,8	1504,5	1807,5	1504,5
Additional INJ_{MPC} [%]	20,4	-		20,1	-	20,1	-	20,1	-
$BESS$ cycles [-]	45,6	15,8		91,2	15,8	99,6	15,8	111,7	15,8
P_{INJ} error (RPD) [%]	0,18	0,24		0,09	0,24	0,08	0,24	0,06	0,24
SoC error [%]	20,3	27,7		27,2	27,7	27,7	27,7	28,7	27,7
Mean cost [-]	0,15	0,19		0,17	0,13	0,15	0,11	0,10	0,19

5.4 Chapter conclusions

The main objective of the first part of this Chapter was related to the choice of the values for the MPC/QP energy management strategy parameters, that are part of the cost function defined in the framework of the hybrid power plant energy management. Using a simple stochastic approach, three profiles were generated that served during the tests as schedule profiles. The schedule and a reference signal for the state-of-charge have been used as the future input references for the algorithm. Along with the references, a vector containing wind production data was supplied stepwise with a sample time of 1 second. Imposing the initial state-of-charge, the proposed strategy calculates the control actions considering optimizing two control objectives and a set of constraints.

Several case studies were investigated focusing the interest on economic or technical aspects of the HPP operation. The impact of the tuning parameters was figured through simulation, allowing to adapt the strategy to a simulation over a period of 27 days using power production data that has been supplied by the operator of a real wind farm. The simulations results obtained after running several simulations without the electric grid context, have proved the optimization capabilities of the proposed MPC algorithm to the manage of the storage system.

In Chapter 6, the lessons learned are applied to the arbitrage of the HPP to inject power into Sainte-Rose PCC of the Guadeloupean power grid in the PowerFactory environment.

CHAPTER

6

Control strategy implementation and co-simulation between PowerFactory and Matlab

Summary

6.1 Introduction	175
6.2 Control strategy definition in PowerFactory	176
6.3 Study cases and co-simulation results	178
6.3.1 Scenario 1: scheduled injection lower than the actual production	179
6.3.2 Scenario 2: scheduled injection greater than the actual production	181
6.3.3 Scenario 3: scheduled injection lower than actual production and power system disturbance.....	182
6.4 Chapter conclusions	185

Chapter overview

In this Chapter the proposed control and optimization strategy is investigated in order to manage the grid-connected power plant in the context of the Guadeloupean power system using PowerFactory.

6.1 Introduction

Along with the PowerFactory models for the HPP and the island grid that were presented in Chapter 3, a control structure was implemented in PowerFactory. Such a structure is a DIgSILENT Simulation Language model serving as an interface to Matlab. Hence, once the

MPC/QP control and optimization strategy described in Chapter 4 or the simple rule-based algorithm introduced in Chapter 5 are implemented as Matlab functions, those instructions can be executed by PowerFactory to dispatch the power output of the HPP. In this Chapter, a brief description of the implemented control structure is presented, followed by the results obtained through co-simulation between PowerFactory and Matlab for three case studies.

6.2 Control strategy definition in PowerFactory

Storage units converters serve as interface among the HPP and the island grid systems implemented in PowerFactory. The aim of the control structure developed is the generation of power set-points for those converters. During simulations the DSL structure executes a m-file containing a Matlab function describing either the MPC/QP or rule-based algorithm equations. In the case of the predictive control-based strategy, the file also contains the model for control in state-space representation. This is sketched in Fig. 6.1.

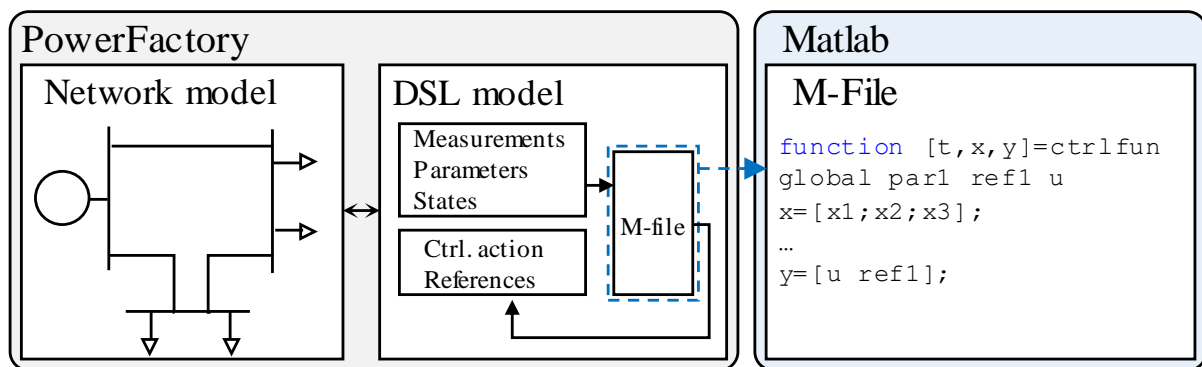


Fig. 6.1. PowerFactory/Matlab co-simulation scheme.

PowerFactory inserts the key signals that are handled by the DSL control structure into a common workspace that can be accessed by Matlab. This way, the simulation takes place in the PowerFactory environment while enabling using the different Matlab functions and toolboxes. The co-simulation can occur, a Matlab's release needs to be installed in the computer where the PowerFactory project is being executed. The linking method here employed is one of several possible approaches. A variation to this interfacing method includes, in addition to the m-file, the use of a Matlab/Simulink model (mdl). References [177-179] discuss the several alternative interfacing methods existing.

The key signals mentioned above are the input and outputs signals received and computed at each timestep through the Matlab script. In Fig. 6.2 and Fig. 6.3 are represented the inputs and outputs of the rule-based and MPC/QP control structures described in DSL. In the case of the rule-based algorithm, the inputs are the current, voltage and *SoC* measurements from the BESS units, voltage and frequency measurements from the PCC, the WECS's instant

power production, and the current element of the firm injection commitment vector. Meanwhile, the outputs are the active and reactive power references to the storage system units' converters. Through the PowerFactory wind farm model, the wind speed dataset presented in Chapter 5 is used to generate instant power production measurements.

Regarding the MPC/QP strategy control structure (Fig. 6.3), the inputs are as in the

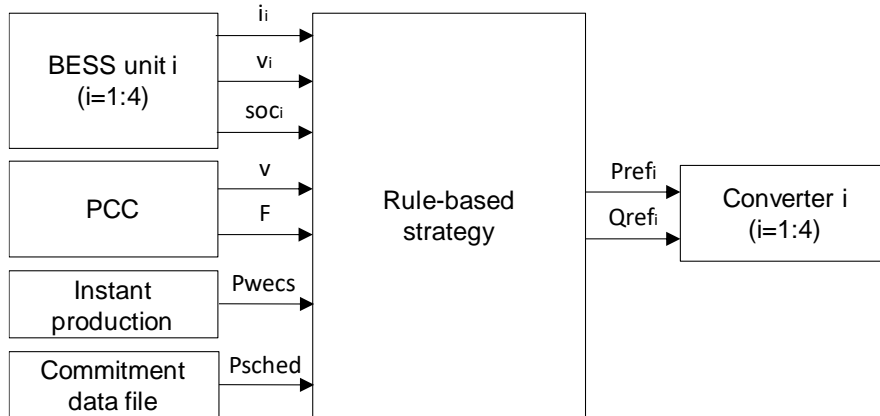


Fig. 6.2. PowerFactory/Matlab rule-based co-simulation implementation scheme.

earlier case except for the references P_{SCHED} and SoC_{ref} that are vectors rather than scalars. Indeed, in accordance with the predictive control philosophy, given a current time k the future control objectives references for the next N_p instants are the samples $k + 1 : k + N_p$ from those reference profiles. Along with the input and output signals, the control structure handles state variables as well as other internal variables and uses the *quadprog* function to determine the

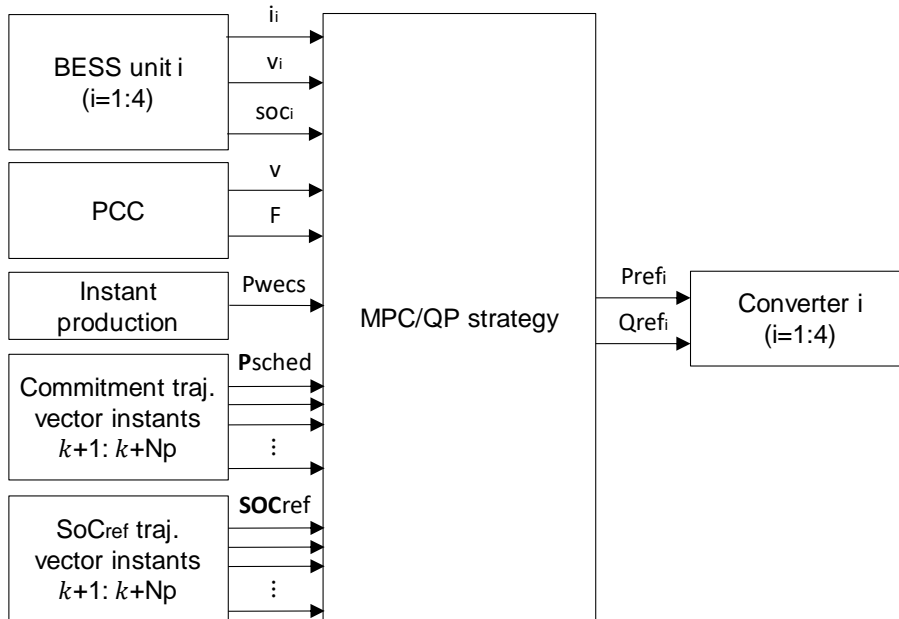


Fig. 6.3. PowerFactory/Matlab MPC/QP co-simulation implementation scheme.

optimal control moves.

In the PowerFactory simulations, the simulation step size measures 20 ms. This value is imposed by the wind turbine system model. Also, the reactive power references are set to zero.

Table 5.2 summarizes the simulation settings employed in the PowerFactory tests.

Table 6.1. Simulation settings for tests in PowerFactory.

Parameter	Description	Unit	Value
T_s	Simulation sample time	ms	20
N_p	Optimization window length	s	10
<i>Tolerance</i>	Injection band tolerance	MW	2

6.3 Study cases and co-simulation results

The production data used in Chapter 5 is also used in the present Chapter as input to the energy management schemes. The situation of loads, reactive compensators and generation units considered for the simulations corresponds to the validation scenario defined in section 3.3.3.2 prior to the disconnection of the unit 2 of Le Moule station (Table 3.7 and Table 3.8).

Table 6.2. PowerFactory implementation: algorithm parameters values Scenario 1, Scenario 2 and Scenario3.

Parameter	Description	Unit	Value
λ_1	Weight of injection cost	-	50
SF_1	Injection cost scale factor	A^2	$[(u^{min} - u^{max})/2]^2$
λ_2	Weight of SoC cost	-	50
SF_2	SoC cost scale factor	$\%^2$	50^2
Q_u	Parameter for adjustment of the control effort	-	0,5
SF_u	Control effort scale factor	A^2	$[(u^{min} - u^{max})/2]^2$
<i>offset</i>	Vertical displacement of P_{SCHED}	MW	-0,2
SoC_{ref}	SoC set-point level	%	50
SoC_{init}	SoC level at the beginning of the simulation	%	70, 30, 23,5
N_p	Optimization window length	s	10

Three simulation cases of the HPP operation are studied with respect to the expected and actual production of the D-day and the initial SoC of the storage system: Scenario 1 considers a power production that is greater than the firm injection commitment and initial SoC near the maximum threshold defined, whereas in Scenarios 2 and 3 the actual power production is below the commitment profile and the initial SoC is close the minimum allowed value. In Scenario 3 only the MPC/QP scheme is tested and the disconnection and reconnection of the biggest generation unit in the system is introduced as perturbation when the storage system SoC is at its minimum (constraint SoC^{min} activated). In opposition to the results presented in the earlier Chapter (Matlab/Simulink simulations), the simulations carried out in PowerFactory consider the HPP in the island grid context.

The commitment profile with maximum 10 % error presented in Chapter 5 is employed. Table 5.13 shows the parameter values used in the simulation of the case studies in PowerFactory.

6.3.1 Scenario 1: scheduled injection lower than the actual production

Scenario 1 investigates the HPP impact on the island grid when the production forecast error is not above 10 %, and the power production is big enough for predominantly requiring the storage system to be charged. Fig. 6.4 presents both the D-1 commitment and the actual generation for the period considered that corresponds to the day 14 of the dataset shown in Fig. 5.3.b. The power produced by the wind turbines during the period analyzed amounts 10,1 MW.

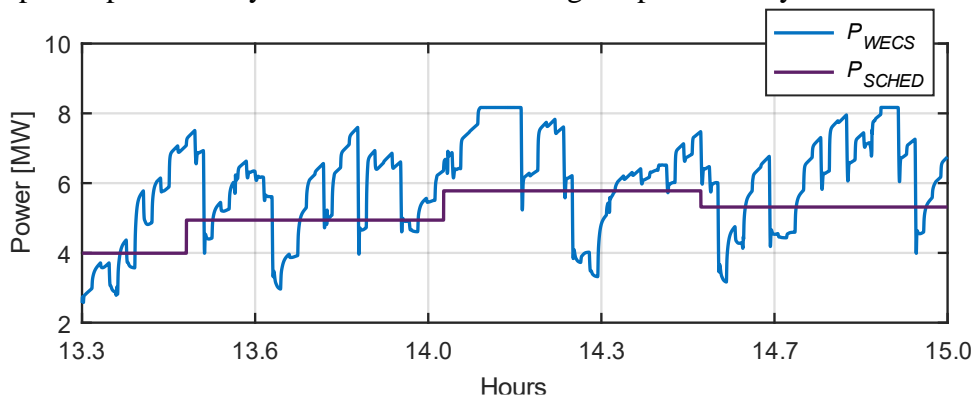


Fig. 6.4. Scenario 1 input data: production and commitment profiles for investigated period.

The resulting injection profiles obtained in PowerFactory from both the proposed algorithm and the rule-based scheme are presented in Fig. 6.5.

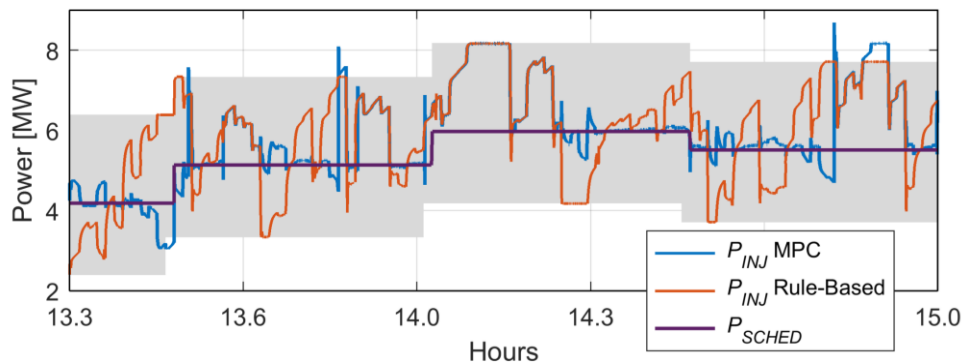


Fig. 6.5. Scenario 1, MPC/QP and rule-based algorithms in PowerFactory: injection profiles with $\lambda_1=\lambda_2=50$, commitment with maximum 10 % error, initial SoC of 70 % and 50 % as SoC set-point.

As can be seen from the figure, the power injected follows the commitment more closely in the case of the MPC/QP algorithm. The resultant injection errors are 11,3 % and 23,6 %, the commitment failures 0 % and 0,7 %, and the total injected power 9,85 MWh and 9,03 MWh for the predictive control and rule-based schemes, respectively. Several peaks in both injection profiles are observed. Relatively rapid variations in the WECS output production originate

those peaks. As shown in Fig. 6.6.a, the predictive control-based algorithm varies P_{BESS} to compensate or to absorb power according to the evolution of the instant production with respect to the commitment. Meanwhile, the rule-based algorithm seeks to avoid the utilization of the

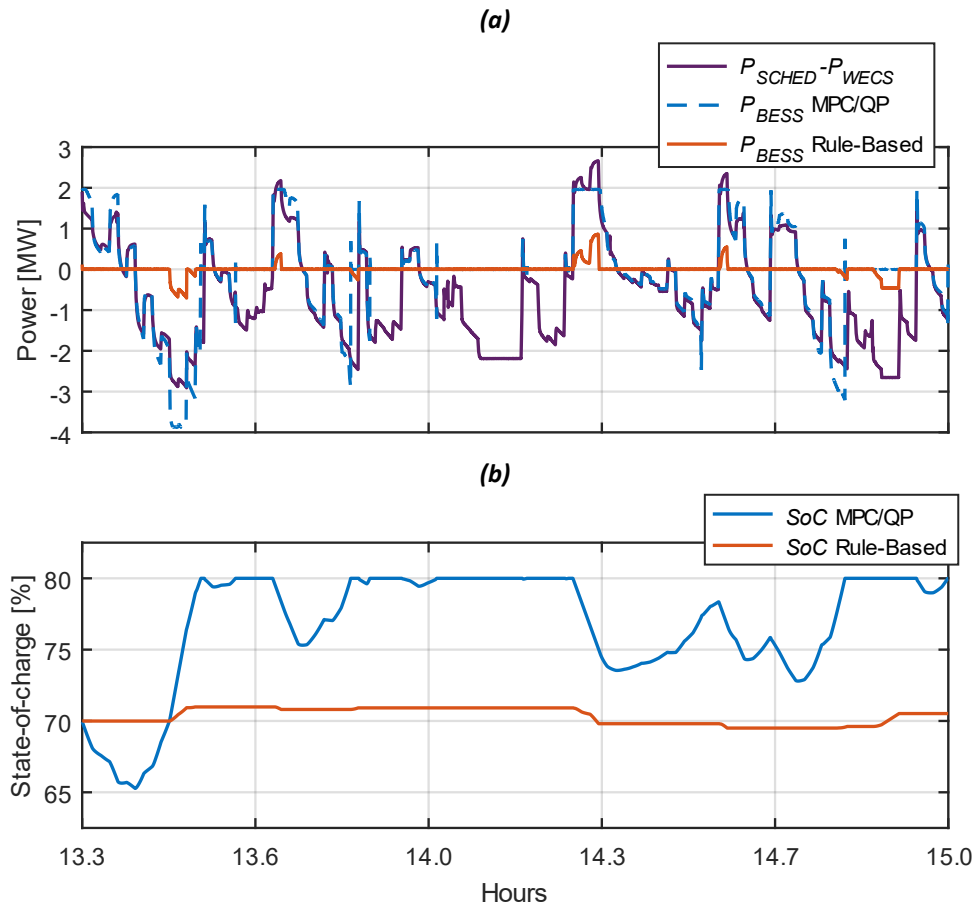


Fig. 6.6. Scenario 1, MPC/QP and rule-based algorithms in PowerFactory: storage system power with $\lambda_1 = \lambda_2 = 50$, commitment with maximum 10 % error, initial SoC of 70 % and 50 % as SoC set-point.

storage system.

With a SoC above 60 % at the beginning of the simulation, the variations in stored energy obtained from the rule-based algorithm are minimal, as shown in Fig. 6.6.b.

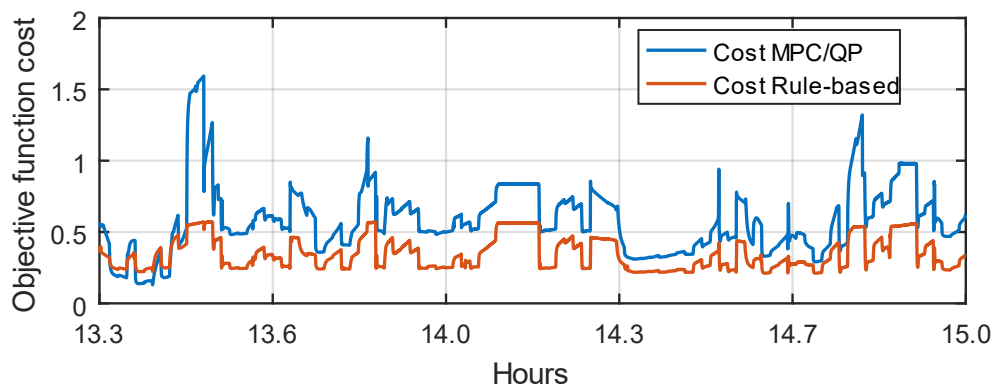


Fig. 6.7. Scenario 1, MPC/QP and rule-based algorithms in PowerFactory: cost with $\lambda_1 = \lambda_2 = 50$, commitment with maximum 10 % error, initial SoC of 70 % and 50 % as SoC set-point.

The MPC/QP strategy presents greater SoC and squared current cost than the rule-based scheme. The costs efforts for both cases are compared in Fig. 6.7, and as can be seen, the MPC/QP total cost is higher.

6.3.2 Scenario 2: scheduled injection greater than the actual production

Scenario 2 investigates the EMS performance during a period where the production is greater than expected. Fig. 6.8 shows the scheduled power injection and the actual power production obtained the day D. The power production data was stored early in the morning during day 14 (Fig. 5.3.b).

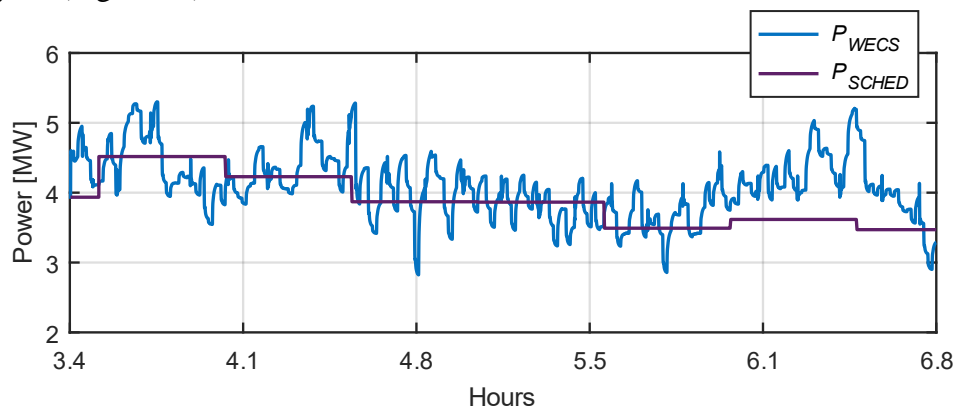


Fig. 6.8. Scenario 2 input data: production and commitment profiles for studied period.

During the period shown the wind turbines generated 14,0 MW. Fig. 6.9 presents the power injection plots, followed by the BESS power and the SoC evolution plots in Fig. 6.10.a and Fig. 6.10.b. The signal P_{BESS} obtained from the algorithm based on simple rules is zero most of the time but for the reasons different than in the earlier case. During the first part of the simulation this algorithm charges from 30 %, initial SoC, until 60%. From there, the variations

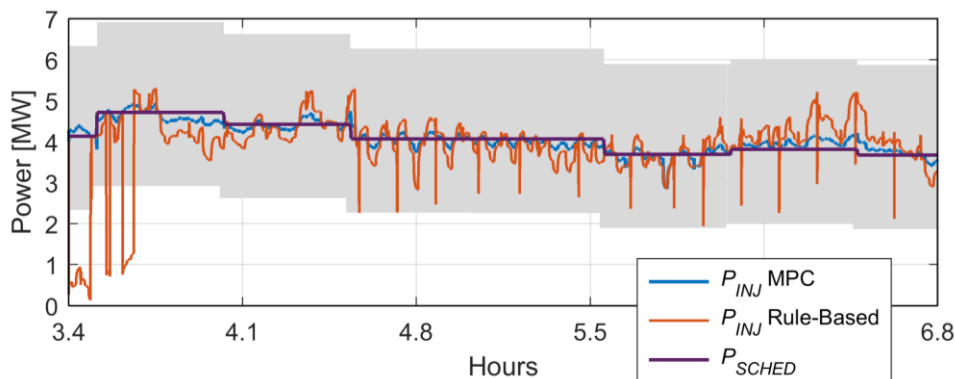


Fig. 6.9. Scenario 2, MPC/QP and rule-based algorithms in PowerFactory: power injection with $\lambda_1=\lambda_2=50$, commitment with maximum 10 % error, initial SoC of 30 % and 50 % as SoC set-point.

in the state-of-charge are minimal.

Unlike the MPC-based controller, the rule-based strategy does not discharge the BESS a single time during the simulation (Fig. 6.10.b). As the initial SoC is smaller than 60 %, whenever P_{WECS} is bigger than P_{SCHED} , the storage system is charged accordingly to the rules explained in section 5.3.1. Then, the charging stops when the 60 % level is reached.

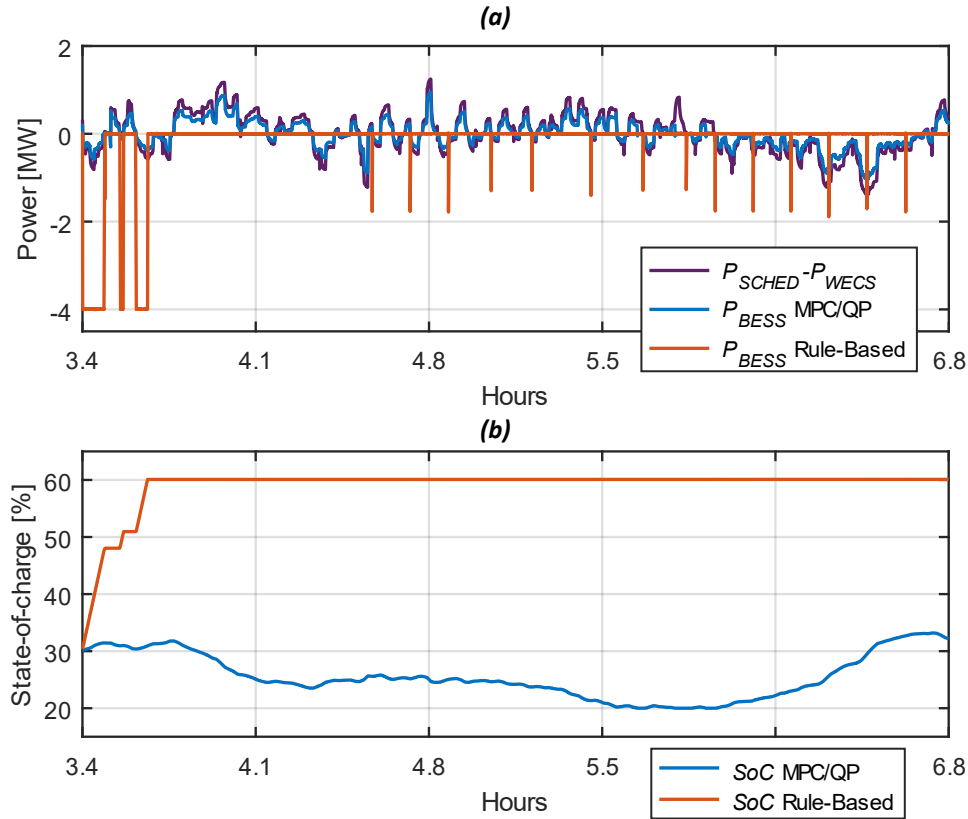


Fig. 6.10. Scenario 2, MPC/QP and rule-based algorithms in PowerFactory: (a) storage system power, and (b) storage system state-of-charge with $\lambda_1 = \lambda_2 = 50$, commitment with maximum 10 % error, initial SoC of 30 % and 50 % as SoC set-point.

As can be seen, the state of charge presents very small variations until the end of the simulation.

6.3.3 Scenario 3: scheduled injection lower than actual production and power system disturbance

In this last Scenario 3, the MPC/algorithm is tested in the PowerFactory environment under an extreme operation condition by including a perturbation in the power grid. As was mentioned, the situation of loads, reactive compensators and generation units in the grid used for the simulations in the present Chapter is the same used in Chapter 3 for the dynamic validation of the grid model. In the present scenario, the generation unit 2 of Le Moule station is disconnected and reconnected with the BESS charged at the minimum admissible level (SoC constraint activated). To do this, the opening and reclosure 50 ms latter of the corresponding

switch in the grid side is configured before the start of the simulation. Fig. 6.11 shows the scheduled injection for the day D+1 and actual production obtained the day D. The total power production for the period with data from day 12 amounts 365,7 MW.

In Fig. 6.12 are presented the resulting injected power profiles, whereas the storage system power and *SoC* plots are shown in Fig. 6.13 and Fig. 6.14.

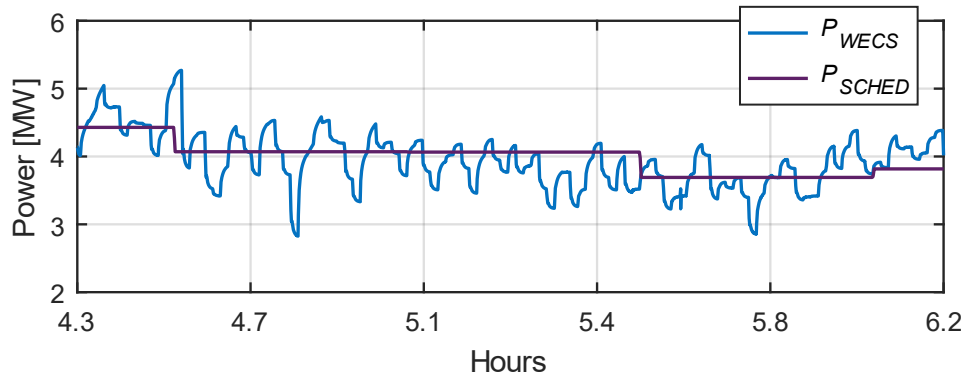


Fig. 6.11. Scenario 3 input data: power production and commitment profiles for studied period.

As the BESS initial *SoC* is below 60 %, from the beginning of the simulation the rule-based algorithm charges the BESS every time the power production is above the commitment.

As in Scenario 2, after the *SoC* reaches 60 % the storage system power becomes zero with several negative peaks associated with concise duration charges (around 10 s each) that affect the power injection.

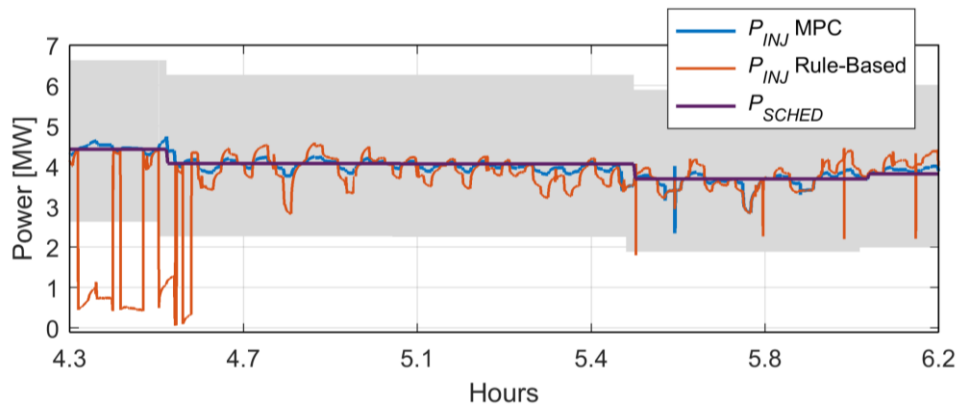


Fig. 6.12. MPC/QP and rule-based algorithms, PowerFactory: power injection profiles with $\lambda_1=\lambda_2=50$, commitment with maximum 10 % error, initial *SoC* of 50 % and 50 % as *SoC* set-point.

Around $t=5,6$ h occurs the disconnection and reconnection of the generation unit. 10 seconds later the oscillation caused on the signal P_{INJ} has been entirely damped, as shown in Fig. 6.15 for both algorithms. During the development of the proposed management strategy, it was found that the wrong parameter tuning of the strategy can lead to unfeasibility of the optimization problem, particularly when the constraints are active. This scenario is considered an extreme condition for the MPC/QP scheme because the disturbance occurs during an off-

peak period with SoC constraint activated. As appreciated in Fig. 6.12 - Fig. 6.14, the perturbation does not stop the two strategies from dispatching the ESS power.

Table 6.3 summarizes the simulation results of the three scenarios considered in the

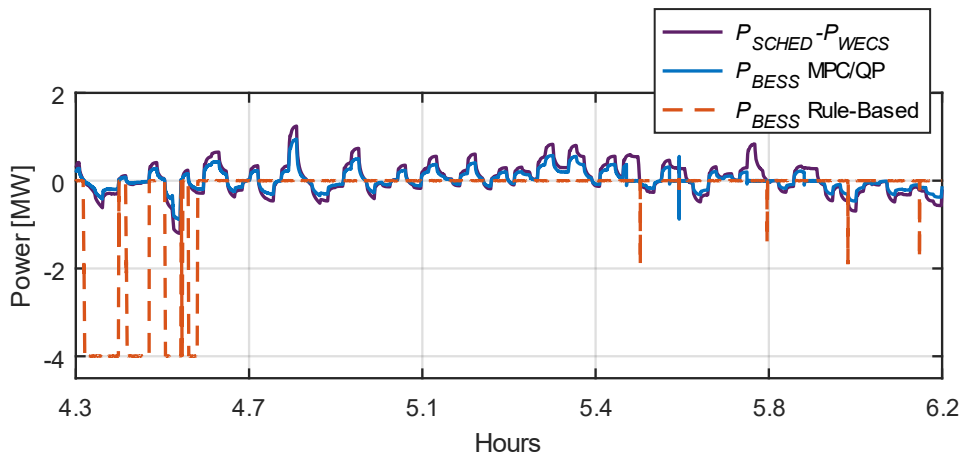


Fig. 6.13. MPC/QP and rule-based algorithms, PowerFactory: power injection profiles with $\lambda_1=\lambda_2=50$, commitment with maximum 10 % error, initial SoC of 50 % and 50 % as SoC set-point.

present Chapter.

In the three cases, the rule-based algorithm presented smaller SoC errors. This happened because the algorithm either reduced the state-of-charge variations to a narrower range (Scenario 1), or conveyed the SoC to evolve closer to the target signal SoC_{ref} (Scenarios 1, 2 and 3), if compared with the decisions made by the MPC/QP scheme. On the opposite, MPC/QP's injection errors were smaller in all the cases.

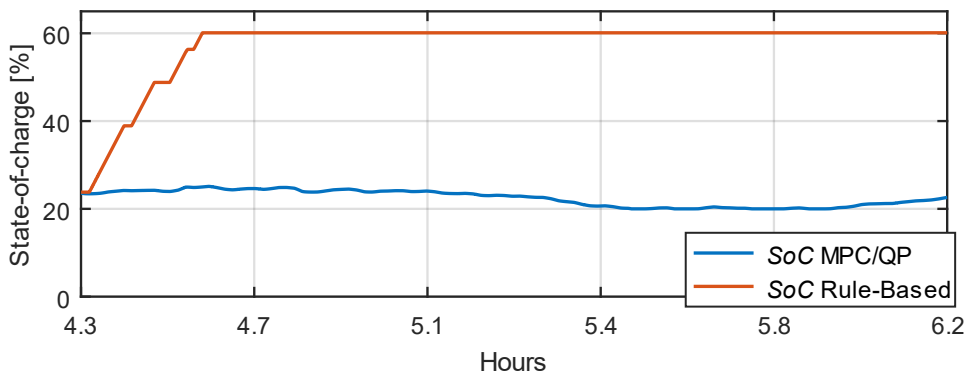


Fig. 6.14. MPC/QP and rule-based algorithms, PowerFactory: power injection profiles with $\lambda_1=\lambda_2=50$, commitment with maximum 10 % error, initial SoC of 50 % and 50 % as SoC set-point.

The injected energy totals were larger with the proposed algorithm, for which the BESS utilization was higher in Scenarios 1 and 2.

While commitment failures, unbilled power and production curtailments were not present at Scenarios 2 and 3, in Scenario 1 the MPC/QP algorithm registered curtailments as around $t=14,8$ h the production is above the tolerated injection region's upper threshold while

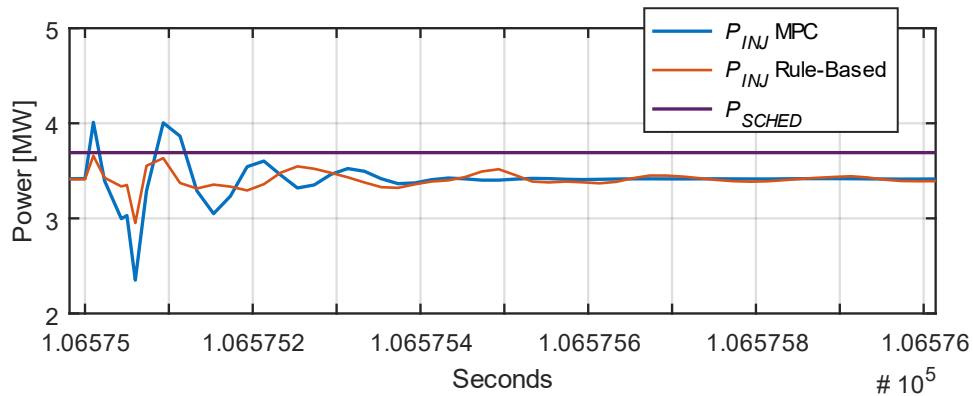


Fig. 6.15. MPC/QP and rule-based algorithms, PowerFactory, zoom around $t=5,6$ h: power injection profiles with $\lambda_1=\lambda_2=50$, commitment with maximum 10 % error, initial SoC of 50 % and 50 % as SoC set-point.

the storage units are fully charged. Meanwhile, the rule-based strategy presented several the storage units are fully charged. Meanwhile, the rule-based strategy presented several overtakes of the band's threshold, the first of them taking place at the first commitment level shift, at $t=13,5$ h. Because of these overtakes, the plant operator cannot bill 8,3 % of the power produced by the wind turbines.

Table 6.3. Results summary of PowerFactory tests.

Indicator	Scenario 1		Scenario 2		Scenario 3	
	MPC/QP	Rule-based	MPC/QP	Rule-based	MPC/QP	Rule-based
CF [%]	0,0	0,7	0,0	0,0	0,0	0,0
$P_{not\ billed}$ [%]	0,0	8,3	0,0	0,0	0,0	0,0
P_{curt} [%]	0,2	0,0	0,0	0,0	0,0	0,0
E_{INJ} [MWh]	9,9	9,0	14,0	13,9	7,4	7,2
BESS cycles [-]	0,5	0,0	0,3	0,2	0,1	0,3
P_{INJ} error [%]	11,3	23,6	3,0	12,0	2,8	14,6
SoC error [%]	53,5	40,7	49,0	19,5	55,1	20,3
Mean cost [-]	0,6	0,3	0,4	0,3	0,4	0,6

6.4 Chapter conclusions

In this Chapter, the PowerFactory/Matlab co-simulation environment has been used to validate the ability of the proposed MPC/QP algorithm to manage the power flow of a wind turbine/BESS power plant connected to the Sainte Rose PCC of the Guadeloupean island power grid. The control structure implemented in DIGSILENT Simulation Language inserts the key control signals into a shared workspace that can be accessed by Matlab. Hence, the simulations integrate the complexity of the Guadeloupean power grid, and the power system analysis and control tools were combined with the mathematical optimization toolbox available in Matlab.

If the co-simulation permitted considering additional models simulation models and power systems analysis tools, a smaller simulation time step made it necessary to reduce the number of samples of the input data. Even in the case of simulations of a few hours, the proposed strategy allowed a better follow-up of the injection targets and a greater transfer of energy towards the utility grid.

The simulation tool implemented for the validation of the management strategy comprises several models (production of electricity with RES, energy storage, weather forecasts and energy conversion) and economic aspects. The control strategy parameters were tuned in this Chapter with values retained from the tests without the grid context, to find through simulation a behavior similar to that obtained in Matlab/Simulink.

The MPC/QP strategy was applied here to the management of a wind farm-battery storage HPP. However, the strategy can be adapted to consider the hybridization of several types of RES-based sources with multiple energy storage technologies, as well as their corresponding physical and technical constraints. Similarly, it can still evolve to accommodate additional grid services such as the supply of voltage and frequency regulation, or the reserve participation.

Conclusions and future research lines

In this PhD study, the energy management strategy for a wind farm-Li-Ion batteries hybrid power plant (HPP) provision of the grid service of complying the day-ahead commitment as the WECS output instantly changes, has been developed. To reach this objective, the storage system is used to absorb the variability in the wind generated power. The power flow is driven using model predictive control and quadratic programming. The strategy minimizes commitment failures while extending the battery energy storage system (BESS) lifetime.

At every control step in the predictive control stage of the strategy, the future system states are estimated over the next 10 seconds. The prediction matrices with all the information of present and future states are sent stepwise to the optimizer, which calculates the control moves over the same period. Comparison to a heuristic decision-making algorithm and analysis of performance indicators revealed the capacity of the strategy to manage the system with up to 30 % forecast error. Co-simulation was also employed to test the EMS using the modelled HPP and island grid.

Therefore, the main contribution of this PhD is the development of an adapted management strategy based on model predictive control and quadratic programming optimization that determines the power flow management of a wind farm-Li-Ion BESS HPP to comply the day-ahead commitment according to the WECS output variations. The solution can be adapted to any number and types of renewable generation and storage technology.

Other contributions of this PhD are summarized as follows:

- Identification of the power and voltage management strategies employed in an island grid along with the grid codes applicable to wind power-based plants in that insular context.
- Identification of the control algorithms that can be used to reactive optimization problems. A detailed analysis of the control algorithms used in the management of hybrid systems has been performed. A final selection has been made considering the need for including the forecasts in the problem.
- Matlab-PowerFactory co-simulation framework: simulation tool for studying the strategy's ability to manage the HPP with respect to the desired operation conditions. Uses the combined power of the mathematical analysis tool Matlab and the dedicated

functionalities of the power system analysis PowerFactory. The co-simulation framework can accommodate different management strategies and architectures of the hybrid plant to test its interaction with the grid.

To complete the research work undertaken during this PhD, the following future research lines were identified:

- Perform a sensitivity analysis for the choice of the weight of the control objectives minimizing the tracking error of the injected power and minimizing the tracking error of the state-of-charge (λ_1 and λ_2).
- Include objectives ancillary services support-related objectives (voltage, frequency, generation reserves) in the cost function.
- Improve the storage system control model (within the predictive controller and the optimization problem) by taking in to account the ageing of the Li-Ion BESS.
- Compute the SoC set-points according to the BESS state-of-health.
- Perform an economic analysis of the proposed strategy.
- Evaluate the intraday market participation of the control of the BESS power. It implies the reception of additional forecast data allowing the update of the injection targets cleared.
- Improve the forecasting method used in the generation of the commitment power injection profiles.

References

- [1] N. Hadjsaïd and J.-C. Sabonnadière, *SmartGrids*: ISTE Ltd., John Wiley & Sons, Ltd, 2012.
- [2] V. Nerubatskyi, O. Plakhtii, O. Ananieva, and O. Zinchenko, "Analysis of the smart grid concept for dc power supply systems " *Industry 4.0* vol. 4, pp. 179-193, 2019.
- [3] M. T. Burr, "Reliability demands drive automation investments," *Fortnightly Magazine*, 1-11-2003.
- [4] (08-12-2020). *Smart Grids*. Available: s3platform.jrc.ec.europa.eu
- [5] D. H. Marin, "Intégration des éoliennes dans les réseaux électriques insulaires," Ecole Centrale de Lille, 2009.
- [6] H. Saadat, "Chapter 12 - Power system control," in *Power System Analysis Third Edition*, 3rd edition ed: PSA Publishing LLC, 2011, pp. 566-615.
- [7] A. Teninge, "PARTICIPATION AUX SERVICES SYSTÈME DE PARCS ÉOLIENS MIXTES : APPLICATION EN MILIEU INSULAIRE," Institut National Polytechnique de Grenoble - INPG, 2009.
- [8] S. Corsi, "Grid Hierarchical Voltage Regulation," in *Voltage Control and Protection in Electrical Power Systems: From System Components to Wide-Area Control*, S. Corsi, Ed., ed London: Springer London, 2015, pp. 161-232.
- [9] T. K. Vrana, D. Flynn, E. Gomez-Lazaro, J. Kiviluoma, D. Marcel, N. Cutululis, *et al.*, "Wind power within European grid codes: Evolution, status and outlook," *WIREs Energy and Environment*, vol. 7, p. e285, 2018/05/01 2018.
- [10] "Basics of Wind Energy Conversion Systems (Weecs)," *Model Predictive Control of Wind Energy Conversion Systems*, pp. 1-60, 2017/02/07 2017.
- [11] E. M. G. Rodrigues, G. J. Osório, R. Godina, A. W. Bizuayehu, J. M. Lujano-Rojas, and J. P. S. Catalão, "Grid code reinforcements for deeper renewable generation in insular energy systems," *Renewable and Sustainable Energy Reviews*, vol. 53, pp. 163-177, 2016/01/01/ 2016.
- [12] A. V. Ntomaris, E. A. Bakirtzis, D. I. Chatzigiannis, C. K. Simoglou, P. N. Biskas, and A. G. Bakirtzis, "Reserve quantification in insular power systems with high wind penetration," in *IEEE PES Innovative Smart Grid Technologies, Europe*, 2014, pp. 1-6.
- [13] T. B. Tsuchida, "Chapter 24 - Renewables Integration on Islands," in *Renewable Energy Integration (Second Edition)*, L. E. Jones, Ed., ed Boston: Academic Press, 2017, pp. 319-329.
- [14] J. Matevosyan, T. Ackermann, and S. M. Bolik, "Technical Regulations for the Interconnection of Wind Farms to the Power System," *Wind Power in Power Systems*, pp. 115-142, 2005/01/21 2005.
- [15] M. Tsili and S. Papathanassiou, "A review of grid code technical requirements for wind farms," *IET Renewable Power Generation*, vol. 3, pp. 308-332, 2009.
- [16] B. S. Rajpurohit, S. N. Singh, and L. Wang, "Electric Grid Connection and System Operational Aspect of Wind Power Generation," in *Wind Energy Conversion Systems: Technology and Trends*, S. M. Mueen, Ed., ed London: Springer London, 2012, pp. 267-293.
- [17] M. Mohseni and S. Islam, "Review of international grid codes for wind power integration: Diversity, technology and a case for global standard," *Renewable and Sustainable Energy Reviews*, vol. 16, pp. 3876–3890, 08/01 2012.
- [18] "Frequency Support Grid Code Requirements for Wind Power Plants," in *Energy Storage in Power Systems*, ed, 2016, pp. 61-91.
- [19] A. Molina-Garcia, A. D. Hansen, E. Muljadi, V. Gevorgian, J. Fortmann, and E. Gomez-Lazaro, "International requirements for large integration of renewable energy sources," in *Large Scale Grid Integration of Renewable Energy Sources*, ed: Institution of Engineering and Technology, 2017, pp. 29-57.

- [20] Q. Wu, "Grid Code Requirements for Wind Power Integration," *Modeling and Modern Control of Wind Power*, pp. 11-36, 2018/01/23 2018.
- [21] E. M. G. Rodrigues, R. Godina, T. D. P. Mendes, J. C. O. Matias, and J. P. S. Catalão, "Influence of Large Renewable Energy Integration on Insular Grid Code Compliance," in *Technological Innovation for Cloud-Based Engineering Systems*, Cham, 2015, pp. 296-308.
- [22] EDF, "Référentiel technique HTB : Relatif aux prescriptions techniques de conception et de fonctionnement pour le raccordement d'une installation de production d'énergie électrique au réseau public des Zones non interconnectées," 2006.
- [23] "Arrêté du 8 mars 2013 fixant les conditions d'achat de l'électricité produite par les installations utilisant l'énergie mécanique du vent situées dans des zones particulièrement exposées au risque cyclonique et disposant d'un dispositif de prévision et de lissage de la production," Ministry of the Ecology and Sustainable Development, Ed., ed, 2013.
- [24] H. Berndt, M. Hermann, H. D. Kreye, R. Reinisch, U. Scherer, and J. Vanzetta, "Transmission Code 2007: Network and System Rules of the German Transmission System Operators," 2007.
- [25] EirGrid, "EirGrid Grid Code - Version 8," 2014.
- [26] EDF, "Référentiel Technique SEI REF 04 (V6) - Protection de découplage pour le raccordement d'une production décentralisée en HTA et en BT dans les zones non interconnectées," 2014.
- [27] Y. Wang, G. Delille, H. Bayem, X. Guillaud, and B. Francois, "High Wind Power Penetration in Isolated Power Systems—Assessment of Wind Inertial and Primary Frequency Responses," *IEEE Transactions on Power Systems*, vol. 28, pp. 2412-2420, 2013.
- [28] P. Keung, P. Li, H. Banakar, and B. T. Ooi, "Kinetic Energy of Wind-Turbine Generators for System Frequency Support," *IEEE Transactions on Power Systems*, vol. 24, pp. 279-287, 2009.
- [29] E.ON Netz GmbH, "Grid code - high and extra high voltage," 2006.
- [30] F. Iov, A. D. Hansen, P. Sorensen, and N. A. Cutululis, "Mapping of grid faults and grid codes," Technical University of Denmark, Roskilde, Denmark 2007.
- [31] T. y. C. Ministerio de Industria, "P.O. 12.2 - SEIE: Instalaciones conectadas a la red de transporte de energia eléctrica: Requisitos mínimos de diseño, equipamiento, funcionamiento y seguridad y puesta en servicio," 2009.
- [32] Red Eléctrica de Espana, "Procedimientos de operación no peninsulares," 2006.
- [33] Red Eléctrica de Espana, "P.O. 12.3: Requisitos de respuesta frente a huecos de tensión de las instalaciones eólicas," 2006.
- [34] "Generating Systems Based on Renewable Power," in *Energy Storage in Power Systems*, ed, 2016, pp. 25-59.
- [35] S. Heier, "Frontmatter," in *Grid Integration of Wind Energy - Onshore and Offshore Conversion Systems*, ed: John Wiley & Sons, Ltd, 2014, pp. x-xii.
- [36] International geothermal association (IGA). (2020). *2020 to become a milestone year for the global geothermal energy sector*. Available: <https://www.geothermal-energy.org>
- [37] WindEurope, "Wind energy in Europe in 2019: Trends and statistics," ed, 2020.
- [38] WindEurope, "Our energy, our future: How offshore wind will help Europe go carbon-neutral," 2019.
- [39] N. Hadjsaïd and J. Sabonnadière, "Liberalization of Energy Markets," in *Power Systems and Restructuring*, ed: John Wiley & Sons, Ltd, 2013, pp. 391-418.
- [40] N. Mazzi and P. Pinson, "10 - Wind power in electricity markets and the value of forecasting," in *Renewable Energy Forecasting*, G. Kariniotakis, Ed., ed: Woodhead Publishing, 2017, pp. 259 - 278.
- [41] P. Haessig, B. Multon, H. Ben Ahmed, S. Lascaud, and P. Bondon, "Energy storage sizing for wind power: impact of the autocorrelation of day-ahead forecast errors," *Wind Energy*, vol. 18, pp. 43-57, 2015-01 2015.
- [42] H. Zhao, Q. Wu, S. Hu, H. Xu, and C. N. Rasmussen, "Review of energy storage system for wind power integration support," *Applied Energy*, vol. 137, pp. 545-553, January 1, 2015 2015.
- [43] S. Tewari and N. Mohan, "Value of NAS Energy Storage Toward Integrating Wind: Results From the Wind to Battery Project," *IEEE Transactions on Power Systems*, vol. 28, pp. 532-541, 2013.

- [44] G. Celli, S. Mocci, F. Pilo, and M. Loddo, "Optimal integration of energy storage in distribution networks," in *2009 IEEE Bucharest PowerTech*, 2009, pp. 1-7.
- [45] J. Morren, S. W. H. d. Haan, W. L. Kling, and J. A. Ferreira, "Wind turbines emulating inertia and supporting primary frequency control," *IEEE Transactions on Power Systems*, vol. 21, pp. 433-434, 2006.
- [46] "Energy storage for grid connected wind generation applications - EPRI-DOE handbook supplement," 2004.
- [47] L. Wang, J. Yu, and Y. Chen, "Dynamic stability improvement of an integrated offshore wind and marine-current farm using a flywheel energy-storage system," *IET Renewable Power Generation*, vol. 5, pp. 387-396, 2011.
- [48] L. Wang, S. Chen, W. Lee, and Z. Chen, "Dynamic Stability Enhancement and Power Flow Control of a Hybrid Wind and Marine-Current Farm Using SMES," *IEEE Transactions on Energy Conversion*, vol. 24, pp. 626-639, 2009.
- [49] H. T. Le, S. Santoso, and T. Q. Nguyen, "Augmenting Wind Power Penetration and Grid Voltage Stability Limits Using ESS: Application Design, Sizing, and a Case Study," *IEEE Transactions on Power Systems*, vol. 27, pp. 161-171, 2012.
- [50] P. S. Moura and A. T. de Almeida, "The role of demand-side management in the grid integration of wind power," *Applied Energy*, vol. 87, pp. 2581-2588, 2010/08/01/ 2010.
- [51] A. Ahmarinezhad, M. Abroshan, N. M. Tabatabaei, and N. Bizon, "Overview of Hybrid Power System," in *Analysis, Control and Optimal Operations in Hybrid Power Systems: Advanced Techniques and Applications for Linear and Nonlinear Systems*, N. Bizon, H. Shayeghi, and N. Mahdavi Tabatabaei, Eds., ed London: Springer London, 2013, pp. 1-39.
- [52] B. Zohuri, "Hybrid Renewable Energy Systems," in *Hybrid Energy Systems: Driving Reliable Renewable Sources of Energy Storage*, ed, 2018, pp. 1-38.
- [53] M. Sechilariu and F. Locment, "Chapter 3 - Backup Power Resources for Microgrid," in *Urban DC Microgrid*, M. Sechilariu and F. Locment, Eds., ed: Butterworth-Heinemann, 2016, pp. 93-132.
- [54] I. Dincer and C. Zamfirescu, "Chapter 8 - Integrated Power Generating Systems," in *Advanced Power Generation Systems*, I. Dincer and C. Zamfirescu, Eds., ed Boston: Elsevier, 2014, pp. 455-516.
- [55] (04-02-2019). *Technology innovation for the local scale optimum integration of battery energy storage*. Available: <https://www.tiloshorizon.eu/>
- [56] Eunice Energy Group. (04-02-2019). *Systems with RES & battery storage: TILOS Project, Greece*. Available: <http://tkm.tee.gr>
- [57] Eunice Energy Group. (2018, 04-02-2019). *TILOS Project*. Available: <http://eunice-group.com>
- [58] ABB. (04-02-2019). *Ross Island research station*. Available: <https://new.abb.com>
- [59] Endesa S.A. (04-02-2019). *El Hierro, an example of sustainability*. Available: <https://www.endesa.com>
- [60] P. Tisheva. (2018, 04-02-2019). *Spain's El Hierro 100% renewable powered for 18 days*. Available: <https://renewablesnow.com>
- [61] M. Á. M. Q. Fernández Centeno, Agustín; Quintero Gutiérrez, Juan Manuel; Nueda, Rafael Caballero; Hart, John. (2012, 04-02-2019). *Creating a Hybrid Hydro-Wind System on a Spanish Island*. Available: <https://www.hydroworld.com>
- [62] (04-02-2019). *Kodiak Alaska Microgrid*. Available: <http://microgridprojects.com/>
- [63] ABB. (2019). *Microgrid, BESS and Distributed Generation Solutions*. Available: <http://search-ext.abb.com>
- [64] A. K. Rohit, K. P. Devi, and S. Rangnekar, "An overview of energy storage and its importance in Indian renewable energy sector: Part I – Technologies and Comparison," *Journal of Energy Storage*, vol. 13, pp. 10-23, October 1, 2017 2017.
- [65] S. Ould Amrouche, D. Rekioua, T. Rekioua, and S. Bacha, "Overview of energy storage in renewable energy systems," *International Journal of Hydrogen Energy*, vol. 41, pp. 20914-20927, 12/2016 2016.

- [66] A. Tuohy and M. O'Malley, "Wind Power and Storage," in *Wind Power in Power Systems*, ed: John Wiley & Sons, Ltd, 2012, pp. 465-487.
- [67] Enercon GmbH. (2018, 28-02-2019). *Husahagi Wind Power Plant and Battery Energy Storage System*. Available: <https://www.etip-snet.eu>
- [68] Wind Europe. (04-02-2019). *Database for wind + storage co-located projects*. Available: <https://windeurope.org>
- [69] J. Dallard, A. Ballereau, X. Peng, and E. Drouet. (2018, Using hydrogen to reach self-sufficiency. *Pour la Science (485)*. Available: <https://www.pourlascience.fr>
- [70] MINES ParisTech. (2018, 28-04-2019). Engie Lab: visit of the SPORE microgrid site on the island of Semakau. *INF'OSE Monthly energy magazine (131)*. Available: <http://ose.cma.mines-paristech.fr>
- [71] l'EnerGeek. (2016, 07-03-2019). *Stockage d'énergie sous-marin : Hydrostor solutionne le problème de l'intermittence des ENR*. Available: <https://lenergeek.com>
- [72] P. Drown. (2017, 07-03-2019). *Implications of a Lithium-Ion Storage Transformation*. Available: www.power-eng.com
- [73] (07-03-2019). *Hydrostor, advanced compress air energy technology*. Available: www.hydrostor.ca
- [74] IEC (International Electrotechnical Commission), "White Paper, Electrical Energy Storage," ed. Geneva, Switzerland, 2011.
- [75] R. L. Hales. (2015, 30-04-2019). *Ireland's First Combined Ultracapacitor & Battery Energy Storage Facility* Available: www.smartmpower.com
- [76] E. Burke-Kennedy. (2015, 30-04-2019). *Over 23% of electricity demand now supplied through wind*. Available: www.irishtimes.com
- [77] M. Y. Worku and M. A. Abido, "Fault Ride-Through and Power Smoothing Control of PMSG-Based Wind Generation Using Supercapacitor Energy Storage System," *Arabian Journal for Science and Engineering*, vol. 44, pp. 2067-2078, MAR 2019 2019.
- [78] DOE and EPRI, "DOE/EPRI 2013 Electricity Storage Handbook in Collaboration with NRECA," ed, 2013, p. 340.
- [79] S. Faias, P. Santos, J. Sousa, and R. Castro, "An overview on short and long-term response energy storage devices for power systems applications," *Renewable Energy and Power Quality Journal*, vol. 1, pp. 442-447, 03/2008 2008.
- [80] M. H. Ali, B. Wu, and R. A. Dougal, "An Overview of SMES Applications in Power and Energy Systems," *IEEE Transactions on Sustainable Energy*, vol. 1, pp. 38-47, April 2010 2010.
- [81] P. Mukherjee and V. V. Rao, "Superconducting magnetic energy storage for stabilizing grid integrated with wind power generation systems," *Journal of Modern Power Systems and Clean Energy*, vol. 7, pp. 400-411, mars 1, 2019 2019.
- [82] Centre for Renewable Energy Sources and Saving (CRES). (04-02-2019). *The pilot project 'Agios Efstratios-Green Island'*. Available: <http://www.rae.gr/>
- [83] Fraunhofer IWES and DERlab. (04-02-2019). *Overview of Microgrids in Europe: Developments in system operation and research and test facilities*. Available: <http://microgrid-symposiums.org>
- [84] Tetra tech. (2018, 04-02-2019). *Auwahi wind farm habitat conservation plan*. Available: <https://dlnr.hawaii.gov>
- [85] (04-02-2019). *Nijjima Island Microgrid - Takaoka Toko Ltd*. Available: <https://www.energystorageexchange.org>
- [86] Tepco. (2017, 04-02-2019). *TEPCO's Initiatives for "Smart Grid": NEDO Demonstration Project in "Nijjima-Island"*. Available: <https://www.nedo.go.jp>
- [87] A. Awasthi, V. Karthikeyan, V. Das, S. Rajasekar, and A. K. Singh, "Energy Storage Systems in Solar-Wind Hybrid Renewable Systems," in *Smart Energy Grid Design for Island Countries: Challenges and Opportunities*, F. M. R. Islam, K. A. Mamun, and M. T. O. Amanullah, Eds., ed Cham: Springer International Publishing, 2017, pp. 189-222.

- [88] M. Jannati, S. H. Hosseini, B. Vahidi, and G.-J. Li, "A survey on energy storage resources configurations in order to propose an optimum configuration for smoothing fluctuations of future large wind power plants," *Renewable and Sustainable Energy Reviews*, vol. 29, pp. 158-172, 1/2014 2014.
- [89] A. Iovine, S. B. Siad, A. Benchaib, and G. Damm, "Management of the interconnection of intermittent photovoltaic systems through a DC link and storage," *European Research Consortium for Informatics and Mathematics*, 2014.
- [90] B. Housseini, A. F. Okou, and R. Beguenane, "Robust Nonlinear Controller Design for On-Grid/Off-Grid Wind Energy Battery-Storage System," *IEEE Transactions on Smart Grid*, vol. 9, pp. 5588-5598, November 2018 2018.
- [91] E. Fertig, J. Apt, P. Jaramillo, and W. Katzenstein, "The effect of long-distance interconnection on wind power variability," *Environmental Research Letters*, vol. 7, p. 034017, August 2012 2012.
- [92] J. Kiviluoma, H. Holttinen, D. Weir, R. Scharff, L. Söder, N. Menemenlis, *et al.*, "Variability in large-scale wind power generation," *Wind Energy*, vol. 19, pp. 1649-1665, 2016 2016.
- [93] X. Dai, K. Zhang, J. Geng, Q. Liu, Y. Wang, K. Yuan, *et al.*, "Study on variability smoothing benefits of wind farm cluster," *TURKISH JOURNAL OF ELECTRICAL ENGINEERING & COMPUTER SCIENCES*, vol. 26, pp. 1894-1908, 2018-7-27 2018.
- [94] R. Sarrias-Mena, L. M. Fernandez-Ramirez, C. Andres Garcia-Vazquez, and F. Jurado, "Fuzzy logic based power management strategy of a multi-MW doubly-fed induction generator wind turbine with battery and ultracapacitor," *Energy*, vol. 70, pp. 561-576, JUN 1 2014 2014.
- [95] P. Ngoc, T. Pham, B. Seddik, and D. Roye, *Optimal operation for a wind-hydro power plant to participate to ancillary services*, 2009.
- [96] Y. Riffonneau, S. Bacha, F. Barruel, and A. Delaille, "Energy flow management in grid connected PV systems with storage - A deterministic approach," in *2009 IEEE International Conference on Industrial Technology*, 2009, pp. 1-6.
- [97] I. Vechiu, O. Curea, and H. Camblong, "Transient Operation of a Four-Leg Inverter for Autonomous Applications With Unbalanced Load," *IEEE Transactions on Power Electronics*, vol. 25, pp. 399-407, 2010.
- [98] S. Semaoui, A. Hadj Arab, S. Bacha, and B. Azoui, "The new strategy of energy management for a photovoltaic system without extra intended for remote-housing," *Solar Energy*, vol. 94, pp. 71-85, 2013/08/01/ 2013.
- [99] A. Etxeberria, I. Vechiu, H. Camblong, S. Kreckelbergh, and S. Bacha, "Operational limits of a three level neutral point clamped converter used for controlling a hybrid energy storage system," *Energy Conversion and Management*, vol. 79, pp. 97-103, 2014/03/01/ 2014.
- [100] S. Aissou, D. Rekioua, N. Mezzai, T. Rekioua, and S. Bacha, "Modeling and control of hybrid photovoltaic wind power system with battery storage," *Energy Conversion and Management*, vol. 89, pp. 615-625, 2015/01/01/ 2015.
- [101] K. Hajar, A. Hably, S. Bacha, A. Elrafhi, and Z. Obeid, "An application of a centralized model predictive control on microgrids," in *EPEC 2016 - IEEE Electrical Power and Energy Conference*, Ottawa, Canada, 2016.
- [102] S. Baudoin, I. Vechiu, H. Camblong, J.-M. Vinassa, and L. Barelli, "Sizing and control of a Solid Oxide Fuel Cell/Gas microTurbine hybrid power system using a unique inverter for rural microgrid integration," *Applied Energy*, vol. 176, pp. 272-281, 2016/08/15/ 2016.
- [103] Q. Tabart, I. Vechiu, A. Etxeberria, and S. Bacha, "Hybrid Energy Storage System Microgrids Integration for Power Quality Improvement Using Four-Leg Three-Level NPC Inverter and Second-Order Sliding Mode Control," *IEEE Transactions on Industrial Electronics*, vol. 65, pp. 424-435, 2018.
- [104] S. Jupin, I. Vechiu, and G. Tapia-Otaegui, "Universal switched state-space representation for model predictive control of power converters," *Electric Power Systems Research*, vol. 180, p. 106120, 2020/03/01/ 2020.

- [105] D. Y. Yamashita, I. Vechiu, and J.-P. Gaubert, "A review of hierarchical control for building microgrids," *Renewable and Sustainable Energy Reviews*, vol. 118, p. 109523, 2020/02/01/ 2020.
- [106] Y. Riffonneau, "Gestion des flux énergétiques dans un système photovoltaïque avec stockage connecté au réseau : application à l'habitat," Joseph Fourier University, 2010.
- [107] R. Rigo-Mariani, "Méthodes de conception intégrée "dimensionnement- gestion" par optimisation d'un micro-réseau avec stockage," Laboratoire Plasma et Conversion d'Energie - LAPLACE, Université de Toulouse, 2015.
- [108] R. Rigo-Mariani, B. Sareni, and X. Roboam, "Integrated Optimal Design of a Smart Microgrid With Storage," *IEEE Transactions on Smart Grid*, vol. PP, pp. 1-9, 2016 2016.
- [109] O. H. Mohammed, Y. Amirat, M. Benbouzid, S. Haddad, and G. Feld, "Optimal sizing and energy management of hybrid wind/tidal/PV power generation system for remote areas: Application to the Ouessant French Island," in *IECON 2016 - 42nd Annual Conference of the IEEE Industrial Electronics Society*, 2016, pp. 4205-4210.
- [110] R. Belfkira, C. Nichita, P. Reghem, and G. Barakat, "Modeling and optimal sizing of hybrid renewable energy system," in *2008 13th International Power Electronics and Motion Control Conference*, 2008, pp. 1834-1839.
- [111] D. Abbes, A. Martinez, G. Champenois, and J.-P. Gaubert, *Etude d'un système hybride éolien photovoltaïque avec stockage. Dimensionnement et analyse du cycle de vie* vol. 15, 2010.
- [112] O. H. Mohammed, Y. Amirat, and M. Benbouzid, "Particle Swarm Optimization Of a Hybrid Wind/Tidal/PV/Battery Energy System. Application To a Remote Area In Bretagne, France," *Energy Procedia*, vol. 162, pp. 87-96, 2019/04/01/ 2019.
- [113] P. Haessig, T. Kovaltchouk, B. Multon, H. Ben Ahmed, and S. Lascaud, *Computing an Optimal Control Policy for an Energy Storage*, 2013.
- [114] Y. Riffonneau, S. Bacha, F. Barruel, and S. Ploix, "Optimal Power Flow Management for Grid Connected PV Systems With Batteries," *IEEE Transactions on Sustainable Energy*, vol. 2, pp. 309-320, 2011.
- [115] Zaheeruddin and M. Manas, "Renewable energy management through microgrid central controller design: An approach to integrate solar, wind and biomass with battery," *Energy Reports*, vol. 1, pp. 156-163, 2015.
- [116] S. Kim, S. Bae, Y. C. Kang, and J. Park, "Energy Management Based on the Photovoltaic HPCS With an Energy Storage Device," *IEEE Transactions on Industrial Electronics*, vol. 62, pp. 4608-4617, July 2015 2015.
- [117] R. Bourbon, S. U. Ngueveu, X. Roboam, B. Sareni, C. Turpin, and D. Hernandez-Torres, "Energy management optimization of a smart wind power plant comparing heuristic and linear programming methods," *Mathematics and Computers in Simulation*, vol. 158, pp. 418-431, April 1, 2019 2019.
- [118] J. Zou, C. Peng, J. Shi, X. Xin, and Z. Zhang, "State-of-charge optimising control approach of battery energy storage system for wind farm," *IET Renewable Power Generation*, vol. 9, pp. 647-652, 2015 2015.
- [119] L. Aldjia, K. Mohamed, A. Djalloul, and A. Chaib, "Energy management and control of a hybrid water pumping system with storage," *Applied Solar Energy*, vol. 53, pp. 190-198, 2017-04-01 2017.
- [120] H. Kirchsteiger, P. Rechberger, and G. Steinmaurer, "Cost-optimal Control of Photovoltaic Systems with Battery Storage under Variable Electricity Tariffs," *e & i Elektrotechnik und Informationstechnik*, vol. 133, pp. 371-380, 12/2016 2016.
- [121] S. Teleke, M. E. Baran, S. Bhattacharya, and A. Q. Huang, "Rule-based control of battery energy storage for dispatching intermittent renewable sources," *IEEE Transactions on Sustainable Energy*, vol. 1, pp. 117-124, 2010.
- [122] H. H. Abdeltawab and Y. A.-R. I. Mohamed, "Market-Oriented Energy Management of a Hybrid Wind-Battery Energy Storage System Via Model Predictive Control With Constraint Optimizer," *IEEE Transactions on Industrial Electronics*, vol. 62, pp. 6658-6670, 2015.

- [123] K. T. Tan, B. Sivaneasan, X. Y. Peng, and P. L. So, "Control and Operation of a DC Grid-Based Wind Power Generation System in a Microgrid," *IEEE Transactions on Energy Conversion*, vol. 31, pp. 496-505, June 2016 2016.
- [124] J. Hu, Y. Shan, Y. Xu, and J. M. Guerrero, "A coordinated control of hybrid ac/dc microgrids with PV-wind-battery under variable generation and load conditions," *International Journal of Electrical Power & Energy Systems*, vol. 104, pp. 583-592, 01/2019 2019.
- [125] M.-H. Lin, J.-F. Tsai, and C.-S. Yu, "A review of deterministic optimization methods in engineering and management," *Mathematical Problems in Engineering*, vol. 2012, 2012.
- [126] A. Chaouachi, R. M. Kamel, R. Andoulsi, and K. Nagasaka, "Multiobjective Intelligent Energy Management for a Microgrid," *IEEE Transactions on Industrial Electronics*, vol. 60, pp. 1688-1699, April 2013 2013.
- [127] M. Tavakkoli, E. Pouresmaeil, R. Godina, I. Vechiu, and J. P. S. Catalão, "Optimal Management of an Energy Storage Unit in a PV-Based Microgrid Integrating Uncertainty and Risk," *Applied Sciences*, vol. 9, p. 169, 2019/1 2019.
- [128] M. S. Taha, H. H. Abdeltawab, and Y. A. I. Mohamed, "An Online Energy Management System for a Grid-Connected Hybrid Energy Source," *IEEE Journal of Emerging and Selected Topics in Power Electronics*, vol. 6, pp. 2015-2030, December 2018 2018.
- [129] Y. Zhang, L. Fu, W. Zhu, X. Bao, and C. Liu, "Robust model predictive control for optimal energy management of island microgrids with uncertainties," *Energy*, vol. 164, pp. 1229-1241, December 1, 2018.
- [130] A. Lew and H. Mauch, "Applications of Dynamic Programming," in *Dynamic Programming: A Computational Tool*, ed Berlin, Heidelberg: Springer Berlin Heidelberg, 2007, pp. 45-100.
- [131] B. Heymann, J. F. Bonnans, P. Martinon, F. J. Silva, F. Lanas, and G. Jiménez-Estévez, "Continuous optimal control approaches to microgrid energy management," *Energy Systems*, vol. 9, pp. 59-77, 2018 February 01 2018.
- [132] M. Moshref-Javadi. *Heuristic Design and Optimization*. Available: <http://www.mit.edu>
- [133] C. Chen, S. Duan, T. Cai, B. Liu, and G. Hu, "Smart energy management system for optimal microgrid economic operation," *IET Renewable Power Generation*, vol. 5, pp. 258-267, May 2011 2011.
- [134] J. Radosavljević, M. Jevtić, and D. Klimenta, "Energy and operation management of a microgrid using particle swarm optimization," *Engineering Optimization*, vol. 48, pp. 811-830, 2016/05/03 2016.
- [135] D. L. Poole and A. K. Mackworth, "Artificial Intelligence and Agents," in *Artificial Intelligence: Foundations of Computational Agents*, 1 edition ed New York: Cambridge University Press, 2010, pp. 3-42.
- [136] T. Bogaraj and J. Kanakaraj, "Intelligent energy management control for independent microgrid," *Sadhana - Academy Proceedings in Engineering Sciences*, vol. 41, pp. 755-769, 2016 2016.
- [137] (2018, 26-11-2019). *Electricity consumption per capita (kWh per person)*. Available: www.indexmundi.com
- [138] Observatoire régional de l'énergie et du climat (OREC), "Les Chiffres Clés de l'Énergie en Guadeloupe," ed, 2019.
- [139] Région Guadeloupe / DEAL. (26-11-2019). *Programmation Pluriannuelle de l'Énergie (PPE) 2016-2018/2019-2023 de la Guadeloupe*. Available: www.ecologique-solidaire.gouv.fr
- [140] European Network of Transmission System Operators for Electricity (ENTSO-E), "High Penetration of Power Electronic Interfaced Power Sources (HPoPEIPS): ENTSO-E Guidance document for national implementation for network codes on grid connection," 29-03-2017 ed.
- [141] Direction des Systèmes Énergétiques Insulaires (SEI) - EDF SA, "Bilan Prévisionnel de l'Équilibre Offre/Demande d'Électricité - Guadeloupe," ed, 2017.
- [142] Commission de régulation de l'énergie (CRE), "Mission de la CRE en Guadeloupe, à Saint-Martin et à Saint-Barthélemy," ed, 2018.

- [143] T. G. Margotin, "Etude du comportement dynamique du réseau de Guadeloupe : Règles de gestion de la réserve primaire et dimensionnement de la puissance unitaire des groupes futurs," *EDF RD*, 1999.
- [144] C. D. Montureux, "Prévisions des consommations électriques de la Guadeloupe : Rapport d'étude," *EDF RD*, 2002.
- [145] EDF. (2008). *Insertion de production éolienne et photovoltaïque dans les réseaux publics des zones non interconnectées*.
- [146] G. M. A. Delille, "Contribution du Stockage à la Gestion Avancée des Systèmes Électriques: approches Organisationnelles et Technico-économiques dans les Réseaux de Distribution," Ecole Centrale de Lille, 2010.
- [147] S. Nourdine, "Commande optimale d'aérogénérateurs pour la réduction de la fatigue mécanique et la régulation primaire de fréquence du réseau," Universidad del País Vasco, 2012.
- [148] Y. Wang, "Evaluation de la Performance des Réglages de Fréquence des Eoliennes à l'Echelle du Système Electrique : Application à un Cas Insulaire," Ecole Centrale de Lille, 2012.
- [149] A. D. Hansen, F. Iov, P. Sørensen, N. Cutululis, C. Jauch, F. Blaabjerg, *et al.*, *Dynamic wind turbine models in power system simulation tool DigSILENT*, 2007.
- [150] B. Wu, Y. Lang, N. Zargari, and S. Kouro, "Wind Generators and Modeling," in *Power Conversion and Control of Wind Energy Systems*, ed, 2011, pp. 49-85.
- [151] DigSILENT GmbH, *Technical Reference "DFIG Template DFIG WTG"*. Gomarigen, Germany, 2016.
- [152] C. M. Shepherd, "Design of Primary and Secondary Cells," *Journal of The Electrochemical Society*, vol. 112, pp. 657-664, 1965 1965.
- [153] O. Tremblay and L.-A. Dessaint, "Experimental Validation of a Battery Dynamic Model for EV Applications," *World Electric Vehicle Journal*, vol. 3, pp. 289-298, 2009-06-26 2009.
- [154] D. Hernandez-Torres, C. Turpin, X. Roboam, and B. Sareni, "Modélisation en flux d'énergie d'une batterie Li-Ion en vue d'une optimisation technico-économique d'un micro-réseau intelligent," in *Symposium de Génie Electrique (SGE'16) - EF-EPF-MGE 2016*, Grenoble, France, 2016, pp. 1-8.
- [155] Y. Zhang, S. Lyden, B. A. L. d. I. Barra, and M. E. Haque, "Optimization of Tremblay's battery model parameters for plug-in hybrid electric vehicle applications," in *2017 Australasian Universities Power Engineering Conference (AUPEC)*, 2017, pp. 1-6.
- [156] DigSILENT GmbH, *Technical Reference "Battery Energy Storing System Template"*, 2013.
- [157] Y. Eren, İ. B. Küçükdemiral, and İ. Üstoğlu, "Chapter 2 - Introduction to Optimization," in *Optimization in Renewable Energy Systems*, O. Erdinç, Ed., ed Boston: Butterworth-Heinemann, 2017, pp. 27-74.
- [158] D. M. Imboden and S. Pfenninger, *Introduction to Systems Analysis: Mathematically Modeling Natural Systems*, Springer-Verlag ed.: Springer, Berlin, Heidelberg, 2013.
- [159] MIT CSAIL. *Quadratic Programming with MATLAB and quadprog*. Available: <https://courses.csail.mit.edu/6.867/wiki/images/e/ef/Qp-quadprog.pdf>
- [160] J. A. Rossiter, *Model-Based Predictive Control: A Practical Approach*. Boca Raton: CRC Press, 2003.
- [161] E. F. Camacho and C. Bordons, "Introduction to Model Predictive Control," in *Model Predictive control*, ed London: Springer London, 2007, pp. 1-11.
- [162] L. Wang, *Model Predictive Control System Design and Implementation Using MATLAB*: Springer Publishing Company, Incorporated, 2009.
- [163] M. Almir, *A Pragmatic Story of Model Predictive Control: Self-Contained Algorithms and Case-Studies*: CreateSpace Independent Publishing Platform, 2013.
- [164] M. A. Xavier, "Efficient Strategies for Predictive Cell-Level Control of Lithium-Ion Batteries," Ph.D. Thesis, 2016.
- [165] M. Hovd, "A brief introduction to Model Predictive Control," Engineering Cybernetics Department, NTNU 2004.

- [166] T. Coleman and Y. Li, "A Reflective Newton Method for Minimizing a Quadratic Function Subject to Bounds on Some of the Variables," *SIAM Journal on Optimization*, vol. 6, pp. 1040-1058, November 1, 1996 1996.
- [167] R. López-Rodríguez, A. Aguilera-González, I. Vechiu, and S. Bacha, "Day-Ahead MPC Energy Management System for an Island Wind/Storage Hybrid Power Plant," *Energies*, vol. 14, 2021.
- [168] R. H. L. Rodriguez, I. Vechiu, S. Jupin, S. Bacha, Q. Tabart, and E. Pouresmaeil, "A new energy management strategy for a grid connected wind turbine-battery storage power plant," in *2018 IEEE International Conference on Industrial Technology (ICIT)*, 2018, pp. 873-879.
- [169] A. Aguilera-Gonzalez, I. Vechiu, R. H. L. Rodriguez, and S. Bacha, "MPC Energy Management System For A Grid-Connected Renewable Energy/Battery Hybrid Power Plant," in *2018 7th International Conference on Renewable Energy Research and Applications (ICRERA)*, 2018, pp. 738-743.
- [170] A. AGUILERA GONZALEZ, R. Lopez Rodriguez, H., and I. Vechiu, "Energy management system for a grid-connected wind farm and battery storage hybrid plant via MPC strategy," presented at the Journée Scientifique Nationale, GT Micro-réseaux, Systèmes d'Énergie Électrique dans leurs Dimensions Sociétales, SEEDS 2018, Compiègne, France, 2018.
- [171] A. Aguilera González, R. Lopez-Rodríguez, I. Vechiu, and B. Seddik, *Model Predictive Control for Optimal Energy Management of an Island Wind Storage Hybrid Power Plant*, 2020.
- [172] I. Vechiu, A. Etxeberria, Q. Tabart, and R. Lopez, "Operational limits of four wires three levels NPC topology for power quality improvement in weak grids," in *2016 IEEE 16th International Conference on Environment and Electrical Engineering (EEEIC)*, 2016, pp. 1-5.
- [173] M. Mehrasa, R. Godina, E. Pouresmaeil, I. Vechiu, R. López Rodríguez, and J. Catalao, *Synchronous active proportional resonant-based control technique for high penetration of distributed generation units into power grids*, 2017.
- [174] E. Pouresmaeil, M. Mehrasa, R. Godina, I. Vechiu, R. L. Rodríguez, and J. P. S. Catalão, "Double synchronous controller for integration of large-scale renewable energy sources into a low-inertia power grid," in *2017 IEEE PES Innovative Smart Grid Technologies Conference Europe (ISGT-Europe)*, 2017, pp. 1-6.
- [175] Saft Groupe S.A. (2013, 06-03-2017). *Intensium Max 20M: Medium power lithium-ion container 1MW – 580 kWh*. Available: <https://www.saftbatteries.com>
- [176] B. Gundogdu and D. T. Gladwin, "A Fast Battery Cycle Counting Method for Grid-Tied Battery Energy Storage System Subjected to Microcycles," in *2018 International Electrical Engineering Congress (iEECON)*, 2018, pp. 1-4.
- [177] S. K. Kerahroudi, M. M. Alamuti, F. Li, G. A. Taylor, and M. E. Bradley, "Application and Requirement of DIgSILENT PowerFactory to MATLAB/Simulink Interface," in *PowerFactory Applications for Power System Analysis*, F. M. Gonzalez-Longatt and J. Luis Rueda, Eds., ed Cham: Springer International Publishing, 2014, pp. 297-322.
- [178] M. Stifter, F. Andrén, R. Schwalbe, and W. Tremmel, "Interfacing PowerFactory: Co-simulation, Real-Time Simulation and Controller Hardware-in-the-Loop Applications," in *PowerFactory Applications for Power System Analysis*, F. M. Gonzalez-Longatt and J. Luis Rueda, Eds., ed Cham: Springer International Publishing, 2014, pp. 343-366.
- [179] J. Garcia-Villalobos, I. Zamora, M. Marinelli, P. Eguia, and J. I. San Martin, "Co-simulation with DIgSILENT PowerFactory and MATLAB: Optimal Integration of Plug-in Electric Vehicles in Distribution Networks," in *Advanced Smart Grid Functionalities Based on PowerFactory*, F. Gonzalez-Longatt and J. L. Rueda Torres, Eds., ed Cham: Springer International Publishing, 2018, pp. 67-91.
- [180] S. Roy, O. P. Malik, and G. S. Hope, "Adaptive control of speed and equivalence ratio dynamics of a diesel driven power-plant," *IEEE Transactions on Energy Conversion*, vol. 8, pp. 13-19, 1993.
- [181] DIgSILENT GmbH, *Technical Reference "PWM Converter"*, 2016.

(This page is intentionally left blank)

Publications

International journals

- [167] R. López-Rodríguez, A. Aguilera-González, I. Vechiu, and S. Bacha, "Day-Ahead MPC Energy Management System for an Island Wind/Storage Hybrid Power Plant," *Energies*, vol. 14, 2021.

International conferences

- [168] R. H. L. Rodriguez, I. Vechiu, S. Jupin, S. Bacha, Q. Tabart, and E. Pouresmaeil, "A new energy management strategy for a grid connected wind turbine-battery storage power plant," in *2018 IEEE International Conference on Industrial Technology (ICIT)*, 2018, pp. 873-879.
- [169] A. Aguilera-Gonzalez, I. Vechiu, R. H. L. Rodriguez, and S. Bacha, "MPC Energy Management System For A Grid-Connected Renewable Energy/Battery Hybrid Power Plant," in *2018 7th International Conference on Renewable Energy Research and Applications (ICRERA)*, 2018, pp. 738-743.
- [170] A. AGUILERA GONZALEZ, R. Lopez Rodriguez, H., and I. Vechiu, "Energy management system for a grid-connected wind farm and battery storage hybrid plant via MPC strategy," presented at the Journée Scientifique Nationale, GT Micro-réseaux, Systèmes d'Énergie Électrique dans leurs Dimensions Sociétales, SEEDS 2018, Compiègne, France, 2018.
- [171] A. Aguilera González, R. Lopez-Rodríguez, I. Vechiu, and B. Seddik, *Model Predictive Control for Optimal Energy Management of an Island Wind Storage Hybrid Power Plant*, 2020.
- [172] I. Vechiu, A. Etxeberria, Q. Tabart, and R. Lopez, "Operational limits of four wires three levels NPC topology for power quality improvement in weak grids," in *2016 IEEE 16th International Conference on Environment and Electrical Engineering (EEEIC)*, 2016, pp. 1-5.
- [173] M. Mehrasa, R. Godina, E. Pouresmaeil, I. Vechiu, R. López Rodríguez, and J. Catalao, *Synchronous active proportional resonant-based control technique for high penetration of distributed generation units into power grids*, 2017.
- [174] E. Pouresmaeil, M. Mehrasa, R. Godina, I. Vechiu, R. L. Rodríguez, and J. P. S. Catalão, "Double synchronous controller for integration of large-scale renewable energy sources into a low-inertia power grid," in *2017 IEEE PES Innovative Smart Grid Technologies Conference Europe (ISGT-Europe)*, 2017, pp. 1-6.

(This page is intentionally left blank)

Annex A: Governor and turbine models for generators

The governor model for diesel machines implemented represents a diesel turbine with 20,9 MW nominal power and inertia of 2,08 MWs/MVA [5]. The model formulations are described in [180].

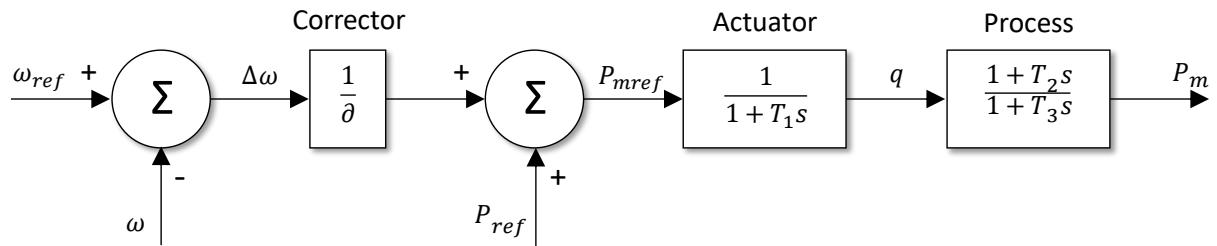


Fig. A.1. Model of diesel turbine participation to primary frequency control.

Fig. A.1 depicts the model of a diesel generator participating to primary frequency control (proportional-action to control the generator speed). Eq. A.1 describes the control law of the frequency controller:

$$P_{mref} = P_{ref} + \frac{\Delta\omega}{\delta} \quad \text{Eq. A.1}$$

where

P_{mref} : reference power (pu)

P_m : mechanical power (pu)

ω_{ref} : reference speed (pu)

ω : generator speed (pu)

$\Delta\omega$: generator speed deviation (pu)

δ : slope of the droop

q : fuel Flow (pu)

The values employed for the parameters are presented in Table A.1.

Table A.1. Diesel governor parameters.

Name	Description	Unit	Value
δ	Slope of the droop	pu	0,04
T1	Actuator time constant	s	0,09
T2	Diesel generator model time constant	s	5,56
T3	Diesel generator model time constants	s	7,52

Fig. A.2 shows the control system diagram representing the governing action for steam turbines. A 32 MW turbine with an inertia of 3,36 MWs/MVA is represented [5].

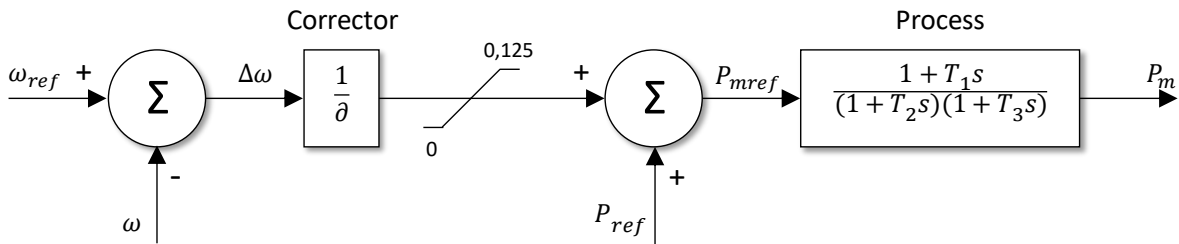


Fig. A.2. Modelisation of steam turbine participation to primary frequency control.

The parameters values are presented in Table A.2.

Table A.2. Steam turbine governor parameters.

Name	Description	Unit	Value
δ	Slope of the droop	pu	0,04
T1	Diesel generator model time constant	s	0,18
T2	Diesel generator model time constant	s	51
T3	Diesel generator model time constants	s	44